Functionalized Lignin derivatives for Flame Retardant, Thermal Insulation, and Coating applications

A Thesis Submitted to the faculty of Graduate Studies of
Lakehead University
by

Saba Khodavandegar

Submitted in partial fulfillment of requirements for the degree of

Doctor of Philosophy in Chemistry and Material Science

Dedication

"To my dearest Dad, Ali and Mom, Mahdieh, your love and belief in me have shaped every step of my life. I owe this journey to your strength and endless support"

"To my beloved husband, Amir, thank you for being my constant source of love, my calm in the storm, and my greatest encourager. This work is as much yours as it is mine"

Abstract

Lignin, a highly branched and heterogeneous biopolymer composed of phenolic units, is a key structural component of plant cell walls, providing mechanical strength, water resistance, and protection against microbial degradation. Due to its complex chemical structure and functional versatility, lignin has gained significant attention for its potential applications in biomaterials, emulsifiers, and sustainable industrial processes. Chitosan, a biopolymer derived from chitin, is widely recognized for its biocompatibility, biodegradability, and antimicrobial properties, making it a valuable material for various industrial and biomedical applications. When combined with lignin, the resulting composite benefits from enhanced structural stability, improved functional properties, and synergistic effects, offering promising potential for sustainable biomaterials, emulsifiers, and advanced functional coatings. In this thesis, functionalized lignin was produced following different pathways and used as an emulsifier for oil-water emulsions and advanced coating applications. It was also combined with chitosan to develop multifunctional materials with enhanced thermal insulation properties.

The first experimental part of this thesis presents a method for producing a phosphorylated lignin-derived (PK) flame retardant following a solvent-free polycondensation reaction of kraft lignin (KL) and phytic acid (PHA). The reaction was optimized for low temperature and high decomposition temperature. Advanced techniques confirmed the covalent bonding between PHA and KL oxygen, resulting in high decomposition temperature and char formation. The study provided a new approach for preparing a fully bio-based flame retardant with limited smoke density and higher limiting oxygen index, following a green chemistry concept.

The second experimental chapter utilized optimized reaction conditions to produce lightweight, thermally insulated, and flame-retardant aerogels (APK) from chitosan (CH) and phosphorylated kraft lignin (PK). The production process improved porosity reduced thermal conductivity, and enhanced compression strength, making APK an excellent thermal insulator for construction.

The third experimental part of this thesis explores the production of sustainable aerogels from carboxymethylated lignin (CM), a biodegradable material with a lower environmental footprint. The research found that increasing the charge density of CM intensified the crosslinking bond between CM and chitosan (CH), reducing porosity and compression strength, and increasing thermal conductivity. The least charged CM (CM1) aerogel had the least thermal conductivity and the highest compression strength. The results of this chapter suggest a promising strategy for creating eco-friendly, sustainable aerogels.

The fourth experimental section of this thesis investigated the interaction between lignin derivatives and oil and water in emulsion systems. The reaction condition for the charge density of -1.5 mmol/g was optimized with Taguchi for both sulfoethylation (SL) and carboxyethylation (CL) of kraft lignin (KL). These modifications were found to generate functional emulsifiers for soybean emulsions at different pH levels, such as 3, 7, and 11. The study found that SL and CL produced Pickering emulsions with oil droplet sizes of 436 and 452 nm at acidic pH but had shorter lifespans under acidic conditions. The study also found that SL had higher elasticity and interaction at pH 11, highlighting the importance of lignin upgrading techniques in generating functional emulsifiers.

Overall, this thesis advances the development of multifunctional materials by combining functionalized lignin with chitosan, resulting in enhanced thermal insulation and flame retardancy. The research introduces innovative methods for producing bio-based flame retardants, lightweight aerogels, and sustainable emulsifiers, highlighting the potential of lignin in various industrial applications. The findings contribute to the creation of environmentally friendly, high-performance materials with improved structural stability and functional properties.

Acknowledgments

First and foremost, I would like to express my deepest gratitude to my supervisor, Prof. Pedram Fatehi, for welcoming me into his research group and for his unwavering support, guidance, and encouragement throughout my Ph.D. journey. His dedication, perseverance, and achievements serve as a true source of inspiration, and I am honored to have had him as a mentor. Beyond academic mentorship, his kindness and support have extended to a personal level, impacting my growth as a researcher and individual. I sincerely appreciate the resources, equipment, financial assistance, and emotional support he has provided to ensure the successful completion of my doctoral studies.

I would like to extend my sincere gratitude to professors Peter Rättö and Ulrica Edlund from RISE and KTH for their invaluable support during my exchange time in Stockholm, Sweden**.** Their assistance, guidance, and generosity greatly contributed to the success of my research. I truly appreciate their willingness to share their expertise and provide the necessary resources, which significantly enriched my experience. Thank you for your kindness and support throughout this journey.

I also extend my heartfelt appreciation to my thesis committee members, Dr. Baoqiang Liao, Dr. Maryam Ebrahimi**,** and Dr. Zongquan Li for their time, constructive feedback, and invaluable insights. Their expertise has been essential in refining my research and strengthening my work.

My appreciation extends to Dr. Weijue Gao for her continuous collaboration, support, and valuable contributions throughout my research. I am immensely grateful to my past and present lab colleagues, who have been an integral part of my journey. Their support and advice have enriched my research experience, and I truly appreciate the kindness and professionalism they have shown from my first day in the lab until now. I want to extend my appreciation to my colleagues, Dr. Banchamlak Bemerw Kassaun and Rozita Zare, for the collaboration outside of this thesis work.

Special thanks to Dr. Guosheng Wu and Mr. Michael Sorokopud from the LUIL department at Lakehead University for their technical expertise and assistance. I also wish to express my heartfelt appreciation to

Dr. Robert Mawhinney as program coordinator and Dr. Brenda Magajna as Ph.D. Program Facilitator and International Student Liaison for unwavering support.

I am forever indebted to my family, whose love, sacrifices, and encouragement have made this achievement possible. Their unwavering belief in me has been my greatest source of motivation. Family is not just one of the important things in life. It is everything.

To my friends, I deeply appreciate your presence and unwavering support throughout this journey. Your friendship has been a source of strength, and I am grateful to have you by my side.

Above all, my deepest love and appreciation go to my love, Amir. Words cannot express how much your kindness, support, and love have meant to me throughout my Ph.D. studies. Your encouragement and unwavering belief in me have been my foundation, and every achievement of mine is equally yours. Thank you for always being there.

Lastly, I would like to acknowledge the financial support from NSERC Canada and MITACS, whose funding has made my Ph.D. studies and living expenses possible. Their support has been instrumental in the completion of this work.

“علم، انسانین قارانلیقدان نوره چیخان یولودور.

علم ، اورَیین ایشیغی، آغلین گؤزگوسودور.

بو یول آسان اولمادی، آما هر آدیمیندا امید واریدی.

بو صحیفه‌لرده‌کی هر جمله، ایللرین زحمتی‌نین سس‌سیز شاهیدی‌دیر.

علم یولوندا یورولسام دا، دؤنمدیم.

چونکی آگاه‌لیغا آپاران یول، منیم حیاتیمین مناسی‌دیر.”

«من یانیمدا اولان هر بیر عزیزه چوخ تشکر ائدیرم»

Table of Contents

List of Tables

List of Figures

Chapter 1: Introduction

1.1. Biopolymers

Lignin, the most abundant biopolymer in nature that is composed of aromatic subunits, is gaining increasing attention for its applications beyond traditional uses (combustion for energy, plasticizer, etc.). It is now being explored for its potential in advanced materials, including aerogels, thermal insulation, flame retardants, emulsions, and packaging coatings. The functionalization of lignin is expected to expand globally through biorefinery processes, driven by its unique properties such as UV resistance, biodegradability, thermal stability, mechanical strength, and moisture resistance. Due to their complementary properties, Lignin and chitosan are essential biopolymers for aerogel fabrication. Lignin provides rigidity and thermal stability, while chitosan enhances flexibility and reinforcement. This results in a structurally robust aerogel. Chitosan creates a porous network, improving thermal insulation efficiency. Lignin's aromatic structure increases flame and moisture resistance. Both materials are renewable and biodegradable, making them suitable for sustainable applications. Additionally, lignin enhances the stability of emulsions and improves coatings, contributing to the development of more sustainable and high-performance products. However, challenges, such as variability in purity, molecular weight, and limited solubility, hinder its direct application in high-value industries. Continued research and innovation are crucial to addressing these limitations and unlocking lignin’s full potential in thermal insulation, coatings, advanced manufacturing, and other industrial applications.

1.2. Hypothesis and research objectives

The hypotheses of this thesis were as follows:

I. Lignin modification pathways, such as phosphorylation and carboxylmethylation, can promote the performance of lignin in aerogel fabrication for thermal insulation and flame retardant applications. Such performance can be controlled by charge density, temperature, concentration, and molecular weight of lignin.

II. The molecular weight of chitosan can influence the porosity, density, and flame retardancy of chitosan-lignin aerogels. Chitosan molecular weight can influence chitosan-lignin aerogels' structural and functional properties, specifically their porosity, density, and flame retardancy. The resultant aerogel provides new insights into the

tunability of bio-based aerogels, paving the way for the development of advanced, sustainable materials with optimized thermal insulation.

III. Lignin modification through phosphorylation, carboxyethylation, and sulfoethylation offers a novel strategy for enhancing its performance as a bio-based flame retardant coating material for wood and paper products. The unique potential of these modifications can improve thermal stability and flame retardancy (due to the presence of phosphorus, carbonyl, and sulfonate groups), providing an innovative, sustainable alternative to conventional synthetic coatings while expanding the functional applications of lignin in advanced material development.

IV. The functionalization of lignin with sulfoethyl and carboxyethyl groups presents a novel approach to tailoring its amphiphilic, electrostatic stabilization, increase surface activity properties, potentially enhancing its performance as a sustainable emulsifier for oil-water emulsions. The unique impact of these modifications on interfacial stability, emulsification efficiency, and long-term emulsion stability offers an innovative, bio-based alternative to conventional synthetic emulsifiers.

V. Lignin-stabilized emulsions can improve their coating performance on paper products by enhancing barrier properties, hydrophobicity, and adhesion. Optimizing lignin modification and emulsion formulation improves moisture resistance and durability, offering a sustainable alternative to synthetic coatings.

The overall objective of this research was to investigate the effects of lignin modification on lignin-based aerogels, emulsions, and coatings for sustainable material applications. It focuses on enhancing lignin's performance in thermal insulation and flame retardant applications, evaluating lignin modification with different molecular weights of chitosan and their impact on aerogel porosity, density, and flame retardancy. Moreover, assessing the effect of lignin modifications on coating materials and optimizing lignin-stabilized emulsions for improved coating performance.

1.3. Novelty

I. A novel lignin modification was developed for sustainable applications in flame retardancy, thermal insulation, and emulsion stabilization. While lignin has been explored for such uses, existing methods often suffer from limited functionality or environmental concerns. This work introduces a new route that enhances lignin's versatility across these critical applications. The production of fully bio-based phosphorus-containing flame retardant derived from lignin and phytic acid, developed via a sustainable, solvent-free polycondensation process.

II. The production of a fully bio-based phosphorus-containing flame retardant, derived from lignin and phytic acid through a solvent-free polycondensation process, addresses the growing demand for green alternatives to synthetic flame retardants. Prior studies have explored phosphorus-lignin systems, but this synthesis route stands out for its renewability, simplicity, and absence of toxic solvents.

III. A key discovery was that phosphorylated lignin materials exhibit enhanced thermal stability, reduced smoke emission, and improved flame retardancy, offering a green substitute for halogenated (toxic) flame retardants. This surpasses conventional lignin modifications in both safety and performance, aligning with modern regulations and sustainability trends.

IV. A novel chitosan–phosphorylated kraft lignin aerogel was created with improved flame retardancy, thermal insulation, and mechanical properties, offering a bio-based alternative to petroleum-derived thermal insulators. Unlike many existing aerogels, which are either fragile or unsustainable, this material demonstrates both structural integrity and eco-compatibility.

V. A biodegradable aerogel based on carboxymethylated lignin and chitosan was developed, featuring tunable thermal and mechanical properties controlled via charge density modification. This contributes to the relatively limited body of work on structurally adaptable, sustainable aerogels suitable for insulation.

VI. A novel approach to developing sustainable emulsifiers was demonstrated by sulfoethylating and carboxyethylating lignin, revealing their distinct roles in emulsion stability via electrostatic and steric mechanisms across various pH conditions. Compared to conventional synthetic or protein-based emulsifiers, this strategy offers a renewable, biodegradable, and chemically tunable alternative, addressing performance and environmental concerns.

These discoveries promote the sustainable use of lignin in environmentally friendly materials and compositions, advancing its industrial potential.

1.4. Research overview

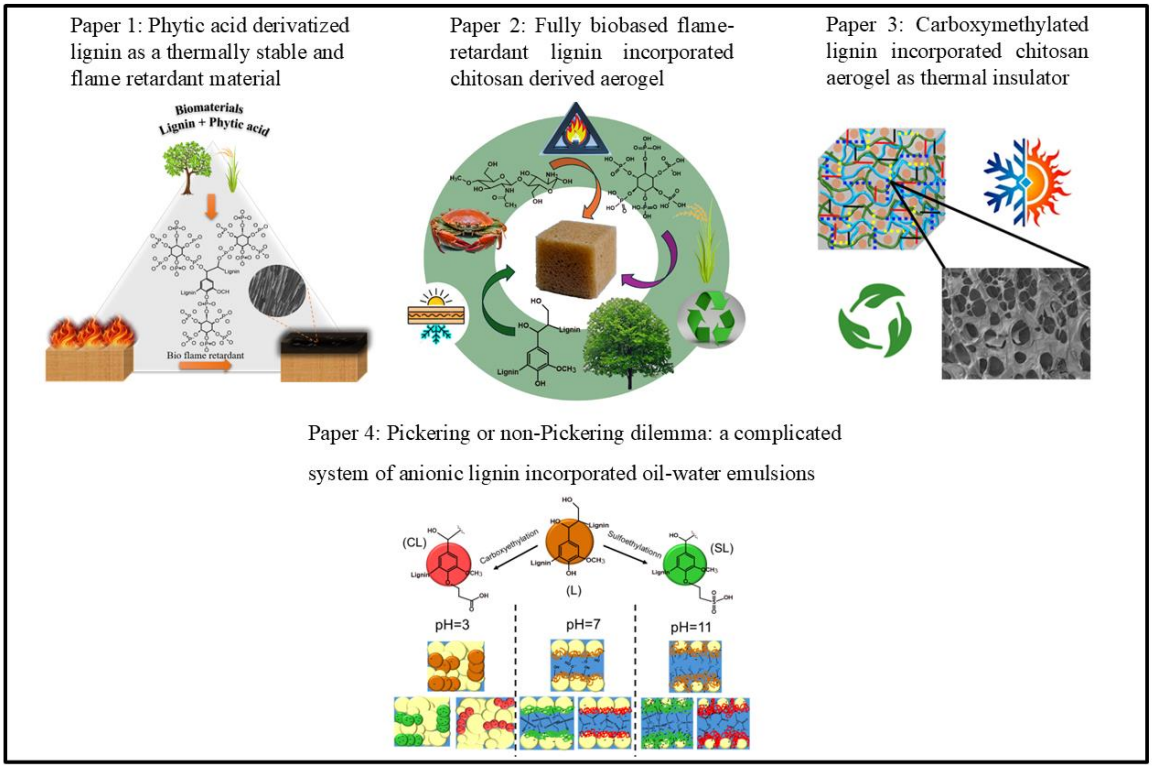

Figure 1.1. Research overview.

Each chapter provides the following objectives and novelties of this thesis:

Chapter one provides the introduction of this thesis.

Chapter two presents a thorough literature review examining and exploring various strategies for modifying lignin to prepare it for different applications. Additionally, recent research and advancements in optimizing lignin as flame retardant or additives to enhance thermal insulation aerogels, coating solutions, and emulsion stabilizers were reviewed.

Chapter three provides a methodology to create a new reactive bio-based flame retardant, which describes the modification of kraft lignin using the bio-based reagent, phytic acid ($C_6H_{18}O_{24}P_6$), PHA, in a simple solvent-free reaction at a low temperature. This effort aimed to produce phosphorylated lignin (PK) with superior flame retardancy by optimizing the reaction parameters. Additionally, the chemical characteristics of the produced lignin derivative were thoroughly examined using advanced chemical analysis methods, such as ^{1}H NMR, ^{31}P NMR, HSQC-NMR, XPS, ICP-AES, SEM, TGA, and DSC. Additionally, the flame retardant properties of PK-coated wood and paper samples were examined using smoke density and limiting oxygen index analyzers.

Chapter four demonstrates the research to create a novel, robust, entirely biobased aerogel containing phosphorylated lignin (PK) with chitosan (CH) that has thermal insulation and flame retardant properties. The induced aerogel's physicochemical properties were thoroughly described using FTIR, NMR, XRD, and XPS. BET, SEM, and a compression analysis were used to evaluate the aerogel's mechanical and structural characteristics. UL-94 flammability analyzers, smoke density, limiting oxygen index (LOI), and TGA were used to examine the aerogel's thermal and flame retardant properties. The findings of this study demonstrate that the recently produced lignin-incorporated aerogel may be a viable substitute for the building sector, where mechanical strength, flame resistance, and thermal insulation are essential for biodegradable aerogel applications.

Chapter five investigated the production of chitosan (CH) and carboxymethylated lignin (CM) aerogels with varying charge densities (CM1, CM2, and CM3). Furthermore, the effects of a particular lignin derivative, ACM1, on aerogel characteristics were evaluated. Notably, no hazardous chemicals were used in the production of this aerogel, according to the fundamental idea of green chemistry. The porosity, viscosity, and mechanical characteristics of the produced aerogels were found to decrease with increasing charge density. Nevertheless, the product's thermal conductivity rose, lowering its thermal insulation efficacy. Additionally, adding lignin derivative to the aerogels increased their Young's modulus (structurally stable and durable) and reduced their thermal conductivity, but it also collapsed their porosity, which, in turn, affected their mechanical and thermal conductivity. Additionally, the biodegradation investigation verified the sustainability and biodegradability. It is interesting to note that the generated aerogel may apply to the thermal insulation construction sector.

Chapter six examined the effect of lignin’s efficacy with two modifications of sulfoethylation and carboxyethylation as an emulsifier. In order to ensure consistent comparison between two changes and investigate their stability in emulsions, each alteration was adjusted using Taguchi to reach a charge density of -1.5 mmol/g. It is thought that lignin's ability to stabilize an emulsion system, including soybean oil, would be enhanced by sulfoethylation and carboxyethylation. The microstructure and interaction of water and oil may be impacted by changes in pH that would alter the size of the particles and the activity of the functional groups. The stability of the solutions and emulsion system was studied through the TSI, Dh, and ζ-potential. Moreover, the particle interactions were investigated by confocal microscopy. To expand the usage of lignin in emulsion systems, this work aimed to examine how two

distinct lignin modifications could impact the stability of soybean oil emulsions across a range of pH values (3, 7, 11).

Chapter seven summarizes the main findings of this thesis and offers a viewpoint for further research in this area.

Chapter 2: Literature review

2.1. Abstract

Lignin, a complex biopolymer obtained from lignocellulosic biomass, is a sustainable alternative for petrol-based materials and has drawn more attention. However, chemical or physical changes are required because of their intrinsic heterogeneity, high polydispersity, purity, and low solubility. In this chapter, different modification routes and the effect of properties of lignin on its performance as a thermal insulator and flame retardant were investigated. Furthermore, lignin functionality as a natural emulsifier to stabilize emulsions for different industrial applications was discussed. Moreover, lignin's affinity as a coating material for paper products was reviewed. This review demonstrates lignin's versatility and potential as a sustainable replacement for high-performance materials.

2.2. Introduction

The production of synthetic materials faces challenges, such as environmental impact, resource depletion, regulatory pressures, and supply chain disruptions [1]. Synthetic materials contribute to pollution, while non-renewable resources like fossil fuels are unsustainable [2]. Biomaterials are sustainable alternatives due to their renewable nature, biodegradability, lower carbon footprint, and versatility with different applications [3]. Biodegradable plastics, water purifiers, and controlled-release fertilizers are examples of these applications [4-5]. Biocomposites, made from natural fibers and biopolymers, are used in the construction industry for their strength, durability, and sustainability [6]. Insulation materials, like cellulose and hemp, provide energy-efficient alternatives to synthetic materials [7]. Integrating biomaterials into these sectors can significantly reduce our dependence on petroleum-based materials. Biomaterials, including those derived from biopolymers like lignin, are increasingly used in sustainable applications to replace synthetic materials across various industries.

Biopolymers are derived from plants, bacteria, and other biological materials, reducing dependence on non-renewable petrochemicals (plastics, resins, adhesives, etc.) [8]. Advances in biopolymer technology have led to materials that match or exceed traditional plastics in performance and align with the principles of a circular economy, promoting resource efficiency and waste reduction [9, 10].

Given the pressing need to replace non-renewable petrochemicals with sustainable alternatives, lignin emerges as a highly promising biopolymer due to its abundance, unique properties, and versatility in various advanced material applications [11]. Lignin is the second most abundant natural polymer on Earth, and it is used in flame retardants and thermal insulation. It contributes to the mechanical strength of composite materials, making it an environmentally friendly alternative to synthetic polymers [12]. Lignin, mostly wood-derived, is a by-product of the paper and pulp industries that is used to build as black liquor [13]. Lignin is a complex polymer comprising phenolic precursors, with coniferyl alcohol, sinapyl alcohol, and p-coumaryl alcohol as its main backbone [14]. Its complex structure with aromatic subunits provides rigidity, thermal stability, hydrophobicity, biodegradability, and mechanical strength [15]. Lignin's high thermal stability makes it suitable for heat-resistant applications, moisture-resistant coatings, and emulsions, making it an environmentally friendly alternative [16, 17]. Nevertheless, lignin's poor solubility continues to be a major problem, which can be solved by several chemical changes. A water-based medium is crucial for lignin applications because it promotes environmental sustainability, facilitates processability, and allows for compatibility with aqueous systems needed for coatings, emulsions, and other bio-based products.

As highlighted in this study, lignin modifications in water-based medium have garnered significant attention in recent years due to their potential applications across various industries. To enhance lignin’s properties for applications, such as thermal insulation, flame retardancy, coatings, packaging, and emulsions, most research has focused on modifying its characteristics through polymerization, grafting, functionalization, and their combinations. This review systematically categorizes and discusses the nature of biopolymers, such as lignin and chitosan, and their modifications, particularly in improving their solubility, charge density, and flame retardant properties. Furthermore, the current literature is examined from an application-oriented perspective, covering topics including lignin modifications, aerogels, emulsions, coatings, thermal insulation, and flame retardants. The challenges, emerging trends, and future prospects of lignin-based materials in these applications are analyzed, providing insights into their development and potential advancements.

2.3. Lignin

Lignin is a key evolutionary adaptation that enabled plant colonization of land by reinforcing cell walls, forming hydrophobic xylem vessels for water transport, and providing structural support through its co-localization with cellulose and hemicellulose in the plant cell wall matrix (Figure 2.1) [18]. Lignin, a paper industry byproduct, is

biosynthesized as lignocellulose and nonconjugated lignin. Various processing methods have been developed to isolate lignin, each with trade-offs regarding reagents and energy required [19]. The kraft-pulping process produces the largest amount of lignin as a byproduct, with approximately 75 million tons produced in the late 1980s [20]. While this amount is slightly lower than the 1980s estimate, it's important to note that only about 2% of this lignin is currently recovered for utilization in applications beyond energy production. Sulfite pulping is another process for the production of lignin, which is the basic process of cleaving α-ether linkages and β-ether linkages during the pulping process [21]. The soda process is the oldest pulping method used to process non-wood material, such as bagasse, sisal, kenaf, hemp, and wheat straw [22]. Although organosolv lignin is sulfur-free and has a low molecular weight, its production involves using organic solvents and energy-intensive processes that can lead to environmental concerns such as solvent emissions, wastewater contamination, and increased carbon footprint [23]. Steam explosion lignin requires high pressure and temperature, resulting in low molecular weight and good solubility in organic solvents [24]. Dilute acid lignin can be produced by pretreatment of biomass feedstock via dilute sulfuric acid, but the overall conversion rate is low and contains sugar-derivative impurities [25]. LignoForce and lignoBoost are two advanced commercialized lignin extraction processes designed to recover high-purity lignin from black liquor in kraft pulping. Understanding how lignin processing can change the chemistry and properties of the material is crucial for researchers.

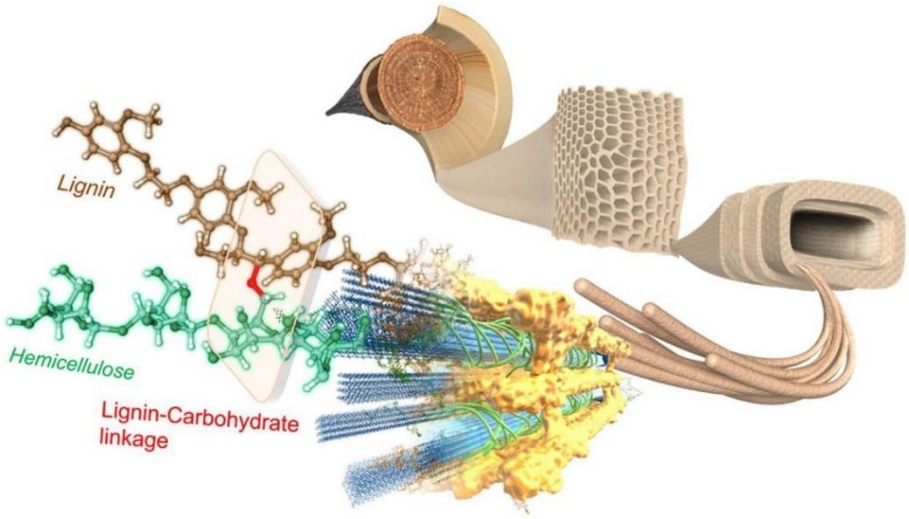

Figure 2.1: A three-dimensional view of the lignin–carbohydrate complex in the wood cell wall [18].

Lignin, a polymer with a complex cross-linking structure, contains aliphatic hydroxyl, phenolic hydroxyl, and methoxyl groups. These groups affect the molecule's reactivity and chemical properties [26]. Lignin precursors

include p-coumaryl alcohol, coniferyl alcohol, and sinapyl alcohol (**Figure 2.2**). Lignin from different plants comprises different percentages of these precursors [27]. Lignin is a polymer composed of various ether and carbon-carbon bonds, contributing to its complexity and rigidity. Common linkages include β-O-4 Arylglycerol ether bonds (45-50%), β-5 phenylcoumaran bonds (9-12%), β-β resinol bonds (5-10%), 5-5 biphenyl bonds (19-25%), 4-O-5 diaryl ether bonds (7-10%), α-O-4 ether bonds (7-8%), and β-1 Spirodienone bonds (3-5%) [29-31]. Softwoods have a higher proportion of these linkages, making them more condensed and resistant to degradation, while hardwoods have more β-O-4 ether linkages, making their lignin easier to break down. Understanding these linkages is crucial for developing efficient biorefinery processes to break down lignin into valuable bioproducts.

Lignin's poor compatibility with polymer matrices limits its practical application, requiring chemical modifications to improve integration despite its valuable antioxidant, UV-stabilizing, and flame retardant properties. Phenolic hydroxyl groups in lignin are responsible for its antioxidant behaviour, which can neutralize free radicals and inhibit oxidative degradation [32, 33]. Lignin can be transformed into valuable products through chemical and physical methods, such as polymerization, depolymerization, grafting, catalytic conversion, irradiation, plasma treatment, etc. [34, 31].

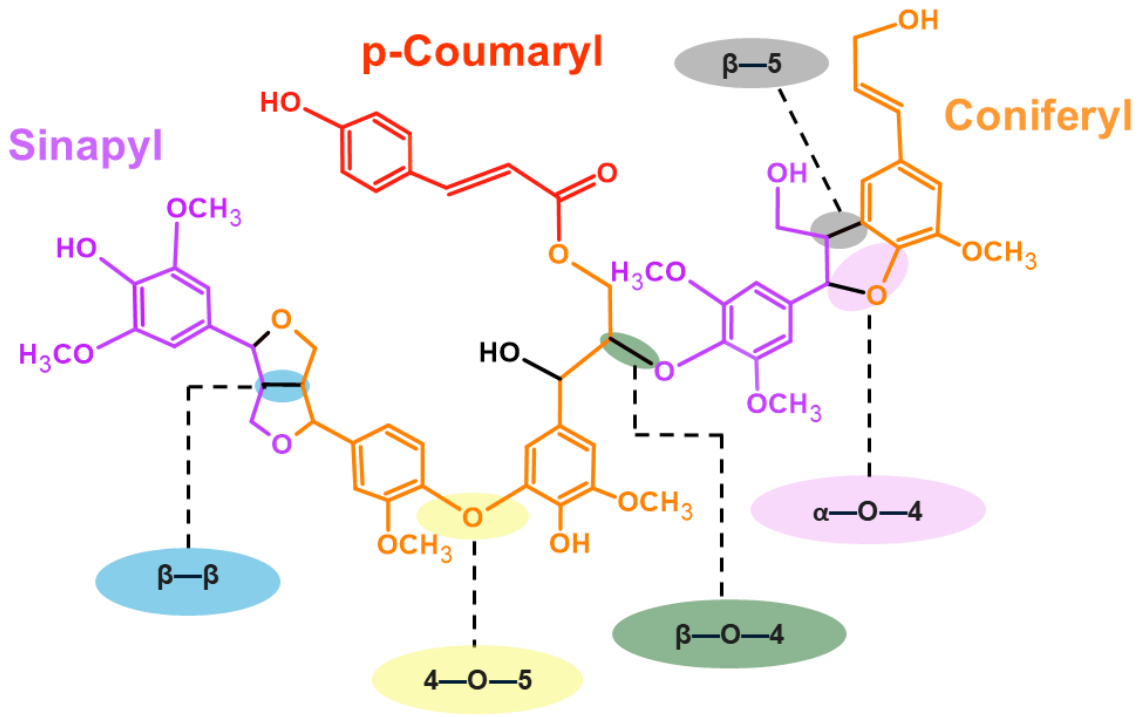

Figure 2.2: Schematic structure of lignin and linkages.

2.3.1. Chemical modification

Lignin modification is crucial for improving purity, enhancing solubility, increasing reactivity, and improving flame retardancy [35]. Lignin can be modified through various chemical methods to improve its properties and applications. Key modifications include etherification, esterification, acetylation, grafting, sulfonation, etc. Etherification enhances solubility in organic solvents, making it suitable for coatings and adhesives [36]. Acetylation reduces hydrogen bonding, making it useful for flexible films and fibers [37]. Grafting improves Lignin's reactivity and compatibility with other materials, which is enhanced by attaching functional groups like carboxyl, sulfonate, phosphorus, or other groups, which is the focus of this thesis [38].

2.3.1.1. Phosphorylation

Phosphorylation is a chemical modification that introduces phosphate groups into lignin, enhancing its properties like flame retardancy and thermal stability [39]. Because lignin contains reactive hydroxyl groups, phosphate groups can form covalent bonds with them, improving the material's performance in various applications [40]. Phosphorylation plays a crucial role in enhancing the properties of lignin, thereby increasing its suitability for diverse industrial applications. A key advantage of this modification is the improvement in flame retardancy, as the incorporation of phosphorus facilitates char formation and decreases flammability, making phosphorylated lignin a valuable additive in flame resistant materials [41]. Furthermore, phosphorylation enhances the thermal stability of lignin, rendering it more resistant to elevated temperatures [42]. This chemical modification also improves lignin’s reactivity, broadening its potential applications in various chemical processes and industrial formulations [43].

Lignin can be phosphorylated through various methods, each utilizing distinct reagents and reaction conditions, some of which are reported in Table 2.1. A widely used approach involves treating lignin with phosphoric acid, which incorporates phosphate groups and enhances its flame retardant properties [42]. Another technique employs thiophosphoryl chloride, which not only improves flame resistance but also increases thermal stability. Additionally, O, O-dialkylthiophosphoric acid chloride can be used for phosphorylation, further strengthening lignin’s flame-retardant characteristics [44]. These modification strategies allow for the customization of lignin’s properties, enhancing its versatility and industrial applicability. This process promotes char formation, reduces flammability, increases thermal stability, and enhances reactivity, making lignin suitable for flame retardant materials and high-temperature resistance polymer composite applications [45].

Table 2.1: Different Phosphorylation Methods for lignin.

Lignin type	Reagent	Solvent	Application	Ref
Hydrolysis	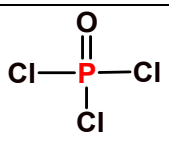 Orthophosphoric acid	Urea	Epoxy resin fillers and flame retardant	[45]
Kraft	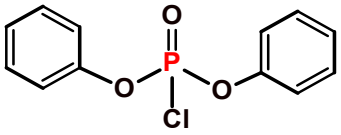 Diphenyl phosphoro chloride	Pyridine	Flame retardant	[46]
Organosolv and alkali	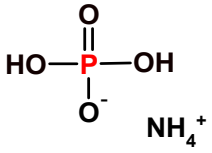 Ammonium phosphate	Acetonitrile	Flame retardant	[47]
Kraft	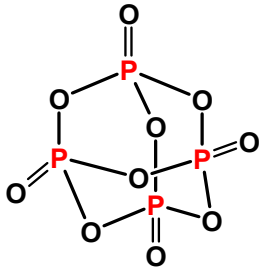 Phosphorus pentoxide	Tetrahydrofuran	Flame retardant	[48]
Alkali wheat straw	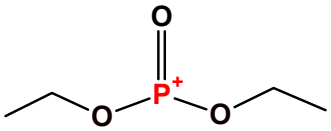 Diethyl phosphite	Formaldehyde and dimethylformamide	Flame retardant	[49]

2.3.1.2.Carboxylation

Carboxylation is a modification technique that introduces carboxyl (-COOH) and alkyl (-R) groups into the lignin structure. This modification increases solubility and improves its adaptability for various uses. Moreover, the introduction of this functional group makes lignin more reactive and interacts with other substances. Adding these

functional groups raises lignin's charge density (due to the carboxyl group's negative charge), making it suitable for electrostatic interaction [50]. These enhancements make it highly suitable for applications in aqueous-based formulations, wastewater treatment, coatings, adhesives, and packaging [51]. Moreover, this is crucial for applications such as emulsion stabilization, where repulsive forces between particles prevent aggregation and improve stability. A summary of the techniques for adding carboxyalkyl groups to lignin is tabulated in Table 2.2, which lists the different reactions and reagents for carboxyalkylating lignin. This table comprises the application of reagents with distinct benefits regarding reaction efficiency and product characteristics, such as sodium chloroacetate and 2-chloropropionic acid. Carboxyalkylated lignin can be utilized as a sustainable dispersant in coal water slurry, a functionalized lignin in nanocomposites, a flame retardant in polymers, and in cosmetic formulation due to its biodegradability and non-cytotoxicity [52].

Table 2.2: Different Carboxyalkylation Methods for lignin.

Lignin type	Reagent	Solvent	Type of alkylation	Application	Ref
Kraft	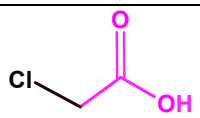 Chloroacetic acid	Ethanol	Methylation	Oil in water emulsion stabilizer	[53]
Hardwood kraft	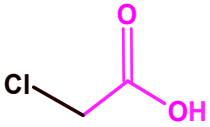 Chloroacetic acid	Water	Methylation	Clay suspension dispersant	[54]
Kraft	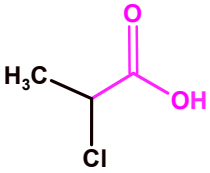 2-chloropropinic acid	Water and isopropyl alcohol	Ethylation	Dispersant	[55]
Lignosulfonate	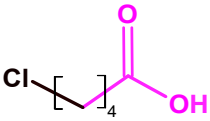 5-chlorovaleric acid	Water	Butylation	Oil in water emulsion stabilizer	[56]
	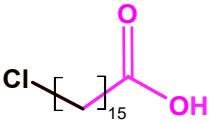 Bromohexadecanoic acid		Carboxypantadecanation		
	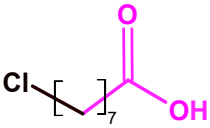 8-bromooctanoic acid		Carboxyheptanation		
	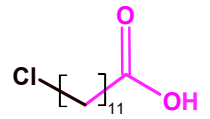 11-bromoundecanoic acid		Carboxydecanation		

2.3.1.3.Sulfonation

Adding sulfonic acid groups to the lignin structure allows lignin to be sulfonated. By improving lignin's water solubility and dispersibility, this technique makes it appropriate for a range of industrial uses [57]. Sulfonated lignin is utilized in various industries, including cement admixtures, concrete additives, agriculture, animal feed, and ceramics [58]. It stabilizes particles, improves strength, and is a sustainable functional ingredient [59, 60].

Table 2.3 lists numerous sulfonation techniques for upgrading lignin. It emphasizes how these changes improve lignin quality for usage in sustainable products, dispersants, and concrete additives.

Table 2.3: Different sulfoalkylation methods for lignin.

Lignin type	**Reagent**	**Solvent**	**Type of sulfonation**	**Application**	**Ref**
Kraft	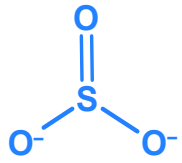 Sulfuric acid	Water	Sulfonation	-	[61]
Phenolyzed lignin	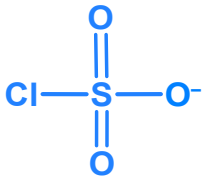 Chlorosulfonic acid	Tetrachloroethane	Sulfonation	Resin	[62]
Softwood kraft	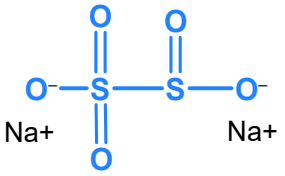 Sodium metabisulfite	Water and formaldehyde	Sulfomethylation	Cement dispersant	[63]
Softwood lignin	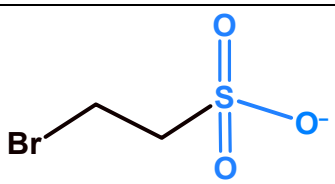 2-bromoethanesulfonate	Water	Sulfoethylation	Emulsifier	[57]

Kraft	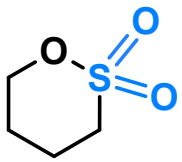 1,4–butane sultone	Water	Solfobutylation	Dispersant	[64]

2.3.2. Physical modification

Lignin can be physically modified to improve its properties without altering its chemical composition. Common techniques include particle size reduction [65], thermal treatment [66], ultrasonication [67], microwave treatment [68], blending and compatibilization [69], electrospinning [70], and solvent fractionation [71]. These methods enhance lignin's processability, dispersibility, solubility, and compatibility with other materials for various applications. These methods are widely used in composites, coatings, adhesives, biofuels, and carbon materials [34]. For example, Souza Jr. et al.'s study used plasma treatment to create crosslinked coatings from lignin. UV irradiation created smooth coatings, suppressing OH band intensity and forming C=O bonds, while plasma treatment caused roughness, resulting in super-hydrophobicity. These properties could be used in self-cleaning, anti-fouling, and anti-corrosive materials [72]. The synthesis of lignin nanoparticles is closely associated with diverse physical modification techniques, which are essential for adjusting lignin’s properties to facilitate nanoparticle formation [73].

2.3.2.1.Lignin nanoparticles

Green chemistry principles encourage the use of renewable resource-based feedstocks to produce nanomaterials. These biodegradable, eco-friendly methods are cost-effective, safer, and simpler, making them a promising and environmentally friendly alternative to traditional physicochemical methods [74]. By converting the lignin to nanoparticles, the surface area of these particles is significantly increased, which improves lignin’s reactivity and affinity to interact with other substances [75]. Due to the increment in the surface area and the presence of phenolic groups, the nanoparticles prepared from lignin exhibit antimicrobial activity [76]. Moreover, lignin nanoparticles are more compatible with various polymers, which helps to create nanocomposites with superior thermal and mechanical properties [77]. In addition, the high surface area of nanoparticles and small size enable the control of the release of active ingredients of materials in applications such as drug delivery and agriculture [78, 79]. Lignin nanoparticles have been produced using various methods, including self-assembly, solvent exchange, dialysis, flash precipitation,

ultrasonication method, CO_2 antisolvent method, polymerization, acid precipitation, etc. These eco-friendly nano particles can be used in biotechnological and nanotechnology applications [80].

The acid precipitation method is one of the famous and green procedures for preparing lignin nano particles. This method is used to prepare lignin nanoparticles by dissolving them in an alkaline solution and then adding an acid to precipitate them as nanoparticles. The pH of the solution is reduced from alkaline to acidic to ensure nanoparticle formation. The lignin nanoparticles are then separated, washed, and dried using freeze-drying or air-drying methods to obtain the final product [81, 82]. Acid precipitation of lignin nanoparticles offers eco-friendly, scalable, and versatile solutions suitable for large-scale production. These nanoparticles can enhance composite material properties, provide UV protection, act as antioxidants, etc. [83]. Lignin nanoparticles have unique antioxidant, antibacterial, antiviral, and UV adsorption characteristics. They are biodegradable, non-toxic, and have applications in bio-composites, anticorrosion, mineral flotation, Pickering emulsions, and cosmetics [84-86].

2.4. Chitosan

The shells of crustaceans, such as shrimp and crabs, contain chitosan, a linear polysaccharide produced from chitin, and have a variety of industrial and biological uses [87]. Chitosan is made up of N-acetyl-D-glucosamine (acetylated unit) and β-(1→4)-linked D-glucosamine (deacetylated unit), which are dispersed randomly (**Figure 2.3**) [88]. It is created under an alkaline environment from chitin [89]. Chitosan is a valuable material due to its biodegradability, which makes it environmentally friendly as it can be broken down naturally [90]. Moreover, chitosan is biocompatible with living tissues, making it suitable for medical and pharmaceutical applications [91]. It also exhibits antimicrobial activity, inhibiting the growth of bacteria and fungi [92]. In addition, the film-forming ability of chitosan makes it useful in food packaging and coating applications, contributing to its diverse applications [93, 94]. Chitosan's soluble nature in acidic solutions and brittle nature may limit its applications due to its limited mechanical strength [95]. Because of these restrictions, chitosan must be modified or combined with other substances to improve its quality and widen its applications. Chitosan's brittle and fragile nature can be enhanced by mixing with other biopolymers, such as lignin, which increases tensile strength and elasticity, making it more durable for various applications [96]. Lignin has bioactive features, such as antimicrobial and antioxidant activities, which are advantageous for medical and food packaging applications [97]. Chitosan and lignin, derived from renewable resources, offer eco-friendly

alternatives to synthetic materials, making chitosan-lignin composites versatile and effective in sustainable material development [98].

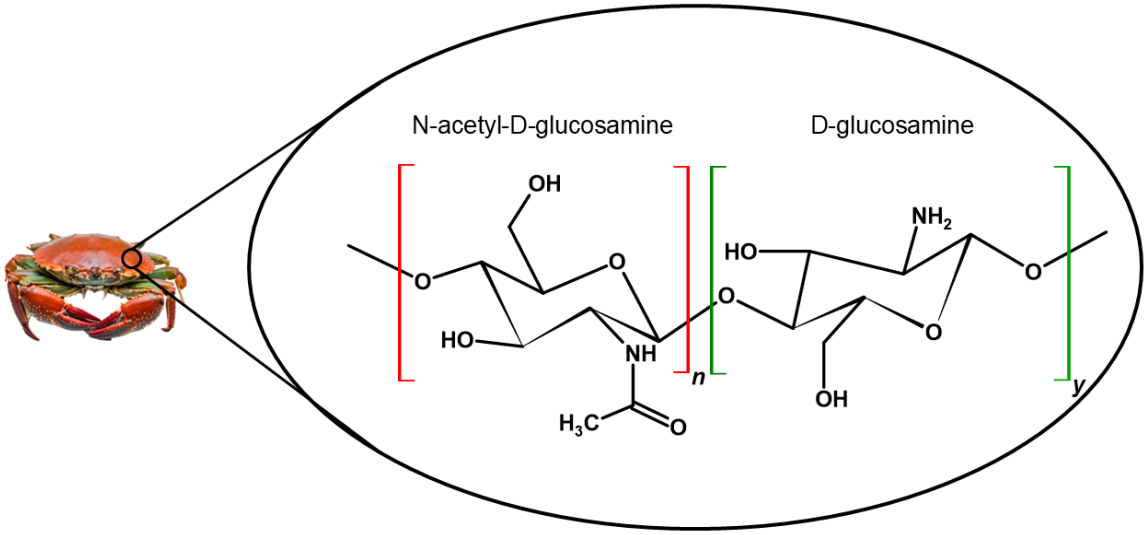

Figure 2.3: Chemical structure of chitosan and its monomers.

2.5. Biobased Aerogel

Aerogel is a light and porous substance made from gel by substituting a gas for the liquid component, producing a solid with a very low density and heat conductivity [99]. There are different methods for aerogel preparation, and the sol-gel process is the most common method for preparing aerogels, involving the transition of a liquid "sol" into a solid "gel" phase and subsequent drying [100]. Supercritical drying, freeze-drying, ambient pressure drying, and rapid supercritical extraction are methods used to produce aerogels with varying properties. These methods prevent gel collapse, preserve porous structure, and reduce time and chemical waste [101, 102]. Industrial aerogel production primarily uses silica, carbon, and polymer-based materials, each with advantages and drawbacks. Silica aerogels offer thermal insulation, high surface area, and low density, but are fragile and expensive [103]. Carbon Aerogels are another type of aerogel mainly produced in industry and offer high electrical conductivity, thermal insulation, and lightweight properties for energy storage and electronic applications. However, it has a complex production process, limited mechanical strength, and potential environmental concerns [104, 105]. Petroleum-based materials like polyurethane, polyimide, and resorcinol-formaldehyde are used in aerogel production for insulation, cushioning, high-temperature applications, and supercapacitors [106]. However, these materials have environmental impacts,

high costs, and potential toxicity. The need for sustainable alternatives like bio-based aerogels is highlighted, offering environmental benefits and reduced toxicity [107, 108].

Bio-based aerogels, such as cellulose, chitosan, lignin, and starch, are highly porous, biodegradable, and suitable for thermal insulation, water purification, biomedical applications, environmental remediation, and drug delivery systems [109, 110]. These sustainable alternatives offer environmental benefits and reduced toxicity, making them a promising alternative to traditional petroleum-based aerogels [111]. Bio-based aerogels, known for their low thermal conductivity, high porosity, and lightweight structure, are increasingly utilized in thermal insulation [112], building insulation [113], refrigeration [114], and space exploration [115] due to their efficiency [116, 117]. Bio-based aerogels, like cellulose and chitosan, are flammable, limiting their use in thermal insulation. Researchers are improving their flame retardancy through flame retardant additives or hybrid organic-inorganic systems, aiming to make them safer and more viable.

2.5.1. Thermal insulation biobased aerogels

Bio-based thermal insulation from sustainable biological sources can lower heat transmission and improve energy efficiency. The high porosity of these aerogels is the key factor in trapping air and decreasing transmission [118]. The pores should be in the nanometer range to reduce heat conductivity (below 0.05 W/m·K) due to the Knudsen effect. Aerogel porosities are classified into micropores (less than 2 nm), mesopores (2-50 nm), and macropores (greater than 50 nm) (**Figure 2.4**) [119]. High porous proportions enhance insulating properties and surface area, requiring precise control. For the best function of aerogels, the control of size and porosity distribution is essential. There are different methods of porosity and pore size distribution measurement in aerogels, such as gas adsorption, mercury intrusion, nitrogen adsorption, thermoporometry, etc. [119, 120]. This analysis is critical for the performance of porous material, especially in insulation applications, where heat transfers differently. Heat transfer in porous materials occurs through three primary mechanisms: conduction, convection, and radiation. Conduction occurs through the solid matrix, convection occurs through fluid-filled pores, and radiation occurs through pores, especially at high temperatures. The overall heat transfer in porous materials combines these processes [121, 122]. Based on the explanation, high porosity, a uniform pore structure, and a pore size distribution can enhance the thermal insulation properties. Bio-based aerogels, like cellulose, are flammable, limiting their use in thermal insulation [123].

Researchers are working to improve their flame retardancy through flame retardant additives or hybrid organic-inorganic systems, aiming to make them safer and more viable [124, 125].

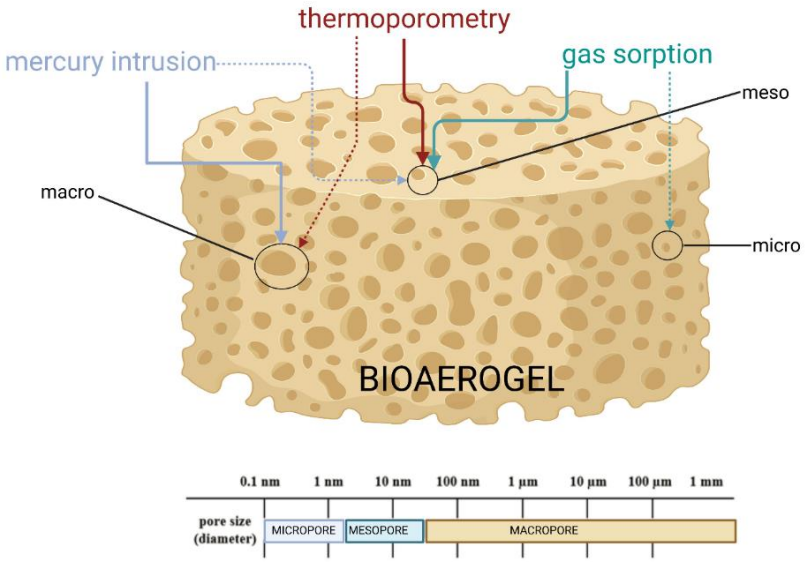

Figure 2.4: Pore size types of biobased aerogels [120].

2.5.2. Flame retardant biobased aerogels

Flame retardant materials are substances used to slow down or prevent fire spread [126]. The ability of a material to prevent ignition, reduce combustion, or stop flame spread is known as flame retardancy. Flame retardants work in a variety of ways in polymeric and composite materials, including gas-phase radical quenching, condensed-phase char formation, and the release of non-flammable gases that dilute flammable vapours, which can be additive or reactive [127]. Different categories of flame retardant materials include organic, halogenated, phosphorus, and nitrogen-based [132]. Flame retardants, like aluminum hydroxide, undergo endothermic degradation, absorbing heat and releasing water vapor, which cools the material and delays ignition [128]. Flame retardants, like intumescent ones, form a protective layer on the material's surface, acting as a barrier against heat and oxygen, slowing down combustion [129]. Like halogenated ones, flame retardants suppress combustion by releasing reactive halogen radicals that interrupt flame-propagating reactions, diluting flammable gases during combustion, slowing down the process, and preventing gas phase interference [130]. Moreover, flame retardants, like nitrogen-based ones, release inert gases to dilute flammable gases and oxygen, reducing ignition and flame spread risk [131]. These materials can be classified as additive, reactive, or additive-reactive flame retardants [133]. Additive flame retardants are commonly used in thermoplastics and can be added before, during, or after polymerization. They can also be used as plasticizers or

fillers [134]. Reactive flame retardants, which are chemically bound to polymer molecules, prevent evaporation and bleeding over time, allowing the polymer to maintain its flame retardant properties without plasticizing it or affecting its thermal stability [135]. Additive-reactive flame retardants are named synergistic flame retardants, enhancing the effectiveness of primary flame retardants when combined with materials such as silicon, phosphorus, or halogen-based materials. However, they do not work as standalone retardants [136]. Halogenated flame retardants containing bromine and chlorine were popular but banned now due to their potential health risks and environmental persistence. These materials can release harmful gases and accumulate in living organisms, posing significant health risks [137]. These materials were replaced with phosphorus-based flame retardants with reduced toxicity, adequate flame retardancy, versatility, and environmental benefits [138]. They produce less toxic smoke and gases, making them safer for human health and the environment. Available in various forms, they can be used in different materials and are more environmentally friendly due to their halogen-free nature [139]. These materials can be used as additives for coating or reactive materials to bond to other materials' backbones with action [140-142]. In addition, they can be used for bio-based flame retardants.

Bio-based flame retardants, derived from renewable resources, are environmentally friendly alternatives to traditional ones. Examples include lignin-derived, phytic acid-based, tannic acid-based, and chitosan-based flame retardants [143, 144]. Lignin has become a promising bio-based flame retardant because of its aromatic and thermally stable structure. The capacity of lignin to encourage char formation and improve thermal stability through chemical modification, such as phosphorylation, makes it a viable and sustainable substitute for traditional halogenated flame retardants. These natural compounds enhance the flame retardancy of polymeric materials, promote char formation, enhance thermal stability, and improve fire resistance in textiles and plastics [145]. These bio-based alternatives offer adequate fire protection while minimizing environmental impact.

2.6. Emulsions

Emulsions are mixtures of immiscible liquids, where one liquid is dispersed in droplets [146]. A good emulsion has key properties such as stability, uniform droplet size, appropriate viscosity, consistent appearance, suitable pH balance, and a long shelf life [147][148]. These properties ensure stability, consistency, ease of use, and proper performance in various applications, including cosmetics, food, and pharmaceuticals [149,150]. Although mechanical agitation can create short-term emulsions from simple mixtures like water and oil, these systems are naturally

unstable and tend to separate over time. Stabilizing agents are usually needed to produce stable emulsions, particularly for industrial or long-term applications. A stable emulsion maintains its properties and effectiveness over time. Emulsions are stabilized by three primary materials: surfactants, polymers, and particles [151][152]. Surfactants reduce surface tension between immiscible liquids [153], while polymers increase different particle interactions, which increase viscosity or form a protective layer [154, 155]. Particles, known as Pickering stabilizers, adsorb at the interface, providing a physical barrier to coalescence [156]. Petroleum-based stabilizers have environmental, toxicity, and regulatory drawbacks, making them less desirable than biopolymers. Biopolymer stabilizer is a sustainable alternative for petroleum-based stabilizer due to its lower toxicity, biodegradability, and costs [157].

Lignin is popular among many biopolymers such as chitosan, xanthan gum, etc., due to its structure, renewable, UV protection, versatility, and antioxidant properties [158-161]. Lignin's amphiphilic nature, aromatic rings, functional groups, and cross-linking ability make it an effective and sustainable option for emulsion stabilization [162, 163]. Its hydrophobic properties reduce interfacial tension, forming a stable barrier around oil droplets [164]. Lignin's different hydrophilic functional groups, such as hydroxyl, methoxyl, and carboxyl, enhance stability by forming hydrogen bonds with water molecules [165]. Lignin's unique structural properties make it a sustainable and effective stabilizer for emulsions, offering a green alternative to synthetic stabilizers in various industrial applications.

2.7. Coating

A coating material is a substance applied to an object's surface, protecting it from corrosion, wear, and environmental damage [166]. It enhances the appearance of objects by adding color, gloss, or texture. Some coatings provide specific functionalities, while others improve performance. Coatings can be applied using spraying [167], dipping [168], brushing [169], bar coating [170], or electroplating [171]. Surfaces need specific coatings for enhanced properties and environmental protection. For example, metal surfaces can be coated with epoxy, which is used for corrosion resistance in industrial settings, pipelines, and marine environments [172, 173]. However, it can change to yellow by absorbing the UV light. For wood surfaces, mainly polyurethane and acrylic are coated on the surface [174]. However, these materials are moisture sensitive, they can burn easily, and the production source is petroleum materials, with adverse environmental effects. One of the biomaterials that can be used for coating purposes is lignin. Not only can it be used as a replacement for urethane and grafting with acrylate [175], but it can also be modified and used as a solution or in emulsion for coating [39]. Its functional properties, such as UV-blocking, oxygen

scavenging, antimicrobial, and barrier properties, make it valuable for coating for packaging, wood veneers, and corrosion inhibitors[175]. It also has potential in waterborne antifouling coatings for marine applications [176]. This development and advantages of lignin and biomaterials support sustainability objectives and be acknowledged as a helpful resource in the nascent area of additive manufacturing.

2.8. Conclusion, Challenges, and Future Perspectives

Lignin, a unique polymer composed of three monomer units, is highly aromatic, rigid, and chemically resistant. Its antioxidant and UV-absorbing properties stem from its aromatic rings, making it versatile for various industrial applications. This review examined how lignin may be functionalized and combined for use in coatings, emulsion stabilizers, thermal insulation aerogels, and flame retardant compounds.

Adding different functional groups to lignin has successfully produced soluble, active, and flame retardant polymers. Grafting lignin with specific functional groups improves its compatibility for various applications.

Functionalized lignin shows great potential due to its abundant availability, biodegradability, and unique chemical properties. It provides a sustainable substitute for polymers derived from petroleum by improving barrier qualities in coatings, stability in emulsions, and flame retardancy. Lignin can be broken down by specific microorganisms and environmental enzymes, making it biodegradable. Because of this, lignin is more environmentally friendly than synthetic or petroleum-derived polymers, which can pollute and remain in the environment for a long time. Lignin offers aerogels with its three-dimensional structure while enhancing their mechanical, thermal, and insulating performance. However, there are still issues for the commercialization of lignin, such as lignin's structural diversity, the difficulty and cost of functionalization, processing issues, and market demands that require more research. To promote acceptance across several industries and boost the economy, future approaches should create sophisticated functionalization processes, combine lignin with other biopolymers, increase production for industrial uses, and highlight sustainability. Functionalized lignin appears to have a bright future in sustainable material research, notwithstanding the obstacles.

2.9. References

[1] Wendy. Rodriguez-Castellanos, Production and characterization of hybrid polymer composites based on natural fibers, (2016).

[2] V. Blass, T.C. Chebach, A. Ashkenazy, sustainable non-renewable materials management, Springer Series in Supply Chain Management. 4 (2017) 87–118.

[3] Z.U. Arif, M.Y. Khalid, M.F. Sheikh, A. Zolfagharian, M. Bodaghi, Biopolymeric sustainable materials and their emerging applications, J. Environ. Chem. Eng. 10 (2022) 108159.

[4] T. Biswal, S.K. BadJena, D. Pradhan, Sustainable biomaterials and their applications: A short review, Mater. Today. Proc. 30 (2020) 274–282.

[5] M. Rujnić-Sokele, A. Pilipović, Challenges and opportunities of biodegradable plastics: A mini review, Waste Management and Research. 35 (2017) 132–140.

[6] Z. Majeed, N.K. Ramli, N. Mansor, Z. Man, A comprehensive review on biodegradable polymers and their blends used in controlled-release fertilizer processes, Reviews in Chemical Engineering. 31 (2015) 69–95.

[7] H. Ahmad, G. Chhipi-Shrestha, K. Hewage, R. Sadiq, A comprehensive review on construction applications and life cycle sustainability of natural fiber bio composites, Sustainability. 14 (2022) 15905.

[8] P. Raja, V. Murugan, S. Ravichandran, L. Behera, R.A. Mensah, S. Mani, A.K. Kasi, K.B.N. Balasubramanian, G. Sas, H. Vahabi, O. Das, A review of sustainable bio-based insulation materials for energy-efficient buildings, Macromol. Mater. Eng. 308 (2023) 2300086.

[9] A. Jha, A. Kumar, Biobased technologies for the efficient extraction of biopolymers from waste biomass, Bioprocess. Biosyst. Eng. 42 (2019) 1893–1901.

[10] L. Zhu, S. Zhang, G. Curtzwiler, L. Hamachi, Y. Huang, A. Kathuria, Editorial: Recent advances in sustainable polymer materials, Front. Mater. 12 (2025) 1576384.

[11] S. Mohan, L. Muthulakshmi, N. Hariharan, Impact of biopolymers in a circular economy, Nanotechnology in the Life Sciences Part F. 3579 (2024) 413–436.

[12] D. Kai, M.J. Tan, P.L. Chee, Y.K. Chua, Y.L. Yap, X.J. Loh, Towards lignin-based functional materials in a sustainable world, Green Chemistry. 18 (2016) 1175–1200.

[13] M. Mariana, T. Alfatah, H.P.S. Abdul Khalil, E.B. Yahya, N.G. Olaiya, A. Nuryawan, E.M. Mistar, C.K. Abdullah, S.N. Abdulmadjid, H. Ismail, A current advancement on the role of lignin as sustainable reinforcement material in biopolymeric blends, Journal of Materials Research and Technology. 15 (2021) 2287–2316.

[14] F. José, B. Gomes, R. Eloy De Souza, A review on lignin sources and uses, J. of Appl. Biotechnol. Bioeng. 7 (2020) 100-105.

[15] R. Katahira, T.J. Elder, G.T. Beckham, A brief introduction to lignin structure, RSC Energy and Environment Series. (2018) 1–20.

[16] S. Sen, S. Patil, D.S. Argyropoulos, Thermal properties of lignin in copolymers, blends, and composites: a review, Green Chemistry. 17 (2015) 4862–4887.

[17] H. Hatakeyama, T. Hatakeyama, Lignin structure, properties, and applications, Adv. Polym. Sci. 232 (2010) 1–63.

[18] P. Figueiredo, K. Lintinen, J.T. Hirvonen, M.A. Kostiainen, H.A. Santos, Properties and chemical modifications of lignin: Towards lignin-based nanomaterials for biomedical applications, Prog. Mater. Sci. 93 (2018) 233–269.

[19] H. Nishimura, A. Kamiya, T. Nagata, M. Katahira, T. Watanabe, Direct evidence for α ether linkage between lignin and carbohydrates in wood cell walls, Scientific Reports. 8 (2018) 1–11.

[20] Lignin in Polymer Composites - Omar Faruk, Mohini Sain - Google Books, William Andrew, 2015.

[21] H. Chung, N.R. Washburn, Chemistry of lignin-based materials, Green Materials. 1 (2015) 137–160.

[22] M. Ek, G. Gellerstedt, G. Henriksson, 15 paper recycling, Pulping Chemistry and Technology 2 (2009) 391.

[23] Leszek. Wanat, The value and profitability of converting sawmill wood by- products to paper production and energy generation the case of poland, Pulp and Paper Processing. (2018) 109.

[24] M.J. de la Torre, A. Moral, M.D. Hernández, E. Cabeza, A. Tijero, Organosolv lignin for biofuel, Ind. Crops. Prod. 45 (2013) 58–63.

[25] J. Li, G. Gellerstedt, K. Toven, Steam explosion lignins; their extraction, structure and potential as feedstock for biodiesel and chemicals, Bioresour. Technol. 100 (2009) 2556–2561.

[26] S. Mettu, P. Halder, S. Patel, S. Kundu, K. Shah, S. Yao, Z. Hathi, K.L. Ong, S. Athukoralalage, N.R. Choudhury, N.K. Dutta, C. Sze, K. Lin, Valorisation of agricultural waste residues, Waste streams in a circular econom. 16 (2020) 51–85.

[27] S. Laurichesse, L. Avérous, Chemical modification of lignins: Towards biobased polymers, Prog. Polym. Sci. 39 (2014) 1266–1290.

[28] C.P. Rodrigo, W.H. James, T.S. Zwier, Single-Conformation ultraviolet and infrared spectra of jet-cooled monolignols: P-coumaryl alcohol, coniferyl alcohol, and sinapyl alcohol, J. Am. Chem. Soc. 133 (2011) 2632–2641.

[29] H. Dao Thi, K. Van Aelst, S. Van den Bosch, R. Katahira, G.T. Beckham, B.F. Sels, K.M. Van Geem, Identification and quantification of lignin monomers and oligomers from reductive catalytic fractionation of pine wood with GC × GC – FID/MS, Green Chemistry. 24 (2022) 191–206.

[30] T. Elder, L. Berstis, G.T. Beckham, M.F. Crowley, Density functional theory study of spirodienone stereoisomers in lignin, ACS. Sustain. Chem. Eng. 5 (2017) 7188–7194.

[31] S. Rath, D. Pradhan, H. Du, S. Mohapatra, H. Thatoi, Transforming lignin into value-added products: Perspectives on lignin chemistry, lignin-based biocomposites, and pathways for augmenting ligninolytic enzyme production, Adv. Compos. Hybrid Mater. 2024 7:1 7 (2024) 1–29.

[32] L. Hu, T. Stevanovic, D. Rodrigue, Compatibilization of kraft lignin-polyethylene composites using unreactive compatibilizers, J. Appl. Polym. Sci. 131 (2014) 41040.

[33] A. Henn, M.L. Mattinen, Chemo-enzymatically prepared lignin nanoparticles for value-added applications, World. J. Microbiol. Biotechnol .35 (2019) 1–9.

[34] K. Komisarz, T.M. Majka, K. Pielichowski, Chemical and physical modification of lignin for green polymeric composite materials, Materials. 16 (2022) 16.

[35] G.C.S. Pompêu, D. Pasquini, Extraction of Lignin and Modifications, Handbook of Biomass. (2023) 1–35.

[36] B. Jacobs, Y. Yao, I. Van Nieuwenhove, D. Sharma, G.J. Graulus, K. Bernaerts, A. Verberckmoes, Sustainable lignin modifications and processing methods: green chemistry as the way forward, Green Chemistry. 25 (2023) 2042–2086.

[37] C. Libretti, L. Santos Correa, M.A.R. Meier, From waste to resource: advancements in sustainable lignin modification, Green Chemistry. 26 (2024) 4358–4386.

[38] S. Mondal, A. Jatrana, S. Maan, P. Sharma, Lignin modification and valorization in medicine, cosmetics, environmental remediation and agriculture: a review, Environmental Chemistry Letters. 21 (2023) 2171–2197.

[39] S. Khodavandegar, P. Fatehi, Phytic acid derivatized lignin as a thermally stable and flame retardant material, Green Chemistry. 26 (2024) 10070-10086.

[40] C. feng Lin, O. Karlsson, O. Myronycheva, O. Das, R.A. Mensah, G.I. Mantanis, D. Jones, O.N. Antzutkin, M. Försth, D. Sandberg, Phosphorylated and carbamylated Kraft lignin for improving fire- and biological-resistance of Scots pine wood, Int. J. Biol. Macromol. 276 (2024) 133734.

[41] B. Prieur, M. Meub, M. Wittemann, R. Klein, S. Bellayer, G. Fontaine, S. Bourbigot, Phosphorylation of lignin: characterization and investigation of the thermal decomposition, RSC. Adv. 7 (2017) 16866–16877.

[42] W. Qin, L. Wu, Z. Zheng, C. Dong, Y. Yang, Lignin hydrolysis and phosphorylation mechanism during phosphoric acid–acetone pretreatment: a DFT study, Molecules. 19 (2014) 21335.

[43] B. Ramadhoni, T. Rahayu, A. Rifathin, F.A. Radini, M. Zain Nur Ichsan, A. Mujadid, S. Marsudi, improved thermal properties of lignin via phosphorylation using disodium hydrogen phosphate dodecahydrate salt, AIP Conf. Proc. 2902 (2023).

[44] M. V. Efanov, A.I. Galochkin, Phosphorylation of technical lignins, Chem. Nat. Compd. 48 (2012) 457–459.

[45] Y.J. Xu, K.T. Zhang, J.R. Wang, Y.Z. Wang, Biopolymer-based flame retardants and flame-retardant materials, Adv. Mater. (2025) 2414880.

[46] A.A. Alalykin, R.L. Vesnin, D.A. Kozulin, Preparation of modified hydrolysis lignin and its use for filling epoxy polymers and enhancing their flame resistance, Russian J. Appl. Chemi. 84 (2011) 1616–1622.

[47] E. Mansour, S. Curling, A. Stephan, G. Ormondroyd, Absorption of volatile organic compounds by different wool types, Green Materials. 4 (2016) 1–23.

[48] L. Ferry, G. Dorez, A. Taguet, B. Otazaghine, J.M. Lopez-Cuesta, Chemical modification of lignin by phosphorus molecules to improve the fire behavior of polybutylene succinate, Polym. Degrad. Stab. 113 (2015) 135–143.

[49] L. Liu, G. Huang, P. Song, Y. Yu, S. Fu, Converting industrial alkali lignin to biobased functional additives for improving fire behavior and smoke suppression of polybutylene succinate, ACS Sustain. Chem. Eng. 4 (2016) 4732–4742.

[50] C. Su, X. Wang, Y. Deng, D. Min, G. Fang, C. Huang, The Enhancement origin of antioxidant property of carboxylated lignin isolated from herbaceous biomass using the maleic acid hydrotropic fractionation, Int. J. Mol. Sci. 25 (2024) 9257.

[51] H.A. Qulatein, W. Gao, P. Fatehi, Carboxyalkylated Lignin as a Sustainable Dispersant for Coal Water Slurry, Polymers (Basel). 16 (2024) 2586.

[52] M.N.A.M. Taib, M.M. Rahman, J. Ruwoldt, I.W. Arnata, D. Sartika, T.A. Salleh, M.H. Hussin, Recent Progress in Development of Functionalized Lignin Towards Sustainable Applications, J. Polym. Envir. 32 (2024) 5423–5467.

[53] S. Li, J.A. Willoughby, O.J. Rojas, Oil-in-Water Emulsions Stabilized by Carboxymethylated Lignins: properties and energy prospects, Chem. Sus. Chem. 9 (2016) 2460–2469.

[54] M.K. Konduri, F. Kong, P. Fatehi, Production of carboxymethylated lignin and its application as a dispersant, Eur. Polym. J. 70 (2015) 371–383.

[55] K. Bahrpaima, P. Fatehi, Synthesis and Characterization of Carboxyethylated Lignosulfonate, Chem. Sus. Chem. 11 (2018) 2967–2980.

[56] Z. Shomali, P. Fatehi, Carboxyalkylated lignin nanoparticles with enhanced functionality for oil-water pickering emulsion systems, ACS Sustain. Chem. Eng. 10 (2022) 16563–16577.

[57] N. Ghavidel, P. Fatehi, Pickering/Non-Pickering Emulsions of nanostructured sulfonated lignin derivatives, Chem. Sus. Chem. 13 (2020) 4567–4578.

[58] T. Aro, P. Fatehi, Production and Application of Lignosulfonates and Sulfonated Lignin, Chem. Sus. Chem. 10 (2017) 1861–1877.

[59] D. Zhao, W. Yang, G. Shen, W. Zhang, H. Feng, Sulfonated lignin-based phenol–formaldehyde resin: stability and structure changes during aggregation, Colloid. Polym. Sci. 302 (2024) 1815–1830.

[60] S. B, B. S, L. G, Application of lignosulphonate a sustainable approach towards strength improvement and swell management of expansive soils, Bull. Eng. Geol. Environ. 80 (2021) 6395–6413.

[61] H. Zhang, Y. Bai, W. Zhou, F. Chen, Color reduction of sulfonated eucalyptus kraft lignin, Int. J. Biol. Macromol. 97 (2017) 201–208.

[62] S. Kamel, Preparation of cation-exchange resin from lignin, Int. J. Polym. Mater. 55 (2005) 283–291.

[63] W. He, P. Fatehi, Preparation of sulfomethylated softwood kraft lignin as a dispersant for cement admixture, RSC Adv. 5 (2015) 47031–47039.

[64] D.Y. Hopa, P. Fatehi, Using Sulfobutylated and Sulfomethylated lignin as dispersant for kaolin suspension, Polymers. 12 (2020) 2046.

[65] S. Beisl, A. Miltner, A. Friedl, Lignin from micro- to nanosize: production methods, Int. J. Mol. Sci. 18 (2017) 1244.

[66] F. Kifani-Sahban, A. Kifani, L. Belkbir, A. Zoulalian, J. Arauzo, T. Cardero, A physical approach in the understanding of the phenomena accompanying the thermal treatment of lignin, Thermochim Acta. 298 (1997) 199–204.

[67] I.A. Gilca, V.I. Popa, C. Crestini, Obtaining lignin nanoparticles by sonication, Ultrason. Sonochem. 23 (2015) 369–375.

[68] W. Yunpu, D. Leilei, F. Liangliang, S. Shaoqi, L. Yuhuan, R. Roger, Review of microwave-assisted lignin conversion for renewable fuels and chemicals, J. Anal. Appl. Pyrolysis. 119 (2016) 104–113.

[69] A. Naseem, S. Tabasum, K.M. Zia, M. Zuber, M. Ali, A. Noreen, Lignin-derivatives based polymers, blends and composites: A review, Int. J. Biol. Macromol. 93 (2016) 296–313.

[70] Q. Cao, H. Zhu, J. Xu, M. Zhang, T. Xiao, S. Xu, B. Du, Research progress in the preparation of lignin-based carbon nanofibers for supercapacitors using electrospinning technology: A review, Int. J. Biol. Macromol. 273 (2024) 133037.

[71] H. Sadeghifar, H. Sadeghifar, A. Ragauskas, A. Ragauskas, A. Ragauskas, A. Ragauskas, Perspective on technical lignin fractionation, ACS Sustain. Chem. Eng. 8 (2020) 8086–8101.

[72] J.R. Souza, J.R. Araujo, B.S. Archanjo, R.A. Simão, Cross-linked lignin coatings produced by UV light and SF6 plasma treatments, Prog, Org, Coat, 128 (2019) 82–89.

[73] C. Vauthier, K. Bouchemal, Methods for the preparation and manufacture of polymeric nanoparticles, Pharm. Res. 26 (2009) 1025–1058.

[74] S. Iravani, R.S. Varma, Greener synthesis of lignin nanoparticles and their applications, Green Chemistry. 22 (2020) 612–636.

[75] S. Beisl, A. Friedl, A. Miltner, Lignin from Micro- to Nanosize: Applications, Int. J. Mol. Sci..18 (2017) 2367.

[76] N.T. Tran, T.T.T. Nguyen, D. Ha, T.H. Nguyen, N.N. Nguyen, K. Baek, N.T. Nguyen, C.K. Tran, T.T. Van Tran, H. Van Le, D.M. Nguyen, D. Hoang, Highly Functional materials based on nano-lignin, lignin, and lignin/silica hybrid capped silver nanoparticles with antibacterial activities, Biomacromolecules. 22 (2021) 5327–5338.

[77] M. Zor, F. Şen, H. Yazıcı, Z. Candan, Thermal, Mechanical and morphological properties of cellulose/lignin nanocomposites, Forests. 14 (2023) 1715.

[78] T.O. MacHado, S.J. Beckers, J. Fischer, B. Müller, C. Sayer, P.H.H. De Araújo, K. Landfester, F.R. Wurm, Bio-based lignin nanocarriers loaded with fungicides as a versatile platform for drug delivery in plants, Biomacromolecules. 21 (2020) 2755–2763.

[79] M. Gigli, G. Fellet, L. Pilotto, M. Sgarzi, L. Marchiol, C. Crestini, Lignin-based nano-enabled agriculture: A mini-review, Front. Plant. Sci. 13 (2022) 976410.

[80] Q. Tang, Y. Qian, D. Yang, X. Qiu, Y. Qin, M. Zhou, Lignin-based nanoparticles: a review on their preparations and applications, Polymers. 12 (2020) 2471.

[81] T. Sewring, J. Durruty, L. Schneider, H. Schneider, T. Mattsson, H. Theliander, Acid precipitation of kraft lignin from aqueous solutions: the influence of pH, temperature, and xylan, J. Wood Chem. Technol 39 (2019) 1–13

[82] J. Azimvand, K. Didehban, S.A. Mirshokrai, Lignin nanoparticles, Bioresources. 13 (2018) 2887–2897.

[83] S. Behera, S. Mohapatra, B.C. Behera, H. Thatoi, Recent updates on green synthesis of lignin nanoparticle and its potential applications in modern biotechnology, Crit. Rev. Biotechnol. 44 (2024) 774–794.

[84] K. Chen, S. Wang, Y. Qi, H. Guo, Y. Guo, H. Li, State of the art: applications and industrialization of lignin micro/nano particles, ChemSusChem. 14 (2021) 1284–1294.

[85] R.A. McIntyre, Common nano-materials and their use in real world applications, Sci. Prog. 95 (2012) 1–22.

[86] Z. Zhang, V. Terrasson, E. Guénin, Lignin nanoparticles and their nanocomposites, Nanomaterials. 11(2021) 1336.

[87] I. Hamed, F. Özogul, J.M. Regenstein, Industrial applications of crustacean by-products (chitin, chitosan, and chitooligosaccharides): A review, Trends. Food. Sci. Technol. 48 (2016) 40–50.

[88] V. Bhaskar, A.S. Nair, L.K. Pappachen, Chitosan as potential carrier for drug delivery, Nat. Biopolymers Drug Deliv. Tissue Eng. (2023) 127–156.

[89] C.Y. Soon, Y.B. Tee, C.H. Tan, A.T. Rosnita, A. Khalina, Extraction and physicochemical characterization of chitin and chitosan from Zophobas morio larvae in varying sodium hydroxide concentration, Int. J. Biol. Macromol. 108 (2018) 135–142.

[90] P.C. Srinivasa, R.N. Tharanathan, Chitin/chitosan safe, ecofriendly packaging materials with multiple potential uses, Food Reviews International. 23 (2007) 53–72.

[91] S. Mohebbi, M.N. Nezhad, P. Zarrintaj, S.H. Jafari, S.S. Gholizadeh, M.R. Saeb, M. Mozafari, Chitosan in biomedical engineering: a critical review, Curr. Stem. Cell. Res. Ther. 14 (2018) 93–116.

[92] D. Raafat, H.G. Sahl, Chitosan and its antimicrobial potential a critical literature survey, Microb. Biotechnol. 2 (2009) 186–201.

[93] H. Wang, J. Qian, F. Ding, Emerging Chitosan-Based Films for Food Packaging Applications, J. Agric. Food. Chem. 66 (2018) 395–413.

[94] M. Mujtaba, R.E. Morsi, G. Kerch, M.Z. Elsabee, M. Kaya, J. Labidi, K.M. Khawar, Current advancements in chitosan-based film production for food technology; A review, Int. J. Biol. Macromol. 121 (2019) 889–904.

[95] C.P. Jiménez-Gómez, J.A. Cecilia, M. Guidotti, R. Soengas, Chitosan: a natural biopolymer with a wide and varied range of applications, Molecules. 25 (2020) 3981.

[96] S. Garg, A. Avanthi, Tuning of chitosan with lignin-derived bioactive properties to develop a lignin-reinforced and sustainable food packaging biomaterial, Biomass. Convers. Biorefin. (2024) 1–17.

[97] K. Li, W. Zhong, P. Li, J. Ren, K. Jiang, W. Wu, Antibacterial mechanism of lignin and lignin-based antimicrobial materials in different fields, Int. J. Biol. Macromol. 252 (2023) 126281.

[98] R. Vijayakumar, Y. Sivaraman, K.M. Pavagada Siddappa, J.P.R. Dandu, Synthesis of lignin nanoparticles employing acid precipitation method and its application to enhance the mechanical, UV-barrier and antioxidant properties of chitosan films, Int. J. Polym. Anal. Charact 27 (2022) 99–110.

[99] A. Bin Rashid, S. Islam Shishir, M. Azim Mahfuz, M. Tanvir Hossain, M. Enamul Hoque, A.B. Rashid, S.I. Shishir, M.A. Mahfuz, M.T. Hossain, M.E. Hoque, Silica aerogel: synthesis, characterization, applications, and recent advancements, Particle & Particle Systems Characterization. 40 (2023) 2200186.

[100] D. Bokov, A. Turki Jalil, S. Chupradit, W. Suksatan, M. Javed Ansari, I.H. Shewael, G.H. Valiev, E. Kianfar, Nanomaterial by Sol-Gel Method: Synthesis and Application, Adv. Mater. Sci. Eng. 1 (2021) 5102014.

[101] M. Lazrag, C. Lemaitre, C. Castel, A. Hannachi, D. Barth, Aerogel production by supercritical drying of organogels: Experimental study and modelling investigation of drying kinetics, J. Supercrit. Fluids. 140 (2018) 394–405.

[102] M.K. Carroll, A.M. Anderson, C.A. Gorka, Preparing silica aerogel monoliths via a rapid supercritical extraction method, J. Vis. Exp. 84 (2014) 51421.

[103] F. Akhter, S.A. Soomro, V.J. Inglezakis, Silica aerogels; a review of synthesis, applications and fabrication of hybrid composites, J. Porous Mater. 28 (2021) 1387–1400.

[104] S. Araby, A. Qiu, R. Wang, Z. Zhao, C.H. Wang, J. Ma, Aerogels based on carbon nanomaterials, J. Mater. Sci. 51 (2016) 9157–9189.

[105] L. Hu, R. He, H. Lei, D. Fang, Carbon aerogel for insulation applications: a review, Int. J. Thermophys. 40 (2019) 1–25.

[106] P.A. Nizam, S. Thomas, Innovations in polymeric foams and new application opportunities including energy and energy devices, Multifunctional Polymeric Foams. (2023) 181–196.

[107] W. Song, X. Pan, X. Wang, H. Wang, J. Li, D. Li, X. Ma, F. Yin, Load-bearing structure inspired cellulose-based aerogel with high resilience and water tolerance, Adv. Funct. Mater. 35 (2025) 2415937.

[108] A. Varamesh, Y. Zhu, G. Hu, H. Wang, H. Rezania, Y. Li, Q. Lu, X. Ren, F. Jiang, S.L. Bryant, J. Hu, Fully biobased thermal insulating aerogels with superior fire-retardant and mechanical properties, Chem. Eng. J. 495 (2024) 153587.

[109] A. Romero-Montero, J.L. Valencia-Bermúdez, S.A. Rosas-Meléndez, I. Núñez-Tapia, M.C. Piña-Barba, G. Leyva-Gómez, M.L. Del Prado-Audelo, Biopolymeric fibrous aerogels: the sustainable alternative for water remediation, Polymers.15 (2023) 262.

[110] P. Saraswat, S. Singh, M. Prasad, R. Misra, V.D. Rajput, R. Ranjan, Applications of bio-based nanomaterials in environment and agriculture: A review on recent progresses, Hybrid Advances. 4 (2023) 100097.

[111] J. Zhou, X. Li, Z. Zhang, T. Hou, J. Xu, Y. Wang, H. Ye, B. Yang, Bio-based and bio-degradable nanofiber materials: A sustainable platform for energy, environmental, and biomedical applications, Chem. Eng. J. 491 (2024) 152105.

[112] S.K. Adhikary, D.K. Ashish, Ž. Rudžionis, Aerogel based thermal insulating cementitious composites: A review, Energy. Build. 245 (2021) 111058.

[113] Y. Wang, R. Rasheed, F. Jiang, A. Rizwan, H. Javed, Y. Su, S. Riffat, Life cycle assessment of a novel biomass-based aerogel material for building insulation, J. Build. Eng. 44 (2021) 102988.

[114] T.B. Umate, P.D. Sawarkar, Thermal performance evaluation of aerogel-enhanced polyurethane insulation panels for refrigerated vehicles: a numerical and experimental study, Thermal Science and Engineering Progress. 53 (2024) 102752.

[115] S.M. Jones, J. Sakamoto, J.A. Paik, Applications of Aerogels in Space Exploration, Springer Handbooks Part F. 1485 (2023) 1505–1524.

[116] A. Giuma, H.P.S.A. Khalil, E.B. Yahya, L. Sukeksi, T. Alfatah, N.M. Nurazzi, M. Jaber, I. Surya, Green thermal insulators: A review into the role of biopolymer-based aerogels in thermal insulation applications, Polym. Eng. Sci. 64 (2024) 4611–4629.

[117] T. Budtova, Bio-based Aerogels: A New Generation of Thermal Superinsulating Materials, Cellul. Sci. Technol. (2018) 371–392.

[118] M. Noroozi, M. Panahi-Sarmad, M. Abrisham, A. Amirkiai, N. Asghari, H. Golbaten-Mofrad, N. Karimpour-Motlagh, V. Goodarzi, A.R. Bahramian, B. Zahiri, Nanostructure of Aerogels and Their Applications in Thermal Energy Insulation, ACS Appl. Energy. Mater. 2 (2019) 5319–5349.

[119] G. Horvat, M. Pantić, Ž. Knez, Z. Novak, A brief evaluation of pore structure determination for bioaerogels, Gels. 8 (2022) 438.

[120] M.R. Hossen, M.W. Talbot, R. Kennard, D.W. Bousfield, M.D. Mason, A comparative study of methods for porosity determination of cellulose based porous materials, Cellulose. 27 (2020) 6849–6860.

[121] A. Pavlenko, Heat and Mass Transfer in Porous Materials, Materials. 16 (2023) 5591.

[122] Y. Mahmoudi, K. Hooman, K. Vafai, Convective Heat Transfer in Porous Media, CRC Press, 2019.

[123] D. Illera, J. Mesa, H. Gomez, H. Maury, Cellulose aerogels for thermal insulation in buildings: Trends and challenges, Coatings. 8 (2018) 345.

[124] L. Yu, L. Chen, L.P. Dong, L.J. Li, Y.Z. Wang, Organic–inorganic hybrid flame retardant: preparation, characterization and application in EVA, RSC Adv. 4 (2014) 17812–17821.

[125] G.C. Lainioti, V. Koukoumtzis, K.S. Andrikopoulos, L. Tsantaridis, B. Östman, G.A. Voyiatzis, J.K. Kallitsis, Environmentally friendly hybrid organic–inorganic halogen-free coatings for wood fire-retardant applications, Polymers. 14 (2022) 4959.

[126] A.B. Morgan, J.W. Gilman, An overview of flame retardancy of polymeric materials: application, technology, and future directions, Fire. Mater. 37 (2013) 259–279.

[127] S. V. Levchik, Introduction to Flame retardancy and polymer flammability, Flame Retardant Polymer Nanocomposites. (2006) 1–29.

[128] A. Charles Wilkie, B. Alexander, Morgan, Flame Retardant Polymeric Materials: A Handbook, CRC Press, 2024.

[129] R.G. Puri, A.S. Khanna, Intumescent coatings: A review on recent progress, Journal of Coatings Technology and Research. 14 (2016) 1–20.

[130] M.N.A.M. Taib, P. Antov, V. Savov, W. Fatriasari, E.W. Madyaratri, R. Wirawan, L.M. Osvaldová, L.S. Hua, M.A.A. Ghani, S.S.A.O. Al Edrus, L.W. Chen, D. Trache, M.H. Hussin, Current progress of biopolymer-based flame retardant, Polym. Degrad. Stab. 205 (2022) 110153.

[131] A.B. Morgan, M. Klatt, Nitrogen-Based Flame Retardants, Non-Halogenated Flame Retardant, Handbook. (2021) 236–270.

[132] N. Djerfaf, Z. Nafa, E. Belaidi, Durability of high-performance concrete to an attack by a mixture of sulfuric acid and acetic acid, Journal of Silicate Based and Composite Materials. 75 (2023).

[133] H. Singh, A.K. Jain, Ignition, combustion, toxicity, and fire retardancy of polyurethane foams: A comprehensive review, J. Appl. Polym. Sci. 111 (2009) 1115–1143.

[134] C. Lassen, S. Løkke, C.A.S. Lina, I. Andersen, Brominated flame retardants-substance flow analysis and assessment of alternatives, Envir. Proj. 494 (1999).

[135] A. Baby, S. Tretsiakova-McNally, M. Arun, P. Joseph, J. Zhang, Reactive and additive modifications of styrenic polymers with phosphorus-containing compounds and their effects on fire retardance, Molecules. 25 (2020) 3779.

[136] P.R. Fisk, A.E. Girling, R.J. Wildey, P.F. Associates, prioritisation of flame retardants for environmental risk assessment, (2003). www.environment-agency.gov.uk.

[137] S.D. Shaw, A. Blum, R. Weber, K. Kannan, D. Rich, D. Lucas, C.P. Koshland, D. Dobraca, S. Hanson, L.S. Birnbaum, Halogenated flame retardants: Do the fire safety benefits justify the risks, Rev. Environ. Health. 25 (2010) 261–305.

[138] V.E. Naiker, S. Mestry, T. Nirgude, A. Gadgeel, S.T. Mhaske, Recent developments in phosphorous-containing bio-based flame-retardant (FR) materials for coatings: an attentive review, Journal of Coatings Technology and Research. 20 (2022) 113–139.

[139] M.S. Özer, S. Gaan, Recent developments in phosphorus based flame retardant coatings for textiles: Synthesis, applications and performance, Prog. Org. Coat. 171 (2022) 107027.

[140] K.A. Salmeia, S. Gaan, G. Malucelli, B. Kandola, A. Boudenne, P. Kiekens, Recent advances for flame retardancy of textiles based on phosphorus chemistry, Polymers. 8 (2016) 319.

[141] G. Jiang, Y. Xiao, Z. Qian, Y. Yang, P. Jia, L. Song, Y. Hu, C. Ma, Z. Gui, A novel phosphorus-, nitrogen- and sulfur-containing macromolecule flame retardant for constructing high-performance epoxy resin composites, Chem. Eng. J. 451 (2023) 137823.

[142] C. Qin, J. Chen, S. Ruan, F. Liu, L. Zhang, Theoretical study on the effect of oxidation states of phosphorus flame retardants on their mode of action, Polym. Degrad. Stab. 223 (2024) 110735.

[143] M. Wang, G.Z. Yin, Y. Yang, W. Fu, J.L. Díaz Palencia, J. Zhao, N. Wang, Y. Jiang, D.Y. Wang, Bio-based flame retardants to polymers: A review, Adv. Ind. Eng. Polym. Res. 6 (2023) 132–155.

[144] Y. Yang, L. Haurie, D.Y. Wang, Bio-based materials for fire-retardant application in construction products: a review, J. Therm. Anal. Calorim. 147 (2021) 6563–6582.

[145] S. Basak, A.S.M. Raja, S. Saxena, P.G. Patil, Tannin based polyphenolic bio-macromolecules: Creating a new era towards sustainable flame retardancy of polymers, Polym. Degrad. Stab. 189 (2021) 109603.

[146] L. Lisuzzo, G. Cavallaro, S. Milioto, G. Lazzara, Pickering Emulsions Stabilized by Halloysite Nanotubes: From General Aspects to Technological Applications, Adv. Mater. Interfaces. 9 (2022) 2102346.

[147] F. Ravera, K. Dziza, E. Santini, L. Cristofolini, L. Liggieri, Emulsification and emulsion stability: The role of the interfacial properties, Adv Colloid Interface Sci 288 (2021) 102344. https://doi.org/10.1016/J.CIS.2020.102344.

[148] W. Liao, A. Gharsallaoui, E. Dumas, A. Elaissari, Understanding of the key factors influencing the properties of emulsions stabilized by sodium caseinate, Compr. Rev. Food. Sci. 21 (2022) 5291–5317.

[149] F. Adams, P Walstra, B. W. Brooks, H. N. Richmond, M. Zerfa, J. Bibette, D. J. Hibberd, M. M. Robins, J. G. Weers, A. S. Kabalnov, D. N. Petsev, T. Obey, B. Vincent, H. Kunieda, R. Pons, C. Solans, T. H. Forster, W. Von Rybinski, P. Smulders, T. Iwanaga, B. Deminiere, A. Colin, F. Caldero, Modern aspects of emulsion science, Royal Society of Chemistry, (2007).

[150] M. Chappat, Some applications of emulsions, Colloid. Surf. A Physicochem. Eng. Asp. 91 (1994) 57–77.

[151] N. Ghavidel, P. Fatehi, Recent Developments in the Formulation and Use of Polymers and Particles of Plant-based Origin for Emulsion Stabilizations, ChemSusChem. 14 (2021) 4850–4877.

[152] S. Ayirala, A. Sofi, Z. Li, Z. Xu, Surfactant and surfactant-polymer effects on wettability and crude oil liberation in carbonates, J. Pet. Sci. Eng. 207 (2021) 109117.

[153] J.K. Ferri, K.J. Stebe, Which surfactants reduce surface tension faster: A scaling argument for diffusion-controlled adsorption, Adv. Colloid. Interface. Sci. 85 (2000) 61–97.

[154] D. Guzey, D.J. McClements, Formation, stability and properties of multilayer emulsions for application in the food industry, Adv. Colloid. Interface. Sci. 128 (2006) 227–248.

[155] A. Benichou, A. Aserin, N. Garti, Double emulsions stabilized with hybrids of natural polymers for entrapment and slow release of active matters, Adv. Colloid. Interface. Sci. 108–109 (2004) 29–41.

[156] E.M.C. Souza, M.R.A. Ferreira, L.A.L. Soares, Pickering emulsions stabilized by zein particles and their complexes and possibilities of use in the food industry: A review, Food Hydrocoll. 131 (2022) 107781.

[157] N. Tamang, P. Shrestha, B. Khadka, M.H. Mondal, B. Saha, A. Bhattarai, A Review of Biopolymers' Utility as Emulsion Stabilizers, Polymers. 14 (2021) 127.

[158] J. Gould, G. Garcia-Garcia, B. Wolf, Pickering Particles Prepared from Food Waste, Materials. 9 (2016) 791.

[159] M. Zembyla, B.S. Murray, A. Sarkar, Water-in-oil emulsions stabilized by surfactants, biopolymers and/or particles: a review, Trends. Food. Sci. Technol. 104 (2020) 49–59.

[160] M.B. Agustin, N. Nematollahi, M. Bhattarai, E. Oliaei, M. Lehtonen, O.J. Rojas, K.S. Mikkonen, Lignin nanoparticles as co-stabilizers and modifiers of nanocellulose-based Pickering emulsions and foams, Cellulose. 30 (2023) 8955–8971.

[161] Y. Pang, Y. Luo, Z. Li, Y. Luo, H. Lou, M. Zhou, Pickering emulsion stabilized by lignin particles: Influence of oil phase, lignin concentration, and particle size, Colloid. Polym. Sci. 302 (2024) 901–909.

[162] R. Li, / Greenchem, C. Huang, W. Yu, K. Zhang, G. Chemistry, J. Gan, Y. Zhan, J. Fan, J. Wang, Q. Gao, Pickering multiphase materials using plant-based colloidal lignin nanoparticles, Green Chemistry. 27 (2025) 1300–1330.

[163] K.S. Mikkonen, Strategies for structuring diverse emulsion systems by using wood lignocellulose-derived stabilizers, Green Chemistry. 22 (2020) 1019–1037.

[164] L. Bai, L.G. Greca, W. Xiang, J. Lehtonen, S. Huan, R.W.N. Nugroho, B.L. Tardy, O.J. Rojas, Adsorption and Assembly of Cellulosic and Lignin Colloids at Oil/Water Interfaces, Langmuir. 35 (2019) 571–588.

[165] J. Tao, Q. Ma, Z. Zhang, Z. Hu, L. Lei, G. Zhao, Improving emulsion stabilizing capacity of sodium caseinate by colloidal lignin particles near the isoelectric point, Food Hydrocoll 151 (2024) 109813.

[166] B. Fotovvati, N. Namdari, A. Dehghanghadikolaei, On Coating Techniques for Surface Protection: A Review, Journal of Manufacturing and Materials Processing. 3 (2019) 28.

[167] R.D. Andrade, O. Skurtys, F.A. Osorio, Atomizing Spray Systems for Application of Edible Coatings, Compr. Rev. Food. Sci. Food Saf .11 (2012) 323–337.

[168] L.E. Scriven, Physics and Applications of DIP Coating and Spin Coating, MRS Proceedings. 121 (1988) 717–729.

[169] K.B. Buhl, A.H. Agergaard, M. Lillethorup, J.P. Nikolajsen, S.U. Pedersen, K. Daasbjerg, Polymer Brush Coating and Adhesion Technology at Scale, Polymers. 12 (2020) 1475.

[170] A.B. Reis, C.M.P. Yoshida, A.P.C. Reis, T.T. Franco, Application of chitosan emulsion as a coating on Kraft paper, Polym. Int. 60 (2011) 963–969.

[171] S. Mersagh Dezfuli, M. Sabzi, Deposition of ceramic nanocomposite coatings by electroplating process: A review of layer-deposition mechanisms and effective parameters on the formation of the coating, Ceram. Int. 45 (2019) 21835–21842.

[172] A. V. Radhamani, H.C. Lau, S. Ramakrishna, Nanocomposite coatings on steel for enhancing the corrosion resistance: A review, J. Compos. Mater. 54 (2020) 681–701.

[173] P.A. Sørensen, S. Kiil, K. Dam-Johansen, C.E. Weinell, Anticorrosive coatings: A review, J. Coat. Technol. Res. 6 (2009) 135–176.

[174] D. Kocaefe, S. Saha, Comparison of the protection effectiveness of acrylic polyurethane coatings containing bark extracts on three heat-treated North American wood species: Surface degradation, Appl. Surf. Sci. 258 (2012) 5283–5290.

[175] J. Ruwoldt, F.H. Blindheim, G. Chinga-Carrasco, Functional surfaces, films, and coatings with lignin – a critical review, RSC Adv. 13 (2023) 12529–12553.

[176] M. Butschle, R. Schlautek, L. Kunschert, M. Schackmann, C.E. Weinell, K. Dam-Johansen, Integration of unmodified kraft lignin powder in waterborne coatings and investigation of antifouling properties, J. Coat. Technol. Res. 21 (2024) 993–1003.

3. Phytic acid derivatized lignin as thermally stable and flame retardant material

Saba Khodavandegar, [a] *Pedram Fatehi* *[a,b]

Published in Green Chemistry Journal., 2024, 26, 10070, 17 July 2024, https://doi.org/ 10.1039/d4gc03169e

[a] Biorefining Research Institute, Lakehead University, 955 Oliver Road, Thunder Bay, Ontario, P7B 5E1, Canada.

[b] Laboratory of Natural Materials Technology, Åbo Akademi University, Henrikinkatu 2, Turku FI-20500, Finland

First author, email: skhodava@lakeheadu.ca, address: 955 Oliver Road, Thunder Bay, ON, Canada, P7B 5E1

Corresponding author, email: pfatehi@lakeheadu.ca, address: 955 Oliver Road, Thunder Bay, ON, Canada, P7B 5E1

The contribution of Saba Khodavandegar to this work was the conception of the original draft, methodology, investigation, experiment, and data Analysis.

Graphic abstract

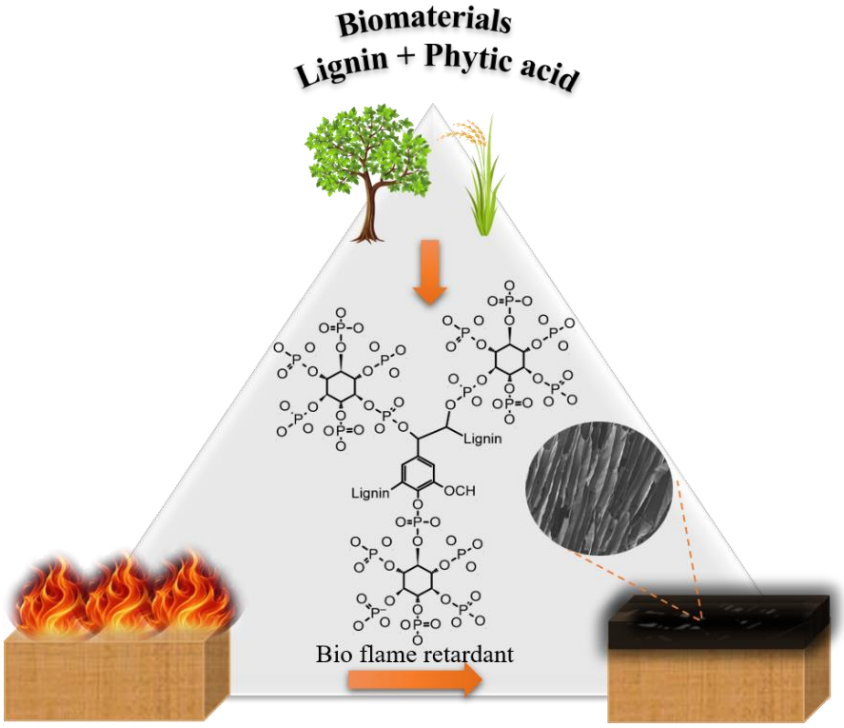

3.1. Abstract

Phosphorus-containing flame retardants have attracted attention due to their outstanding flame retardancy, enhanced thermal stability, and limited toxic smoke emission. Bio-based phosphorus-containing flame retardants could be excellent options to impart environmental benefits, renewability, and sustainability to these materials. Lignin is an underutilized but abundant and sustainable material that can be used to serve this purpose. In the present work, a lignin-derived flame retardant was produced following the facile solvent-free polycondensation reaction of kraft lignin (KL) and phytic acid (PHA) at a low temperature in an aqueous system. The optimized conditions for this reaction were 1/0.4 mol/mol KL/PHA, pH 11, 20 °C, and 20 min. By utilizing advanced NMR (H, P, and HSQC), XPS, and FTIR techniques, the covalent bonding of the phosphorus of PHA with the oxygen of aliphatic and aromatic hydroxyl groups of KL was confirmed. C–P–O and P–O–P bonds provided high decomposition temperature (T_{max}), high glass transition temperature (Tg), and char formation in the product. The presence of phosphorus atoms was observed on the combusted material by EDS mapping and EDX, illustrating the increase in the intensity of this element after combustion at 800 °C. The results of this work provided a new approach for preparing a fully bio-based flame-retardant with limited smoke density (i.e., a decrease from 34% for KL to 17.7% for modified KL) and a higher limiting oxygen index (i.e., an increase from 21.8% for KL to 26% for modified KL) following a green chemistry concept.

3.2. Introduction

Flame retarding materials have extensive use in industry to delay or prevent the spread of fire [1, 2]. They are necessary for sectors where the fire risk is high and safety is paramount, such as construction, textile, painting, *etc.*, specifically where wood structures are available. Wood is a renewable and eco-friendly material with aesthetics, strength, and cost advantages, and it has been used extensively in various industries, such as interior design, construction, and furniture [3]. However, its flammability restricts its use in many areas [4]. Applying a flame retardant *via* coating the wood surface is recognized as an efficient and environmentally friendly method to shield wood products from fire [5].

Chemicals, such as halogenated, nitrogen-containing, silicon-containing, and nano-metric compounds, are the major types of fire retardants [6]. However, these flame retardants have been proved to possess detrimental environmental

and health effects, such as their persistence in nature for a long time and potential carcinogenicity [7]. Earlier, halogen-based flame retardants, polychlorinated biphenyls (PCBs), and brominated flame retardants (BFRs), such as penta- and octa-bromodiphenyl ether and hexabromocyclododecane, were used due to their efficiency in interacting with fabrics and biopolymers [8]. However, their use was restricted due to generating toxic and corrosive gases when burned, which is dangerous for humans, animals, and the environment [9]. Mineral flame retardants, such as aluminum trihydroxide, are particularly effective in reducing fire risks and, hence, are frequently utilized. Nevertheless, their low efficiency requires their significant quantity to be used to attain the desired increased fire retardancy in materials [10]. Therefore, there is a need to produce safer and more effective flame retardants that fulfill environmental and health requirements. Considering environmental protection and human safety, halogenated flame retardants have been suggested to be replaced by bio-based phosphorus materials [11]. In this context, phosphorus-containing biomacromolecules have been assessed as sustainable flame retardants [12]. For example, phosphorus-containing flame retardants were reported to promote carbonization, dehydrogenation, and the creation of physical protective layers *via* radical-capturing char formation [13].

Phosphorylated flame retardants are known for their lower toxicity and reduced environmental persistence compared to their traditional counterparts. Additionally, they exhibit efficient flame retardant properties without releasing harmful byproducts during combustion [9]. In contrast, halogenated flame retardants, while effective, are often associated with higher levels of corrosivity and toxicity with environmental concerns. Moreover, they are mostly derived from non-renewable resources and may not leave significant carbon residue due to the presence of less carbon in their structure to make a char layer [2]. These facts underscore the growing preference for phosphorylated flame retardants in applications where health and environmental safety are paramount.

Lignin, among other biopolymers, has received significant attention due to its three-dimensional structure, vast availability [14], and biodegradability [15]. Lignin is an amorphous biopolymer of polyphenolic molecules with many functional groups, including hydroxyl, phenoxyl, carbonyl, methoxyl, and carboxyl [16]. In the past, lignin was modified to be used in drug delivery [17], antimicrobial [18], thermal insulating [19], flocculant, dispersant [20], and biosensor applications [21]. Lignin can also be used as a flame retardant because of its active functional groups, aromatic ring, and ability to form char [22]. However, it cannot be used in pristine form as a flame retardant because of its low fire resistance [23]. Interestingly, lignin can be modified to improve its flame retardancy and fire

resistance. Generally, chemical reagents containing halogens, nitrogen, silane, and phosphorus elements are used to improve the flame retardancy of materials [24-27]. Among these elements, phosphorus with different oxidation states from 0 to +5, which reacts differently with organic and inorganic materials, is a suitable alternative for mimicking lignin flame retardants and fire resistance [28].

Phytic acid (PHA) is an eco-friendly organic acid and biocompatible material widely available in plants [29]. PHA is considered an excellent flame retardant because of the six phosphate groups present in its structure, which produces a char layer when burned to protect the material underneath it [30]. Interestingly, the phosphorus element in the phytic acid structure is active and covalently bound to the active functional groups, resulting in excellent flame-retardant efficiency [31, 32]. In the past, phytic acid was used along with chitosan, silane sol, and collagen to produce flame retardant materials. However, phytic acid was primarily blended physically with these materials [33–35]. Consequently, it tended to leach out from the blends due to a lack of chemical bonds, which could affect the mechanical properties and processability of the products [36]. Also, PHA was used as a flame retardant to coat textile materials. Still, as it is soluble in water, the flame retardant properties of the textile were reduced by washing the textile materials [37]. In this regard, PHA would be more effective if it is covalently bound to the material, as it can have a permanent flame retarding effect.

In previous studies, the modification of lignin was carried out mainly using different phosphorus reagents, for example, ammonium dihydrogen phosphate ($NH_4H_2PO_4$), phosphorus pentoxide (P_2O_5), phosphoric acid (H_3PO_4), 9,10-dihydro-9-oxa-10-phosphaphenanthrene-10-oxide (DOPO), *O,O*-dialkylthiophosphoric acids, and sodium 3-chloro-2-hydroxypropyl phosphate [38–45]. However, phosphorus reagents, such as DOPO, need a high temperature to be activated for reaction [38]. Generally, phosphorylation is conducted in the presence of urea and tetrahydrofuran (THF) to prevent its degradation at high reaction temperatures [46]. Interestingly, it was observed that the number of phosphorus atoms in a biomaterial is directly correlated to its flame retardancy [47]. Compared with the above-mentioned reagents, not only is the large number of phosphorus atoms with OH active sites in the PHA structure considerable, but also its eco-friendliness makes PHA a better option to achieve phosphorylated kraft lignin [48]. Interestingly, this modified lignin can be used for different applications, such as coating wood.

This work reported the modification of kraft lignin with $C_6H_{18}O_{24}P_6$, PHA, a bio-based reagent, in a facile solvent-free reaction at a low temperature to produce a novel reactive bio-based flame retardant. This work aimed to optimize

the reaction conditions to generate phosphorylated lignin with excellent flame retardancy. Moreover, the chemical properties of the fabricated lignin derivative were comprehensively analyzed by advanced techniques, such as ^{1}H NMR, ^{31}P NMR, HSQC-NMR, XPS, ICP-AES, SEM, TGA, and DSC. Also, smoke density and limiting oxygen index analyzers were used to investigate the flame retardant behavior of modified lignin for wood and paper samples.

3.3. Experimental

3.3.1. Modification of lignin via phosphorylation

The modification reaction used phytic acid sodium salt hydrate (PHA) as the phosphorylating reagent. In each reaction setup, KL with a molecular weight of 180 g mol^{-1} (1.5 g) was dispersed in deionized (DI) water (25 g L^{-1}), and the pH of the mixture was adjusted to 12 using 1 M NaOH. The mixture was stirred for 24 hours at room temperature to complete the deprotonation. Different concentrations of the reagent (PHA) were dispersed in 30 mL of deionized water. Then, the mixtures were added to the KL solution to make different molar ratios of KL/PHA solutions. Afterward, the mixtures were transferred to three-neck round-bottom flasks in a water bath with a reflux condenser. Upon completion, the reaction mixtures were cooled to room temperature, neutralized with 1 M H_2SO_4, and purified for 48 hours *via* a dialysis membrane in DI water to remove unreacted reagents and salts. The product was then dried at 60 °C in an oven. The product of this reaction, phosphorylated lignin, was denoted as PK. This experiment was repeated under different conditions of KL/PHA molar ratios of 1 : 0.02, 0.06, 0.16, 0.2, 0.3, and 0.4, pH values, solvents (DI water and urea), time (20–240 minutes), and temperature (20–80 °C) to optimize the modification reaction. The pH was adjusted using 1 M NaOH solution and 1 M HCl. In strategy one, the pH dropped to 3 after adding the reagent, the reaction was exploited, and the samples were neutralized and dialyzed after the reaction. In strategy two, the pH of the reaction was adjusted to 11 after adding the reagent, and the reaction ran at pH 11. Afterward, the reaction medium was neutralized and dialyzed. A control sample (CK) of KL was produced following all steps outlined in the reaction, pH adjustment, purification, and drying procedures stated above in the absence of PHA.

3.3.2. Charge density, solubility, elemental analysis, and molecular weight measurements

The charge density of PK samples was determined using a particle charge detector (PCD 04, BTG Mütek GmbH, Germany) using a 0.005 mol L^{-1} PDADMAC solution as the titrant. The solubility of the samples was measured

according to the process described previously [49]. The organic elements of the samples were analyzed using an organic elemental analyzer, Vario EL, following the combustion method [50]. The molecular weight of the samples was investigated *via* gel permeation chromatography (GPC, Malvern GPCmax VE2001 Module + Viscotek TDA305 with multi-detectors) with the columns of PolyAnalytic 206 and PAA203.

3.3.3. ^{1}H, HSQC, HMBC, and ^{31}P NMR analysis

The chemical structure of lignin samples was characterized by proton nuclear magnetic resonance (^{1}H NMR) and two-dimensional heteronuclear single-quantum coherence NMR (HSQC), and for phosphorus element analysis, ^{1}H–^{31}P HMBC measurements were performed using a Bruker Avance spectrometer at room temperature.

^{31}P NMR spectroscopy was carried out quantitatively and qualitatively. Quantitative ^{31}P NMR analysis assessed the content of phenolic hydroxyl, aliphatic hydroxyl, and carboxyl groups of KL and PK17 [51].

3.3.4. FTIR analysis

The FTIR analysis of KL and PK samples was carried out to monitor the chemical structures of the samples using a Bruker Tensor 37 instrument in transmittance mode (Germany, Germany, ATR accessory).

3.3.5. XPS and ICP-AES analyses

The surface chemical composition was determined by X-ray photoelectron spectroscopy using a photoelectron spectrometer (XPS, Escalab 250XL+, Thermo Fisher Scientific, USA). The phosphorus content of the samples was determined by inductively coupled plasma-atomic emission spectrometry (ICP-AES).

3.3.6. Thermal analysis

Thermogravimetric analysis (TGA) was performed to investigate the samples' thermal response in a thermal analyzer (TGA i1000, Instrument Specialists Inc.).

Differential scanning calorimetry (DSC) was performed to estimate the glass transition temperature (T_g) of KL and PK in a differential scanning calorimeter (DSC Q2000, TA Instruments, DE, USA).

3.3.7. Flame retardant behaviour analysis

For flame retardant behavior analysis, wood and filter paper samples were first coated with KL and PK17 solutions. Before coating, the wood samples were washed with ethanol, rinsed with DI water, and dried at 60 °C for 2 hours. Three different concentrations (1, 2, and 3 wt%) of KL and PK17 were diluted in deionized water and labeled KC1, KC2, and KC3 for KL-coated wood and PC1, PC2, and PC3 for PK17-coated wood and UW for uncoated wood, respectively. The wood samples were immersed and dip-coated in solution at 60 °C for 4 hours. After coating, each sample was dried at 60 °C until reaching a stable weight. To further analyze the flame retardant behavior of PK17, the filter paper was immersed and coated with 3 wt% PK17 and dried at 60 °C.

The fire resistance behavior of the samples was measured using a limiting oxygen index (LOI) analyzer (Netzsch Taurus Instrument, Germany) according to the ASTM D 2863 standard. The static smoke release of coated wood was tested using a smoke detector instrument (Smoke Density Advanced Instruments Co., Ltd, AIC-2843) according to the ASTM D2843 standard.

3.3.8. Morphological study of burned wood

Scanning electron microscopy (SEM) was used to analyze the surface morphology of the wood samples after the flame retardancy test. Specifically, after burning the wood samples in the smoke density analyzer, the burned samples were collected, and the morphologies of char formed on uncoated wood (UW), coated wood with KL (KC), and coated wood with PK17 (PC) were analyzed using SEM. Also, PK17 and KL before and after combustion at 800 °C by TGA were collected and analyzed by FE-SEM; Hitachi Su-70 with a voltage of 5 kV. Also, the surface element mapping and elemental analysis of the samples were carried out by energy dispersive spectroscopy (EDS) and energy-dispersive X-ray spectroscopy (EDX) at a voltage of 200 kV, where the samples were coated with gold and carbon glue. The details of characterization are available in the ESI.

3.4. Results and discussions

3.4.1. Solubility, charge density, and molecular weight

Solubility, charge density, and molecular weight measurements were carried out for reaction optimization to obtain the modified lignin with the highest phosphorylated group, and the results are reported in **Table S3.1** in the ESI. The

effect of different molar ratios of the reagent is illustrated in this table and **Figure 3. 1a**–**d**. When the molar ratio of PHA increased from 0.02 to 0.4, the phosphorus (P) content, charge density, and molecular weight of phosphorylated lignin were increased from 0.8% to 4.4%, −1.8 mmol g^{-1} to −4.3 mmol g^{-1}, and 3900 g mol^{-1} to 4560 g mol^{-1}, respectively. Because of the presence of hydroxyl groups in KL and PHA, a further increment in the molar ratio would cause crosslinking of the P–OH groups of PHA and the OH of KL to make P–O–P and P–O–C bonds during the reaction [52]. This crosslinking will cause a decrease in solubility (occurring when the molar ratio > 0.3). The elemental analysis results in **Table S3.2** (ESI) show that by increasing the molar ratio of KL/PHL, the carbon and hydrogen contents decreased from 62.7 wt% for KL to 42.44 wt% for PK6 and from 6.9 wt% for KL to 5.37 wt% for PK6, respectively, which is attributed to the attachment of phosphorus to the KL backbone. The ICP-AES and XPS analyses confirmed the increment of the P element in the PK by increasing the PHA molar ratio in the reaction medium (**Table S3.2**). The sulfur content of KL was less than 1.2 wt%, which can originate from its introduction to lignin during kraft pulping and the acid-washing treatment in the LignoForce process for producing KL in industry [53].

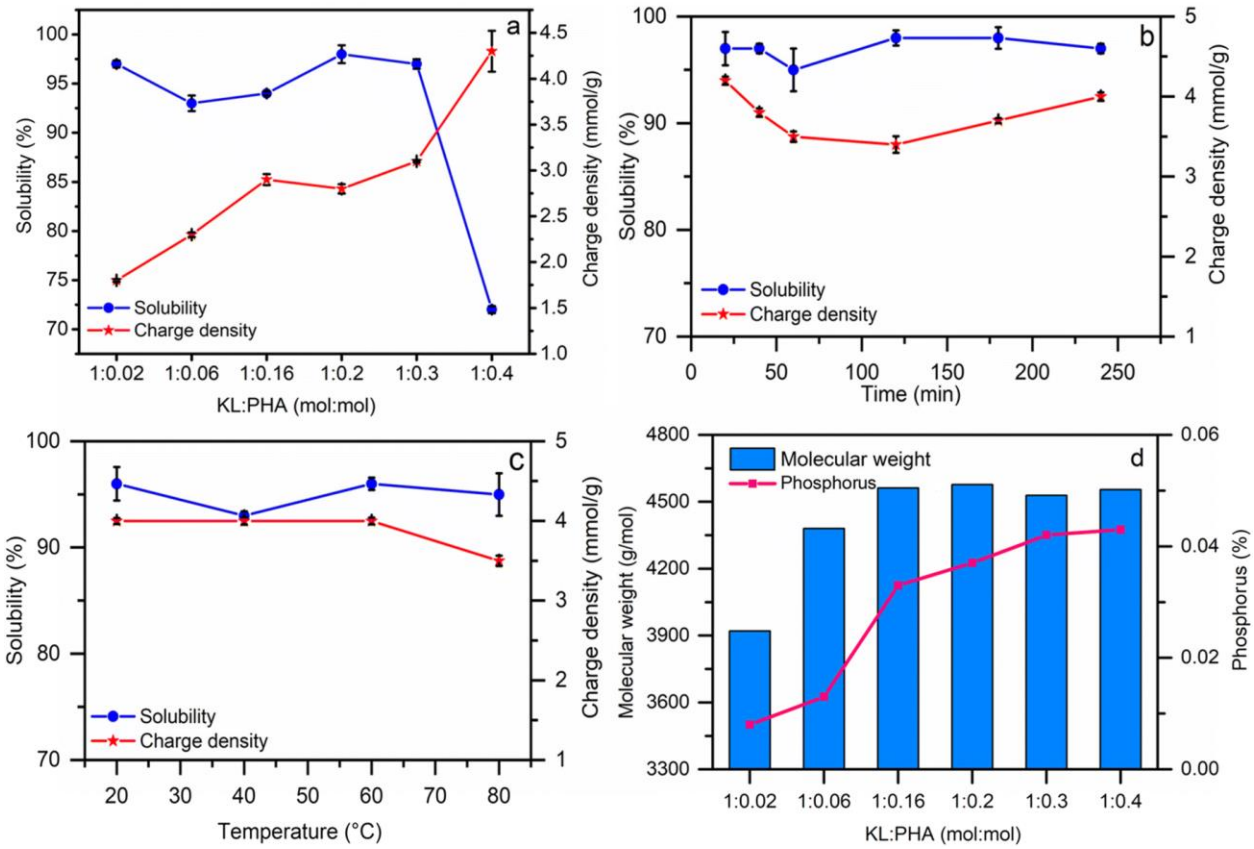

Figure 3.1. The effect of the molar ratio (a, PK1–PK6), time (b, PK11–PK16), and temperature (c, PK11, PK17–PK19) on the reaction. The effect of the molar ratio on molecular weight (M_w) and phosphorus content (d, PK1–PK6).

The results show that time and temperature did not have a significant influence on the charge density and solubility of the resulting PK (**Figure 3.1b** and **c**). The effect of the molar ratio of KL/PHA was investigated, and the results are available in **Figure 3. 1a, d** and **Table S3.1**. Increasing the molar ratio decreases the pH of the reaction medium as PHA is acidic, promoting the aggregation and protonation of KL, resulting in a reduction in solubility. In addition, the activities of the hydroxyl and phosphate ions are pH dependent [54, 55]. Higher PHA concentrations facilitate a pH drop and suggest that the phosphate groups start to crosslink among themselves instead of reacting with KL because PHA is more active under acidic conditions, which would increase the average molecular weight of PK (**Figure 3. 1d**) [56]. Also, the aggregation of KL would decrease the reactivity of OH groups and its solubility due to its protonation under acidic conditions. This phenomenon will transform fractal-like KL into closed-packed aggregates, which would cause less solubility and phosphorylation [57]. The effect of pH on the reaction efficiency was also investigated at the KL/PHA ratio of 1 : 0.4 mol : mol (PK6 and PK7 in **Table S3.1**). The results confirmed that the reaction under alkaline conditions was preferred as the PK was produced with a higher solubility. In the pH range of 9–11, hydroxyl and phosphate groups would actively compete to interact with KL and promote different crosslinking scenarios, such as monophosphate, phosphodiester, and orthophosphate [58].

Also, the effect of urea (as a solvent of the reaction) was studied at three reaction temperatures, and the results are reported in **Table S3.1**. In earlier research, urea was utilized not only as a solvent but also as a degradation inhibitor of the lignin structure at high reaction temperatures (>90 °C), as the phosphorylation was primarily studied in the high-temperature range of 90–120 °C [59]. However, our results confirmed that urea did not significantly affect the phosphorus group, charge density, and solubility of the induced phosphorylated samples (PK7 and PK8).

The reaction experiments confirmed that the optimized conditions for generating phosphorylated samples, PK17, with the highest molecular weight (M_w) of 4800 g mol^{-1}, solubility of 97%, and charge density of −4.2 mmol g^{-1} were the KL/PHA molar ratio of 1 : 0.4 (mol : mol), water as the solvent, 20 min reaction time at 20 °C and pH 11 (*i.e.*, strategy 2), and this sample was selected for further analysis.

3.4.2. NMR characterization

^{1}H NMR was used to characterize the chemical structures of PK17 and KL. The spectra in **Figure 3. 2** show the structures of KL and PK17. In the KL spectrum, the protons of phenolic and aliphatic hydroxyl groups are at chemical

shifts of around 8.7 (a) and 5.5 (g and g′) ppm, respectively. After the modification, both hydroxyl groups participated in the reaction and disappeared from the spectrum of KL. The aromatic protons of the guaiacyl unit show a broad peak in the 7.5–6.1 ppm range (b and b′). The intense peaks at 4.1–3.1 ppm is associated with the protons of methoxyl groups on the lignin structure (c–e). Three strong peaks at 4.70, 2.5, and 0 ppm belong to D_2O, DMSO, and TMSP, respectively, which were used as solvents for sample preparation and the internal standard. Also, two characteristic peaks in the PK17 spectrum at 4.5 and 4.2 ppm were ascribed to the PHA protons, confirming the success of phosphorylation [60]. **Figure S3.1a** in the ESI shows the ^{1}H NMR spectra of the samples at different molar ratios of KL/PHA in the reaction. By increasing the molar ratio of KL/PHA, both aromatic and aliphatic hydrogens decreased due to their participation in the reaction, and more phosphorus atoms were attached to the KL backbone. In addition, the intensity of the peaks in the range of 4–4.7 ppm was increased, which showed the presence of protons on phosphorus groups. By increasing the molar ratio of KL/PHA (PK1 to PK6 in **Figure S3.1a**), two peaks in the 1–4 ppm region had a slight decrease due to the crosslinking of the hydroxyl group of phosphorus groups.

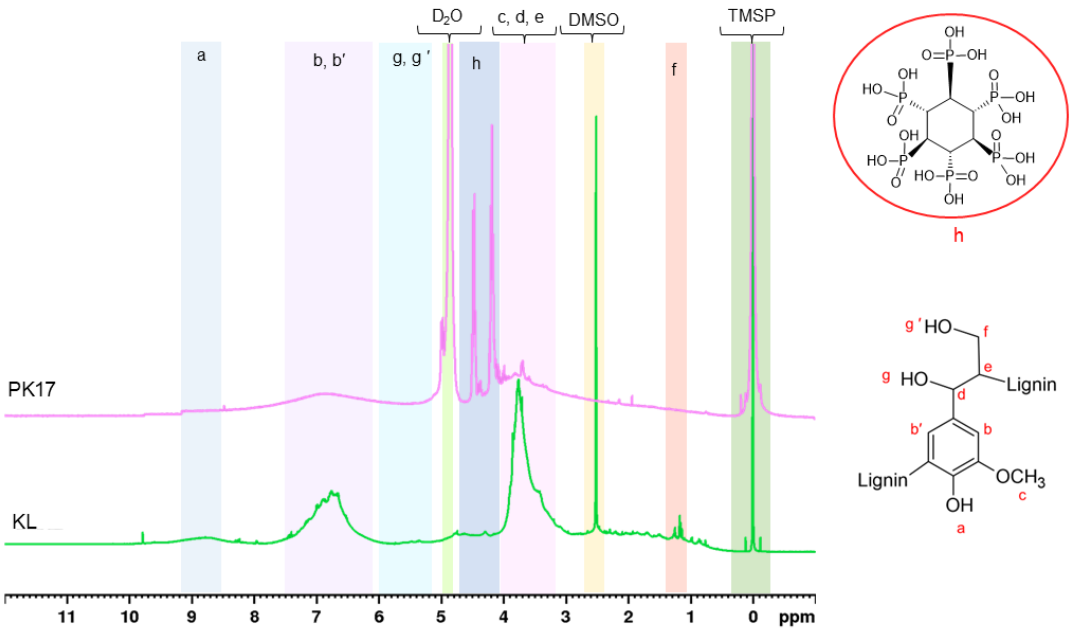

Figure 3.2. ^{1}H NMR spectra of KL and PK17. Shaded peaks are identified as described in the text.

Quantitative ^{31}P NMR spectroscopy was carried out to confirm the chemical structures of KL and PK17 samples, and the results are shown in **Figure 3. 3** and **Table 3.1.** This analysis provided quantitative information on the concentration of each hydroxyl group of lignin participating in the reaction. The cyclohexanol peak (internal standard)

appears at 144.8 ppm. The decrease in the aliphatic, phenolic, and carboxylic hydroxyl groups proved that these groups participated in the modification reaction. A significant drop in the amount of phenolic hydroxyl groups from 3.33 mmol g^{-1} to 0.63 mmol g^{-1} confirmed the high activity of phenolic hydroxyl groups in KL and phosphorylation at this site by polycondensation [61]. After the phosphorylation of KL, the aliphatic hydroxyl group decreased from 1.72 mmol g^{-1} for KL to 0.63 mmol g^{-1} for PK17. In addition, there is a significant drop from 0.41 mmol g^{-1} to 0.06 mmol g^{-1} for carboxylic hydroxyl content, inferring that the reaction happened on the aliphatic, aromatic, and carboxyl hydroxyl groups. The sharp peak in the phenolic hydroxyl region is for PHA's hydroxyl groups, confirming the successful phosphorylation reaction.

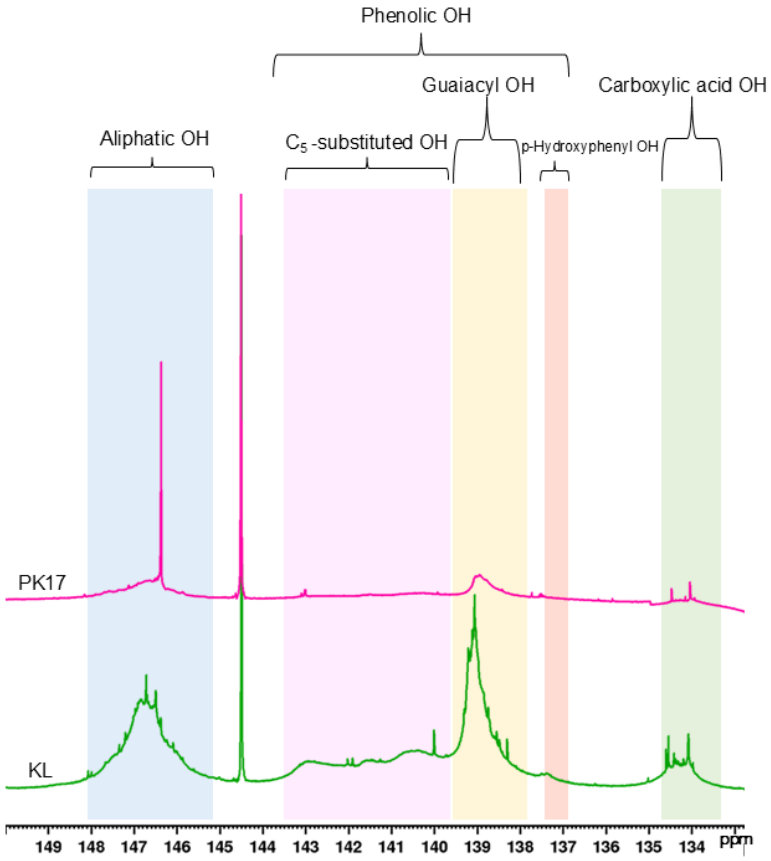

Figure 3.3. Quantitative ^{31}P NMR of KL and PK17. Shaded peaks indicate the type of OH functional group.

Sample name	Aliphatic OH (mmol/g)	Phenolic OH (mmol/g)	C_5 –substituted (mmol/g)	Guaiacyl OH (mmol/g)	p-Hydroxyphenyl OH (mmol/g)	Carboxylic acid OH (mmol/g)
KL	1.72	3.33	1.5	1.6	0.11	0.41

PK17	0.63	0.71	0.29	0.39	0.02	0.06

Table 3.1. The OH functional group content (mmol/g) obtained via quantitative ^{31}P-NMR analysis (**Figure 3.3**)

The qualitative ^{31}P NMR spectra of KL and PK17 are shown in **Figure 3. 4**. No peak can be characterized for KL, inferring that KL did not have any phosphorus-containing group. Based on previous studies, ^{31}P NMR of PHA was assigned to four different peaks at 1, 0.5, 0, and −0.8 ppm [62]. As explained earlier, the phosphorylation of lignin could happen on aliphatic, phenolic, and carboxylic hydroxyl groups. In addition, an esterification reaction and crosslinking could occur between phosphate and hydroxyl groups, resulting in a chemical shift from 5 ppm [38, 63]. **Figure S3.1b** in the ESI shows the ^{31}P NMR spectra of PK generated at different molar ratios, and by increasing the molar ratio of KL/PHA, the intensity of ^{31}P NMR peaks increased. At a higher KL/PHA molar ratio than 1 : 0.16 (mol : mol), PK started to exhibit different crosslinking types (phosphate (a), orthophosphate (b), and phosphodiester (c)), especially type c, that had lower solubility (**Table S3.1**).

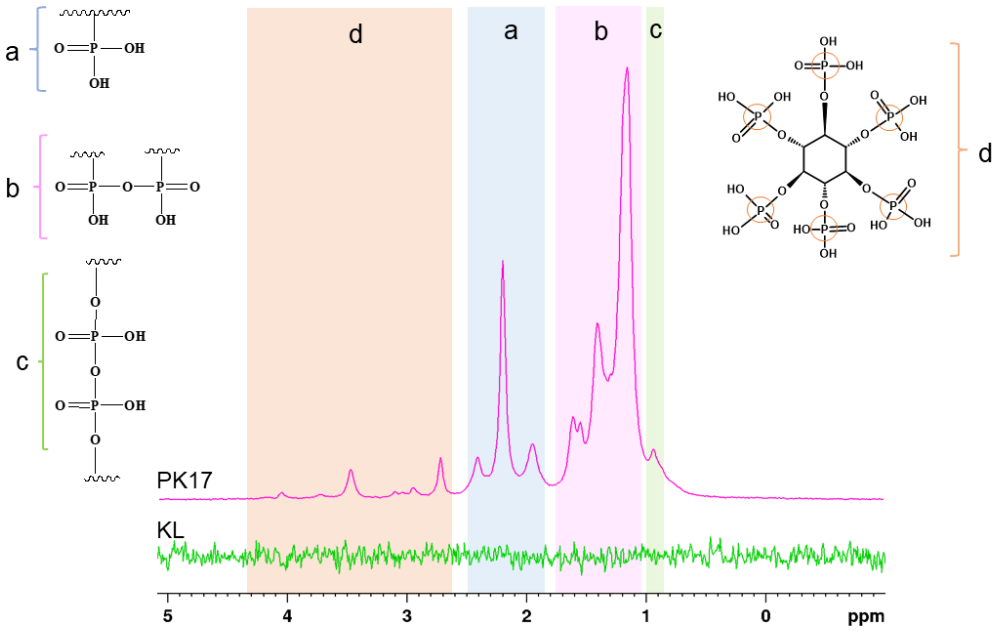

Figure 3.4. Qualitative ^{31}P NMR of KL and PK17.

HSQC NMR was used to understand the changes in the structure of lignin, and the ^{1}H-^{13}C HSQC spectra of KL and PK17 are displayed in **Figure 3. 5a**–**5d**. The detailed structures of signal assignment of each bond of aromatic (δ_C /δ_H 100–140/ 6.1–7.9), aliphatic (δ_C /δ_H 45–100/ 3–5.6), and side chain (δ_C /δ_H 10–60/ 0.2–2.8) are shown in **Table S3.3** [64, 65]. In **Figure 3. 5a** and **5b**, the aromatic region, G-type structure appears in both KL and PK17, implying that no degradation of KL happened after modification [66]. In addition, **Figure 3. 5c** shows the aliphatic region in both KL and PK17 [67]. The large area in **Figure 3. 5d** and **5e** belongs to C–H in $–OCH_3$ (methoxy) in the aliphatic region (δ_C /δ_H 57.3/ 3.7). Two linkages of B_γ (δ_C /δ_H 72.7/3.7-4.1) and B_β (δ_C /δ_H 55/3.2) disappeared and cleaved after modification (PK17 compared with KL), which can be attributed to the crosslinking or polycondensation of the hydrogen element of these linkages during modification [68].

Due to the proton transferring effect of aromatics' groups on the lignin backbone, the aromatic region does not correlate in the HSQC NMR spectra. This behavior was more vital when the sample was prepared in D_2O, as exchangeable protons such as hydroxyl groups increased the typical widening in the resonances [69]. A detailed study was conducted in D_2O because phosphorous groups were not detectable in DMSO due to the high polarity and less solubility of PK17 [65]. **Figure 3. 5f** shows the presence of a new linkage of lignin with PHA based on the four different protons and their correlation with carbons on the PHA structure [70]. The HSQC NMR spectrum of PHA is shown in **Figure S3.2**. It is observable that the linkages of PHA mostly appear in the aliphatic region of KL (δ_C /δ_H 75-85/3.5-5). These linkages were not detectable for the sample prepared in DMSO due to the high negative charge density around the nucleus and high opposite magnetic field around the copolymer, which will have a great shield covering the linkages in this region. Due to this shielding, ^{1}H- ^{31}P HMBC NMR was used (**Figure S3.3**). The P and H linked to the same C on the 6-membered ring were detected by the cross-peaks on the HMBC spectrum [71]. These findings show that the skeletal structure of lignin was preserved during phosphorylation, which might be attributed to the moderate reaction conditions [72].

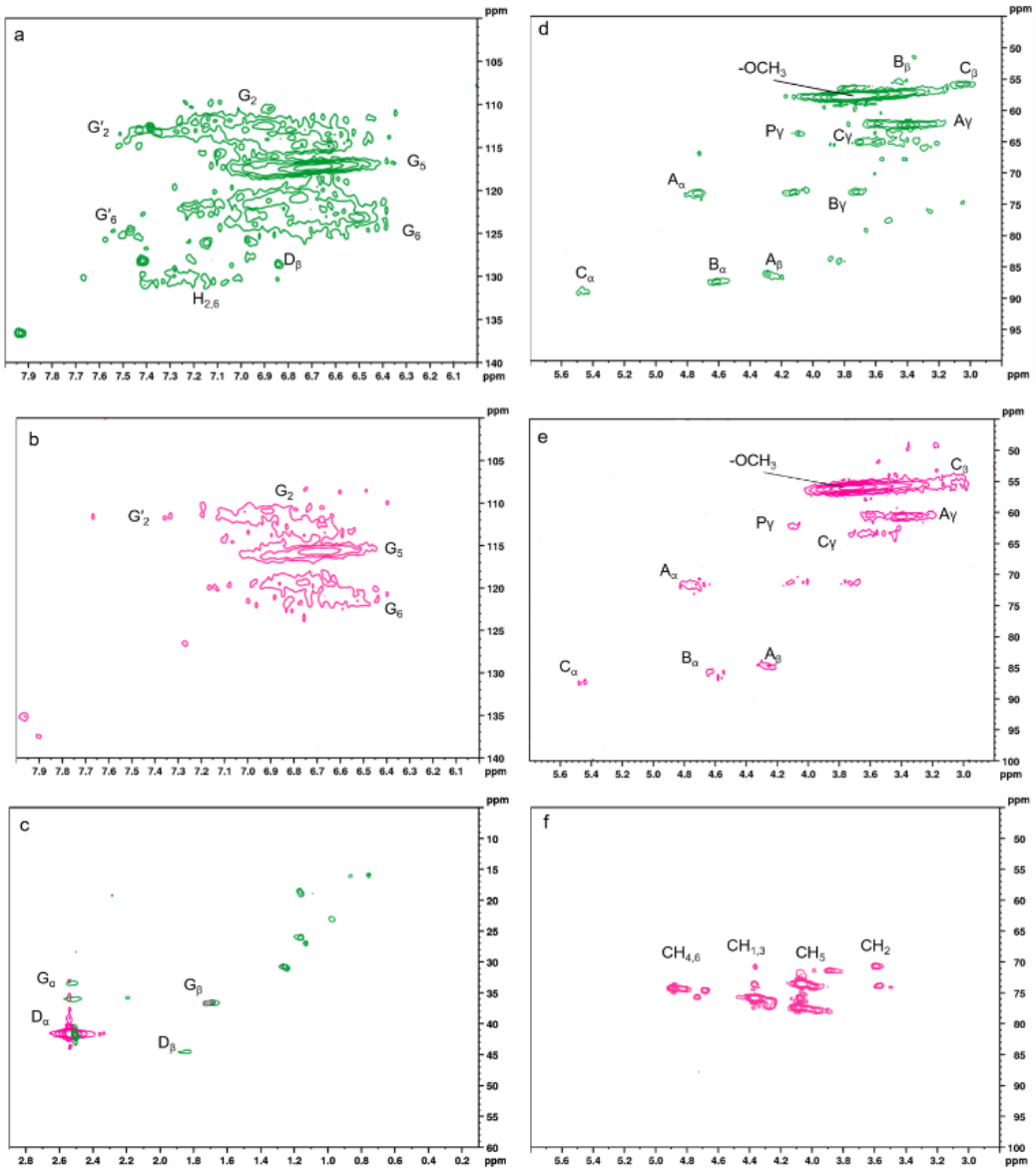

Figure 3.5. HSQC NMR spectra (a and d) of KL, (b and e) PK17 in DMSO, (c) aliphatic region of both KL and PK17 in DMSO, (f) PK17 in D_2O.

3.4.3. FTIR analysis

The FTIR spectra of KL and PK17 are shown in **Figure 3. 6**. The characteristic bands in KL were comprehensively determined in previous studies [73]. The O–H aliphatic and aromatic stretching vibration groups show a broad transmittance band at 3400 cm^{-1} (region a). After phosphorylation, the band intensity decreased, which could prove the participation of these O–H functional groups in the phosphorylation reaction. The aliphatic C–H stretching vibration of methyl and methylene groups showed transmittance bands at around 2930 cm^{-1} and 2830 cm^{-1} (region b). The phenylpropane monomer bands in KL were established at 1591 cm^{-1}, 1510 cm^{-1}, and 1450 cm^{-1}, which are assigned to the stretching vibrations of the C–C bonds. However, the intensity of these peaks after modification

decreased (region c). Both ether bands of C–O–C and the stretching vibration of C–O were assigned to the bands at 1280 cm^{-1}, 1200 cm^{-1}, 1120 cm^{-1}, and 1030 cm^{-1} (region d). IR spectroscopy does not show intense bands of phosphate moieties [74]. However, minor alterations in the 1250 cm^{-1} and 1300 cm^{-1} bands belong to P=O. After phosphorylation, the appearance of three new bands proved that KL was modified successfully with PHA. These bands are PO_4^{3-}, P–O–C aliphatic, and the P–O stretching band (region f), which are assigned to 990 cm^{-1}, 960 cm^{-1}, and 850 cm^{-1}, respectively [75–77]. In region f, two bands of bending and stretching are assigned to P–O–P, which can be determined at 760 cm^{-1} and 810 cm^{-1}, respectively [78]. The P–O bond in PK17 overlapped with the aromatic C–O–C structure, which shifted the band from 1120 cm^{-1} to 1020 cm^{-1} in the C–O stretching of the guaiacyl group of KL (region e) [79]. All these changes in the FTIR bands confirmed that KL was modified with phosphorus groups on phenolic, aromatic, and carboxylic hydroxyl groups for generating PK17.

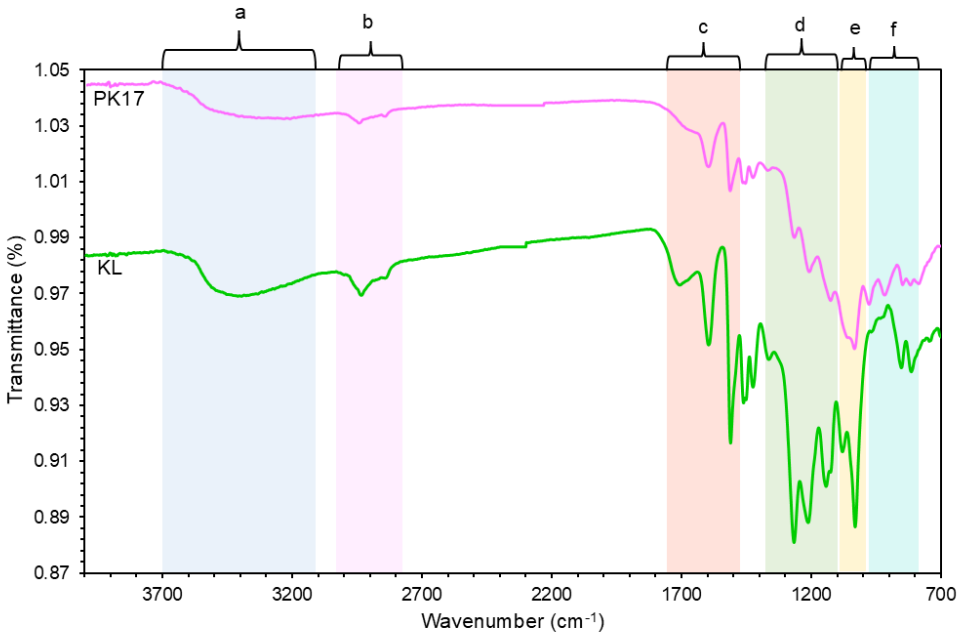

Figure 3.6. FTIR spectra of KL and PK17. Shaded peaks are identified as described in the text.

3.4.4. XPS and ICP-AES analyses

The chemical compositions of the samples were analyzed by X-ray photoelectron spectroscopy. The broad XPS spectra of KL and PK17 are shown in **Figure 3. 7a.** These graphs showed two major peaks of C 1s and O 1s. In the broad spectrum of KL, two other signals are assigned to S 2p and Si 2p that remained from the pulping process of lignin extraction [80]. The presence of two new peaks in the spectrum of PK17 was attributed to the phosphorus

element after modification with PHA [81]. These peaks were found at 134.5 eV and 199 eV, respectively, assigned to P 2p and P 1s. The fitted C 1s, O 1s, and P 2p spectra for KL and PK17 are shown in **Figure 3. 7b–f** and **Tables S3.4–S3.7**. According to the C 1s spectra and the result of mass concentration, three significant peaks are shown in KL at 281.1 eV for C–C, 284.2 eV for C–OH, and 285.7 eV for O=C–OH with a mass concentration of 42.44%, 55.2%, and 2.35%, respectively. After the modification, PHA covalently bonded to KL, and by adding PHA to the KL backbone, the C–C bond increased to 48.41%.

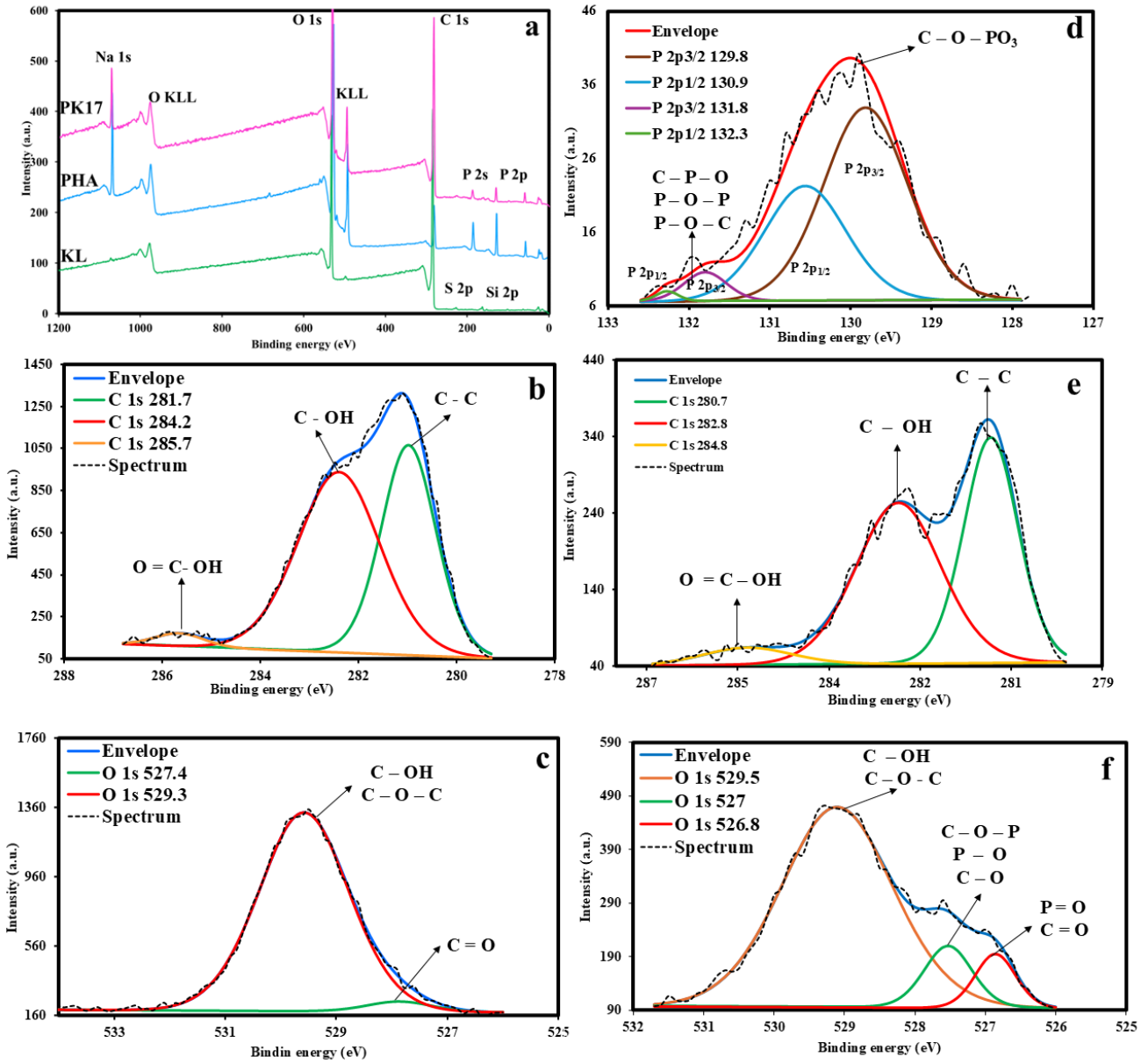

Figure 3.7. XPS broad spectra (a), C 1s and O 1s spectra of KL (b and c), C 1s and O 1s, and P 2p spectra of PK17 (d–f).

In **Figure 3. 7d,** two new bonds in PK17 (C–O–PO_3 and C–P–O) proved that the reaction happened *via* polycondensation with the hydroxyl groups on KL, confirming the results verified by ^{31}P NMR analysis. The phosphorus content of the samples was also determined from XPS and ICP-AES data, and the results are reported in **Table S3.2**. The phosphorus group content increased from 0 wt% to 7 wt% after the modification of KL with PHA. As noted, the amount of P determined in both ICP-AES and XPS results is similar.

One strong peak at 527.4 eV was observed in the fitted O 1s spectra of KL and PK17 (**Figure 3. 7**), corresponding to C–OH and C–O–C with 96.49% mass concentration dropping to 81.31% after phosphorylation. The peak intensity at 526.8 eV increased due to the overlap between the new P═O bond and the existing C═O bond in this region. Previous studies suggest that the C═O and P═O groups in the phosphate group exhibited the same binding energy in the spectrum [82, 83]. The increase in these bands from 3.51% to 7.93% is the reason for this overlap. The appearance of the C–O–P bond in the oxygen graph after modification at 527 eV is evidence of polycondensation in the route of phosphorylation.

The fitted P 2p spectrum, **Figure 3. 7d,** shows one prominent intense peak at 129.6 eV for C–O–PO_3, which was characteristic of phosphorus in both polyphosphates and phosphates, and one small shoulder peak at 131.5 eV for both C–P–O and P–O–P [84]. Such evidence confirmed that the –PO_3 group replaced a part of the aliphatic, phenolic, and carboxylic hydroxyl groups on the KL structure through the nucleophilic reaction [85].

3.4.5. Mechanism of reaction

The mechanism of reaction is proposed in **Figure 3. 8a** and **b**. The reaction occurs in two repetitive steps: first, phosphoric anhydride is formed with the elimination of water by a polycondensation reaction, and second, the phosphate atom leads to electron transfer from the oxygen in PA to the hydrogen of hydroxyl in the KL to form a new ester bond on the KL (**Figure 3. 8a**) [43]. The appearance of new peaks related to phosphorus groups in ^{1}H NMR in the range of 4–4.7 ppm, C–O–PO_3 and C–P–O bonds in XPS at 130 eV and 132 eV, and PO_4^{3-}, P–O–C aliphatic, and P–O stretching bands at 990 cm^{-1}, 960 cm^{-1}, and 850 cm^{-1}, in FTIR, respectively, confirms the reaction between KL and PHA. Moreover, quantitative ^{31}P NMR results approved the reduction of the hydroxyl groups of KL after modification. Phosphate groups on PHA are covalently bonded with different crosslinking types (a–c). This reaction can occur through both intra-chain and inter-chain routes, as shown in **Figure 3. 8b** [86, 87]. According to the results

of qualitative ^{31}P NMR (**Figure 3. 4**), the intensities of two peaks, a and b, are high, confirming that the modification mainly occurred *via* the intra-chain route [55]. It can be concluded that PHA reacted with the hydroxyl groups of KL and exhibited two types of a and b crosslinks that were stronger than the c type (**Figure 3. 4**).

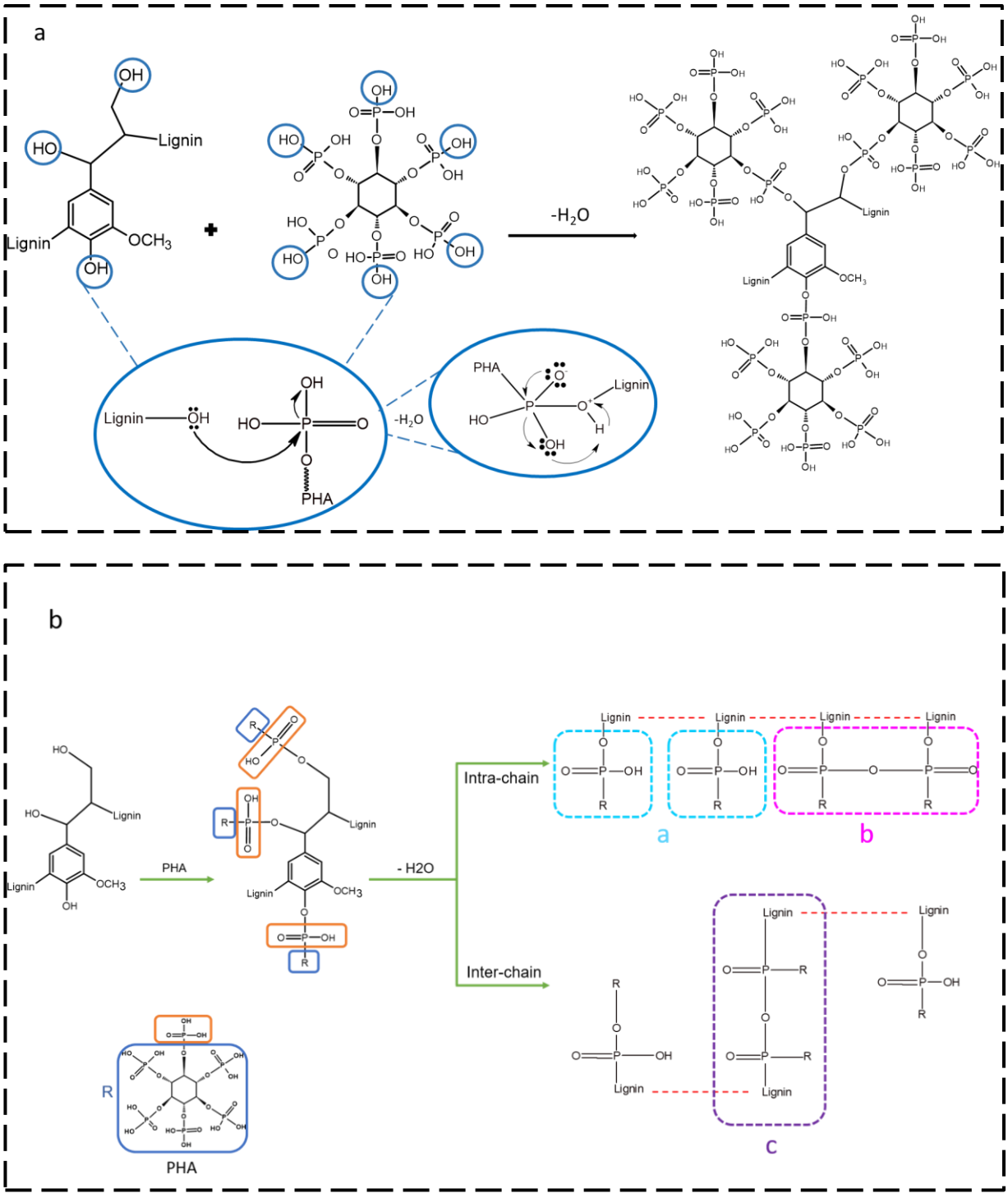

Figure 3.8. The reaction scheme of phosphorylation, (b) scheme of all possibility of crosslinking (a, b, and c).

3.4.6. Thermal properties

The thermal behavior of KL and PK17 was evaluated by thermogravimetric analysis (TGA) and is reported in **Figure 3. 9a**. The decomposition of lignin is divided into three main stages: the initial slight weight loss in the range of 25–100 °C is because of the evaporation of moisture, CO and CO_2. The weight loss between 175 °C and 550 °C is attributed to the degradation of aromatic rings and C–C linkages, such as C–C and β–β in KL [88]. The final weight loss at >550 °C was less and related to the decomposition and degradation of organic materials and carbonization [89, 90]. After the moisture removal from KL, the temperature corresponding to 5 wt% weight loss (T_d) increased from 210 ± 2 °C to 262 ± 2 °C after modification. T_{onset} is the temperature at which the major decomposition starts to occur. This temperature for KL and PK17 is 260 ± 2 °C and 300 ± 2 °C, respectively, implying that the modification improved the T_{onset} temperature by about 40 °C. Introducing the phosphorus group to KL increased the maximum decomposition temperatures (T_{max}) from 545 °C to 650 °C, and the weight loss rate decreased from 0.064 wt% $°C^{-1}$ to 0.026 wt% $°C^{-1}$ [86].

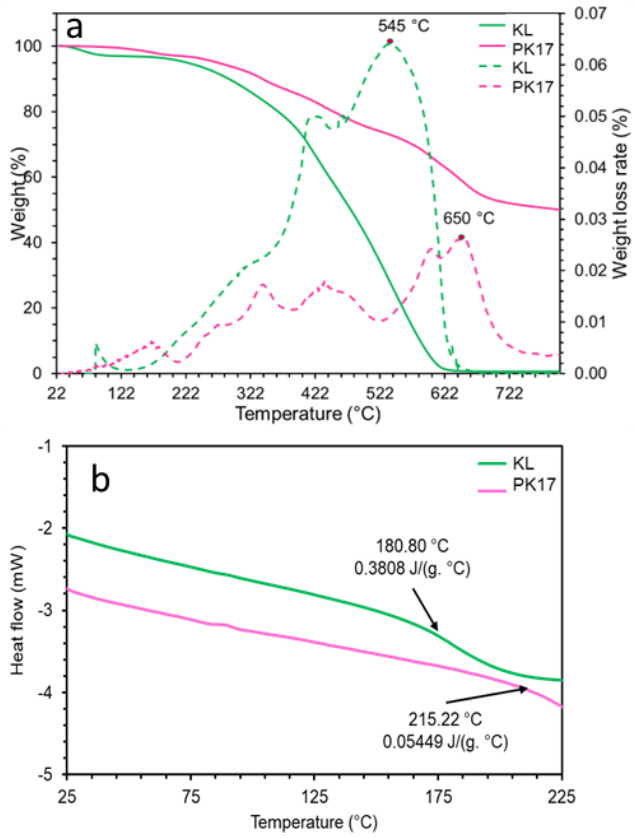

Figure 3.9. Thermal analysis of KL and PK17. TGA curves with an arrow indicating T_{max} (a). DSC curves showing the T_g and C_p (b).

It is also seen that KL did not remain at >620 °C, while 65 wt% of PK17 remained. At 800 °C, the char mass of PK17 was about 50 wt%, implying the improved char formation *via* phosphorylation.

The differential scanning calorimetry (DSC) analysis of the samples is shown in **Figure 3. 9b.** The molecular weight, crosslinking degree, branching degree, and chain length can affect the T_g of the material due to their impacts on segment mobility when heated/cooled [91, 92]. As reported in **Figure 3. 9b**, the T_g for KL was found at 180.8 °C, which increased to 215.2 °C after modification. The presence of phosphorus atoms after the modification and crosslinking of hydroxyl groups on the KL in the presence of the active sites of PHA contributed to an increased T_g [93]. In addition, PK17 had a lower heat capacity (C_p) than KL, 0.0544 J (g °C)$^{-1}$ and 0.3808 J (g °C)$^{-1}$, respectively. Less mobility, resistance to breakdown, and crosslinking would be the causes of this decreased heat capacity [94, 95]. In addition, inorganic compounds, such as phosphor, contributed to the increased T_g and decreased C_p [96].

3.4.7. Flame retardant performance

The flame retardancy of materials is commonly determined by the limiting oxygen index (LOI), and the results are listed in **Figure 3. 10.** Generally, with the increase in LOI values, the flame retardancy of the sample increased. As shown in **Figure 3. 10**, the LOI value of uncoated wood (UW) was 21.8%, implying that it could burn quickly with a small ignition. Different concentrations (1, 2, and 3 wt%) of KL (KC1, KC2, and KC3) were used for coating the wood species, respectively. Upon increasing the concentration of PK17 to 1, 2, and 3 wt%, the LOI value increased to 23.8%, 24.6%, and 26.0% for the samples of PC1, PC2, and PC3, respectively. Moreover, filter paper coated with 3 wt% PK17 demonstrated an increment in the LOI from 18% to 21%. Jiang *et al.* found that 10 wt% of *N,N*-biguanide-diethyl phosphonic acid can increase the LOI value of filter paper by >10% [97].

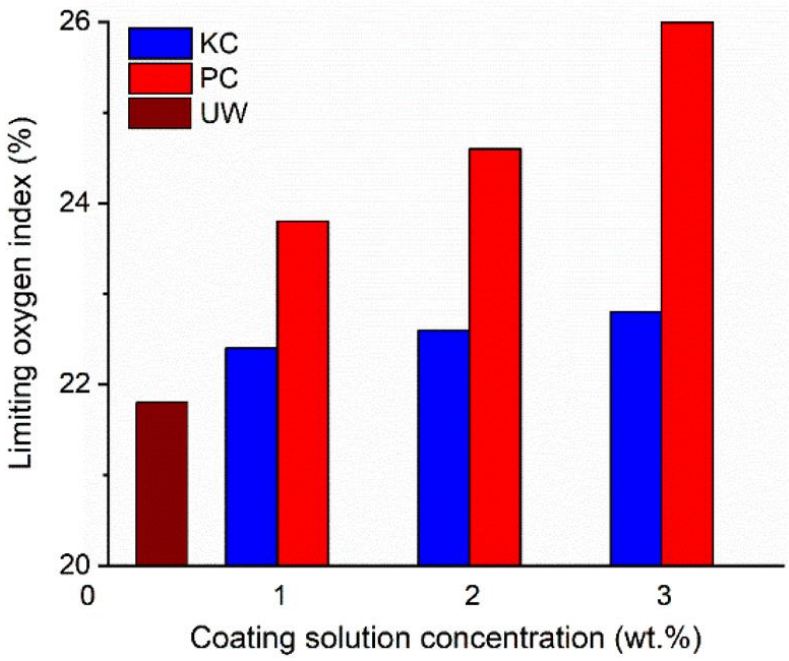

Figure 3.10. LOI values of the UW, KL, and PC (PK17 coated) samples.

As shown in **Figure 3. 11a** and **b**, the smoke density rate (SDR) in 240 s and light absorption of the uncoated wood (UW) were 34% and 50%, respectively. Generally, introducing KL to wood will affect wood species' flame retardancy. Coating wood with 1, 2, and 3% KL decreased the SDR value to 23.8%, 24.7%, and 27.8%, respectively. The introduction of 1, 2, and 3 wt% of PK17 reduced the light absorption to about 30%. The PK17-coated woods indicated a decrease in smoke production after 200 seconds, mainly because of the protective char layer of phosphorus–carbon [98]. Interestingly, the light absorption value peaked at around 180 s and subsequently declined since less smoke was released due to the char formation acting as a protective layer to lower the smoke density. PC3 (coated wood with 3 wt% of PK17) showed the lowest light absorption of 17.7% (*i.e.*, 16% lower than UW).

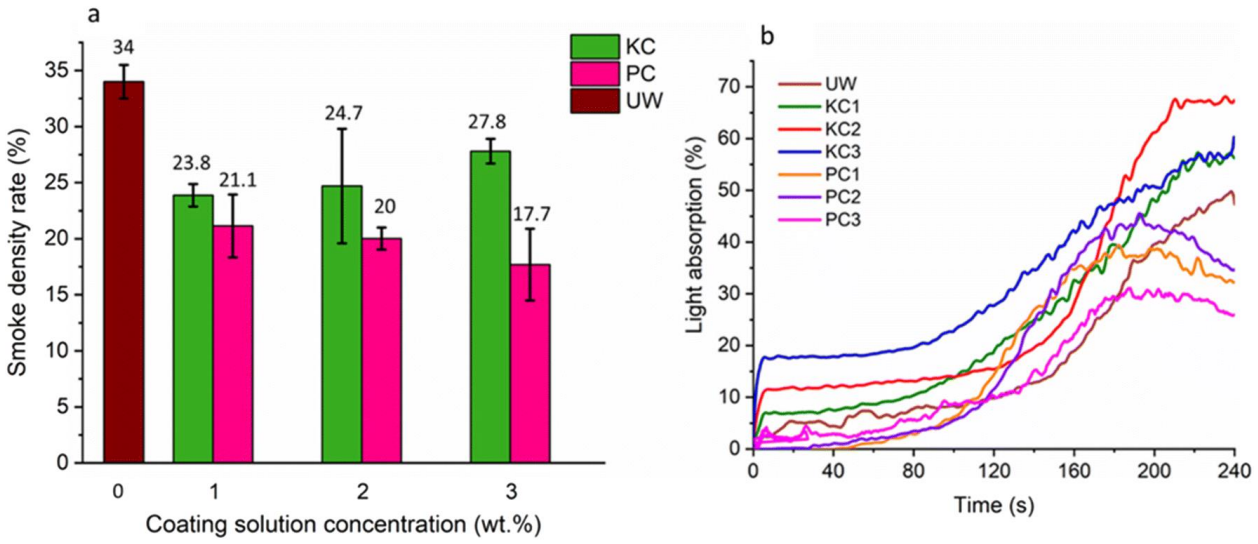

Figure 3.11. Smoke density rating values (a) and light absorption curves (b) of the UW, KL, and PC (PK17 coated) samples.

3.4.8. Morphological study of burned wood

The influence of phosphorylated lignin on the surface morphology of wood is generally determined by investigating char residues with SEM after smoke detector analysis [88]. **Figure S3.4** (in the ESI) and **Figure 3. 12** show char morphology after completing the combustion of UW and PC3, respectively. The spherical pores of some broken structures (**Figure S3.4a–d**) show the released gas caused by the combustion of UW, while these pores are compact in PC3 [99]. **Figure 3. 12a–d** show the blocked pores because of phosphoric acid production during thermal degradation. This would lead to increased dehydration and carbonization of PK17 to form char and phosphorus crystals to penetrate the pores and block them [100, 101]. **Figure 3. 12d** shows the phosphorus crystals after combustion. A char layer covered the PC3 after burning due to phosphorus groups' dehydration of PK17 and wood [102]. In addition, EDX observation indicated the presence of phosphorus atoms after burning PC3 (**Figure 3. 12f**).

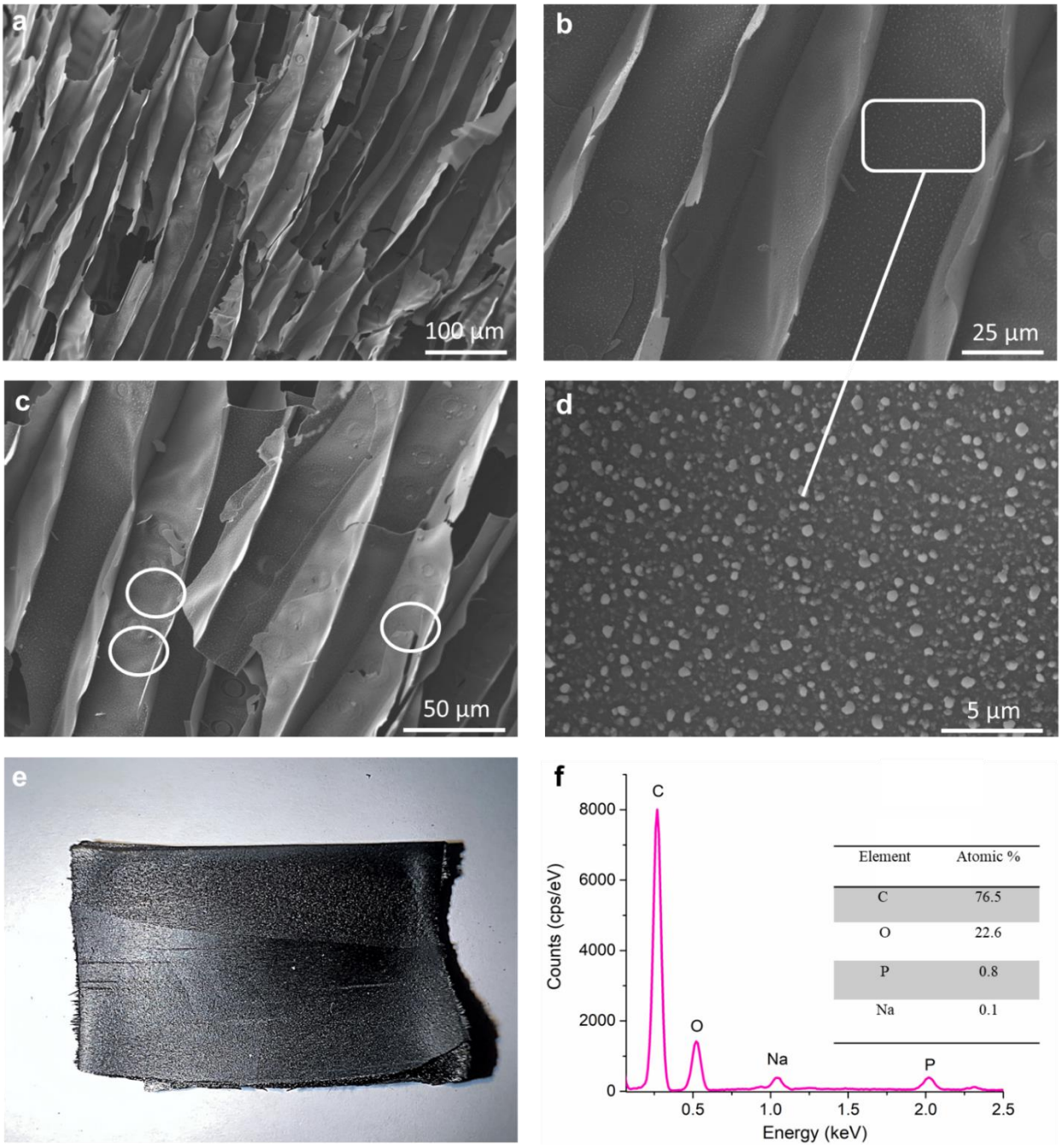

Figure 3.12. SEM images (a–d), digital picture (e), and EDX graph (f) of char residue after burning PC3 in smoke density analysis.

3.4.9. The mechanism of flame retardancy

FRs are employed to interrupt the combustion process in two ways: they create a dense char that shields the substrate from combustible gases (*i.e.*, oxygen) and heat (condensed phase mechanism), and they generate radical scavengers that can halt the chain propagation of the combustion reaction (vapor phase mechanism) [103]. The flame retardancy of PK17 can happen in both gas and condensed phases, chemically and physically. Phosphorus is an inorganic element that will produce radicals after decomposition to accelerate char formation as a protective layer from heat degradation

[104]. During combustion, triphenyl phosphate and triphenylphosphine oxide can break down into small radicals, such as $HPO^{\cdot}$, $PO_2^{\cdot}$, $PO^{\cdot}$, and $P_2^{\cdot}$ [105]. Because of ignition, these phosphorus radicals can function as an adsorbent for $H^{\cdot}$ and $OH^{\cdot}$ radicals released in the gas phase needed for ignition. A decrease in these radicals will reduce the flame [106].

In the condensed phase, phosphorus compounds start to decompose, and the protective char layer of phosphorus–carbon begins to form [92]. This protective layer could hold the flammable gases released from inner layers and keep away the heat from unburned wood layers [107, 108].

For a better understanding of how PK17 works as a flame retardant fundamentally, XPS analysis was carried out on the samples collected from TGA after treatment at four different temperatures (220, 320, 600, and 800 °C). **Figure S3.5–S3.8** show how the intensity of each peak changed, and the mass concentrations of each element and bond are reported in **Tables S3.4–S3.7** in detail. The mass concentration of P 2p increased from 7% at 25 °C to 26.9% at 800 °C (**Table S3.4**). Also, the C–C bond concentration remained almost the same (about 42%) (**Table S3.5**), but there was a decrease in the mass concentration of C–OH and C–O–C bonds from 81.31 to 15.22%. However, there was an increment in P–O, C═O, and P═O bonds from 3.51% to 49.49% (**Table S3.6**). These results confirmed that P and C remained as by-products of burning in the form of –P═O, C═O, C–O–P, P–O, P–O–P, and C–P–O, while oxygen was released. Also, the mass concentration of C–P–O and P–O–P increased from 4.36% to 70.33% (**Table S3.7**) [109]. Wang *et al.* argued that thermal oxidation resistance can be confirmed by an increment in C═O, which exhibits a thermal flame retardancy mechanism [110].

A deep analysis was carried out on a microscale using SEM, EDS, and EDX for PK17 before and after combustion at 800 °C. It was found (**Figure 3. 13a** and **c**) that the morphology of PK17 changed from a regular structure to irregular with some crystal structures [111], which was confirmed by SEM in coated wood after burning (**Figure 3. 12d**). In addition, the homogeneous distribution of C, P, and N elements in the PK17 and KL samples before and after combustion (**Figure 3. 13 and S3.9b, d**) was confirmed in the EDS images. Still, the intensity of the phosphorus element increased after combustion for PK17. Flame retardancy is mainly related to the concentration of phosphorus that can delay the transfer of heat, block the diffusion of flame efficiently, and increase oxygen demand for burning, inducing a more efficient flame retardancy (**Figure 3. 10** and **11b**) [112].

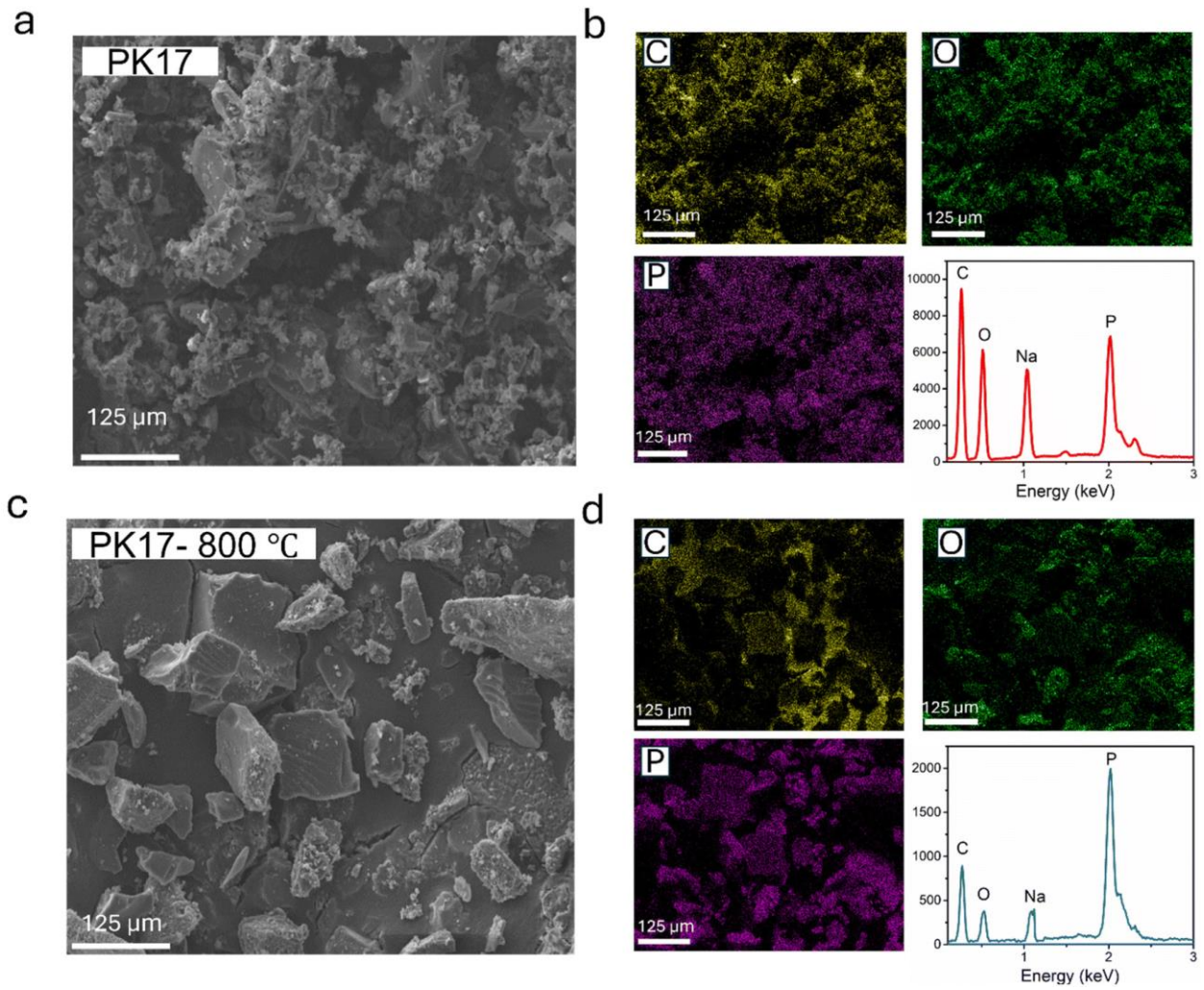

Figure 3.13. The SEM images (a and c), EDS elemental mapping, and EDX (b and d) of the surface of PK17 before and after combustion.

To understand how PK17 would function as a flame retardant, the SEM and EDX images of PC3 samples after combustion were analyzed in detail. The results (**Figure S3.7** and **12**) provide evidence for the elemental composition of phosphorus crystals, char residue formation, filled porous structures, gaps, and cracks in wood after burning. These results imply that PC3 acted as a protection shield to disrupt the penetration of gas (oxygen) and heat flow during combustion [107]. In addition, the char formation would work as a protective layer that would decrease smoke release, leading to a lower smoke density rate and light adsorption (**Figure 3. 11**).

The performance and reaction route of phosphorylated lignin products were compared with other phosphorylated lignin products in **Table 3.2**. Our sample, a pioneering biomaterial, sets itself apart by being free from solvent (water base) and bio-phosphorus reagent (PHA) while exhibiting outstanding high heat resistance and flame retardancy. Unlike conventional materials that are listed in **Table 3.2**, made of oil-derived chemical reagents and under harsh

and environmentally unfriendly conditions, our biomaterial was produced using environmentally friendly reagents, a water-based reaction at room temperature, ensuring a safer and more sustainable approach. The elimination of solvents not only reduces the environmental impact but also minimizes potential health hazards associated with their use. Additionally, our biomaterial's heat resistance is outstanding, offering enhanced heat resistance. This combination of solvent-free processing and excellent heat resistance with high thermal performance underscores the material's potential in advancing eco-friendly and high-performance applications. Theoretically, other types of lignin, *e.g.*, alkali, lignosulfonate, and organosolv, may be used for reacting with PHA in a similar manner as they all have OH functional groups. However, their efficiency may be different, which will be attested in our future work.

Table 3.2. Comparative study of lignin phosphorylation routes according to the literatures.

Source of lignin	**Reagent (reagent: lignin)**	**Reaction condition**	**Solvent**	**TGA and DTG**	**Char residue at 800 °C**	**Application**	**ref**
Softwood kraft lignin	Ammonium dihydrogen phosphate 9:1 (mol: mol)	1 h at 70 °C	Urea	T_{max} from 541 °C to 620 °C	From 0 % to 15 %	Not tested	[38]
Softwood kraft lignin	Phosphoric acid (85%) 0.5:0.14 (g:g)	50 °C	Acetone and urea	Not reported	Not reported	Not tested	[113]
Kraft lignin	Phosphorus pentoxide 2.5: 1 (phr: g)	1 to 24 h at 70°C	Tetrahydrofuran	T_{max} not reported	From 0 % to 38 %	Polypropylene-based composites	[114]
Alkaline lignin	Phosphorus pentoxide 5.5: 1 and 2.5: 1 (mol:mol)	2 h at 5 °C Nitrogen gas	Methane sulfonic acid, purification by diethyl ether, acetone, or methanol	T_{max} from 465 °C to 572 °C and 607 °C	From 44.4 % to 13.5 % and 10.3 %	Epoxy resin	[115]

Kraft lignin	Phosphorus pentoxide Not reported	7 to 8 h at room temperature	Tetrahydrofuran	T_{max} from 370 °C to 409 °C	From 45 % to 53 %	Not tested	[116]
Kraft lignin	Phosphorus chloride 6.5: 10 (g: g)	17 h at 60 °C	Mixture of CHCl3/N-methyl-2-pyrrolidone precipitation and washed in cooled isopropyl alcohol and diethyl ether	Not available	Not available	polyester based composites	[117]
Kraft lignin	Phytic acid 0.4: 1 (mol:mol)	20 min at room temperature	Water	T_{max} from 545 °C to 640 °C	From 0 % to 50 %	Coating	This work

3.5. Conclusion

A sustainable flame retardant was prepared in an aqueous medium, *i.e.*, green solvent, from KL and PHA. The reaction conditions that yielded the lignin derivative with the highest phosphorus element were a KL : PHA molar ratio of 1 : 0.4 mol/mol, a reaction time of 20 min, a temperature of 20 °C, and a pH of 11. These optimized conditions resulted in PK17 with −4.2 mmol g^{-1} charge density, 9.7 g L^{-1} solubility in water, and an M_w of 4800 g mol^{-1}. The reaction under the optimized conditions decreased the aliphatic and phenolic hydroxyl groups of KL from 1.72 to 0.63 mmol g^{-1} and 3.33 to 0.71 mmol g^{-1}, respectively. ^{1}H, HSQC, and ^{31}P NMR confirmed that the aliphatic and aromatic OH groups of KL participated in the reaction with PHA and generated a covalent bond of P–O–C. The qualitative ^{31}P NMR confirmed the three different crosslinking types of phosphate groups based on the reaction conditions, such as monophosphate, phosphodiester, and orthophosphate. Also, FTIR, XPS, and ICP-AES analyses confirmed the presence of phosphorus atoms and the new C–O–P bond between KL and PHA.

The TGA analysis confirmed that the phosphorylation of KL improved the thermal stability of lignin by improving its decomposition temperature from 545 °C to 650 °C with char formation at 800 °C, while KL did not produce any char at 625 °C. The DSC results confirmed the increment in T_g from 180.8 °C to 215.2 °C after phosphorylation. The combustion completion was analyzed by SEM, EDX, and EDS for PK17, and the change in sample morphology from regular to irregular and the increment in the intensity of phosphorus were confirmed after combustion. By increasing the concentration of PK17 solution from 1 wt% to 3 wt% in the wood coating process, the LOI of wood rose from 21.8% to 26.0%, and the smoke density rate decreased from 34.0% to 17.7% due to the formation of thermally stable char and the release of non-flammable gases. The promising flame retardant performance of PK17 on wood and filter paper paves the way for the production pathway of PK17 as a simple and effective aqueous-based reaction to produce phosphorylated lignin.

3.6. References

1. E.D. Weil and S. V Levchik, *J. Fire Sci.*, 2008, **26**, 243-281.
2. A.B. Morgan and J.W. Gilman, *Fire Mater.*, 2013, **37**, 259–279.
3. S.K. Pandit, B.K. Tudu, I.M. Mishra and A. Kumar, *Prog. Org. Coat.*, 2020, **139**, 105453.
4. M. Li, X. Hao, M. Hu, Y. Huang, C. Tang, Y. Chen and L. Li, *Prog. Org. Coat.*, 2022, **172**, 107161.
5. T. Ma, L. Li, Q. Wang and C. Guo, *Compos. B. Eng.*, 2019,**177**, 107357.
6. M. Dogan, S. Dilem Dogan, L. Atabek Savas, G. Ozcelik and U. Tayfun, *Compos. B. Eng.*, 2021, **222**, 109088.
7. J. De Boer and H.M. Stapleton, *Science*, 2019, **364**, 231–232.
8. F. Xu, L. Zhong, C. Zhang, P. Wang, F. Zhang and G. Zhang, *ACS Sustain. Chem. Eng.*, 2019, **7**, 13999−14008.
9. I. van der Veen and J. de Boer, *Chemosphere*, 2012, **88**, 1119–1153.
10. L. Costes, F. Laoutid, S. Brohez and P. Dubois, *Mater. Sci. Eng. R.*, 2017, **117**, 1–25.
11. H.S. Hendriks, M. Meijer, M. Muilwijk, M. Van Den Berg, Remco and H.S. Westerink, *Arch. Toxicol.*, 2014, **3**, 857–869.
12. M. Ghanadpour, F. Carosio, P. Tomas Larsson and L. Wa, *J. Biol. Macromol.*, 2015, **16**, 3399−3410.
13. M. Wang, G.-Z. Yin, Y. Yang, W. Fu, J. Luis Díaz Palencia, J. Zhao, N. Wang, Y. Jiang and D.-Y. Wang, *Adv. Ind. Eng. Polym. Res.*, 2022, **6**, 132-155.
14. K. Ahmad, H.R. Ghatak and S.M. Ahuja, *J. Environ. Chem. Eng.*, 2022, 275–309.
15. G. Atiwesh, | Christopher, C. Parrish, J. Banoub and T.A.T. Le, *Biotechnol. Prog.*, 2021, **38**, 3226.
16. Q. Shao, Y. Luo, M. Cao, X. Qiu and D. Zheng, *Chem. Eng. J.*, 2023, **476**, 146678.
17. Y. Li, X. Qiu, Y. Qian, W. Xiong and D. Yang, *Chem. Eng. J.*, 2017, **327**, 1176–1183.
18. Y.F. Gao, C.Y. Ma, Q. Sun, X.X. Zhang, J. Liu, J.L. Wen, R.X. Chen, H.L. Wang and T.Q. Yuan, *Chem. Eng. J.*, 2024, **481**, 148514.
19. B. Yan, M. Li, H. Lu, M. Pi, J. Mu, W. Cui and R. Ran, *Chem. Eng. J.*, 2024, **481**, 148540.
20. B. Wang, X.F. Cao, S.X. Yu, Z.H. Sun, X.J. Shen, J.L. Wen and T.Q. Yuan, *J. Clean Prod.*, 2023, **387**, 135801.
21. L. Meng, S. Chirtes, X. Liu, M. Eriksson and W.C. Mak, *Biosens. Bioelectron.*, 2022, **218**, 114742.
22. T. Yao, R. Yang, C. Sun, Y. Lin, R. Liu, H. Yang, J. Chen and X. Gu, *Molecules*, 2023, **28**, 2699.
23. D. Zhang, J. Zeng, W. Liu, X. Qiu, Y. Qian, H. Zhang, Y. Yang, M. Liu and D. Yang, *Green Chem.*, 2021, **23**, 5972-5980.

24. H. Yang, B. Shi, Y. Xue, Z. Ma, L. Liu, L. Liu, Y. Yu, Z. Zhang, P.K. Annamalai and P. Song, *J. Compos. Sci.*, 2021, **22**, 1432–1444.
25. L. Costes, F. Laoutid, M. Aguedo, A. Richel, S. Brohez, C. Delvosalle and P. Dubois, *Eur. Polym. J.*, 2016, **84**, 652–667.
26. Y. Liu, W. Zhao, X. Yu, J. Zhang, Y. Ren, X. Liu and H. Qu, *Polym. Degrad. Stab.*, 2022, **203**, 110062.
27. Y. Guo, C. Cheng, T. Huo, Y. Ren and X. Liu, *Polym. Degrad. Stab.*, 2020, **181**, 109362.
28. T. Mariappan, Y. Zhou, J. Hao and C.A. Wilkie, *Eur. Polym. J.*, 2013, **49**, 3171–3180.
29. Z. Xiong, Y. Zhang, X. Du, P. Song and Z. Fang, *ACS Sustain. Chem. Eng.*, 2019, **7**, 8954–8963.
30. X. Cheng, L. Shi, Z. Fan, Y. Yu and R. Liu, *Polym. Degrad. Stab.*, 2022, **199**, 109898.
31. X. Qian, L. Song, S. Jiang, G. Tang, W. Xing, B. Wang, Y. Hu and R.K.K. Yuen, *Ind. Eng. Chem. Res.*, 2013, **52**, 7307–7315.
32. X.W. Cheng, Z.Y. Wang, W.J. Jin and J.P. Guan, *Ind. Crops. Prod.*, 2022, **187**, 115332.
33. X. Cheng, L. Shi, Z. Fan, Y. Yu and R. Liu, *Polym. Degrad. Stab.*, 2022, **199**, 109898.
34. M. Barbalini, L. Bertolla, J. Toušek and G. Malucelli, *Polym. J.*, 2019, **11**, 1664.
35. L. Li, Z. Chen, J. Lu, M. Wei, Y. Huang and P. Jiang, *ACS Omega*, 2021, **6**, 3930.
36. T.C. Mokhena, E.R. Sadiku, S.S. Ray, M.J. Mochane, K.P. Matabola and M. Motloung, *J. Appl. Polym. Sci.*, 2022, **139**, 52495.
37. L. Costes, F. Laoutid, L. Dumazert, J.M. Lopez-Cuesta, S. Brohez, C. Delvosalle and P. Dubois, *Polym. Degrad. Stab.*, 2015, **119**, 217–227.
38. C. Gao, L. Zhou, S. Yao, C. Qin and P. Fatehi, *Int. J. Biol. Macromol.*, 2020, **162**, 1642–1652.
39. B. Prieur, M. Meub, M. Wittemann, R. Klein, S. Bellayer, G. Fontaine and S. Bourbigot, *Polym. Degrad. Stab.*, 2016, **127**, 32–43.
40. G.L. Bykov and B.G. Ershov, *Russ. J. Appl. Chem.*, 2010, **83**, 316–319.
41. Y. Guo, C. Cheng, T. Huo, Y. Ren and X. Liu, *Polym. Degrad. Stab.*, 2020, **181**, 109362.
42. S.J. Marciano, F. Avelino, L.R.R. da Silva, S.E. Mazzetto and D. Lomonaco, *Biomass Convers. Biorefin.*, 2022, **12**, 619–631.
43. Y.M. Zhang, Q. Zhao, L. Li, R. Yan, J. Zhang, J.C. Duan, B.J. Liu, Z.Y. Sun, M.Y. Zhang, W. Hu and N.N. Zhang, *RSC Adv.*, 2018, **8**, 32252–32261.
44. M. V Efanov and A.I. Galochkin, *Chem. Nat. Compd.*, 2012, **48**, 457–459.
45. Xiong, X. Qiu, R. Zhong and D. Yang, *Holzforschung*, 2016, **70**, 937–945.
46. C. Gao, L. Zhou, S. Yao, C. Qin and P. Fatehi, *Int. J. Biol. Macromol.*, 2020, **162**, 1642–1652.
47. C. Gao, L. Zhou, S. Yao, C. Qin and P. Fatehi, *Int. J. Biol. Macromol.*, 2020, **162**, 1642–1652.
48. V. Carretier, M.F. Pucci, C. Lacoste, A. Regazzi and J.M. Lopez-Cuesta, *Appl. Surf. Sci.*, 2022, **579**, 152159.
49. H. Qiao, Y. Liang, G. Xu, Y. Wang, J. Yang and J. Hu*, Des. Monomers Polym.*, 2019, **22**, 114–121.
50. L. Oatway, T. Vasanthan and J.H. Helm, *Food Rev. Int.*, 2007, **17**, 419–431.
51. S. Gharehkhani, N. Ghavidel and P. Fatehi, *ACS Sustain. Chem. Eng.*, 2019, **7**, 2370–2379.
52. G.S. Dhaliwal, N. Gupta, S.S. Kukal and M. Kaur, *Commun. Soil Sci. Plant Anal.*, 2011, **42**, 971–979.
53. F. Kong, S. Wang, J.T. Price, M.K.R. Konduri and P. Fatehi, *Green Chem.*, 2015, **17**, 4355.
54. X. Meng, C. Crestini, H. Ben, N. Hao, Y. Pu, A.J. Ragauskas and D.S. Argyropoulos, *Nat. Protoc.*, 2019, **14**, 2627–2647.
55. R. Ravichandran, V. Seitz, J. Reddy Venugopal, R. Sridhar, S. Sundarrajan, S. Mukherjee, E. Wintermantel and S. Ramakrishna, *Macromol. Biosci.*, 2013, **13**, 366–375.
56. P. Tomani, *cellulose Chem. Technol.*, 2010, **44**, 53–58.
57. D.R. Bhumkar and V.B. Pokharkar, *AAPS Pharm. Sci. Tech.*, 2006, **7**, 138–143.
58. C. Cagnin, B.M. Simões, F. Yamashita, G.M. de Carvalho and M.V.E. Grossmann, *Polym. Eng. Sci.*, 2021, **61**, 388–396.
59. L. Xia, F. Song, F. Meng, L. Wang and S. Zhao, *ACS ES and T Water*, 2023, **3**, 1923–1934.
60. L. Jiang, J. Guan, L. Zhao, J. Li and W. Yang, *Colloids Surf. A. Physicochem. Eng. Asp.*, 2009, **346**, 216 - 220.
61. J.Y. Park and E.Y. Park, *Int. J. Biol. Macromol.*, 2023, **226**, 312–320.
62. H. Huo, Y. Yu, X. Zhang, M. Tang, C. Chen, S. Wang and D. Min, *Ind. Crops Prod.*, 2022, **188**, 115727.
63. D. Wang, Y. Wang, T. Li, S. Zhang, P. Ma, D. Shi, M. Chen and W. Dong, *ACS Sustain. Chem. Eng.*, 2020, **8**, 10265–10274.

64. J. Pretula, K. Kaluzynski, B. Wisniewski, R. Szymanski, T. Loontjens and S. Penczek, *J. Polym. Sci. Part A.: Polym. Chem.*, 2007, **46**, 830–843.
65. S.P.J. Brooks, D. Oberleas, B.A. Dawson, B. Belonje and B.J. Lampi, *J. AOAC Int.*, 2001, **84**, 1125–1129.
66. C. Gao, L. Zhou, S. Yao, C. Qin and P. Fatehi*, Int. J. Biol. Macromol.*, 2020, **162**, 1642–1652.
67. F. Rol, C. Sillard, M. Bardet, J.R. Yarava, L. Emsley, C. Gablin, D. Léonard, N. Belgacem and J. Bras, *Carbohydr. Polym.*, 2020, **229**, 115294.
68. S.N. Sun, M.F. Li, T.Q. Yuan, F. Xu and R.C. Sun, *Ind. Crops Prod.*, 2013, **43**, 570–577.
69. N.M. Stark, D.J. Yelle and U.P. Agarwal, *Cellulose*, 2016, **4**, 6811–6831.
70. C. Crestini, H. Lange, M. Sette and D.S. Argyropoulos, *Curr. Green Chem.*, 2017, **19**, 4104.
71. Z. Shomali and P. Fatehi, *ACS Sustain. Chem. Eng.*, 2022, **10**, 16563–16577.
72. A. Hoffmann, J.P. Nong, A. Porzel, M. Bremer and S. Fischer, *React. Func. Polym.*, 2019, **142**, 112–118.
73. C. Heitner, Don. Dimmel and J.A. Schmidt, *CRC press*, 2010.
74. A.T. Bauman, G.M. Chateauneuf, B.R. Boyd, R.E. Brown and P.P.N. Murthy, *Tetrahedron. Lett.*, 1999, **40**, 4489–4492.
75. A. Chen, L. Zhu and Y. Arai, *Sci. Total Environ.*, 2022, **840**, 156700.
76. G.J. Jiao, J. Ma, J. Hu, X. Wang and R. Sun, *J. Hazard. Mater.*, 2023, **448**, 130988.
77. B. Prieur, M. Meub, M. Wittemann, R. Klein, S. Bellayer, G. Fontaine and S. Bourbigot, *Polym. Degrad. Stab.*, 2016, **127**, 32–43.
78. G. Nourry, D. Belosinschi, M.P. Boutin, F. Brouillette and R. Zerrouki, *Cellulose*, 2016, **23**, 3511–3520.
79. F.Z. Semlali, A. Ait Benhamou, K. El Bourakadi, A.E.K. Qaiss, R. Bouhfid, J. Jacquemin and M. El Achaby, *Chem. Eng. J.*, 2023, 473, 145268.
80. R.J. Coleman, G. Lawrie, L.K. Lambert, M. Whittaker, K.S. Jack and L. Grøndahl, *Biomacromolecules*, 2011, **12**, 889–897.
81. F. Zhang, W. Liu, C. Liu, S. Wang, H. Shi, L. Liang and K. Pi, *Colloids Surf. A. Physicochem. Eng. Asp.*, 2021, **617**, 126390.
82. H. Liu, J. Ma, J. Gong and J. Xu, *J. Non. Cryst. Solids*, 2015, **419**, 92–96.
83. Y. Yu, S. Fu, P. Song, X. Luo, Y. Jin, F. Lu, Q. Wu and J. Ye, *Polym. Degrad. Stab.*, 2012, **97**, 541–546.
84. J. Yang, Z. Feng, Q. Gao, L. Ni, Y. Hou, Y. He and Z. Liu, *Renew. Energy*, 2021, **174**, 178–187.
85. X. Gao, Z. Cao, C. Li, J. Liu, X. Liu and L. Guo, *New J. Chem.*, 2022, **46**, 18952-18960.
86. B. Tian, B. Tian, B. Smith, M.C. Scott, Q. Lei, R. Hua, Y. Tian and Y. Liu, *Proc. Natl. Acad. Sci. USA*, 2018, **115**, 4345–4350.
87. C. Viornery, Y. Chevolot, D. Léonard, B.-O. Aronsson, P. Péchy, H.J. Mathieu, P. Descouts and M. Grä, *Langmuir*, 2002, **18**, 2582-2589.
88. M. Shimizu, Y. Tsushima and S. Arai, *ACS Omega*, 2017, **2**, 4306–4315.
89. Q. Zhang, X. Wang, Z. Li, W. Wu, J. Liu, H. Wu, S. Cui, K. Guo, *RSC Adv.*, 2014, **4**, 19710–19715.
90. Y.J. Lee, B. Bingöl, T. Murakhtina, D. Sebastiani, W.H. Meyer, G. Wegner and H.W. Spiess, *J. Phys. Chem. B*, 2007, **111**, 9711–9721.
91. M. Farrokhi, M. Abdollahi and A. Alizadeh, *Polymer (Guildf)*, 2019, **169**, 215–224.
92. Z. Ma, Q. Sun, J. Ye, Q. Yao and C. Zhao, *J. Anal. Appl. Pyrolysis*, 2016,**117**, 116–124.
93. C. Gao, L. Zhou, S. Yao, C. Qin and P. Fatehi, *Int. J. Biol. Macromol.*, 2020, **162**, 1642–1652.
94. M. Wądrzyk, R. Janus, M. Lewandowski and A. Magdziarz, *J. Renew. Energy*, 2021, **177**, 942–952.
95. H. Zheng, X. Han, Q. Wei, C. Zheng, C. Huang, Z. Jin, Y. Li and J. Zhou, *Chem. Eng. J.*, 2022, **437**, 135412.
96. I.E. Raschip, G.E. Hitruc, C. Vasile and M.C. Popescu, *Int. J. Biol. Macromol.*, 2013, **54**, 230–237.
97. I. Ribca, M.E. Jawerth, C.J. Brett, M. Lawoko, M. Schwartzkopf, A. Chumakov, S. V Roth and M. Johansson, *ACS Sustain. Chem. Eng.*, 2021, **9**, 1692−1702.
98. S. Luo, J. Cao and A.G. McDonald, *Ind. Crops Prod.*, 2018, **121**, 169–179.
99. S. Montserrat, *Polymer*, 1995, **36**, 435-436.
100. H. Li and A.G. McDonald, *Ind. Crops Prod.*, 2014, **62**, 67–76.
101. D. Tarasov, M. Leitch and P. Fatehi, *Fuel Process Technol.*, 2017, **158**, 146–153.
102. S. Zhao, B. Xu, H. Shan, Q. Zhang and X. Wang, *Polymers (Basel)*, 2023, **15**, 1917.
103. A. Sethurajaperumal, A. Manohar, A. Banerjee, E. Varrla, H. Wang and K. Ostrikov, *Nanoscale Adv.*, 2021, **14** ,4235-4243.
104. F. Wang, J.Y. Cheong, Q. He, G. Duan, S. He, L. Zhang, Y. Zhao, I.D. Kim and S. Jiang, *Chem. Eng. J.*, 2021, **414**, 128767.
105. H. Bin Yuan, R.C. Tang and C.B. Yu, *Int. J. Mol. Sci.*, 2021, **22**, 9631.

106. J. Liu, P. Qi, D. Meng, L. Li, J. Sun, H. Li, X. Gu, S. Jiang and S. Zhang, *Ind. Crops Prod.*, 2022, **186**, 115239.
107. P. Wang and Z. Cai, *Polym. Degrad. Stab.*, 2017, **137**, 138–150.
108. D. Niu, W. Yu, W. Yang, P. Xu, T. Liu, Z. Wang, X. Yan and P. Ma, *Chem. Eng. J.*, 2023, **474**, 145753.
109. M.M. Velencoso, A. Battig, J.C. Markwart, B. Schartel and F.R. Wurm, *Angew. Che. Int. Ed.*, 2018, **57**, 10450–10467.
110. L. Yan, Z. Xu and N. Deng, *Prog. Org. Coat.*, 2019, **135**, 123–134.
111. K. Bansal, S. Swarup and M. Quadir, *Prog. Org. Coat.*, 2022, **172**, 107093.
112. Z. Ma, D. Meng, Z. Zhang and Y. Wang, *Thermochim. Acta*, 2022, **707**, 179118.

4. Fully biobased flame retardant lignin incorporated chitosan derived aerogel

Saba Khodavandegar, Pedram Fatehi *

Published in Chemical Engineering Journal

Green Processes Research Center and Chemical Engineering Department, Lakehead University, 955 Oliver Road, Thunder Bay, ON P7B5E1, Canada

First Author, email: skhodava@lakeheadu.ca, address: 955 Oliver Road, Thunder Bay, ON, Canada, P7B 5E1

Corresponding author: E-mail: pfatehi@lakehadu.ca, address: 955 Oliver Road, Thunder Bay, ON, Canada, P7B 5E1

The contribution of Saba Khodavandegar to this work was writing of original draft, visualization, validation, methodology, experiment, formal analysis, data curation, and conceptualization

Graphic abstract

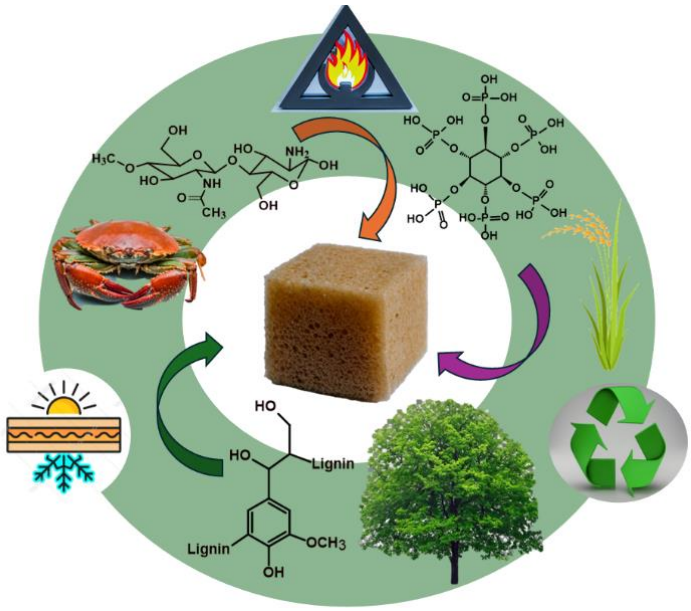

4.1. Abstract

Petroleum-based aerogels have broad applications in the construction industry as thermal insulators, but their non-degradability and high flammability pose significant environmental and safety challenges. The incorporation of biobased material in aerogel fabrication has been considered a strategy to address the biocompatibility and degradability of aerogels. However, the low strength and flammability of biobased aerogels still make their practical use impaired. This study focused on the fabrication of chitosan (CH) and phosphorylated kraft lignin (PK) aerogel to develop a strong lightweight, thermally insulated, and flame retardant aerogel (APK). The optimized fabrication process, exploited by Taguchi design, were medium molecular weight CH, 1 mmol/g charge density of PK, 2 wt.% PK concentration, at 30 °C reaction temperature. The FTIR, NMR and XPS confirmed the new chemical bonds of C–P=O and C–N in –C–N–P, while XRD revealed both crystalline and amorphous structures of APK aerogel. This physicochemical alteration improved the porosity, reduced the thermal conductivity, and improved the compression strength and Young's modulus of the aerogel to 0.947 cm^3/g, 0.35 W/mK, 0.83 and 6.21 MPa, respectively, which are substantially better than those of pristine chitosan and kraft lignin-based aerogels. The flame retardant mechanism of APK was confirmed by smoke density release, limiting oxygen index (LOI), and UL-94 methods. APK aerogel enhanced the low degradation due to the presence of phosphorus, leading to a high-quality char layer that served as an effective barrier for flame progress. Additionally, due to excellent thermomechanical performance and biodegradability, the generated aerogel can serve as an excellent thermal insulator for the construction industry.

Keywords: Lignin, chitosan, aerogel, thermal stability, thermal insulation, sustainable process, biodegradable

4.2. Introduction

Aerogels are porous materials with three-dimensional networks characterized by low density, low thermal conductivity, and a large surface area [1]. Lightweight aerogels with rich surface functionality, and uniform

porosity, are valued for their low density and excellent thermal properties [2-4]. With the growing focus on energy efficiency and environmental sustainability, there is an increasing demand for eco-friendly insulation. Currently, most insulation materials made of porous petrochemical materials, such as polystyrene [5, 6] and polyurethane [7, 8], which pose environmental challenges. There is a need to develop bio-based aerogels for use as thermal insulation materials [9].

In recent years, there has been a notable rise in the demand for advanced insulation and flame retardant materials, primarily due to the elevated safety standards and improving energy efficiency in building construction and design [10]. Among the materials under investigation, chitosan has garnered considerable attention due to its unique properties [11]. Chitosan (CH), a copolymer of N-acetyl glucosamine and D-glucosamine linked by 1,4-glycosidic bonds, is the most abundant biomass after cellulose and lignin, it is characterized by its biodegradability, non-toxicity, and inherent flame retardant capabilities [12, 13]. The incorporation of chitosan into insulation materials offers a promising approach to enhancing fire resistance [9], thereby improving their safety profile for the construction applications. However, the mechanical properties of this aerogel are low due to the weak physical interaction (e.g., hydrogen bonds and electrostatic interactions) of chitosan molecules in aerogel structure [14]. Logically, the addition of a crosslinker or other material is necessary to improve the mechanical strength of chitosan derived aerogels [15].

In this regard, chitosan has been blended with other materials for aerogel fabrications. For example, Huawei et al. prepared silica-fly ash containing chitosan aerogels to prepare nanoporous, three-dimensional network aerogels with thermal conductivity values ranging 0.0474 -0.0521 W/mK, shy of 0.004 W/mK, limiting its use for thermal insulation materials [16]. In another study, Du et al. used fractionated chitosan and methyl phosphoric acid to develop flame retardant aerogels. Nevertheless, owning to limited physical interaction between the constituents of the produced materials, it still had weak compression strength making it unsuitable for the proposed applications [9]. Therefore, there is still a need for incorporating other materials into chitosan-based formulation for achieving acceptable mechanical and thermal characteristics.

Lignin, a naturally occurring polymer, has garnered considerable interest for its application in the fabrication of flame retardant composites. Lignin can serve as a valuable additive to chitosan to produce aerogels due to its several beneficial properties, e.g., high thermal stability, and mechanical strength [17, 18]. When integrated with chitosan, a synergistic composite material that leverages the unique properties of both lignin and chitosan can be manufactured. Specifically, lignin could contribute inherent flame retardant characteristics, while chitosan would contribute to the generation of protective char layer during combustion. This combination would result in the production of a highly efficient flame retardant material [19]. The lignin-chitosan composite holds considerable promise for applications in the construction industry, where fire safety is a critical concern [17]. Additionally, the use of bio-based components in the composite supports sustainable construction practices, aligning with the growing demand for environmentally friendly building materials [20].

However, the incorporation of lignin into chitosan-derived composites or aerogels for insulating applications has faced significant limitations. These challenges stem from lignin's heterogeneous structure, poor solubility, and low compatibility with other materials [20]. Such issues impede the uniform dispersion of lignin within the composite matrix, thereby compromising the mechanical strength and thermal efficiency of the final product [21]. Furthermore, the variability in lignin's composition, which is influenced by its source, complicates the optimization of its properties for specific uses [22]. The heterogeneous structure and limited solubility of lignin are well-documented challenges that significantly impact its compatibility with other polymers, such as chitosan [23]. Studies have shown that the poor dispersion of lignin within polymer matrices could lead to reduced mechanical and thermal properties [24]. Tran et al. discussed the fabrication of cellulose–chitosan aerogels and lignin/silica hybrids. They encountered difficulties with the compatibility and dispersion of lignin within the aerogel matrix, impacting the thermal and mechanical performance [25]. In other study, Tang et al., prepared biomass-derived composite aerogels containing chitosan and other components. The authors reported difficulties with the compatibility and dispersion of lignin within the aerogel matrix, impacting the thermal and mechanical performance [26]. To

overcome these obstacles, advanced processing techniques or chemical modifications are required to enhance lignin's compatibility and functionality within composite systems.

To improve lignin's solubility and flame retardant affinity, the phosphorylation of lignin can be considered a strategy for upgrading lignin prior to its incorporation in chitosan derived aerogels [27]. Generally, phosphorylation preserves lignin's inherent thermal stability and mechanical strength [28]. Lignin provides structural integrity to plants through its compressive strength, rigidity, and thermal stability, with decomposition temperatures above 200°C. Its chemical composition, and reactivity enable diverse industrial applications, such as bio-based chemicals and composites. Additionally, lignin’s biodegradability enhances its appeal for sustainable material development [29, 30]. The phosphorylation of lignin presents significant advantages in fabricating lignin chitosan-based aerogels. It is hypothesized that introducing phosphate groups to lignin would increase its solubility in aqueous and polar solvents, ensuring a more uniform dispersion of lignin within the chitosan matrix and improving structural homogeneity of the aerogel [31]. Moreover, phosphorylated lignin would presumably enhance the aerogel's flame retardancy, thereby mitigating the risks of ignition and fire spread [32]. This modification would promote increased crosslinking density, contributing to a more stable and robust aerogel structure [33, 34]. This study aims to develop a new fully biobased and strong lignin incorporated aerogel with flame retardant and thermal insulation features. The physicochemical characteristics of the induced aerogel were characterized comprehensively using FTIR, NMR, XRD, and XPS. The structural and mechanical properties of the aerogel was assessed by BET, SEM and universal testing instrument. The thermal and flame retarding features of the aerogel were investigated by TGA, smoke density, limiting oxygen index (LOI) and UL-94 flammability analyzers. The results of this work confirmed that the new generated lignin incorporated aerogel can be a sustainable alternative for the construction industry where thermal insulation, flame retardancy, and mechanical strength are crucial for aerogel applications with biodegradable properties.

4.3. Material and method

4.3.1. Materials

Softwood kraft lignin (KL) was extracted via Lignoforce technology and obtained from FPInnovations, Hinton, Alberta. Phytic acid sodium salt hydrate ($C_6H_{18}O_{24}P_6$) (PHA), acetic acid (≥99.7%), chitosan, (CH), deacetylated chitin, poly (D-glucosamine) with different molecular weights (low molecular weight, MW, of50-190 kDa, medium MW of 100–1000 kDa [35], and high MW of 310-375 KDa), hydrochloric acid (HCl) (37%), and poly (diallyl dimethylammonium chloride) (PDADMAC) (100–200 kg/mol), disodium phosphate (Na_2HPO_4), monopotassium phosphate (KH_2PO_4), ammonium chloride (NH_4Cl), calcium chloride ($CaCl_2$), sodium chloride (NaCl), potassium hydroxide (KOH), starch $(C_6H_{10}O_5)_n$, and ethanol (C_2H_6O) were all purchased from Millipore Sigma, Oakville, Canada. The 1000 g/mol cut-off dialysis membrane made of cellulose acetate was purchased from Spectrum Labs.

4.3.2. Phosphorylation of KL

Phosphorylated KL (PK) was synthesized following the procedure described in the literature [28]. In brief, 2 g of KL was dissolved in 120 mL deionized (DI) water, its pH was adjusted to 12 and maintained for 24 hours before the reaction. This solution was then combined with varying concentrations of PHA as outlined in **Table S4.1**, and the reaction was carried out for 1 h at 25 ℃ in a 100 mL three-neck glass round bottom flask with continuous stirring at 300 rpm. After the reaction, the solution was cooled to room temperature, and the pH was adjusted to 7 using a 1 M hydrochloric acid solution. Unreacted reagents were removed using membrane dialysis with a molecular weight cut-off of 1000 g/mol, with water changing every 12 hours for two days. The purified samples were dried at 60 ℃ and collected for further evaluation and aerogel preparation. Three different charge densities (1, 3, and 5 mmol/g) were investigated, resulting in phosphorylated KL samples labeled as PK1, PK2, and PK3, respectively.

4.3.3. Aerogel preparation

Taguchi experimental design L9 (3^4) was conducted to understand the effect of different parameters, such as Mw of CH, charge density (1, 3, and 5 mmol/g), PK concentration (0.8, 2, 3.2 wt.%), and temperature (30, 60, and 90 ℃) on aerogel properties, and the results are reported in **Table S4.2**. The suspension of 5 wt.% CH was prepared with DI water and stirred for 30 minutes at room temperature. Subsequently, 50 mL of 2% v/v acetic acid was added to the suspension and stirred for 1 hour at 60 ℃ (in a water bath) with a mechanical stirring speed of 120 rpm. The solutions of PK1, PK2, and PK3 were prepared by dissolving them in DI water (at the concentrations of 0.8, 2, 3.2 wt.%). The CH suspension was mixed with these prepared solutions and stirred for 1 hour under the reaction conditions (**Table S4.2**). The resulting mixture was transferred to a mold and allowed to cool at room temperature for 1 hour to complete gelation and interaction to prepare hydrogel. This hydrogel was frozen at -20 ℃ for two days. The frozen hydrogels were freeze-dried under vacuum at -50 ℃ for 48 hours. The reaction conditions were optimized based on the response of the viscometer, tensile, thermal conductivity, and density measurements as reported in **Table S4.3**. The aerogel prepared with CH is denoted ACH, which generated a blank sample to compare with lignin-based aerogels.

4.3.4. Characterization

4.3.4.1. Viscosity analysis

The viscosity of hydrogels was determined at 25 °C using a Brookfield DV-II+ Pro viscometer. During these experiments, 6 mL of hydrogel was placed in a cylinder with the spindle NO. S64 of the viscometer, with the spindle rotation adjusted from 1 to 100 rpm, to measure the viscosity of the hydrogels. The viscosity of all hydrogels was reported at shear rate of 10 Pa.s to optimize reaction conditions. The viscosity measurement could provide information on crosslinking of hydrogels indirectly [36].

4.3.4.2. Mechanical analysis

The compression strength of the aerogels was measured using a universal testing machine equipped with a 50 kN load cell (Shimadzu-6800 series, Japan) at room temperature. Aerogel samples with 13 mm in height and 43 mm in diameter were placed on a circular platform. The tests were conducted at a 4 mm/min speed, reaching a maximum strain of 80% following ASTM D5750 method. Each set of measurements was performed three times, and the average results were reported.

4.3.4.3. Thermal analysis

Thermogravimetric analysis (TGA) was conducted to assess the thermal stability of the aerogels. Samples weighing 70 mg were examined in a nitrogen atmosphere using a thermal analyzer (TGA i1000, Instrument Specialists Inc.) at a gas pressure of 20–30 psi and 15 mL/min flow rate. The temperature was increased from 25 °C to 800 °C at a rate of 10 °C/min.

The thermal conductivity of the samples was measured using a FOX50 thermal conductivity analyzer (Model 110C, Serial Number 21073060, TA Instruments-Waters LLC) at room temperature. The instrument operated in single dX test mode and was calibrated using a standard VESPEL-sn3060 material to ensure accuracy. The samples, with dimensions of 13 mm in height and 43 mm in diameter, were carefully positioned on the heating surface. A non-conductive protective ring was employed to prevent any deformation or crushing of the samples during the test. The measurements were conducted over a temperature range of 15 to 35 °C to evaluate the thermal conductivity under controlled conditions.

Infrared imaging was conducted using a handheld thermal infrared camera (model TC004, TOPDON Technology Co., Ltd., China). Samples with a diameter of 45 ± 1 mm and a height of 20 ± 1 mm were positioned on a preheated hot plate set at 70 °C, and imaging was then carried out at different times.

4.3.4.4. Swelling measurement

The gravimetric approach was used to investigate the swelling behavior of aerogel in deionized water. Dry samples were weighed and then immersed in deionized water at 25 °C. Then, the samples were removed

and put on the filter paper to remove the residual water, and the sample was weighted again. Swelling rate (SR) was calculated according to Equation (4.1):

$$SR = M_t - M_0 / M_0 \times 100\% \quad (4.1)$$

where M_0 and M_t represent the initial weight and wet weight of the composite aerogel, respectively. This analysis was repeated with three replicas.

4.3.4.5. FTIR analysis

FTIR analysis was performed on a 50 mg powder sample pre-dried at 60 °C. The samples were analyzed with a resolution of 4 cm^{-1}, covering a spectral range from 4000 to 500 cm^{-1}, and using 32 scans in absorbance mode.

4.3.4.6. Solid-state NMR

Solid-state ^{13}C cross-polarization/magic angle spinning (CP/MAS) NMR spectra of the samples were recorded using an AVANCE NEO- 500MHz spectrometer from Bruker Corporation, USA, with resonance frequencies of 500.2 MHz for ^{1}H and 125.79 MHz for ^{13}C. The system had a 4 mm dual broadband CP/MAS probe. NMR data points and spectra were processed using Top Spin 4.0.9 software (2020 Bruker BioSpin GmbH). The freeze-dried samples were crushed and compressed into Bruker LabScape Consumables K1910, 106/99 µl, BL 4/3 before analysis.

4.3.4.7. XRD analysis

The crystal structure of the aerogels was analyzed using X-ray diffraction (XRD) with a Bruker D8 Advance instrument, utilizing Cu Kα radiation (λ = 0.154 nm). Peak intensities were recorded at 2θ angles ranging from 5° to 40°. The XRD instrument measured the samples' crystallinity with an acceleration voltage of 40 kV and a 2°/min scanning rate.

4.3.4.8. XPS analysis

The surface chemical composition was examined using X-ray Photoelectron Spectroscopy (XPS) with a monochromatic Al Kα X-ray source (1486.7 eV), operating at 15 kV (90 W) in FAT mode (fixed analyzer transmission). A 10 mg dried sample was tested at 60 °C. The energy pass was set to 40 eV and 80 eV for the Survey region. The C 1s binding energy was calibrated using a voltage of 284.6 eV. Full-spectrum, narrow high-energy resolution spectra, elemental composition, and functional groups were analyzed using ESCape software to fit graphs and assess elemental composition, functional group binding energies, and bond mass concentrations.

4.3.4.9. Morphological analysis

Nitrogen adsorption analysis was carried out to determine the specific surface area of the aerogel samples using the Brunauer-Emmett-Teller (BET) method with a NOVA 2200e (Quantachrome Instruments). This analysis was performed in the N_2 adsorption isotherm with nitrogen gas at a pressure range of $p/p_0 = 0.01–0.99$. Before measurement, the aerogel samples (0.124 g) were degassed under vacuum at 105 °C for 4 hours.

Scanning electron microscopy (SEM) was conducted to analyze the surface morphology of the aerogel. The data of this analysis was recorded by FE-SEM, Hitachi Su-70, with a voltage of 5 kV. Additionally, the samples' surface element mapping and elemental analysis were conducted using energy-dispersive spectroscopy (EDS) and energy-dispersive X-ray spectroscopy (EDX) at a voltage of 200 kV. The samples were coated with gold and carbon adhesive for this analysis.

The static contact angle of the samples was measured using an optical tensiometer (Theta Lite, Bolin Scientific, Finland) equipped with a digital camera and a manual tilting stage. For the test, the prepared hydrogels were applied onto glass slides using spin coating and subsequently dried at 60 °C for 3 hours. The sessile liquid droplet method, controlled by the One Attention software, was employed for this analysis on the hydrogels. Each measurement was repeated three times, and the average values along with their

standard deviations were reported. The measurements were performed in triplicate, and the average values along with standard deviations were reported. Wettability test was carried out using a force tensiometer (Attention Sigma 700/701, Biolin Scientific, Finland) equipped with a metal probe. The Washburn technique was employed to evaluate the wettability of the aerogels. For each test, approximately 0.1 g of aerogel was placed in the instrument's cylindrical metal tube, with an immersion depth set at 6 mm and a speed of 20 mm/min. The aerogel's wettability was determined by measuring the amount of liquid absorbed by the powder bed over time, as the holder was immersed in water for a duration of 1 hour.

4.3.4.10. Flame retardancy analysis

The static smoke release of aerogels was tested per the ASTM D2843 standard using a smoke detector instrument (Smoke Density Advanced Instruments Co., Ltd, AIC-2843). Aerogels were prepared in 40 mm × 40 mm × 1 mm and repeated three times. The specimens' limiting oxygen index (LOI) values were measured according to ASTM D2863 using an oxygen index apparatus (HC-2, Jiangning Analysis Instrument Company, China). The aerogels were prepared in a dimension of 140 mm × 20 mm × 10 mm, and five replicas were used for each. The vertical burning test (UL-94) was performed by the ASTM D3801. The dimensions of all samples were 140 mm × 10 mm × 1 mm. Aerogel flammability was qualitatively evaluated by exposure to direct flame from a butane torch. The burning behavior of aerogels was visually assessed. To ascertain the flammability of the material, observations from the torch burn test were analyzed in correlation with combustion tests.

4.3.4.11. Biodegradability

The biodegradability of aerogels was assessed through aerobic biodegradation following ISO 14851:2019. An AER-800 S&C Respirometer with bubble counting sensors tracked microbial oxygen consumption, while photo sensors monitored the oxidation of organic compounds into biomass, CO_2, and H_2O. Samples of ACH, AKL, APK, KL, CH, and starch (150 mg) were dissolved in a 500 mL nutrient solution at 24 °C. The medium contained Na_2HPO_4, KH_2PO_4, NH_4Cl, NaCl, and $CaCl_2$ [37, 38]. A 5 mL microbial inoculum

(Polyseed, NX) was added, and CO_2 emissions were captured using 30% KOH. Each sample was tested in triplicate, and biodegradability (R) was calculated using Equation (4.2):

$$R = \frac{Q_T - Q_b}{C_T \times ThOD_T} \times 100 \qquad (4.2)$$

Where Q_T (mg/L) represents the oxygen consumption of the test substance, Q_b is the oxygen consumption of the blank, C_T (mg/L) refers to the concentration of the test substance, and $ThOD_T$ is the theoretical oxygen demand (mg O_2 per mg of substance) [38].

4.4. Results and discussion

4.4.1. Optimization via Taguchi responses

To determine the optimal aerogel preparation conditions, the Taguchi L9 (3^4) orthogonal array was employed (**Table S4.2**). Four factors were analysed, such as charge density (mmol/g), PK solution concentration (g/25 mL), chitosan MW (low, medium, and high), and reaction temperature (℃). The prepared viscosity of hydrogels, and young's modulus, thermal conductivity, and density of aerogels were analysed, as responses (**Table S4.3**). The effect of each parameter on hydrogel and aerogel properties was discussed in detail and reported in Appendix 4A in **Figure S4.1–S4.4** (a–g). The **Figure 4.1**(a–c) shows that the hydrogels' viscosity increased with the change in their MW. In addition, all factors, such as charge density, PK solution concentration, and reaction temperature, could affect the viscoelasticity behavior of hydrogels [25]. Free OH, amine and phosphorous groups in CH and PK would result hydrogen and covalent bonding and thus increased resistance to flow in the fabricated hydrogel [39, 40].

The network of aerogels achieved through the incorporation of PK into CH under different mixture conditions improved the compressive strength, as demonstrated in **Figure 4.1**(d–f). At 100% strain level, (AIH), (AEM) and (AGH) samples exhibit superior compression resistance to the rest of the samples (abbreviations of these samples are available in Appendix 4A). The aerogel synthesized under different reaction conditions demonstrated low mechanical strength and Young's modulus (as detailed in **Table S4.3**).

This reduced performance is attributed to insufficient physicochemical interaction in the fabricated material, which limits its structural integrity and ability to withstand mechanical stress [41]. The digital photos of ABL, AEM, and AGH show more crosslinking (**Figure S4.5**).

Thermal insulation efficiency depends on thermal conductivity, influenced by solid, gas, and radiative conduction, which are linked to pore size in porous materials [42, 43, 1]. This study analyzed aerogel insulation through thermal conductivity (**Figure 4.1**(g)), highlighting how reaction conditions affect pore size and internal crosslinking, i.e., key factors in conductivity of the material. Detailed information regarding the effect of each factor on density is reported in **Figure 4.1**(h), and AGH has the lowest thermal conductivity among other samples. The crosslinking network of aerogels, which varies significantly with reaction condition alterations, affects pore size and consequently density. It was concluded that, while high MW of chitosan did not affect aerogel's density, charge density and concentration of PK, and reaction temperature played more significant roles in density and thermal conductivity of the aerogels.

Water absorption is essential characteristics of aerogels, and the result of this analysis was reported in **Figure 4.1**(i). These materials undergo volume expansion, while absorbing water due to their porous structure and their hydrophilic nature. As a result, the swelling rate can indirectly reflect the pore size of the aerogel network [44]. Thus, the variation in the water absorption capacity of the aerogel is attributed to the voids formed during the high vacuum freeze-drying and crosslinking network fabrication of aerogels [45]. The increased crosslinking density made the pore structure more compact, making water absorption more challenging and reducing the swelling rate [46]. It can be concluded that AIH aerogel had the lowest water swelling and a more compact structure, which was observed with the highest young's modulus. This sample was generated using high MW CH, highest concentration of PK (3.2 wt.%), and charge density (5 mmol/g) at 90 ℃ reaction temperature, which led to the highest crosslinking and smallest pore sizes, thereby hindering swelling [47, 48].

The design of experiments based on statistical techniques is regarded as an excellent approach for optimizing the reaction conditions to achieve the samples with the most desirable characteristics (**Table**

S4.3). Based on the responses, the reaction conditions of CH with medium MW, PK with 1 mmol/g charge density, 2 wt.% PK concentration, at 30 °C reaction temperature should generate the best sample. Therefore, experiment was conducted under these conditions to generate APK, and two control samples prepared under the same conditions using CH in the absence and presence of and KL, and labeled ACH and AKL, respectively.

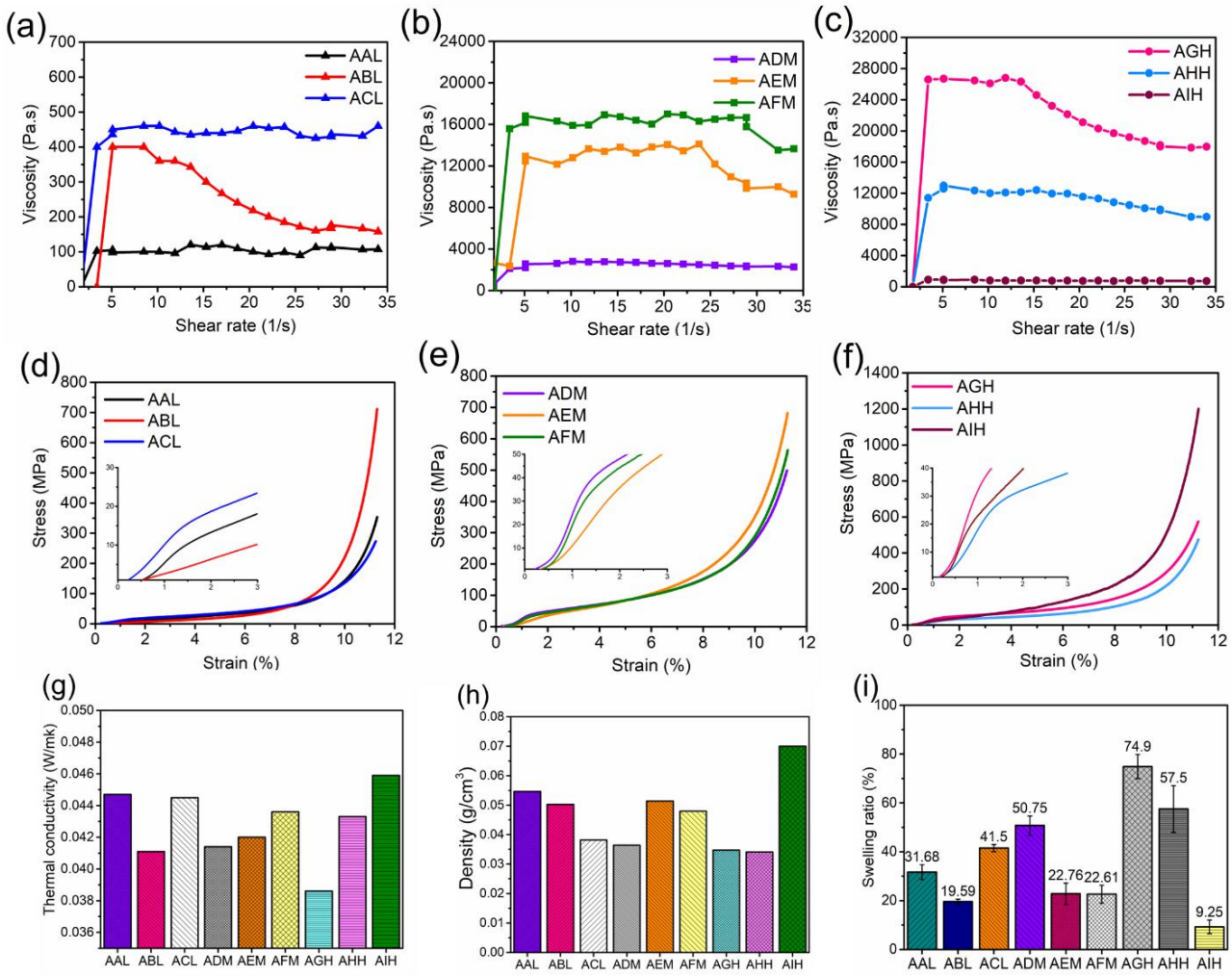

Figure 4.1. (a and d) the viscosity as a function of shear rate and compression for low MW of CH, (b and e) medium MW of CH, and (c and f) high MW of CH, (g) thermal conductivity, (h) density of aerogels, and (i) swelling behavior of aerogels generated under different reaction conditions (Table S4.2). The abbreviations of the samples are available in Appendix 4A

4.4.2. Characterization of aerogel

4.4.2.1. FTIR spectroscopy

The comparative FTIR spectra of ACH, AKL, and APK powders were shown in **Figure 4.2**(a). Overlapping stretching vibration peaks at 3500 cm^{-1}, 3200 cm^{-1}, and 2860 cm^{-1} corresponded to –OH, $–NH_2$, and $–CH_2$ groups in ACH, respectively. Peaks at 2930 cm^{-1} and 2870 cm^{-1} were attributed to asymmetrical and symmetrical C–H stretching vibrations from $–CH_2–$ or $–CH_3$ groups [49]. Additionally, characteristic peaks at 1663 cm^{-1} and 1596 cm^{-1} indicated C=ONHR (amide I) and N–H bending (amide II, NH_2) vibrations, respectively [50]. The peak at 661 cm^{-1} was associated with O–H out-of-plane bending vibrations [51].

When KL was incorporated into CH, the intensity of the peaks at 3500 cm^{-1}, 3200 cm^{-1}, and 2930 cm^{-1}, corresponding to phenolic and aliphatic –OH groups, decreased. Similarly, the peaks associated with C–H stretching in aromatic, methoxy, and alkyl groups in KL also diminished [52]. Moreover, the peak at 1596 cm^{-1} in AKL disappeared, suggesting the interaction between CH's secondary amine and KL's aromatic group likely due to hydrogen and ionic bond formation [18].

In APK aerogel, FTIR displayed the characteristic peaks of ACH and AKL powders, indicating that the aerogel contained KL derivative and CH. The introduction of PK significantly diminished the stretching vibration of $–CH_2$ at 2930 cm^{-1} in CH, and the characteristic peaks of –OH and –NH shifted to a lower frequency and became broader. This observation suggests that the stretching vibration of $–CH_2$ was influenced by the formation of hydrogen bonds between the hydroxyl group associated with the sub-methyl group of CH and the phosphate of PK [53, 54]. In addition, the FTIR spectrum of APK revealed a new characteristic absorption peak at 610 cm^{-1}, which could be attributed to the presence of $-PO_4^{3-}$ within the PK structure [55]. The newly observed peaks at 1250 cm^{-1} and 950 cm^{-1} indicate P = O stretching and P–O stretching from phosphate, respectively [56, 57]. The minor peak observed at 1422 cm^{-1} corresponded to the bending vibrations of C–P=O and C–N in –C–N–P. The reduced sharpness of peaks at 1596 cm^{-1} and 1663 cm^{-1} indicated the substantial substitution of amino groups with methyl phosphonic acid groups [58-60]. A new small C=O stretching vibration peak at 1770 cm^{-1} appeared, indicating the formation of ester

groups from the reaction between acetic acid and the hydroxyl groups at CH on the C_6 position [53]. Moreover, the disappearance of the N–H deformation peak of NH_2 at 1596 cm^{-1} and the new vibration peak at 1540 cm^{-1}, corresponding to the deformation of the secondary amine (N–H), would indicate the reaction involving the amino groups of CH and P–OH of PK [56, 1]. The newly observed peaks at 1440 cm^{-1}, 750 cm^{-1}, and 700 cm^{-1} were attributed to vibrations within the benzene structure and the out-of-plane bending vibrations of aromatic C–H, respectively [61]. In conclusion, the FTIR analysis confirmed chemical crosslinking and physical interaction between PK and CH in APK.

4.4.2.2. Solid-state NMR

Solid-state ^{1}H, and ^{13}C, NMR was conducted to analyze the chemical structure of aerogel, and the results were reported in **Figure 4.2**(b–d). The broad peak observed in ACH, attributed to hydrogen bonding, became narrower and less intense after adding KL, indicating the disruption of hydrogen bonds between CH segments by KL [62]. However, by adding PK, the ^{1}H NMR peak broadening at -40 ppm to 0 ppm was more pronounced than that in the other two aerogels, confirming more hydrogen bonding between PK and CH in APK.

In all ^{13}C NMR, the signals corresponding to the primary components of CH and KL are identified and labeled in **Figure 4.2**(c). Carbons are numbered from 1 to 9 and designated as C_1 to C_9 in the solid-state NMR [63]. Two peaks at 24 ppm and 174 ppm correspond to CH_3 (C_8) and C=O (C_7) of the acetylamino unit of CH [64]. The AKL spectrum was divided into three regions. The first region, 220 ppm to 160 ppm, pertains to carbonyl group carbons. The second region, between 160 and 100 ppm, pertains to the aromatic region. The third region, from 100 ppm to 20 ppm, pertains to aliphatic carbons [65]. Two peaks at the range of 148-158 ppm are associated with C_3 and C_5 of the S and G units of KL, respectively. Additionally, the peaks in the 60–110 ppm range are saturated carbon and ether groups appear of KL. The peaks at 188 ppm, 134 ppm, and 56 ppm are attributed to aliphatic carbonyl, C_1 and C_4 of the S unit of KL, and the methoxyl group (R–O–CH_3) of KL, respectively [66].

For APK, the peak associated with the C_2 carbon atom was divided into two distinct signals, and the peak corresponding to the C_6 carbon atom appeared as a shoulder on the C_2 peak (**Figure 4.2**(d)). This suggests that the electron density near the C_1 and C_3 carbon atoms increased due to the presence negatively charged $H_3PO_4^-$ and positively charged NH_3^+ group on the C_2 carbon atom. In addition, C_4 peak overlap due to the change in the magnetic field that high chemical crosslinking and physical interaction [67].

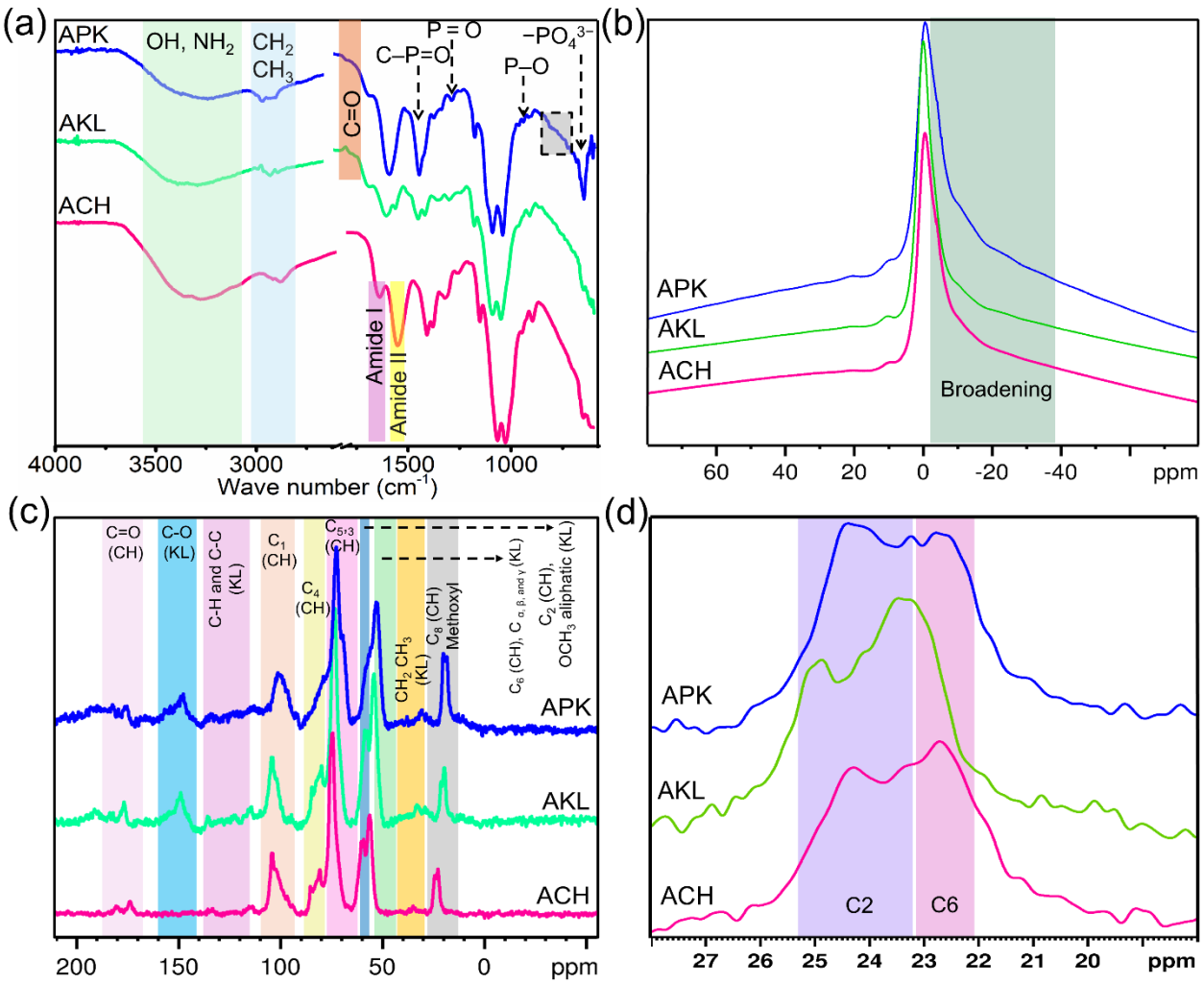

Figure 4.2. FTIR spectra (a), solid-state ^{1}H NMR (b), ^{13}C NMR (c), and maximized C_6 and C_2 (d) of ACH, AKL, and APK.

4.4.2.3. XPS analysis

Figure 4.3(a–e) display the wide spectra and elemental analysis (C1s, N1s, O1s, and P2p) of ACH, AKL, and APK, respectively. In the spectra of ACH and AKL, only C1s (285 eV), N1s (400 eV), and O1s (533 eV) signals were observed. Meanwhile, the spectrum of APK showed two additional peaks at 191 eV and 133 eV, which would correspond to the P2s and P2p. The high resolution of C1s spectra indicated the existence of multiple carbon species, which deconvoluted into three components that were labeled on spectra (**Figure 4.3**(b)).

From the C1s spectra of ACH, the characteristics peaks of C–C, C–N/C–O–C, and C=O are attributed at 284.94 eV, 286.39 eV, and 288.1 eV binding energy, respectively [69]. By adding KL to CH in AKL, the intensity of C–O–C bonds increased due to the polycondensation reaction between the hydroxyl groups of KL and CH. The C1s spectra of APK indicated the increment in the intensity of C=O, C–O–C, and C–O–P due to the esterification and condensation. The XPS spectra of N1s were represented in **Figure 4.3**(c) and fitted into two peaks at 398 eV and 400 eV, respectively, which were attributed to $–NH_2$ and N–C/N–P.

The O1s (**Figure 4.3**(d)) spectra of ACH were deconvoluted to two characteristic peaks of C–O and C=O at 529.5 eV and 531 eV. After adding KL to CH in AKL, due to the polycondensation of hydroxyl groups, the C–O intensity increased. However, the addition of PK changed the chemical structure and new bonds of P–O–P presented in APK (**Figure 4.3**(e)) due to the inter crosslinking of phosphorus functional groups of PK [28]. In addition, the peak at 531 eV intensity increased because of P–O and C–O–P bonds relating to PK.

4.4.2.4. XRD analysis

The crystalline characteristics of aerogels are compared and reported in **Figure 4.3**(f). It is evident that the pattern of ACH has two substantial peaks at $2\theta = 10°$ and 20°, which are attributed to the anhydrous crystal structure of CH. The small crystal structures within ACH chains were primarily due to interactions from intramolecular or intermolecular hydrogen bonds among highly electronegative N and O atoms. The

prominent peak in the AKL pattern at 2θ = 22° signified its amorphous bulky structure. This peak's intensity diminished after mixing with CH to form AKL. The addition of KL disrupted the ordered structure of CH molecular chains, leading to reduced crystallinity [25]. The XRD pattern following the incorporation of PK did not display a distinct diffraction peak, suggesting the absence of a well-defined crystalline structure. The diffraction pattern of APK closely resembled that of ACH and AKL; however, its peak intensities were comparatively lower. This reduction in intensity confirms that APK consists of both CH and KL components [68]. The characteristic peaks were significantly less intense for crosslinked materials compared to ACH and AKL, indicating a transformation from crystalline polymers to amorphous phases [62].

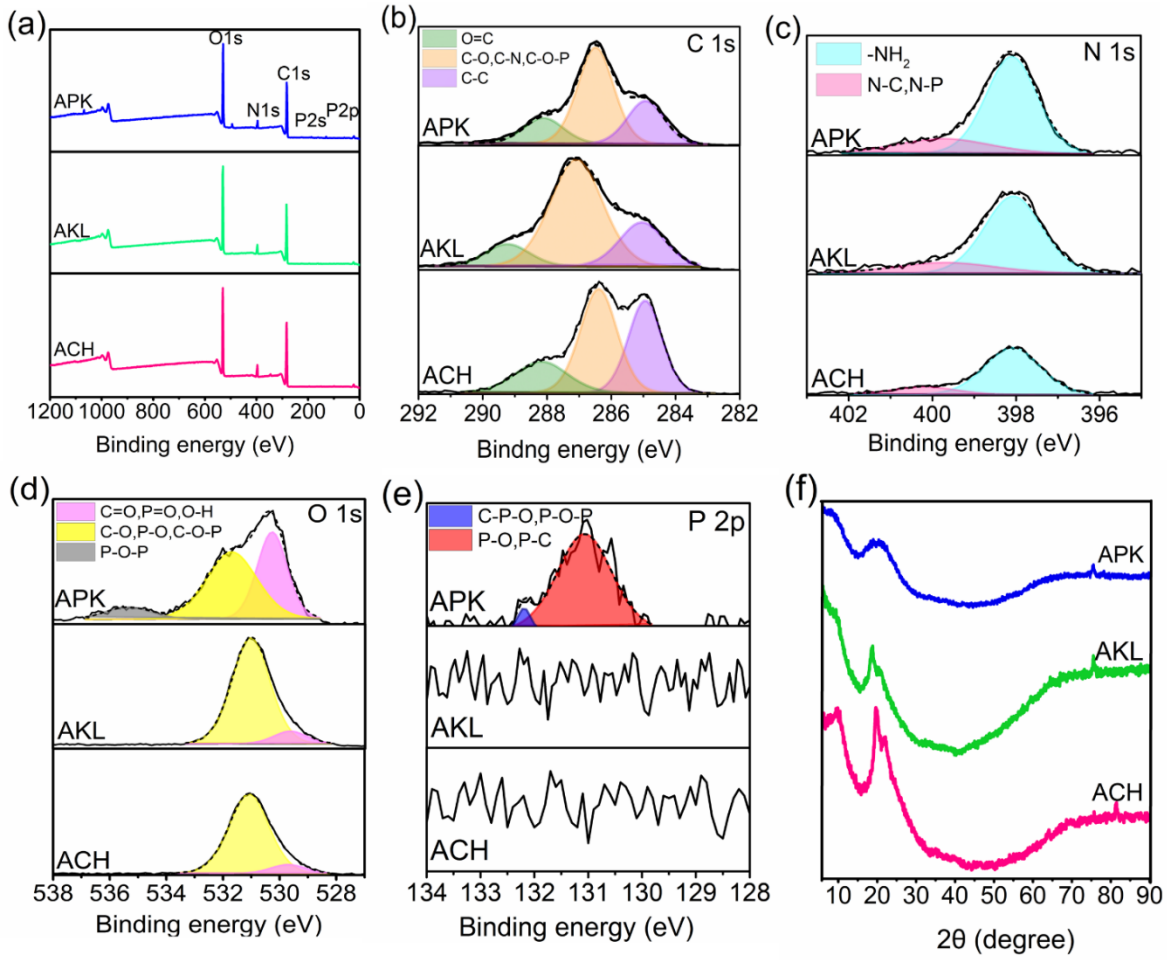

Figure 4.3. (a) XPS wide spectra, (b–e) elemental analysis, and (f) XRD analysis of ACH, AKL, and APK aerogels.

Figure 4.4 shows the proposed structure of APK, which was generated based on the FTIR, NMR and XPS analyses for APK. The chemical structure of APK involves (a) CH amine groups forming ionic bonds with free phosphate ions of PK, which was confirmed by disappearing of peak at 1596 cm^{-1} in AKL and suggested interactions between CH's secondary amine and KL's aromatic ring (**Figure 4.2**(a)) (blue color), (b) CH was esterified by PK's hydroxyl group at the C6 position, as confirmed by the FTIR C=O stretching vibration peak at 1770 cm−1 in **Figure 4.2**(a), while the XPS analysis of APK in **Figure 4.3**(b) showed increased intensities of C=O, C–O–C, and C–O–P (red color); (d) inter or intrachain hydrogen bonds between protonated amine groups of CH chains and phosphate groups of PK, which was confirmed by the ^{1}H NMR peak broadening at -40 ppm to 0 ppm (gray color); and (e) the formation of pyrophosphate through the condensation of phosphates (P–O–P) within chitosan chains (represented in yellow), which was confirmed by FTIR, with peaks observed at 1250 cm^{-1} and 950 cm^{-1} corresponding to P=O stretching and P–O stretching, respectively, as well as XPS analysis (**Figure 4.3**(e)) [69, 70].

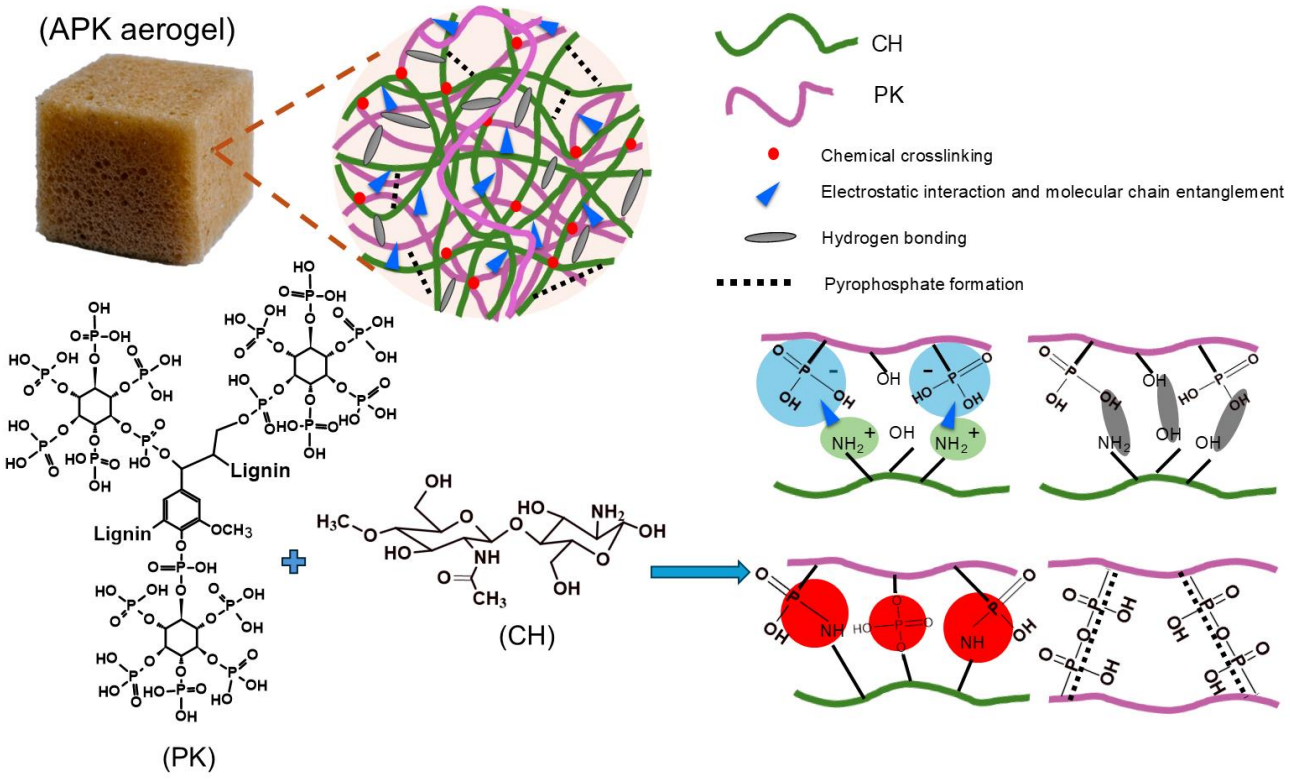

Figure 4.4. Schematic illustration of chemical and physical interactions in APK aerogel.

4.4.2.5. Structural and mechanical characteristics

The surface morphologies and structures of the aerogels were examined using SEM and EDX analyses, and the results were reported in **Figure 4.5**(a–f). The ACH aerogel featured a smooth, closely connected lamellar network structure (**Figure 4.5**(a)). Introducing KL disrupted the laminar sheet-like morphology of the ACH aerogels, creating small pores and wrinkles on the laminar sheets (**Figure 4.5**(b)). Adding PK to the CH aerogel enhanced its porosity (in APK), forming a cellular structure between the lamellar sheets with cell dimensions shape (**Figure 4.5**(c)). These features resulted in increased surface roughness and the development of a fibrous microstructure. Moreover, the EDX graphs (**Figure 4.5**(d–f)) indicated the phosphorus elements originating from PK in APK. In addition, the specific surface area and pore volume of the ACH were 205.3 m^2/g and 0.952 cm^3/g, and they decreased to 148.3 m^2/g and 0.951 cm^3/g via including KL (in AKL), likely due to partial agglomeration of the insoluble particles in KL (**Table 4.2**). The inclusion of PK slightly increased the surface area to 193.4 m^2/g and pore volume to 0.947 cm^3/g. After adding PK, the surface analysis revealed the distinct internal structure characteristics of the microspheres with organized pore structures due to crosslinking [71].

The water uptake of the samples can be affected by hydrophilicity and network structure of aerogels. ACH had about 4.5 g/g water absorption that platitude after 16 minutes (**Figure 4.5**(g)) and water contact angle of 82° (**Figure S4.6**). This behavior was due to hydrophilic groups, such as amine and hydroxyl and porous structures of ACH that captured water [72]. Introducing KL into the CH aerogels lowered water absorption (4 g/g) and higher water contact angle (102°) due to the increase in hydrophobicity as KL was a hydrophobic material. However, APK had the highest water absorption, i.e., 7 g/g and water contact angle of 79°, and was saturated after about 25 minutes, not only because of hydrophilic phosphorus groups but also due to the ordered and micro porous structure of APK. The digital photos of aerogels are indicated in **Figure 4.5**(h), and the low density of APK aerogel is shown **in Figure 4.5**(i).

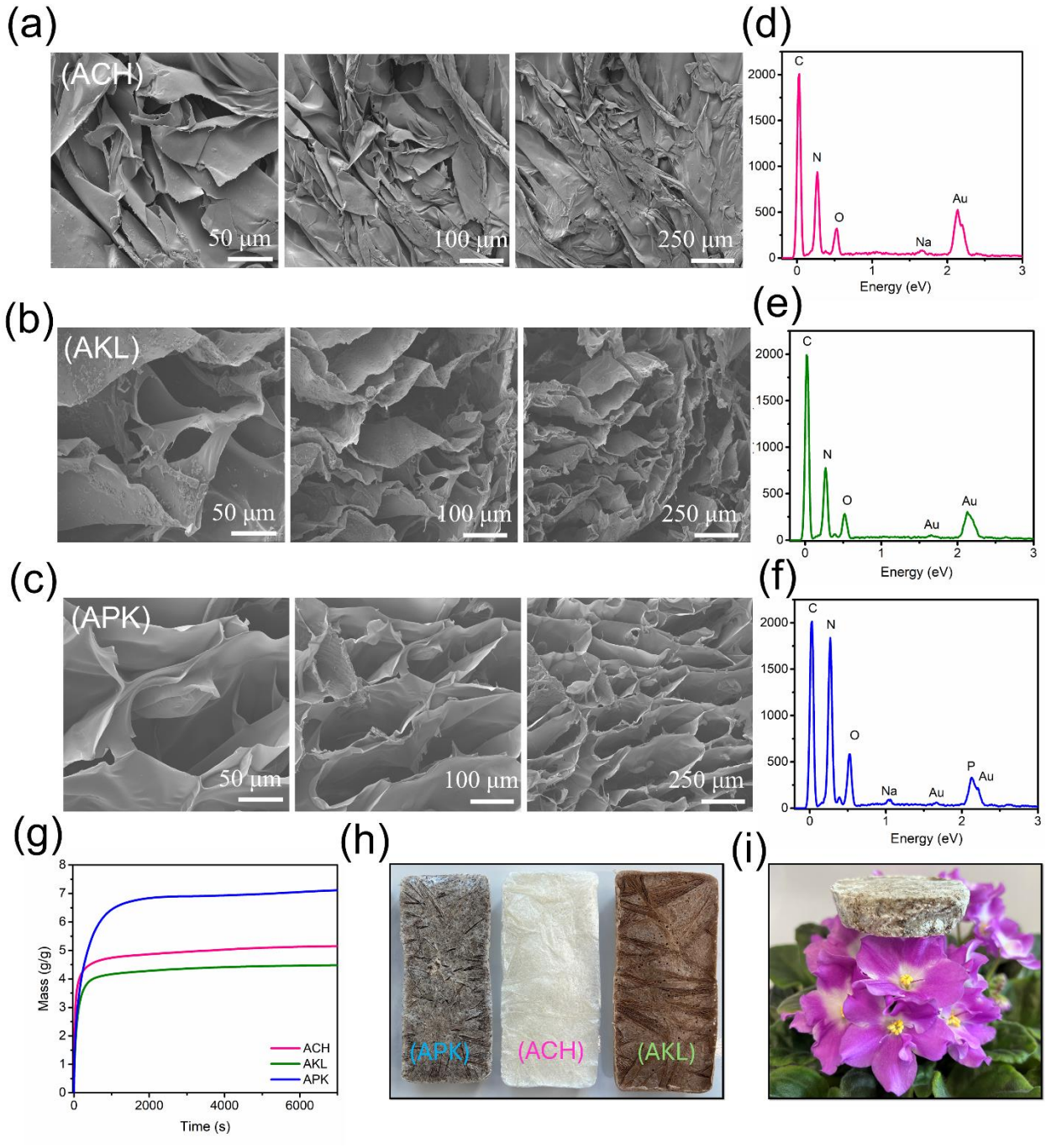

Figure 4.5. (a–c) the SEM images, (d–f) EDX, (g) water adsorption, (h) digital photos of ACH, AKL and APK, and (i) photograph highlighting the light weight APK aerogel.

Table 4.1. The surface characteristics of ACH, AKL, and APK.

Sample ID	Surface area (m^2/g)	Average pore radius (µm)	Total pore volume (cm^3/g)
ACH	205.3	0.00178	0.952
AKL	148.3	0.00173	0.951
APK	193.4	0.00178	0.947

The compression stress-strain graph and Young's modulus of the aerogels are shown in **Figure 4.6** (a and b), respectively. All aerogels could withstand a compressive strain of 80% without cracking or fracturing. The stress-strain curve of aerogels showed a typical compression behavior characterized by three phases: (1) a linear elastic stage at low strain, (2) a plateau phase beyond the yield point, and (3) a densification region occurring at compressive strains exceeding 80% [73]. The ACH showed less compressive stress of 0.37 MPa with the Young's modulus of 2.67 MPa, which increased to 0.64 MPa and 5.76 MPa in the presence of KL, respectively. Adding KL to CH changed the microstructure and increased the porosity due to the physical interaction confirmed by other analyses, such as FTIR, XPS, and SEM (**Figure 4.2–4.5**), which increased both compression stress and Young's modulus.

When PK was added to CH, the compression modulus increased to 0.83 KPa, and Young's modulus reached 6.21 MPa. Although improving porosity (**Figure 4.5**(c)) would reduce compressive strength, additional factors, such as pore size, crosslinking density, and wall corrugation within the composite, would contribute to hardening and reinforcement, leading to high compression performance [74, 75]. Additionally, **Figure 4.6**(c) presents the digital images of APK weighing 500 g and 1 kg, confirming the aerogel's high mechanical strength.

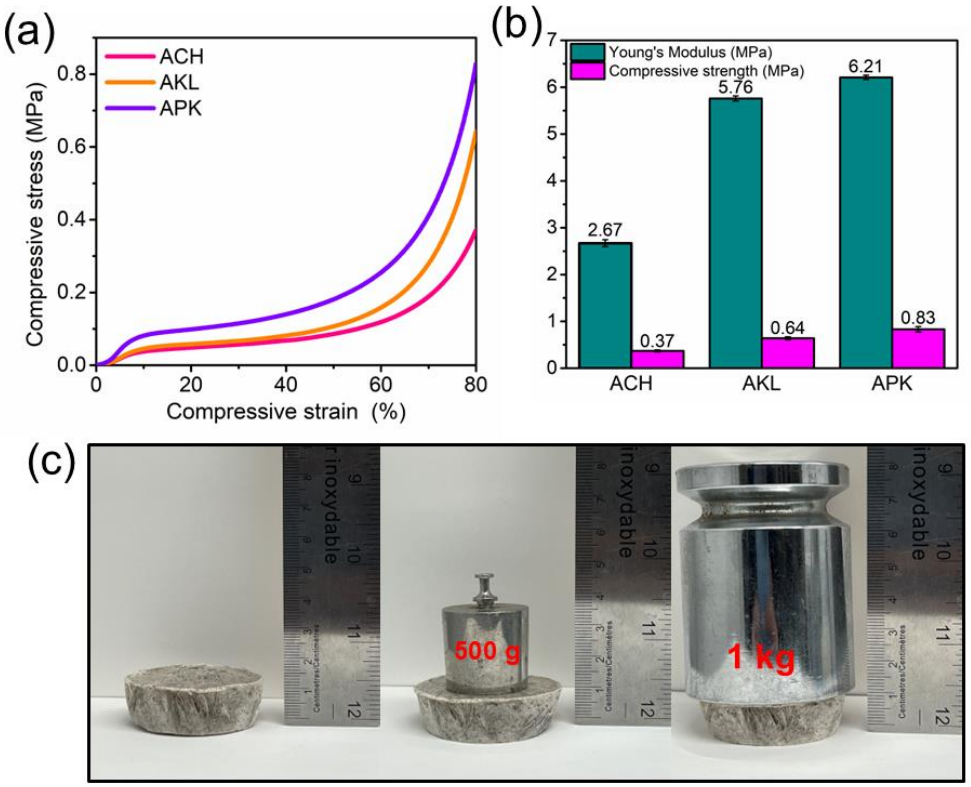

Figure 4.6. (a) stress−strain curves, (b) Young's modulus of ACH, AKL, and APK, (c) photograph highlighting the strength of APK.

4.4.2.6. Thermal analysis

The TGA curve of aerogels was studied to investigate the thermal stability changes in different stages, and the results were reported in **Figure 4.7**(a and b). The first 10% of mass loss occurred between 25 °C to 150 °C that is mostly related to evaporation of water [18]. The second stage, typically between 200 °C and 500 °C, is where most of the mass loss in all aerogels would occur. This significant weight reduction is due to the breakdown, or depolymerization, of the polymer network structure within the aerogels. As the temperature rose, the chemical bonds in the polymer chains degraded, causing the material to lose mass [76]. During this phase, the aerogels experienced a more significant weight reduction, corresponding to the complete breakdown of the network structure between CH, KL, and PK polymers. The last substantial weight loss took place from 500 °C, marking the full thermal decomposition of polysaccharides into inorganic components (ashes) [77].

In ACH, the T_d and T_{onset} are at 95 °C and 170 °C, respectively. However, adding KL increased T_d to 97 °C and decreased T_{onset} to 150 °C. In comparison with other aerogels, APK showed a high T_{onset} due to the increment in crosslinking. This suggests that more thermal energy was required to break the bonds and initiate segmental motion in the amorphous phase [78]. Moreover, the char mass of APK at 800 °C was about 18%, whereas it was negligible for ACH and AKL at this temperature. This is attributed to the condensation and crosslinking reactions of the amino functional groups within and PK macromolecules. The improved thermal stability is primarily attributed to the strengthened interaction and crosslinking between the PK with CH [79].

The addition of PK (**Figure 4.7**(b)) to CH caused the sharp and prominent decomposition peaks of ACH and AKL to be replaced by two smaller peaks. In addition, the T_{max} of ACH, which was 290 °C, decreased to 250 °C for APK, that is due to its improved porosity [80]. This significant reduction in peak height and area indicated that adding PK effectively facilitated the formation of a denser char layer, which prevented heat from penetrating the inner aerogel structure and slowed the diffusion of oxygen [81]. In addition, there was a peak in the APK graph at 750 °C that was related to the breakage of the P–P and P–N bonds, which needed more bonding energy for breakage and the pyrolysis of nitrogen and ammonia, illustrating that these bonds had an essential role in thermal resistance [82, 83].

Thermal conductivity is an essential component of insulating materials. This analysis was conducted for ACH, AKL, and APK and the results are reported in **Figure 4.7**(c). The thermal conductivity for ACH was 0.042 W/mK, which slightly decreased to 0.04 W/mK after adding KL and due to the change in the microporous structure that made the heat transfer path longer [84] After adding the PK, there was a considerable change in thermal conductivity, dropping to 0.032 W/mK. Evidently, the high chemical structure and a three-dimensional porous structure of APK could be responsible for blocking the heat transfer [85]. The APK aerogel demonstrated the lowest thermal conductivity of 0.032 W/mK. This value is comparable to, or lower than, those reported for polystyrene foam (0.03–0.06 W/mK), gelatin composite aerogels (0.034–0.037 W/mK), and cotton rock (0.033–0.064 W/mK) [96, 72].

The thermal insulation properties and heat transferring of the aerogels were evaluated by placing the samples on a 70 °C hot plate and visualizing heat transfer with a thermal infrared camera. Side-view thermal images, as reported in **Figure 4.7**(d), showed that heat penetrated the ACH and AKL aerogels faster than the APK aerogel, with the center temperature rising from approximately ~28 °C to ~37.9 °C and ~ 30.2 °C to ~41°C, respectively. However, the APK aerogel slowed the transformation of heat, which increased from 27 °C to 31.9 °C at prolonged time and a center temperature of about ~30.3 °C after 60 minutes. This indicated the superior thermal insulation properties of APK to other samples. Generally, aerogels' heat transfer characteristics are significantly influenced by their porosity, which traps air and minimizes conduction and convection. The size and distribution of pores would enhance insulation by reducing heat transfer pathways and disrupting solid conduction. Additionally, porosity would affect radiative heat transfer by scattering infrared radiation through excessive porosity [86].

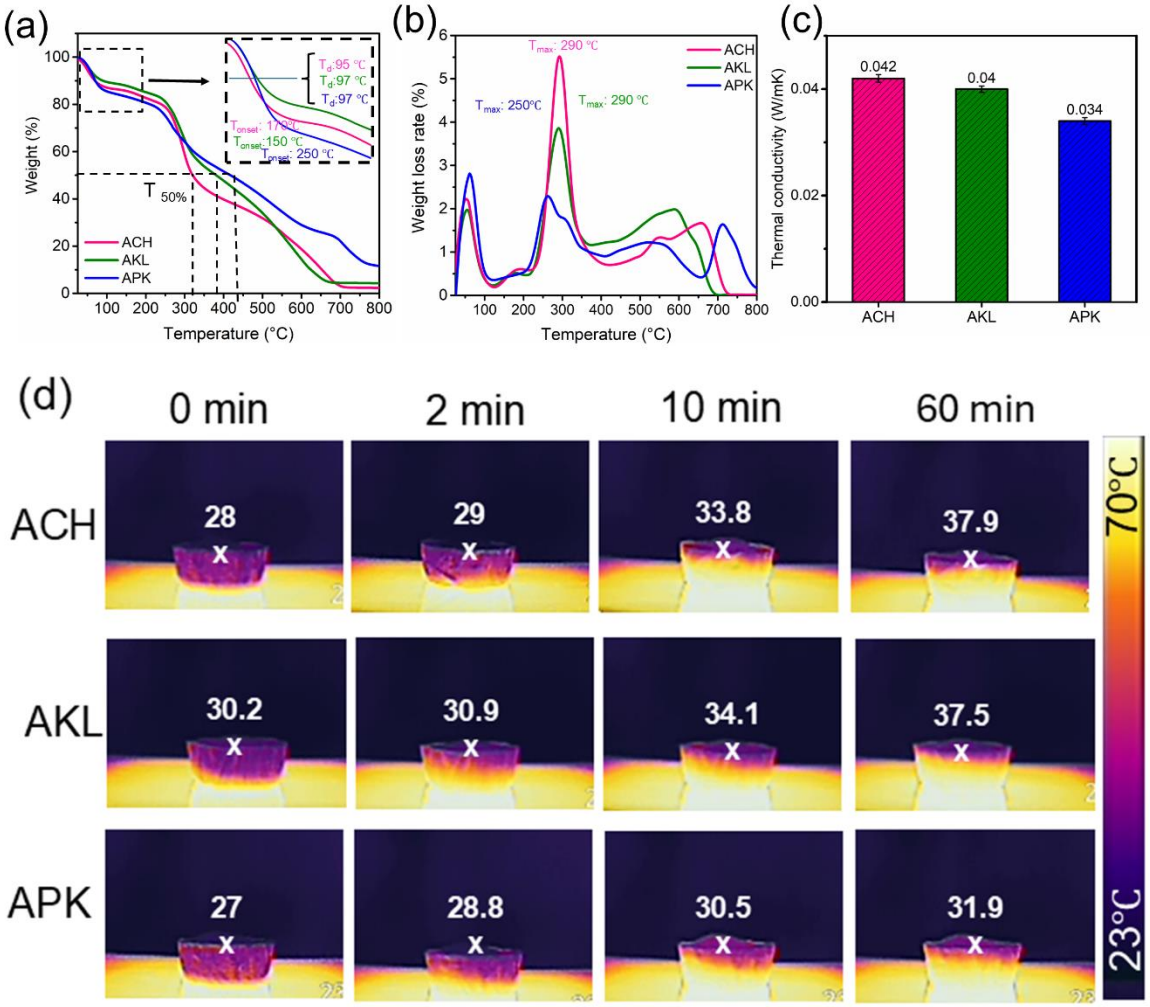

Figure 4.7. (a and b) the thermogravimetric analysis, (c) thermal conductivity analysis, and (d) infrared thermal images of ACH, AKL, and APK aerogels.

4.4.2.7. Flame retardancy analysis

The smoke density analysis, LOI, and UL-94 vertical combustion tests were conducted to assess the flame retardancy of aerogels. As shown in **Figure 4.8**(a), ACH had the highest peak of smoke production (25%) after 100 s, decreasing to 10% after 250 s. Adding KL and PK to CH reduced smoke production to 15% and 12%, and after 250 s, to 9% and 6%, respectively, suggesting that APK improved self-extinguishing properties [87]. The LOI values in **Figure 4.8**(b) show that materials with an LOI over 27% were difficult to ignite [88]. ACH had a value of 30%, which was attributed to its compact structure and nitrogen content [89]. Adding KL decreased the LOI to 28.5% due to increased porosity (**Table 4.2**), which can be related

to its higher porosity allowing more oxygen to penetrate the material for combustion [90]. The LOI of PK raised to 33%, likely due to nitrogen and phosphor compounds forming a protective char layer that enhanced flame retardancy [91, 92]. The results confirmed that the flame retardant properties of the aerogel are influenced not only by their porous structure but also by the chemical composition of their framework. While porosity can promote char formation and enhance thermal insulation [81], it may also increase gas permeability, which can elevate flammability [93].

Additionally, the images of the samples after the UL-94 test were displayed in **Figure 4.8**(c). The aerogels retain their shape well, with some char residue forming at the bottom. Furthermore, all aerogels pass the UL- 94 test with V-0 in the vertical burning test. Moreover, the real-time combustion of aerogels was investigated by the torch burn test and as reported in **Figure 4.8**(d). APK exhibited less flammability for than control samples. It is observed that these aerogels ignited quickly, with the flame spreading rapidly, and ignition lasted for 5 seconds after being removed from the fire and after 10 s just char remained. The addition of PK decreased the rate of flame propagation and reduced the burning length. Additionally, once the aerogel was removed from the fire, the flame extinguished immediately with no afterglow, demonstrating the material's self-extinguishing properties [94]. By reburning for 10 s and increasing the ignition, it lasted for 5s for both ACH and AKL and then the char remained. For APK, auto-extinguishable feature dominated by removing the ignition source with less char residue [87]. It was clear that aerogels showed a flame retardancy in the fire test, and APK had the highest rate.

To further clarify the impact of this flame retardant, the morphology and elemental composition of the residual char were examined using SEM, EDX, and EDS, respectively. As illustrated in **Figure 4.9**(a), the ACH structure shrank and was significantly damaged after burning, leading to the loss of its original structure. In addition, it exhibited intumescent bubbles, indicating the rapid generation of gas during the char's expansion due to the release of non-flammable gases [95]. In AKL aerogel (**Figure 4.9**(b)), the char formation and intensity of carbon element increased due to the aromatic structure of KL [96]. In addition, the few bubbles were observed, primarily due to the less combustion gas release.

As depicted in **Figure 4.9**(c), the continuous, dense, and compact char layers formed after the burning were well-preserved in aerogel, serving as an effective barrier against the transfer of heat and flame. This presence of phosphorus effectively prevented the internal skeleton's thermal degradation and blocked combustible gas transport [28]. Additionally, the thermal degradation of the internal skeleton released non-flammable gases, like ammonia, nitrogen, and carbon dioxide, which could dilute combustible gases and delayed flame ignition [97]. Moreover, the EDX graphs were reported in **Figure 4.9**(d–f) and indicated the increment in carbon intensity after adding the KL to CH, which proved more char formation. The APK showed that the high intensity of the phosphor graph worked as a flame retardant in this aerogel.

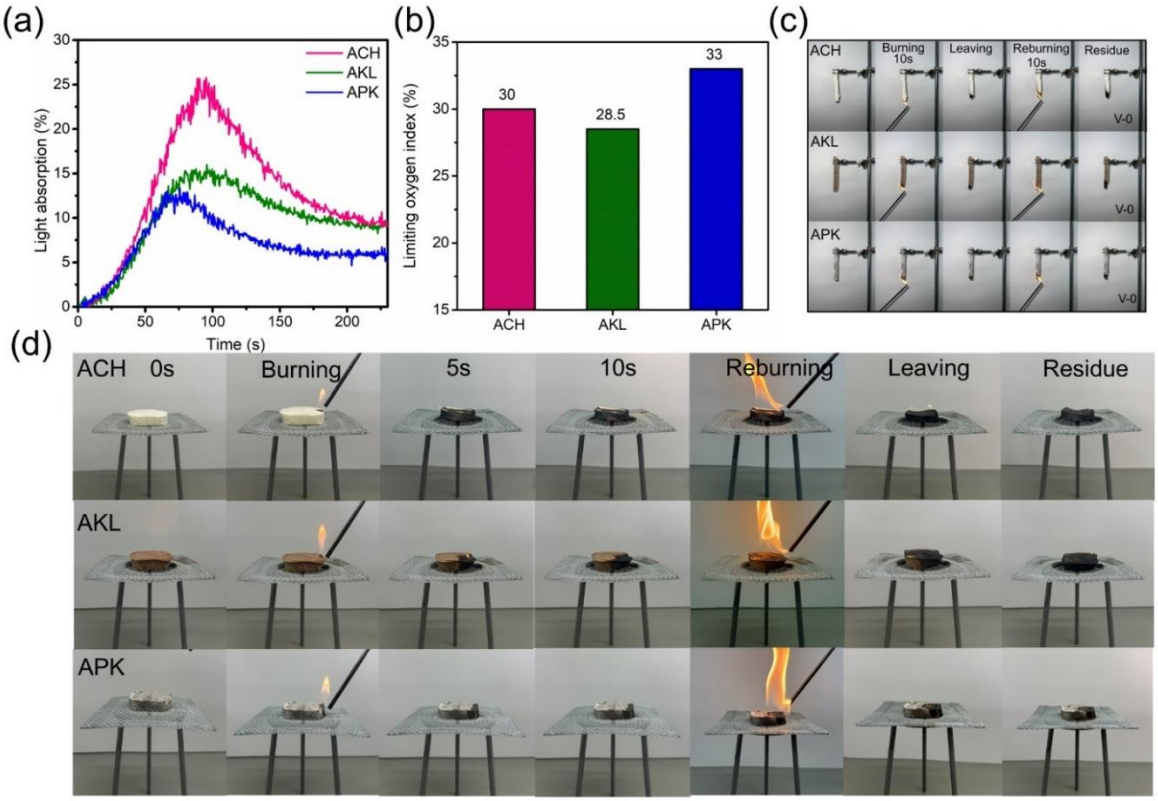

Figure 4.8. (a) smoke density analysis, (b) LOI, (c) UL-94 analysis, (d) torch burns test images of ACH, AKL, and APK aerogels.

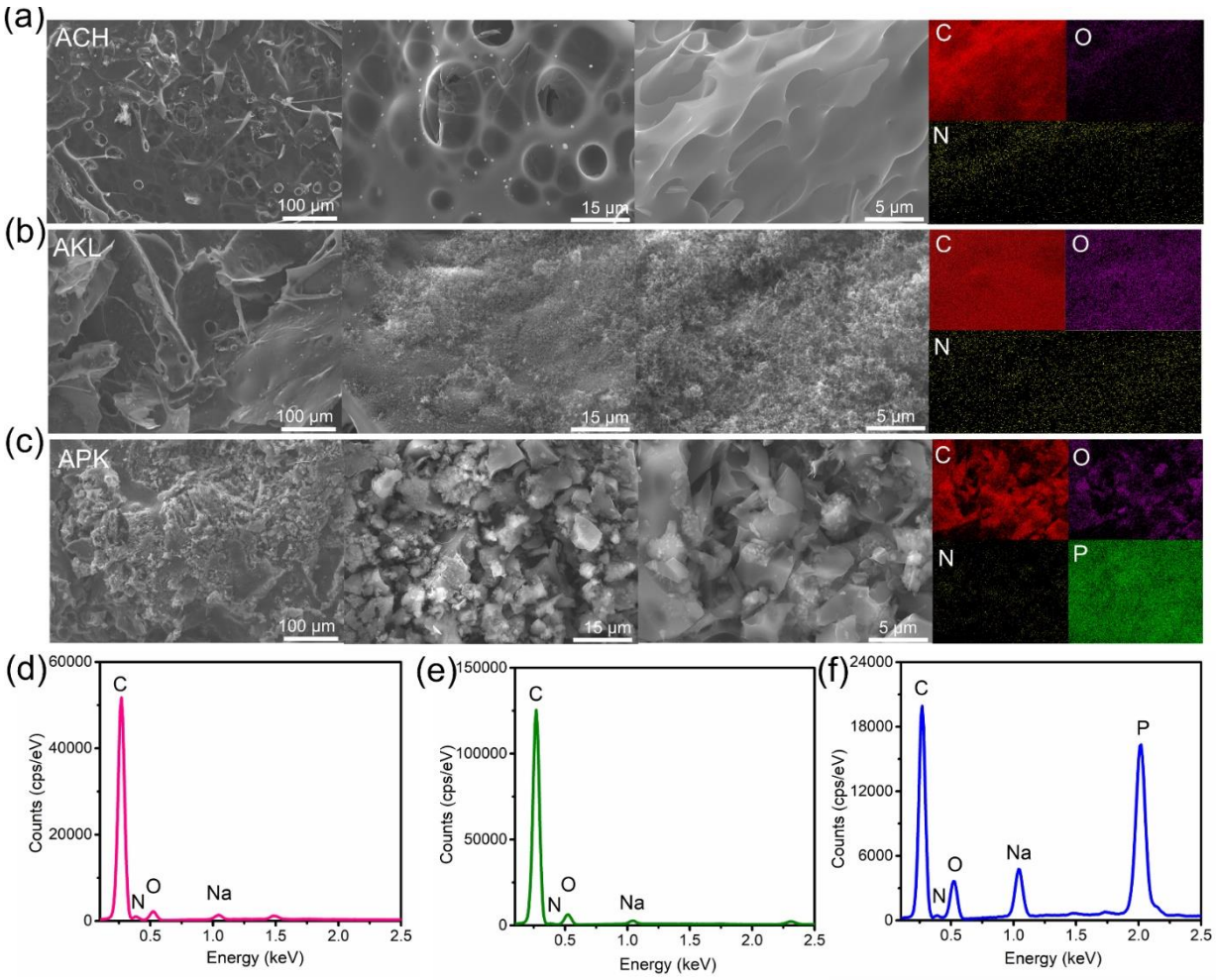

Figure 4.9. (a–b) the SEM and EDS mapping, (d–f) EDX of ACH, AKL, and APK.

4.4.3. Durability

A durability test was conducted under UV light exposure for a duration of four hours to assess its impact on the thermal, mechanical, and flame retardancy properties of the samples. The results of this test were reported in Figure 4.10(a-e). The comparison between ACH aerogel before and after UV treatment confirmed that there was a reduction in smoke density rate from 25% to 11%, in LOI from 30% to 29.5%, with a marginal alteration in the thermal conductivity from 0.042 W/mK to 0.039 W/mK. However, the mechanical properties of ACH changed after UV irradiation, and Young's modulus increased to 4.12 MPa from 2.67 MPa. This can be attributed to the degradation and cross-linking of chitosan under UV radiation,

altering its morphology and potentially impacting its mechanical properties [98]. In one study, the UV was proved to change the chemical structure of CH, such as the formation of carbonyl compounds [99].

In the past, lignin's UV-blocking properties, attributed to its aromatic structure and phenolic groups, rendered lignin aerogels highly suitable for UV protection applications in coatings and packaging [100]. However, UV exposure could induce some degradation in AKL aerogels, which has been observed to reduce the smoke release from 15% to 7%, and the LOI from 28.5% to 26.5%. Despite undergoing some degradation, the mechanical properties of AKL aerogels remained largely unaffected by UV exposure, with a slight reduction from 5.76 MPa to 5.18 MPa. Notably, AKL aerogels exhibited lower UV-induced degradation compared to ACH aerogels. Conversely, the APK samples demonstrated significant changes under UV exposure, with a marked decrease in smoke density from 12% to 6%, LOI values from 33% to 28.5%, and mechanical properties from 6.21 MPa to 3.39 MPa. This degradation is attributed to the breakdown of phosphorus-containing components under UV radiation.

UV radiation degrades phosphorus-based flame retardants, reducing their effectiveness. However, this degradation leads to a decrease in smoke density, which contributes to improved flame retardancy in specific contexts. On the other hand, the reduction in LOI indicates diminished flame retardancy, likely caused by the generation of free radicals under UV exposure that accelerated material decomposition. UV radiation alters the chemical structure and decomposition pathways of the aerogels, which can either enhance or impair the flame retardant performance depending on the property being measured [101, 102]. In conclusion, while UV exposure did not significantly affect the thermal conductivity of these materials, it notably impacted their flame retardancy and mechanical properties, with APK aerogels being more adversely affected compared to other samples.

4.4.4. Biodegradability

The biodegradation behavior of ACH, AKL, APK, KL, PK, and CH was studied and reported in **Figure 4.10**(f), including starch as reference. The initial graphs for all samples displayed a lag phase, indicating

minimal observable microbial degradation in the given aqueous conditions. This phase is likely due to the microbes' acclimatization to the environmental conditions [37]. Starch was selected as a reference due to its strong biodegradation characteristics [103]. Starch showed the biodegradation about 50% after 14 days. CH, KL, and PK demonstrated comparable biodegradation trends; however, PK exhibited significantly higher biodegradability, approximately 20% greater than the others. However, KL after 14 days showed biodegradation about 20 % and CH about 10 %. The addition of KL to CH increased the biodegradation, but it was still lower than that of KL. KL's higher hydrophobicity likely extended the microbial action duration by one day due to its resistance to chain cleavage [104, 105].

The lag phase in APK can be attributed to the high chemical bond and crosslinking that extended the microbial action that was the resistance to chain cleavage. After one day, the biodegradation rate increased subsequently, and it reached to 56 %, which was the highest in comparison of other samples. This can be due to the higher hydrophilicity of APK aerogel that could dissolve in water easily and microorganism could reach them and cause more defects. Furthermore, the phosphorylation of chitosan altered its biological and chemical properties, enhancing its bactericidal and osteo inductive capabilities [106]. Several studies have shown that different phosphorus and nitrogen compounds played a crucial role in enhancing the biodegradation of hydrocarbons and have been successfully applied in the remediation of petroleum-contaminated environments, such as soil and water [107]. Phosphorus is essential for enhancing biodegradability by supporting microbial growth and activity in breaking down hydrocarbons, with optimal levels accelerating the degradation of organic compounds in soil and water [108].

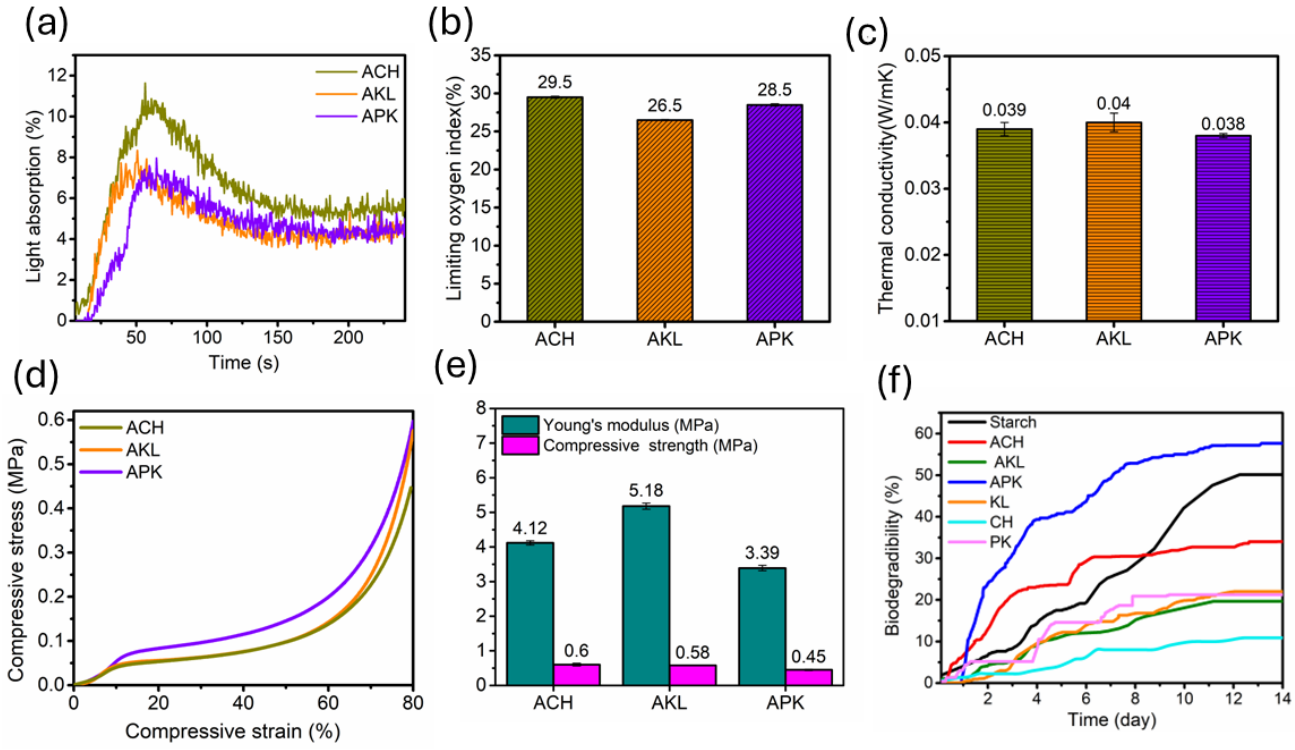

Figure 4.10. (a) smoke density analysis, (b) LOI, (c) thermal conductivity, (a and e) compression test of ACH, AKL, and APK after UV treatment, and (f) biodegradability analysis of starch, ACH, AKL, APK, KL, and CH.

4.5. Discussion

The reaction conditions were optimized based on the highest viscosity, Young's modulus, lowest thermal conductivity and density (**Table S4.3**) outcomes, and the samples generated under the conditions of medium MW CH, 1 mmol/g PK charge density, 2 wt.% PK concentration, at 30 °C reaction temperature. The physical interaction and chemical crosslinking in APK aerogel were confirmed via the FTIR (**Figure 4.2**(a)) analysis with the minor peak at 1422 cm^{-1} indicated the bending vibration of C–P=O and C–N in –C–N–P. Solid state NMR (**Figure 4.2**(b-d)) proved that C_2 carbon peak split into two signals, with the C_6 carbon peak appearing as a shoulder. This suggests increased electron density near the C_1 and C_3 carbons due to $H_3PO_4^-$ and NH_3^+ groups on the C_2 carbon and C_4 peak overlapped due to magnetic field changes. The appearance and increment in the intensity of P–O–P, –C–N–P, C–O–P which was confirmed by XPS proved the chemical interaction of PK with CH (**Figure 4.3**(a-e). XRD patterns (**Figure 4.3**(f)) confirmed that APK had both crystalline and amorphous structure as CH and KL. The SEM, EDX (**Figure 4.5**(a-f)), and

BET (**Table 4.2**) showed that APK with its high crosslinking affinity had pore structures, with characteristics elements such as P, and pore size 0.00178 μm. APK exhibited the highest water absorption, approximately 7 g/g, reaching saturation in about 25 minutes. This is attributed not only to the hydrophilic phosphorus regroups but also to its organized and microporous structure. Adding PK to CH increased crosslinking, enhanced their mechanical performance, and increased in the compression modulus to 0.3 KPa and the Young's modulus to 1.91 MPa (**Figure 4.6**(a-c). The T_{max} of ACH and AKL decreased from 290 °C to 250 °C for APK due to increased porosity (**Figure 4.7**(a and b). Additionally, thermal conductivity is a key parameter for thermal insulation materials, which reached to 0.032 W/mK via adding PK to CH. Adding PK to CH replaced the sharp decomposition peaks of ACH and AKL with two smaller peaks. (**Figure 4.7**(c and d). The LOI increased to 33% and smoke density release decreased (**Figure 4.8**(a and b)). In addition, durability test confirmed that, ACH and APK could degrade in the presence of UV, but AKL had more resistance in UV exposure (**Figure 4.10**(a-e). The biodegradability showed the highest amount of degradation was about 56% for APK, which was the best among other aerogels that was due to the presence of phosphorus elements of PK (**Figure 4.10**(f)). In conclusion, it was found that the addition of PK to CH aerogels increased the mechanical and thermal properties.

Chitosan and lignin aerogels hold considerable promise as sustainable materials; however, research dedicated to their use in thermal insulation applications remains scarce. As indicated in **Table S4.4**, these aerogels have been examined for various other purposes, such as wastewater treatment and dye adsorption, yet studies specifically addressing their thermal insulation capabilities are limited. This underscores the necessity for further exploration of their thermal properties and performance to thoroughly evaluate their potential as environmentally friendly insulation solutions.

In this work, a fully bio-based material composed of chitosan and lignin was developed, exhibiting exceptional properties including high thermal conductivity, superior thermal insulation, flame retardancy, mechanical strength, and biodegradability. As shown in **Table 4.3**, a comparative analysis with other bio-based composite materials demonstrated that APK not only exceled in thermal and flame retardant

capabilities but also offered significantly improvement in mechanical properties and biodegradability. For better understanding, the APK was compared with the aerogel produced from chitosan, phosphoric acid, and methyl triethoxy silane [9]. APK aerogel demonstrated a lower thermal conductivity of 0.034 W/m·K, i.e., compared to a similar study, which reported a higher thermal conductivity of 0.04 W/m·K. Furthermore, the density of APK aerogel was approximately 0.034 g/cm³, whereas the density reported in the other study was significantly higher (0.0883 g/cm³). Notably, APK aerogel achieved a compressive strength of 1.91 MPa through strong chemical bonds without the inclusion of additional materials. In contrast, the incorporation of silane groups in the alternative study resulted in a slightly higher compressive strength of 1.96 MPa. Both aerogels achieved a UL-94, V-0 flammability rating; however, the limiting oxygen index (LOI) of APK aerogel was 33%, which was lower than the 35.5% reported in the other work, likely due to the presence of the inorganic silane element in the latter. This distinctive combination of sustainable and high-performance properties underscores the potential of APK aerogel for eco-friendly applications.

Table 4.2. Chitosan derived aerogels for thermal insulation application.

Aerogel materials	Fabrication and drying	Crosslinking type	Thermal conductivity (W/mK)	Density (g/cm^3)	Compressive strength and young modulus (MPa)	Peak of Heat Release Rate, Total Heat Release, smoke density	LOI (%), UL-94	Ref
Chitosan, methyl phosphonic acid, acetic acid	Ion exchange reaction, directional freeze-drying	Physical interaction	0.025		1.7 and 2.1	91.7% and 69.5%	-	[9]
Chitosan, methyl trimethoxy silane	Freeze drying	Unidirectional freeze casting	Radial 0.03, Axial 0.006		0.292 ± 0.14	-	-	[109]
Chitosan, phosphoric acid, methyl triethoxy silane	Freeze drying	Freeze-thawing process	0.04	0.088	0.80 and 1.96	13.7 ± 0.3kW/m^2 23.0 ± 3.2 m^2/m^2	35.5, 38.5 V-0	[53]
Nanocellulose fiber, chitosan, methyl trimethoxy silane	Lyophilized	Directional freeze-casting and chemical cross-linking	Radial 0.028, Axial 0.036	~0.084	0.0993	-	-	[110]
Chitosan, hollow glass microsphere, glutaraldehyde, methyl trimethoxy silane	Freeze drying	Chemical cross-linking	0.065- 0.046	0.06	0.05 and 0.800	-	-	[111]
Chitosan, poly (vinyl alcohol), ammonium polyphosphate	Freeze drying	Ionic interaction	0.122- 0.127	0.635	0.24 and 0.15	68.1 kW/m^2 17.5 MJ/m^2	V-1,V-0	[112]
Chitosan, phosphorylated lignin (phytic acid)	Freeze drying	Chemical and physical crosslinking	0.034	0.034	0.31 and 1.91	~6% (light absorption)	33,V-0	This work

4.6. Conclusion

This study suggests an environmentally friendly approach for preparing bioaerogel by utilizing chitosan, kraft lignin, and phytic acid, all extracted from bioresources. The addition of KL to CH increased the porosity and mechanical properties of induced AKL aerogel due to improved crosslinking density. The

Taguchi experimental design confirmed the effect of charge density and concentration of PK as the primary factors in generating the aerogel, and the best sample was produced under the conditions of medium MW of CH, 1 mmol/g charge density of PK, 2 wt.% PK concentration, at 30 ℃ reaction temperature. The existence of new bond of –C–N–P, P–O–P, and hydrogen bonding interaction was confirmed. KL addition to CH disrupted hydrogen bonds, shown by narrower, less intense peaks in AKL spectrum, while PK increased hydrogen bonding, indicated by broader peaks in ^{1}H NMR analysis. Via ^{13}C NMR analysis, AKL's distinct carbonyl, aromatic, and aliphatic structures were observed, while electron density and peak overlapped due to intensive crosslinking and interactions were observed for APK. Crystalline polymers of CH and amorphous phases of KL and APK in the aerogels was confirmed with crystallography. The incorporation of PK into CH enhanced the pore volume and surface area with an organized lamellar structure of the induced aerogels. The improved porosity, chemical bonds and phosphorous elements contributed to the thermal stability of aerogel (Tonset of 250 °C and Tmax of 250 °C) and reduced thermal conductivity (0.034 W/mK). The presence of phosphorus element improved the formation of a dense and stable char layer, which provided effective thermal shielding. As a result, APK exhibited excellent fire safety (V-0), with less smoke density (6%) and high LOI (33%). Well-defined 3D network structure significantly enhanced APK compressive strength of 0.83 KPa and elastic modulus with the amount of 6.21 MPa. Moreover, it had high biodegradability due to the presence of phosphorus and nitrogen that could degrade easily. The use of fully biobased resources, coupled with a green and industrially attractive fabrication method, enables the production of novel phosphorylated kraft lignin and chitosan in a one-step aqueous system. This approach presents a viable strategy for fabricating fully biobased flame retardant aerogels with exceptional properties. However, the performance of APK aerogels could adversely affect by UV exposure, which compromised their flame retardancy, thermal stability, and mechanical properties. To mitigate these effects, protective measures, such as coating or incorporating additional lignin to shield the material from UV radiation, are recommended. Furthermore, the high biodegradability of APK aerogels, while advantageous in many contexts, could pose a limitation when used as insulation material in construction. This challenge can be addressed by applying hydrophobic coatings on the aerogel surface,

such as silane, to enhance durability and resistance to environmental degradation while in use. Such layer can be separated, and the aerogel can be degraded easily after its lifetime as a thermal insulator.

4.7. Reference

[1] F. Zou, T. Budtova, Polysaccharide-based aerogels for thermal insulation and superinsulation: An overview, Carbohydr Polym. 266 (2021) 118130. https://doi.org/10.1016/j.carbpol.2021.118130.

[2] J. Li, P. Guo, C. Hu, S. Pang, J. Ma, R. Zhao, S. Tang, H.M. Cheng, Fabrication of large aerogel-like carbon/carbon composites with excellent load-bearing capacity and thermal-insulating performance at 1800 °c, ACS Nano. 16 (2022) 6565–6577. https://doi.org/10.1021/acsnano.2c00943.

[3] Y. Zhu, H. Li, C. Peng, J. Ma, S. Huang, R. Wang, B. Wu, Q. Xiong, D. Peng, S. Huang, J. Chen, Application of protein/polysaccharide aerogels in drug delivery system: A review, Int. J. Biol. Macromol. 247 (2023) 125727. https://doi.org/10.1016/j.ijbiomac.2023.125727.

[4] L. Lujan, M.L. Goñ, R.E. Martini, Cellulose−chitosan biodegradable materials for insulating applications, ACS Sustain. Chem. Eng. 36 (2022) 12000–12008. https://doi.org/10.1021/acssuschemeng.2c03538.

[5] B. Gautam, M.R. Huang, C.C. Lin, C.C. Chang, J.T. Chen, A viable approach for polymer upcycling of polystyrene (styrofoam) wastes to produce high value predetermined organic compounds, Polym. Degrad. Stab. 217 (2023) 110528. https://doi.org/10.1016/j.polymdegradstab.2023.110528.

[6] A. Mountassir, T. Tirri, P. Sund, C.E. Wilén, Sulfenamides as standalone flame retardants for polystyrene, Polym. Degrad. Stab. 188 (2021) 109588. https://doi.org/10.1016/j.polymdegradstab.2021.109588.

[7] Z. Ma, J. Zhang, L. Liu, H. Zheng, J. Dai, L.C. Tang, P. Song, A highly fire-retardant rigid polyurethane foam capable of fire-warning, Composites Communications. 29 (2022) 101046. https://doi.org/10.1016/j.coco.2021.101046.

[8] H. Shao, Q. Zhang, H. Liu, W. Guo, Y. Jiang, L. Chen, L. He, J. Qi, H. Xiao, Y. Chen, X. Huang, J. Xie, T.F. Shupe, Renewable natural resources reinforced polyurethane foam for use of lightweight thermal insulation, Mater. Res. Express. 7 (2020) 055302. https://doi.org/10.1088/2053-1591/ab8d87.

[9] C. Du, Y. Xu, C. Yan, W. Zhang, H. Hu, Y. Chen, M. Xu, C. Wang, B. Li, L. Liu, Facile construction strategy for intrinsically fire-safe and thermal-insulating bio-based chitosan aerogel, Sustain. Mater. Technol. 39 (2024) e00794. https://doi.org/10.1016/j.susmat.2023.e00794.

[10] A. Ali, A. Issa, A. Elshaer, A comprehensive review and recent trends in thermal insulation materials for energy conservation in buildings, Sustainability. 16 (2024) 8782. https://doi.org/10.3390/su16208782.

[11] F.F. Li, Comprehensive review of recent research advances on flame-retardant coatings for building materials: chemical ingredients, micromorphology, and processing techniques, Molecules. 28 (2023) 1842. https://doi.org/10.3390/molecules28041842.

[12] A. Pellis, G.M. Guebitz, G.S. Nyanhongo, Chitosan: Sources, Processing and Modification Techniques, Gels. 8 (2022) 393. https://doi.org/10.3390/gels8070393.

[13] S. Namli, O. Guven, F.N. Simsek, A. Gradišek, G. Sumnu, M.E. Yener, M. Oztop, Effects of deacetylation degree of chitosan on the structure of aerogels, Int. J. Biol. Macromol. 250 (2023) 126123. https://doi.org/10.1016/j.ijbiomac.2023.126123.

[14] M.A.S. Abourehab, S. Pramanik, M.A. Abdelgawad, B.M. Abualsoud, A. Kadi, M.J. Ansari, A. Deepak, Recent advances of chitosan formulations in biomedical applications, Int. J. Mol. Sci. 23 (2022) 10975. https://doi.org/10.3390/ijms231810975.

[15] Y. Kong, J. Xu, W. Guan, S. Sun, Y. Yang, G. Li, Tailoring the elasticity of nerve implants for regulating peripheral nerve regeneration, Smart. Mater. Med. 4 (2023) 266–285. https://doi.org/10.1016/j.smaim.2022.11.004.

[16] H. Zhuo, Y. Chen, H. Xie, X. Huang, V.P. Guro, K. Tadjiev, Y. Li, Nanoporous silica-chitosan aerogels for thermal Insulation and flame retardancy, ACS Appl. Nano Mater. 7 (2024) 4784–4795. https://doi.org/10.1021/acsanm.3c05287.

[17] M. Fazeli, S. Mukherjee, H. Baniasadi, R. Abidnejad, M. Mujtaba, J. Lipponen, J. Seppälä, O.J. Rojas, O.J. Rojas, Lignin beyond the status quo: recent and emerging composite applications, Green Chem. 26 (2024) 593–630. https://doi.org/10.1039/d3gc03154c.

[18] L. Chen, C.Y. Tang, N.Y. Ning, C.Y. Wang, Q. Fu, Q. Zhang, Preparation and properties of chitosan/lignin composite films, Chi. J. Polym. Sci. 27 (2009) 739–746. https://doi.org/10.1142/S0256767909004448.

[19] N.N. Solihat, A.F. Hidayat, M.N.A.M. Taib, M.H. Hussin, S.H. Lee, M.A.A. Ghani, S.S.A.O. Al Edrus, H. Vahabi, W. Fatriasari, Recent developments in flame-retardant lignin-based biocomposite: manufacturing, and characterization, J. Polym. Environ. 30 (2022) 4517–4537. https://doi.org/10.1007/s10924-022-02494-2.

[20] S. Garg, A. Avanthi, Tuning of chitosan with lignin-derived bioactive properties to develop a lignin-reinforced and sustainable food packaging biomaterial, Biomass Convers. Biorefin. (2024) 1–17. https://doi.org/10.1007/s13399-024-06037-8.

[21] S. Sen, S. Patil, D.S. Argyropoulos, Thermal properties of lignin in copolymers, blends, and composites: a review, Green Chemi. 17 (2015) 4862–4887. https://doi.org/10.1039/c5gc01066g.

[22] S. Rath, D. Pradhan, H. Du, S. Mohapatra, H. Thatoi, Transforming lignin into value-added products: Perspectives on lignin chemistry, lignin-based biocomposites, and pathways for augmenting ligninolytic enzyme production, Adv. Compos. Hybrid Mater. 7 (2024) 1–29. https://doi.org/10.1007/S42114-024-00836-3.

[23] K. Crouvisier-Urion, F. Regina Da Silva Farias, S. Arunatat, D. Griffin, M. Gerometta, J.R. Rocca-Smith, G. Weber, N. Sok, T. Karbowiak, Functionalization of chitosan with lignin to produce active materials by waste valorization, Green Chemi. 21 (2019) 4633–4641. https://doi.org/10.1039/c9gc01372e.

[24] G. Engelmann, J. Ganster, Lignin reinforcement in thermosets composites, Lignin Polym. Compos. (2016) 119–151. https://doi.org/10.1016/b978-0-323-35565-0.00007-2.

[25] V.T. Tran, T.M. Le, T.T.N. Trinh, C.L. Tran, Y.H.P. Duong, V.Q. Huynh, D.T. Le, P.K. Le, Development of facile and green fabrication of cellulose–chitosan composite aerogel and lignin/silica hybrid from agro-wastes, Fibers Polym. 24 (2023) 403–411. https://doi.org/10.1007/s12221-023-00097-9.

[26] L. Tang, S. Zhuang, B. Hong, Z. Cai, Y. Chen, B. Huang, Synthesis of light weight, high strength biomass-derived composite aerogels with low thermal conductivities, Cellulose. 26 (2019) 8699–8712. https://doi.org/10.1007/s10570-019-02704-6.

[27] S. Laurichesse, L. Avérous, Chemical modification of lignins: towards biobased polymers, Prog. Polym. Sci. 39 (2014) 1266–1290. https://doi.org/10.1016/j.progpolymsci.2013.11.004.

[28] S. Khodavandegar, P. Fatehi, Phytic acid derivatized lignin as a thermally stable and flame retardant material, Green Chemi. 26 (2024) 10070-10086. https://doi.org/10.1039/d4gc03169e.

[29] H. Hatakeyama, T. Hatakeyama, Lignin structure, properties, and applications, Adv. Poly. Sci. 232 (2010) 1–63. https://doi.org/10.1007/12-2009-12.

[30] T.A. Shah, L. Zhihe, L. Zhiyu, Z. Andong, T.A. Shah, L. Zhihe, L. Zhiyu, Z. Andong, Composition and Role of Lignin in Biochemicals, Lignin - Chemistry, Structure, and Application. IntechOpen, (2022). https://doi.org/10.5772/intechopen.106527.

[31] C. Gao, L. Zhou, S. Yao, C. Qin, P. Fatehi, Phosphorylated kraft lignin with improved thermal stability, Int. J. Biol. Macromol. 162 (2020) 1642–1652. https://doi.org/10.1016/j.ijbiomac.2020.08.088.

[32] M.N.A.M. Taib, P. Antov, V. Savov, W. Fatriasari, E.W. Madyaratri, R. Wirawan, L.M. Osvaldová, L.S. Hua, M.A.A. Ghani, S.S.A.O. Al Edrus, L.W. Chen, D. Trache, M.H. Hussin, Current progress of biopolymer-based flame retardant, Polym. Degrad. Stab. 205 (2022) 110153. https://doi.org/10.1016/j.polymdegradstab.2022.110153.

[33] L. Gong, H. Wu, X. Shan, Z. Li, Facile fabrication of phosphorylated alkali lignin microparticles for efficient adsorption of antibiotics and heavy metal ions in water, J. Environ. Chem. Eng. 9 (2021) 106574. https://doi.org/10.1016/j.jece.2021.106574.

[34] F. Niu, N. Wu, J. Yu, X. Ma, Gelation, flame retardancy, and physical properties of phosphorylated microcrystalline cellulose aerogels, Carbohydr. Polym. 242 (2020) 116422. https://doi.org/10.1016/j.carbpol.2020.116422.

[35] C. Gonçalves, N. Ferreira, L. Lourenço, Production of low molecular weight chitosan and chitooligosaccharides (COS): a review, polymers (Basel). 13 (2021) 2466. https://doi.org/10.3390/polym13152466.

[36] K. Lewandowska, M. Szulc, Rheological and film-forming properties of chitosan composites, Int. J. Mol. Sci. 23 (2022) 8763. https://doi.org/10.3390/ijms23158763.

[37] S. Muniyasamy, A. Patnaik, Biodegradable behavior of waste wool and their recycled polyester preforms in aqueous and soil conditions, J. Renew. Mater. 9 (2021) 1661–1671. https://doi.org/10.32604/jrm.2021.014904.

[38] D. Šašinková, L. Serbruyns, M. Julinová, A. FayyazBakhsh, B. De Wilde, M. Koutný, Evaluation of the biodegradation of polymeric materials in the freshwater environment: an attempt to prolong and accelerate the biodegradation experiment, Polym. Degrad. Stab. 203 (2022) 110085. https://doi.org/10.1016/j.polymdegradstab.2022.110085.

[39] S. Locarno, P. Arosio, F. Curtoni, M. Piazzoni, E. Pignoli, S. Gallo, Microscopic and macroscopic characterization of hydrogels based on poly(vinyl-alcohol)–glutaraldehyde mixtures for fricke gel dosimetry, Gels. 10 (2024) 172. https://doi.org/10.3390/gels10030172.

[40] A.I. Saenz-Mendoza, P.B. Zamudio-Flores, M.C. García-Anaya, C.R. Velasco, C.H. Acosta-Muñiz, J. de Jesús Ornelas-Paz, M. Hernández-González, A. Vargas-Torres, M.Á. Aguilar-González, R. Salgado-Delgado, Characterization of insect chitosan films from Tenebrio molitor and Brachystola magna and its comparison with commercial chitosan of different molecular weights, Int. J. Biol. Macromol. 160 (2020) 953–963. https://doi.org/10.1016/j.ijbiomac.2020.05.255.

[41] G. Churu, B. Zupančič, D. Mohite, C. Wisner, H. Luo, I. Emri, C. Sotiriou-Leventis, N. Leventis, H. Lu, Synthesis and mechanical characterization of mechanically strong, polyurea-crosslinked, ordered mesoporous silica aerogels, J. Sol-Gel. Sci. Technol. 75 (2015) 98–123. https://doi.org/10.1007/s10971-015-3681-9.

[42] Q. Cen, S. Chen, D. Yang, D. Zheng, X. Qiu, Full bio-based aerogel incorporating lignin for excellent flame retardancy, mechanical resistance, and thermal insulation, 11 (2023) 4473-4484. https://doi.org/10.1021/acssuschemeng.2c07652.

[43] V. Apostolopoulou-Kalkavoura, P. Munier, L. Bergström, Thermally insulating nanocellulose-based materials, Adv. Mater. 33 (2021) 2001839. https://doi.org/10.1002/adma.202001839.

[44] Z. Tan, L. Hu, D. Yang, D. Zheng, X. Qiu, Lignin: Excellent hydrogel swelling promoter used in cellulose aerogel for efficient oil/water separation, J. Colloid. Interface. Sci. 629 (2023) 422–433. https://doi.org/10.1016/j.jcis.2022.08.185.

[45] A.A. Alhwaige, H. Ishida, S. Qutubuddin, Chitosan/polybenzoxazine/clay mixed matrix composite aerogels: preparation, physical properties, and water absorbency, Appl. Clay. Sci. 184 (2020) 105403. https://doi.org/10.1016/j.clay.2019.105403.

[46] M. Zhang, N. Guo, Y. Sun, J. Shao, Q. Liu, X. Zhuang, C.B. Twebaze, Nanocellulose aerogels from banana pseudo-stem as a wound dressing, Ind. Crops. Prod. 194 (2023) 116383. https://doi.org/10.1016/j.indcrop.2023.116383.

[47] J. Yang, M. Li, Y. Wang, H. Wu, N. Ji, L. Dai, Y. Li, L. Xiong, R. Shi, Q. Sun, High-strength physically multi-cross-linked chitosan hydrogels and aerogels for removing heavy-metal ions, 67 (2019) 13648-13657. https://doi.org/10.1021/acs.jafc.9b05063.

[48] M. V. Reyes-Peces, A. Pérez-Moreno, D.M. De-Los-santos, M.D.M. Mesa-Díaz, G. Pinaglia-Tobaruela, J.I. Vilches-Pérez, R. Fernández-Montesinos, M. Salido, N. de la Rosa-Fox, M. Piñero, Chitosan-GPTMS-silica hybrid mesoporous aerogels for bone tissue engineering, Polymers. 12 (2020) 2723. https://doi.org/10.3390/polym12112723.

[49] T. Liu, S. Gou, Y. He, S. Fang, L. Zhou, G. Gou, L. Liu, N-methylene phosphonic chitosan aerogels for efficient capture of Cu2+ and Pb2+ from aqueous environment, Carbohydr. Polym. 269 (2021) 118355. https://doi.org/10.1016/j.carbpol.2021.118355.

[50] S. Li, Y. Li, Z. Fu, L. Lu, J. Cheng, Y. Fei, A 'top modification' strategy for enhancing the ability of a chitosan aerogel to efficiently capture heavy metal ions, J. Colloid. Interface. Sci. 594 (2021) 141–149. https://doi.org/10.1016/j.jcis.2021.03.029.

[51] Q. Wang, W. Zuo, Y. Tian, L. Kong, G. Cai, H. Zhang, L. Li, J. Zhang, An ultralight and flexible nano fibrillated cellulose/chitosan aerogel for efficient chromium removal: Adsorption-reduction process and mechanism, Chemosphere. 329 (2023) 138622. https://doi.org/10.1016/j.chemosphere.2023.138622.

[52] T. Bashir, J. Dutta, S. Masarat, G.Z. Kyzas, Formulation and characterization of lignin modified chitosan beads, Adsorption. 6 (2024) 1–9. https://doi.org/10.1007/s10450-024-00478-3.

[53] H. Cui, N. Wu, X. Ma, F. Niu, Superior intrinsic flame-retardant phosphorylated chitosan aerogel as fully sustainable thermal insulation bio-based material, Polym. Degrad. Stab. 207 (2023) 110213. https://doi.org/10.1016/j.polymdegradstab.2022.110213.

[54] J. Huang, B. Huang, T. Jin, Z. Liu, D. Huang, Y. Qian, Electrosorption of uranium (VI) from aqueous solution by phytic acid modified chitosan: An experimental and DFT study, Sep. Purif. Technol. 284 (2022) 120284. https://doi.org/10.1016/j.seppur.2021.120284.

[55] Q. Yin, J. Liu, Z. Zhong, Y. Zhang, F. Zhang, M. Wang, Synthesis of phytic acid-modified chitosan and the research of the corrosion inhibition and antibacterial properties, Int. J. Biol. Macromol. 253 (2023) 126905. https://doi.org/10.1016/j.ijbiomac.2023.126905.

[56] X. He, S. Li, R. Shen, Y. Ma, L. Zhang, X. Sheng, Y. Chen, D. Xie, J. Huang, A high-performance waterborne polymeric composite coating with long-term anti-corrosive property based on phosphorylation of chitosan-functionalized Ti3C2Tx MXene, Adv. Compos. Hybrid. Mater. 5 (2022) 1699–1711. https://doi.org/10.1007/s42114-021-00392-0.

[57] M.H. Gouda, N.A. Elessawy, A. Toghan, Novel crosslinked sulfonated PVA/PEO doped with phosphated titanium oxide nanotubes as effective green cation exchange membrane for direct borohydride fuel cells, Polymers (Basel). 13 (2021) 2050. https://doi.org/10.3390/polym13132050.

[58] P. Dadhich, B. Das, S. Dhara, Microwave assisted rapid synthesis of N-methylene phosphonic chitosan via Mannich-type reaction, Carbohydr. Polym. 133 (2015) 345–352. https://doi.org/10.1016/j.carbpol.2015.06.105.

[59] H. Yang, S. Zhang, J. Yan, Chitosan-Reinforced MFC/NFC aerogel and antibacterial property, Adv. Poly. Tech. 1 (2020) 7890215. https://doi.org/10.1155/2020/7890215.

[60] K. Wang, Q. Liu, Chemical structure analyses of phosphorylated chitosan, Carbohydr. Res. 386 (2014) 48–56. https://doi.org/10.1016/j.carres.2013.12.021.

[61] X. Ma, N. Wu, P. Liu, H. Cui, Fabrication of highly efficient phenylphosphorylated chitosan bio-based flame retardants for flammable PLA biomaterial, Carbohydr. Polym. 287 (2022) 119317. https://doi.org/10.1016/j.carbpol.2022.119317.

[62] M. Xia, R. Gao, G. Xu, Y. You, X. Li, J. Dou, F. Fan, Fabrication and investigation of novel monochloroacetic acid fortified, tripolyphosphate-crosslinked chitosan for highly efficient adsorption of uranyl ions from radioactive effluents, J. Hazard. Mater. 431 (2022) 128461. https://doi.org/10.1016/j.jhazmat.2022.128461.

[63] S. Takeshita, S. Zhao, W.J. Malfait, Transparent, aldehyde-free chitosan aerogel, Carbohydr. Polym. 251 (2021) 117089. https://doi.org/10.1016/j.carbpol.2020.117089.

[64] W.M. Facchinatto, D.M. dos Santos, A. Fiamingo, R. Bernardes-Filho, S.P. Campana-Filho, E.R. de Azevedo, L.A. Colnago, Evaluation of chitosan crystallinity: A high-resolution solid-state NMR spectroscopy approach, Carbohydr. Polym. 250 (2020) 116891. https://doi.org/10.1016/j.carbpol.2020.116891.

[65] J. Bortoluz, A. Cemin, L.R. Bonetto, F. Ferrarini, V.I. Esteves, M. Giovanela, Isolation, characterization and valorization of lignin from Pinus elliottii sawdust as a low-cost biosorbent for zinc removal, Cellulose. 26 (2019) 4895–4908. https://doi.org/10.1007/s10570-019-02399-9.

[66] J.-S. Mun, J. Alfred, P. Iii, S.-P. Mun, Ł. Klapiszewski, T. Jesionowski, Chemical characterization of kraft lignin prepared from mixed hardwoods, Molecules. 26 (2021) 4861. https://doi.org/10.3390/molecules26164861.

[67] J. Sun, R. Hu, X. Zhao, T. Liu, Z. Bai, A novel chitosan/cellulose phosphonate composite hydrogel for ultrafast and efficient removal of Pb(II) and Cu(II) from wastewater, Carbohydr. Polym. 336 (2024) 122104. https://doi.org/10.1016/j.carbpol.2024.122104.

[68] S. Fan, J. Chen, C. Fan, G. Chen, S. Liu, H. Zhou, R. Liu, Y. Zhang, H. Hu, Z. Huang, Y. Qin, J. Liang, Fabrication of a CO2-responsive chitosan aerogel as an effective adsorbent for the adsorption and desorption of heavy metal ions, J. Hazard. Mater. 416 (2021) 126225. https://doi.org/10.1016/j.jhazmat.2021.126225.

[69] I.F. Amaral, P.L. Granja, M.A. Barbosa, Chemical modification of chitosan by phosphorylation: an XPS, FT-IR and SEM study, J. Biomater. Sci. Polym. 16 (2005) 1575–1593. https://doi.org/10.1163/156856205774576736.

[70] V. Sydorchuk, O.I. Poddubnaya, M.M. Tsyba, O. Zakutevskyy, O. Khyzhun, S. Khalameida, A.M. Puziy, Photocatalytic degradation of dyes using phosphorus-containing activated carbons, Appl. Surf. Sci. 535 (2021) 147667. https://doi.org/10.1016/j.apsusc.2020.147667.

[71] P. Grzybek, Ł. Jakubski, G. Dudek, Neat Chitosan Porous Materials: A Review of Preparation, Structure Characterization and Application, Int. J. Mol. Sci. 23 (2022) 9932. https://doi.org/10.3390/ijms23179932.

[72] Y. Wang, Y. Wan, X. Meng, L. Jiang, H. Wei, X. Zhang, N. Ma, Bio-inspired MXene coated wood-like ordered chitosan aerogels for efficient solar steam generating devices Composites & nanocomposites, J. Mater. Sci. 57 (2022) 13962-13973. https://doi.org/10.1007/s10853-022-07494-0.

[73] A. Chaudary, · Mohammed, K. Patoary, M. Zhang, T. Chudhary, A. Farooq, L. Liu, A. Chaudary, · M K Patoary, · M Zhang, · A Farooq, · L Liu, Structurally integrated thermal management of isotropic and directionally ice-templated nanocellulose/chitosan aerogels PDMS Polydimethylsiloxane PTFE Polytetrafluoroethylene, Cellulose. 29 (2022) 8265–8282. https://doi.org/10.1007/s10570-022-04781-6.

[74] A. Tabernero, L. Baldino, A. Misol, S. Cardea, E.M.M. del Valle, Role of rheological properties on physical chitosan aerogels obtained by supercritical drying, Carbohydr. Polym. 233 (2020) 115850. https://doi.org/10.1016/j.carbpol.2020.115850.

[75] M. Biernat, A. Woźniak, M. Chraniuk, M. Panasiuk, P. Tymowicz-Grzyb, J. Pagacz, A. Antosik, L. Ciołek, B. Gromadzka, Z. Jaegermann, Effect of selected crosslinking and stabilization methods on the properties of porous chitosan composites dedicated for medical applications, Polymers (Basel). 15 (2023). https://doi.org/10.3390/polym15112507.

[76] H. Ma, B. Wang, J. Qi, Y. Pan, C. Chen, Fabrication of mechanically strong silica aerogels with the thermally induced phase separation (TIPS) method of poly(methyl methacrylate), Materials. 16 (2023) 3778. https://doi.org/10.3390/ma16103778.

[77] J. Pan, Y. Li, K. Chen, Y. Zhang, H. Zhang, Enhanced physical and antimicrobial properties of alginate/chitosan composite aerogels based on electrostatic interactions and noncovalent crosslinking, Carbohydr. Polym. 266 (2021) 118102. https://doi.org/10.1016/j.carbpol.2021.118102.

[78] S. Luo, J. Cao, A.G. McDonald, Cross-linking of technical lignin via esterification and thermally initiated free radical reaction, Ind. Crops. Prod. 121 (2018) 169–179. https://doi.org/10.1016/j.indcrop.2018.05.007.

[79] Y. Zhu, B.K. Qi, H.N. Lv, Y. Gao, S.H. Zha, R.Y. An, Q.S. Zhao, B. Zhao, Preparation of DES lignin-chitosan aerogel and its adsorption performance for dyes, catechin and epicatechin, Int. J. Biol. Macromol. 247 (2023) 125761. https://doi.org/10.1016/j.ijbiomac.2023.125761.

[80] M.A. Ahmed, S. Mearaj, V. Thithai, C.J. Weon, Production and characteristic features of lignin-PVA aerogels for oil spillage applications, Mater. Chem. Phys. 289 (2022) 126455. https://doi.org/10.1016/j.matchemphys.2022.126455.

[81] K. Wu, Z. Ye, J. Cheng, Y. Zeng, R. Wang, W. Sun, Y. Kuang, F. Jiang, S. Chen, X. Zhao, Excellent thermal insulation and flame retardancy property of konjac glucomannan/sodium alginate aerogel reinforced by phytic acid, Ind. Crops. Prod. 205 (2023) 117495. https://doi.org/10.1016/j.indcrop.2023.117495.

[82] L.-P. Dong, C. Deng, R.-M. Li, Z.-J. Cao, L. Lin, L. Chen, Y.-Z. Wang, Poly(piperazinyl phosphamide): a novel highly-efficient charring agent for an EVA/APP intumescent flame retardant system, 36 (2016) 30436-30444. https://doi.org/10.1039/c6ra00164e.

[83] B. Chen, H. Lu, H. Zhu, Z. Huang, X. Lai, H. Li, X. Zeng, Superhydrophobic and flame-retardant chitosan/ammonium polyphosphate/montmorillonite aerogel-based piezoresistive pressure sensor for human motion detection, Sens. Actuators. A Phys. 369 (2024) 115135. https://doi.org/10.1016/j.sna.2024.115135.

[84] Y.L. He, T. Xie, Advances of thermal conductivity models of nanoscale silica aerogel insulation material, Appl. Therm. Eng. 81 (2015) 28–50. https://doi.org/10.1016/j.applthermaleng.2015.02.013.

[85] J. Xu, X. Ao, J. De La Vega, F. Guo, Z. Xie, F. Liang, D.-Y. Wang, J. Wu, Poly(vinyl alcohol) Composite Aerogel toward Lightweight, Remarkable Flame Retardancy, and Thermal Insulation Properties by Incorporating Carbon Nanohorns and Phytic Acid, Cite This: ACS Appl. Polym. Mater 6 (2024) 8039. https://doi.org/10.1021/acsapm.4c00729.

[86] F. Lou, S. Dong, K. Zhu, X. Chen, Y. Ma, Thermal insulation performance of aerogel nano-Porous materials: characterization and test methods, Gels. 3 (2023) 220. https://doi.org/10.3390/gels9030220.

[87] H. He, Y. Wang, Z. Yu, J. Liu, Y. Zhao, Y. Ke, Ecofriendly flame-retardant composite aerogel derived from polysaccharide: Preparation, flammability, thermal kinetics, and mechanism, Carbohydr. Polym. 269 (2021) 118291. https://doi.org/10.1016/j.carbpol.2021.118291.

[88] X. Jiang, J. Zhang, F. You, C. Yao, H. Yang, R. Chen, P. Yu, Chitosan/clay aerogel: microstructural evolution, flame resistance and sound absorption, Appl. Clay. Sci. 228 (2022) 106624. https://doi.org/10.1016/j.clay.2022.106624.

[89] H. Vahabi, F. Gholami, Martin Tomas, Elnaz Movahedifar, Mohsen, K. Yazdi, Mohammad, R. Saeb, S. Aerogel, hydrogel and aerogel-based flame-retardant polymeric materials: A review, J. Vinyl. Addit. Technol. 30 (2024) 5–25. https://doi.org/10.1002/vnl.22041.

[90] T. Aizawa, Y. Wakui, Membranes correlation between the porosity and permeability of a polymer filter fabricated via CO 2-assisted polymer compression, Membrane 10. 12 (2020) 391. https://doi.org/10.3390/membranes10120391.

[91] F. Li, Y.C. Wang, M.Y. Lai, H.J. Zhang, J.P. Zhao, Recycling cenospheres to construct chitosan bonded-ammonium polyphosphate/dipentaerythritol hybrid geopolymer coatings for flame-retarding plywood, J. Mater. Res. Technol. 25 (2023) 3865–3883. https://doi.org/10.1016/j.jmrt.2023.06.177.

[92] H. Ding, Shuilai. Qiu, Xin. Wang, Lei. Song, Yuan. Hu, Highly flame retardant, low thermally conducting, and hydrophobic phytic acid-guanazole-cellulose nanofiber composite foams, Cellulose. 28 (2021) 9769-9783. https://doi.org/10.1007/s10570-021-04159-0.

[93] P. Fu, S. Hu, J. Xiang, L. Sun, S. Su, J. Wang, Evaluation of the porous structure development of chars from pyrolysis of rice straw: Effects of pyrolysis temperature and heating rate, J. Anal. Appl. Pyrolysis. 98 (2012) 177–183. https://doi.org/10.1016/j.jaap.2012.08.005.

[94] J.Y. Yang, Y. Xia, J. Zhao, L.F. Yi, Y.J. Song, H. Wu, S.Y. Guo, L.J. Zhao, J.R. Wu, Flame-retardant and self-healing biomass aerogels based on electrostatic assembly, Chin. J. Polym. Sci. 38 (2020) 1294–1304. https://doi.org/10.1007/s10118-020-2444-4.

[95] H. Wang, C. Hao, T. Shu, P. Li, T. Yu, L. Yu, N. Yan, Flame-retardant Janus ramie fabric with unidirectional liquid transportation, moisture-wicking, and oil/water separation properties, J. Chem. Eng. 474 (2023) 145518. https://doi.org/10.1016/j.cej.2023.145518.

[96]08 H. Yang, B. Yu, X. Xu, S. Bourbigot, H. Wang, P. Song, Lignin-derived bio-based flame retardants toward high-performance sustainable polymeric materials, Green Chemi. 22 (2020) 2129-2161. https://doi.org/10.1039/d0gc00449a.

[97] M.E. Li, Y.W. Yan, H.B. Zhao, R.K. Jian, Y.Z. Wang, A facile and efficient flame-retardant and smoke-suppressant resin coating for expanded polystyrene foams, Compos. B. Eng. 185 (2020) 107797. https://doi.org/10.1016/j.compositesb.2020.107797.

[98] A.M. Abdelghany, · D M Ayaad, · A M Aboelkheir, The effects of prolonged UV irradiation on the physicochemical characteristics of chitosan lamellar films modified with nanoparticulate silver vanadate nanorods, Polymer Bulletin. 77 (2020) 5489–5503. https://doi.org/10.1007/s00289-019-03029.

[99] S. Meynaud, G. Huet, D. Brulé, C. Gardrat, B. Poinssot, V. Coma, Impact of UV Irradiation on the Chitosan Bioactivity for Biopesticide Applications, Molecules. 28 (2023) 4954. https://doi.org/10.3390/molecules28134954.

[100] G. Ma, X. Wang, W. Cai, C. Ma, X. Wang, Y. Zhu, Y. Kan, W. Xing, Y. Hu, Preparation and study on nitrogen- and phosphorus- containing fire resistant coatings for wood by UV-cured methods, Front. Mater. 9 (2022) 851754. https://doi.org/10.3389/fmats.2022.851754.

[101] B. Scharte, Phosphorus-based flame retardancy mechanisms—old hat or a starting point for future development?, Materials. 3 (2010) 4710–4745. https://doi.org/10.3390/ma3104710.

[102] X. Wang, W. Xing, L. Song, B. Yu, Y. Shi, W. Yang, Y. Hu, Flame retardancy and thermal properties of novel UV-curing epoxy acrylate coatings modified by phosphorus-containing hyperbranched macromonomer, J. Polym. Res. 20 (2013) 1–11. https://doi.org/10.1007/s10965-013-0165-x.

[103] I.T. Junior, T.C. Dal Bosco, J. Bertozzi, R.N. Michels, S. Mali, Biodegradability assessment of starch/glycerol foam and poly(butylene adipate-co-terephthalate)/starch film by respirometric tests, Braz. J. Food Technol. 23 (2020) 2018248. https://doi.org/10.1590/1981-6723.24818.

[104] J. Yun, L. Wei, W. Li, D. Gong, H. Qin, X. Feng, G. Li, Z. Ling, P. Wang, B. Yin, Isolating high antimicrobial ability lignin from bamboo kraft lignin by organosolv fractionation, front. Bioeng. biotechnol. 9 (2021) 683796. https://doi.org/10.3389/fbioe.2021.683796.

[105] L. Yao, H. Yang, X. Meng, A.J. Ragauskas, Toward a Fundamental Understanding of the role of lignin in the biorefinery process, Front. Energy. Res. 9 (2022) 804086. https://doi.org/10.3389/fenrg.2021.804086.

[106] C.P. Jiménez-Gómez, J.A. Cecilia, M. Guidotti, R. Soengas, molecules chitosan: A natural biopolymer with a wide and varied range of applications, Molecules. 17 (2020) 3981. https://doi.org/10.3390/molecules25173981.

[107] B. Chen, J. Fang, L. Dong, S. Xia, J. Wang, Enhancement of biodegradability of lubricants by biodegradation accelerants, Lubrication Science. 20 (2008) 311–317. https://doi.org/10.1002/ls.68.

[108] R. Margesin, F. Schinner, Bioremediation (Natural Attenuation and biostimulation) of diesel-oil-contaminated soil in an alpine glacier skiing area, Appl. Environ. Microbiol. 67 (2001) 3127–3133. https://doi.org/10.1128/aem.67.7.3127-3133.2001.

[109] W. Xiao, P. Wang, X. Song, B. Liao, K. Yan, J.-J. Zhang, Facile fabrication of anisotropic chitosan aerogel with hydrophobicity and thermal superinsulation for advanced thermal management, ACS Sustain. Chem. Eng. 28 (2021) 9348-9357. https://doi.org/10.1021/acssuschemeng.1c02217.

[110] M. Zhang, S. Jiang, F. Han, M. Li, N. Wang, L. Liu, Anisotropic cellulose nanofiber/chitosan aerogel with thermal management and oil absorption properties, Carbohydr Polym. 264 (2021) 118033. https://doi.org/10.1016/j.carbpol.2021.118033.

[111] P. Wang, B. He, Z. An, W. Xiao, X. Song, K. Yan, J. Zhang, Hollow glass microspheres embedded in porous network of chitosan aerogel used for thermal insulation and flame retardant materials, Int. J. Biol. Macromol. 256 (2024) 128329. https://doi.org/10.1016/j.ijbiomac.2023.128329.

[112] M. Luo, J. Xu, S. Lv, X. Yuan, X. Liang, Enhanced thermal insulation and flame-retardant properties of polyvinyl alcohol-based aerogels composited with ammonium polyphosphate and chitosan, Int. J. Polym. Sci. 2021 (2021) 5555916. https://doi.org/10.1155/2021/5555916.

5. Carboxymethylated lignin incorporated chitosan aerogel as thermal insulator

Saba Khodavandegar, Rozita Zare, Pedram Fatehi *

Under review in Biomacromolecule journal

Chapter 1: Green Processes Research Center and Chemical Engineering Department, Lakehead University, 955 Oliver Road, Thunder Bay, ON P7B5E1, Canada

First Author, email: skhodava@lakeheadu.ca, address: 955 Oliver Road, Thunder Bay, ON, Canada, P7B 5E1

Corresponding author: email: pfatehi@lakehadu.ca, address: 955 Oliver Road, Thunder Bay, ON, Canada, P7B 5E1

The contribution of Saba Khodavandegar to this work was writing original draft, methodology, investigation, visualization, validation, experiment, and data analysis.

Graphical abstract

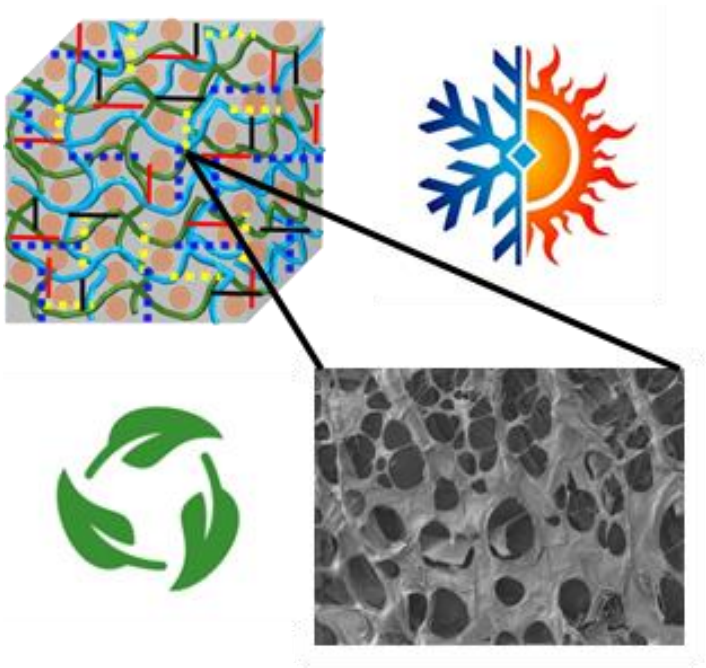

5.1. Abstract

Aerogels have been used in many applications, including thermal insulation. However, most of these aerogels were produced using petrochemical materials with adverse environmental footprints. Biodegradable materials, such as chitosan (CH) and lignin, can promote the green manufacturing of sustainable aerogels. In this work, aerogels were produced from carboxymethylated lignin (CM). The NMR and XPS confirmed the crosslinking of CM and CH via an increment in the intensity of the O=C–N bond in the network of lignin-chitosan composite. This work assessed a hypothesis that carboxymethylated lignin derivatives would improve the critical characteristics of aerogels required for insulation purposes. As the charge density of CM increased, the crosslinking bond of CM and CH was intensified, reducing the porosity and compression strength and imposing higher thermal conductivity. In addition, the increment in the charge density of CM increased the elasticity and hardness of the induced aerogels. The least charged CM (CM1) fabricated aerogel had the least thermal conductivity and highest compression strength. Moreover, the addition of CM increased the biodegradability of the aerogels. The results of this work provided a promising strategy to fabricate a sustainable and biodegradable aerogel using only green materials and following environmentally friendly aqueous-based systems.

Keywords: chitosan, lignin, aerogel, thermal insulation, sustainability.

5.2. Introduction

Heating energy waste from buildings is an important environmental challenge. The high demand for energy can be reduced by using appropriate thermal insulation materials. Generally, thermal insulants are porous substances [1]. Commercial insulation materials are made of polymeric foams and mineral wool with a low thermal conductivity of 0.020–0.040 W/m·K [2]. However, the lack of sufficient mechanical properties and high production costs are problematic for the use of such materials [3]. Aerogels can be another alternative with acceptable thermal insulating properties, a low density (approximately 0.1 g/cm^3), mesoporous

structure (pore sizes ranging from 2 to 50 nm), and high strength [4, 5]. In the past, aerogels were mostly made from inorganic polymers, such as clay, silica, carbon, and graphene [6]. However, their unacceptable biodegradability, sustainability, and long-term environmental footprints have challenged their uses [7].

Biopolymer-derived aerogels represent a more environmentally friendly substitute for inorganic-based aerogels with numerous precursor options, such as cellulose, alginate, chitin, chitosan, pectin, and starch, alongside protein and lignin [8]. Due to their sustainability, non-toxicity, and antioxidant functionalities, these materials have been proposed for various applications, such as food [9], construction [10], and biomedical [11].

Chitosan is a renewable and nontoxic biopolymer. However, pristine chitosan-based aerogels may not provide all the desired properties, such as high surface area, strength, and thermal conductivity for applications like thermal insulation. Modifying chitosan or combining it with other materials can enhance its functionality, e.g., mechanical and thermal properties [12, 13]. For example, the amino groups of chitosan were crosslinked with non-friendly and frequently toxic crosslinkers, such as formaldehyde, glutaraldehyde, glyoxal, and diisocyanates, to improve their properties. These chemicals could offset some of the advantages of chitosan in aerogel fabrications, and thus, their uses are not the most desirable option.

Lignin, after cellulose, is the second most abundant biomass resource in the world. It has an amorphous aromatic structure with hydroxyl, carbonyl, and methyl groups and potential physicochemical crosslinking capability [14]. Lignin with different modification pathways can be an appropriate option for aerogel fabrication, which can potentially improve the mechanical strength and thermal stability of chitosan aerogels. Since lignin is insoluble in water, it cannot be dispersed in water well for aerogel production with chitosan [15]. Therefore, modifying lignin with different functional groups may be an appropriate approach for manufacturing lignin-chitosan-based aerogels [16]. We previously demonstrated the generation of carboxymethylated lignin to be used as a dispersant for suspension systems [17]. Alternatively, the possible use of such a lignin derivative in aerogel fabrication may offer a better alternative than pristine lignin

because of the more intense reactivity of such lignin [18]. One objective of this work was to investigate the production of carboxymethylated lignin-chitosan aerogels.

The charge of electrophilic polymers has a great influence on their interaction with other polymers [19]. The charged groups, such as carboxylate groups, may create repulsion in polymeric networks in wet states, altering the porosity development of aerogels. On the other hand, charges may promote the crosslinking reaction with amine and hydroxyl groups of chitosan, condensing the structure of subsequent lignin-chitosan aerogels. As structural, mechanical, and thermal functionalities of aerogels will be affected by its polymeric network structures [20], understanding the impact of the charge density of carboxymethylated lignin on the properties of lignin-chitosan aerogels was the second objective of this study.

This work examined a hypothesis that the incorporation of carboxymethylated lignin will facilitate the production of chitosan-derived aerogels with improved thermal and insulation characteristics. In this study, aerogels from chitosan and carboxymethylated lignin with different charge densities (CM1, CM2, and CM3) were fabricated. In addition, the concentration of selected lignin derivative, i.e., ACM1, on aerogel properties was assessed. Notably, following the basic concept of green chemistry, no toxic reagents were introduced in this aerogel manufacturing. It was found that by increasing the charge density, the porosity, viscosity, and mechanical properties of generated aerogels decreased, reducing their thermal insulation performance. Moreover, concentrating the lignin derivative in the aerogels enhanced Young's modulus and decreased thermal conductivity, but it collapsed the porosity and, thus, the mechanical and thermal conductivity of aerogels. Furthermore, the biodegradation analysis confirmed the sustainability and biodegradability of the induced aerogels. Interestingly, the produced aerogel has the potential to be used for thermal insulation in the construction industry.

5.3. Methodology

5.3.1. Material

Softwood kraft lignin (KL) was obtained from FPInnovations and produced via Lignoforce technology. Sodium chloroacetate ($C_2H_2ClNaO_2$) (SC), chitosan (medium molecular weight) (CH), acetic acid (CH_3COOH), sodium hydroxide (NaOH) (≥97 %), hydrochloric acid (HCl) (≥37 %), deuterium oxide (D_2O-d_6) (99.9 %), dimethyl sulfoxide-d_6 (DMSO-d_6) (99.8 %), 3-(trimethylsilyl) propionic-2,2,3,3-d_4 acid sodium salt tetramethyl silane (TMSP) (≥98.5 %), cyclohexanol (99 %), 3-2-chloro-4,4,5,5-tetramethyl-1,3,2-dioxaphospholane (CDP) (95 %), pyridine (C_5H_5N), chloroform ($CHCl_3$), chromium (III) acetylacetonate (97 %), sodium azide (NaN_3) (≥99.5 %), poly (diallyl dimethylammonium chloride) (PDADMAC) (100–200 kg/mol), disodium phosphate (Na_2HPO_4), monopotassium phosphate (KH_2PO_4), ammonium chloride (NH_4Cl), calcium chloride ($CaCl_2$), sodium chloride (NaCl), potassium hydroxide (KOH), starch ($(C_6H_{10}O_5)_n$), and ethanol (C_2H_6O) were all purchased from Millipore Sigma, Oakville, Canada. The 1000 g/mol cut-off dialysis membrane made of cellulose acetate was purchased from Spectrum Labs. A microbial inoculum (Polyseed, NX) containing non-pathogenic Bacillus bacteria was purchased from Interlab Supply. A microbial inoculum (Polyseed, NX) for biodegradability test was purchased from Interlab Supply and contained non-pathogenic Bacillus bacteria.

5.3.2. Preparation of carboxymethylated lignin

The carboxymethylation of KL (CM) was carried out according to the literature [21]. Under various reaction conditions, 2 g of KL was dissolved in 120 mL of deionized (DI) water, and its pH was adjusted to 12 overnight before the reaction. The prepared solution was combined with different concentrations of SC under various reaction conditions, which was reported in **Table S5.1** in the Appendix 5A. The experiments were conducted in a 100 mL three-neck glass round bottom flask at 300 rpm. After reaction completion, the solution was cooled to room temperature, and its pH was adjusted to 7 with a 1 M hydrochloric acid solution. Unreacted reagents were isolated using membrane dialysis with a molecular weight cut-off of 1000 g/mol,

while water was changed every 12 hours for two days. The purified samples were dried at 60 °C and collected for further evaluation and aerogel preparation. Based on different conditions (**Table S5.1**), carboxymethylated lignin was produced with three different charge densities of 1, 1.5, and 2 mmol/g and labeled as CM1, CM2, and CM3, respectively.

5.3.3. Carboxymethylated lignin incorporated chitosan aerogel

Chitosan suspension (5 wt.%) was prepared and stirred for 30 minutes. Then, 50 mL of acetic acid (2 v/v %) was added to the suspension and stirred for 1 hour at 60 °C and 300 rpm in a water bath. A series of carboxymethylated lignin solutions were prepared by dissolving CM1, CM2, and CM3 (2 wt.%) in DI water. Then, the chitosan suspension was mixed with prepared lignin solutions and stirred for 1 hour under the same conditions. The prepared mixture was transferred to a mold and cooled down to room temperature for 1 hour to complete the gelation and prepare hydrogel. The prepared hydrogel was then frozen at -20 °C for two days. The schematic procedure was reported in **Figure S5.1** in Appendix 5A. The samples were freeze-dried under vacuum (-50 °C) for 48 h to prepare aerogels. The obtained aerogels were labeled as ACM1, ACM2, and ACM3, corresponding to the samples containing CM1, CM2, and CM3, respectively. The two control samples were prepared under the same conditions without adding KL and labeled ACH, and with KL, they were labeled as AKL. In addition, CM1 with two concentrations of 2 and 3.2 wt.% was prepared and mixed with CH solution (5 wt.%) and ACM1 following the same method stated above and labeled based on their dosage. Then, the mechanical and thermal properties of these aerogels were analyzed.

5.3.4. Characterization of carboxymethylated lignin

5.3.4.1. Charge density, solubility, molecular weight, and elemental analyses

The charge density, solubility, molecular weight, and elemental analyses were carried out for all powder samples, and the experimental details are available in Appendix 5A.

5.3.4.2. Quantitative ^{31}P NMR analysis

The ^{31}P NMR spectroscopy was used for the quantitative hydroxyl group analysis of KL and carboxymethylated samples (CM1, CM2, and CM3) [22]. After dissolving 70 mg of sample in 1 mL of pyridine/$CDCL_3$ (1.6:1) mixture, 200 µL of 2-chloro-4,4,5,5-tetramethyl-1,3,2-dioxaphospholane as the phosphorylation reagent and 70 µL of cyclohexanol as the internal standard were added to the mixture. The quantitative data of ^{31}P NMR was collected at a pulse angle of 90°, room temperature, 0.65 acquisition time, and 25 s pulse delay with spectral parameters of a decoupling pulse sequence. The spectra were obtained using a nuclear magnetic resonance spectroscopy (AVANCE NEO-1.2 GHz, Bruker Corporation, USA) with 1024 scans per sample at 25 °C, a 0.6 s acquisition time, a 90° pulse, and a 5 s relaxation delay time.

5.3.5. Characterization of aerogels

5.3.5.1.FTIR analysis

FTIR (Fourier Transform Infrared Spectroscopy) analysis was conducted for ACH, AKL, ACM1, ACM2, ACM3, KL, CH, and CM samples. The samples were first dried in an oven at 60 °C for 24 hours to evaporate any moisture. Aerogel samples were crushed after freeze-dried samples. The measurement was recorded using 0.5 g of samples in the mode range of 400 to 4000 cm^{-1} with a resolution of 4 cm^{-1}.

5.3.5.2.Solid state NMR

The freeze-dried samples were crushed and squeezed in the Bruker LabScape Consumables 106/99 µl, BL 4/3. Then, solid-state ^{13}C cross-polarization/magic angle spinning (CP/MAS) NMR spectra of samples were recorded on a Bruker AVANCE Neo NMR-500 MHz apparatus USA, with a resonance frequency of 500.2 MHz for ^{1}H and 125.79 MHz for ^{13}C analyses. The system was equipped with a 4 mm dual broadband CP/MAS probe. The Top Spin 4.0.9 software was used to process NMR data points and spectra (2020 Bruker BioSpin GmbH).

5.3.5.3. XPS analysis

X-ray photoelectron spectroscopy of dried samples (10 mg) was performed at 60 °C. A photoelectron spectrometer (XPS, Escalab 250XL+, Thermo Fisher Scientific, USA) with a monochromatic Al K X-ray source (1486.7 eV) operating at 15 kV (90 W) in FAT mode (fixed analyzer transmission) was used in this analysis. The ROI region's energy pass amount was 40 eV, whereas the Survey region's energy pass amount was 80 eV. The C 1s binding energy was calibrated using a voltage of 284.6 eV. Full-spectrum, narrow high-energy resolution spectra, elemental composition, and functional groups were evaluated using ESCape software for fitting graphs, elemental composition, functional group binding energy, and bond mass concentration of the samples.

5.3.5.4.XRD analysis

The crystal structure of the aerogels was characterized by X-ray diffraction (XRD) (Bruker, D8 Advance) employing a Cu Kα radiation source (λ = 0.154 nm). Peak intensity was recorded at 2θ ranging from 5° to 40°. An X-ray diffraction instrument was used to measure the crystallinity degree of the samples with an acceleration voltage of 40 kV at a scanning rate of 2°/min.

5.3.5.5.Structural analysis

Nitrogen adsorption analysis was conducted to determine the specific surface area (S_{BET}) of the aerogel samples following the Brunauer-Emmett-Teller (BET) method using a NOVA 2200e machine (Quantachrome Instruments) in the N_2 adsorption isotherm at the pressure range of p/p_0 = 0.01–0.99. Aerogel samples (0.124 g) were degassed in a vacuum at 105 °C for 4 h before performing the measurement.

The static contact angle of the samples was investigated by an optical tensiometer (Theta Lite, Bolin Scientific, Finland) with a digital camera and a manual tilting stage. In this test, the prepared hydrogels were coated on glass slides with spin coating and dried at 60 °C for 3 hours. The sessile liquid droplet from the One Attention program was utilized in this analysis. Three replications of the measurement were made, and the mean values with the standard deviation were reported. The wettability test was conducted using a

force tensiometer (Attention Sigma 700/701, Biolin Scientific, Finland) fitted with a metal probe. The wettability of aerogels was assessed using the Washburn technique. The cylinder-shaped metal tube of the instrument was filled with 0.1 g of aerogels in a series of tests with an immersion depth of 6 mm and speed of 20 mm/min. The aerogel's wettability was determined by quantifying liquid absorbed by the powder bed over time as the powder holder was submerged in the water for 1 hour.

The density of the samples was carried out using the methodologies stated in the Appendix 5A. Scanning electron microscopy (SEM) was used to analyze the surface morphology of the aerogel samples. The data for this analysis was recorded by FE-SEM, Hitachi Su-70, at a voltage of 5 kV.

5.3.5.6.Mechanical analysis

The compression strength of aerogels was characterized using universal testing equipment with a 50 kN load cell (Shimadzu-6800 series, Japan) at room temperature. Aerogels with a 13 mm height and 43 mm diameter were positioned on the circular geometry platform, which was conducted at 4 mm/min speed and a maximum strain of 80 % following ASTM D5750. Each set of aerogel measurements was performed three times, and the average results were then reported.

All aerogels were subjected to indentation analysis using an Anton Paar Bioindenter UNTH^3 instrument with Ruby Ball Indentor. A series of loading and unloading indent at a 3.0 mN/min rate was carried out for each loading mode at room temperature. The analysis' holding time and maximum loading time were 5 s and 0.5 mN, respectively. The comparatively large error bars were attributed to the impacts of surface roughness and heterogeneity of the aerogel surface, which was challenging to detect and regulate for ultralow-density nonporous materials. Indentation data, such as hardness and elasticity, were determined using the Oliver and Pharr models to extract the hardness and elasticity of aerogels [23].

5.3.5.7.Thermal analysis

Thermogravimetric analysis (TGA) was performed to investigate the thermal stability of aerogels. Samples (78 mg) were heated by a thermal analyzer (TGA i1000, Instrument Specialists Inc.) with a nitrogen gas

pressure of 20–30 psi and flow rate of 15 mL/min. The temperature of analysis was changed from 25 °C to 800 °C at the rate of 10 °C/min.

The thermal conductivity of the samples was assessed by a FOX50 (110C SN:21073060, TA instruments-Waters LLC) instrument at room temperature with the test mode of single dX and calibration of VESPEL-sn3060. Samples with 13 mm height and 43 mm diameter were located on the heating surface with a non-conductive protective ring to prevent samples from crushing, and the analysis was conducted in the temperature range of 15 and 35 °C.

5.3.5.8.Biodegradability

The biodegradability of aerogels was assessed under controlled aerobic biodegradation following ISO 14851:2019. An AER-800 S&C respirometer with bubble counting sensors was used to measure microbial oxygen consumption. A real-time system with photo sensors monitored the oxidation of aerogels, transforming organic compounds into microbial biomass, CO_2, and H_2O. Samples (0.15 g of AKL, ACM1, KL, ethanol, and starch) were ground and dissolved in a 500 mL nutrient solution at 24 °C. The nutrient medium contained Na_2HPO_4 (6 g/L), KH_2PO_4 (3 g/L), NH_4Cl (1 g/L), NaCl (0.5 g/L), and $CaCl_2$ (3 mg/L) [24]. A microbial inoculum, a non-pathogenic Bacillus bacterium, was used. For biodegradation, 5 mL of inoculum was added to 500 mL of sterilized mineral salt medium. A bottle with 30% KOH solution captured CO_2 emissions. Each sample was tested in triplicate. The biodegradability, R, was calculated following Equation(5.1):

$$R = \frac{Q_T - Q_b}{C_T \times ThOD_T} \times 100 \qquad (5.1)$$

Where Q_T (mg/L) is the oxygen consumption of the substance, Q_b is the oxygen consumption of the blank, C_T (mg/L) is the concentration of the test substance, and $ThOD_T$ is the theoretical oxygen demand (mg O_2/mg substance) [25].

5.4. Results and Discussion

5.4.1. Carboxymethylation performance

The effect of molar ratio (KL: SC), time, and temperature on the charge density and solubility of the lignin derivatives was discussed in the literature, and more details were reported in Appendix 5A in **Table S5.2** [26]. In addition, the chemical structure of KL and modified KL samples (CM1, CM2, and CM3) was confirmed using ^{31}P NMR spectroscopy and reported in **Figure S5.2** and **Table S5.3**.

Among the different chemical modification methods used to alter lignin functionalities, carboxymethylation is particularly notable for its ability to introduce a high concentration of carboxylic acid groups into the lignin structure [27]. Carboxymethylation enhances lignin's reactivity by increasing the number of functional sites (i.e., carboxylic group) available for chemical reactions, thereby reinforcing the structural integrity of the aerogel. Additionally, carboxymethylation improves the compatibility between lignin and chitosan through electrostatic interactions between the carboxylic group of lignin and the amine groups of chitosan, leading to the development of stronger composite materials [28].

5.4.2. Chemical insights of aerogel derivatives

5.4.2.1.XRD analysis

The X-ray powder diffraction patterns were examined to investigate the chemical structures of ACH, AKL, ACM1, ACM2, and ACM3 (presented from 5° to 100° (2θ)) in **Figure 5.1**(a) and of CH and KL in **Figure S5.3**. It was observed that CH and ACH patterns have two substantial peaks at 2θ = 10° and 20°, which are attributed to the anhydrous crystal structure of chitosan [29, 30]. The large peak in the KL pattern (**Figure S5.3**) at 2θ = 25° indicated its amorphous structure nature, which was reduced after mixing with CH to prepare AKL [31–33]. In this case, the incorporation of KL disrupted the ordered structure of the molecular chains of CH, reducing its crystallinity [34].

Adding CM to CH decreased the crystallinity of CH, which is due to its dense network structure of interpenetrating polymer chains crosslinked with CM1, CM2, and CM3 [35]. The presence of amorphous KL and CM1 in the reaction medium with CH increased X-ray scattering and caused the diffraction angle to shift from 2θ = 20° to 21° in AKL, ACM1, ACM2, and ACM3 and the disappearance of the peak at 2θ =10° was related to the decrement in crystallinity of CH [36, 33]. Thus, the XRD pattern of aerogels prepared from lignin derivatives showed crystallinity characteristics and an amorphous polymer. In addition, KL and CM1 had a significant detrimental influence on the anhydrous crystal structure of CH at 2θ = 20° [37]. This result indicates that the slight interlayer expansions of CH sheets would happen due to the insertion of KL and CM [34].

5.4.2.2. FTIR

The Fourier transform infrared spectra (FTIR) were carried out to analyze chemical bonds and functional groups of lignin derivatives and aerogels. The results are shown for ACH, AKL, ACM1, ACM2, and ACM3 in **Figure 5.1**(b) and for CH, KL, and CMs in **Figure S5.3**. The FTIR spectra of CH and ACH illustrated characteristic bands at 3450 cm^{-1} to 3120 cm^{-1} for the N–H stretching of primary amides and O–H stretching [38]. Peaks at 1290 cm^{-1}, 1000 cm^{-1}, and 1670 cm^{-1}, 1596 cm^{-1} in the spectra of CH and ACH represent –CH_2OH functional groups, 1,4 glycoside bonds (C–O–C), and N–H bending of amide I and amide II, respectively [39, 40]. As hydroxyl and amine groups interact with each other via hydrogen bonding, the spectra of ACH and CH were identical [41].

The KL spectrum (**Figure S5.4**) shows the characteristics bonds of 3400 to 3100, 2930, and 2300 cm^{-1}, which correspond to O–H phenolic and aliphatic, C–H stretching, and C=C, respectively [42]. The three strong peaks of aromatic skeletal vibration can be found at 1600, 1500, and 1400 cm^{-1}. Interestingly, the intensity of the peaks at 1600, 1263, and 1030 cm^{-1} was elevated by increasing the charge densities of CMs, which was related to the introduction of carboxy methyl groups to KL (**Figure S5.4**) [43, 44].

After adding the KL and CM samples to CH to prepare AKL, ACM1, ACM2, and ACM3, the characteristic peaks of CH, KL, and CMs, such as the wide band of O–H and N–H at 3200 cm^{-1} to 3600 cm^{-1}, C–O stretching at 1066 cm^{-1} and 1028 cm^{-1}, N–H bending at 1630 cm^{-1}, were preserved in the aerogels. The small peak around 2850 cm^{-1} represented the C–H symmetric stretching. However, the intensity of these wide bands decreased after aerogel preparation due to the presence of intermolecular hydrogen bonds of N–H, and O–H and the attribution of these functional groups in the reaction between the amine group of CH and carboxyl groups of KL, CM1, CM2, and CM3 [45, 46]. The peaks at 1510 cm^{-1}, 1428 cm^{-1}, and 1280 cm^{-1} are attributed to the N–H deformation of NH_2, N–H deformation of –NH–, and C–N, respectively [47]. Moreover, the N–H bending at 1638 cm^{-1} disappeared, and both new peaks appeared at 1710 cm^{-1} and 1660 cm^{-1}, which are related to the aldehyde bond and C=O, respectively. The intensity of C–O peaks decreased after aerogel preparation due to the cross-linking reaction that formed the amide O=C–N bond between the amine groups of CH and carboxyl groups via amide condensation reaction (**Figure S5.5**) [48].

5.4.2.3.Solid-state NMR

The solid-state NMR experiment can be used to identify the composition and molecular structures of materials [49]. The assignments of CH peaks and KL solid-state NMR are labeled in **Figures S5.6** and **S5.7**, respectively. In all spectra, signals associated with the two main components of the CH and KL are identified and labeled in **Figure 5.1**(c). The carbons are labeled from 1 to 9 and assigned on the solid-state NMR (**Figure 5.1**(c)) with the symbols of C_1 to C_9 [50]. Two peaks at 24 ppm and 174 ppm are related to CH_3 (C_8) and C=O (C_7) of the acetylamino unit of CH [51], and these results are in harmony with those reported in a previous work [52].

The spectrum of KL shows three regions [53]. The first region, between 220 and 160 ppm, is related to the carbons of carbonyl groups. The second region, between 160 and 100 ppm, is related to the aromatic region. The third region, between 100 to 20 ppm, is related to aliphatic carbons [54]. Two peaks at 148 ppm are associated with C_3 and C_5 of the S and G units of lignin, respectively. Furthermore, the peaks of saturated carbon and ether groups of lignin are shown in the range of 60–110 ppm [55]. The peaks at 188 ppm, 134

ppm, and 56 ppm, respectively, are attributed to aliphatic carbonyl, C_1 and C_4 of the S unit, and methoxyl group (R–O–CH_3) of lignin [56].

The NMR spectra of AKL, ACM1, ACM2, and ACM3 were compared to CH and KL to observe the changes in chemical crosslinking caused by aerogel preparation (**Figures 5.1**(c) **and S5.7**). The distinct splitting of the C_2 and C_6 signals was observed; however, this splitting disappeared upon the addition of KL or CMs. This disappearance was attributed to the chemical reaction and physical interaction that occurred as a result of the interaction [57]. The peak observed at 25 ppm corresponded to the methyl carbon of acetamido groups [58]. This peak appeared weak in ACH but became stronger in AKL, ACM1, ACM2, and ACM3, likely as a result of chemical cross-linking. The resonance range of 170 to 180 ppm indicated the presence of carboxymethyl groups that were not involved in the crosslinking process, as well as carbonyl carbon groups [45]. In addition, the small peak at 82 ppm was intensified by increasing the charge density of CM, which was attributed to the presence of more methylene groups in CM [59].

It can be seen that, after aerogel preparation, the characteristic peaks of CH and KL were observed in the aerogel structure. In addition, carbonyl groups present at 175 ppm in AKL and ACM1, ACM2, and ACM3 (**Figure 5.1**(c)). Still, its intensity increased and shifted slightly to a higher field, which could be due to the chemical crosslinking as amide condensation and physical interaction, such as hydrogen bonding and electrostatic interaction between carboxyl and amine groups [60].

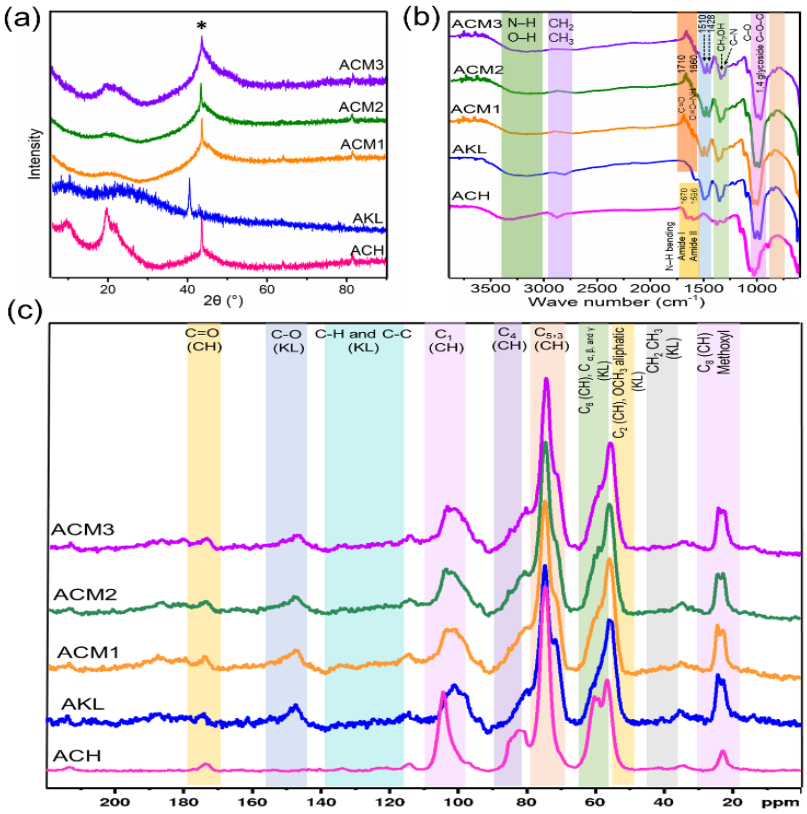

Figure 5.1. (a) FTIR spectra, (b) XRD pattern (*) Peaks corresponding to the aluminum sample holder) [61], and (c) solid-state ^{13}C NMR spectra of the ACH, KL, AKL, ACM1, ACM2 and ACM3.

5.4.2.4.XPS analysis

The representative high-resolution wide XPS spectra and elemental decomposition of O1s, C1s, and N1s are presented in **Figure 5.2**(a–d) and **Figure S5.8**. The wide XPS spectra in **Figure 5.2**(a) revealed that the primary elements in the samples were C, O, and N elements, and the shift in strength of each peak and new peaks may be used to determine the degree of reactivity between functional groups. For ACH, O 1s (**Figure 5.2**(b)) showed two main sub-peaks at 529.5 eV and 531.5 eV, which were ascribed to C=O and C–O or C–O–C bonds, respectively. By incorporating KL into ACH, the intensity of those two peaks was enhanced due to the new increment in functional groups, such as hydroxyl and carboxyl, and interactions between hydroxyl groups via hydrogen bonds [62]. By adding CM to CH with different charges, the intensity of C=O groups in ACM increased due to the carboxyl groups of CMs. Moreover, the C–O bonds decreased due to the amino condensation reaction between CM and CH (**Figure S5.5**).

The spectrum pertaining to C1s (**Figure 5.2**(c)) consists of three components, whereby the main peak at 286.5 eV was assigned to the single bond of C–O or C–N, while the smaller peak (284.8 eV) showed the typical binding of carbon to carbon and hydrogen (C–C/C–H) in all aerogels. There was an insufficient change in the intensity of C1s, which was attributed to the amino condensation reaction between amine and carboxyl groups. This reaction involved the breaking of C–O bonds and the formation of C–N bonds, both of which exhibited the same binding energy; thus, it was an insufficient change.

The N1s peaks were deconvoluted into two distinct electronic states, as shown in **Figure 5.2**(d): amine groups at 397.5 eV ($C–NH_2$) and secondary amide groups (–HN–C=O) at 398 eV, respectively [63]. The smallest area near the 288.0 eV energy level was attributed to the acetal and amide groups, which was due to the new bond's intensities (N–C=O) and increased after the aerogel preparation [64]. For AKL, the peak of O=C–N was attributed to the new bonds between carboxyl groups of KL [65] and amine groups of CH. In addition, by increasing the charge density of CM, the intensity in the O=C–N bonds was intensified due to the more chemically crosslinking, which was the confirmation of the amide condensation and polycondensation in the aerogel reaction [66].

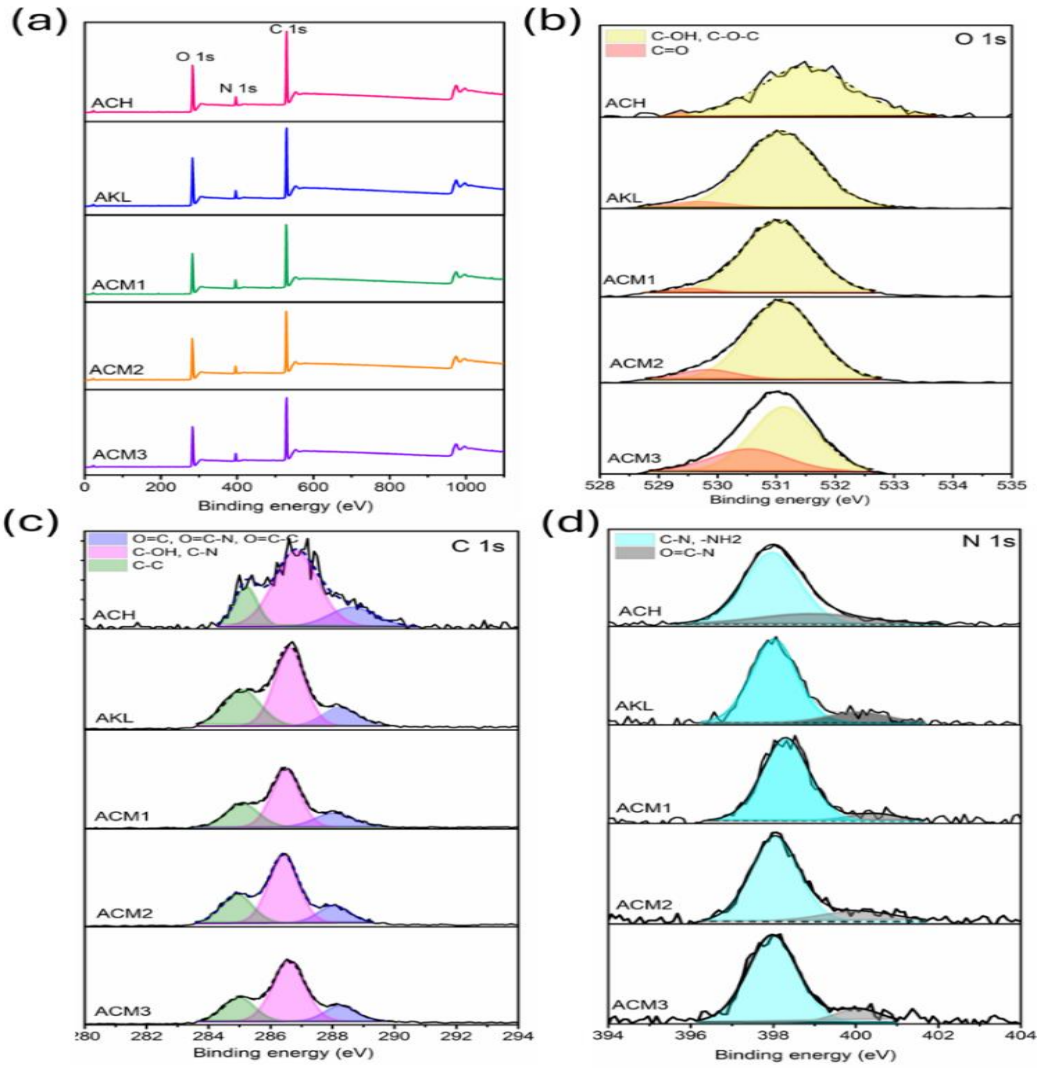

Figure 5.2. The XPS (a) wide spectra, (b) O1s, (c) C1s, and (d) N1s of ACH, AKL, ACM1, ACM2, and ACM3.

5.4.2.5.Structural analysis

The structural properties of the aerogels are presented in **Table 5.1**. Pure chitosan aerogel (ACH) had the lowest density value of 0.03 g/cm^3 [67]. The overall loading of KL and CM raised the density of aerogels. The specific surface area of ACH was about 205 m^2/g. The incorporation of KL improved the specific surface area of aerogel to 266 m^2/g (i.e., the highest amount among aerogels) [68]. Also, as the charge density of CM increased from 1 to 2 mmol/g (CM1, CM2, and CM3), the surface area decreased from 211.2 m^2/g to 152.5 m^2/g. In addition, the smallest pore volume (0.167 cm^3/g) and largest pore size (2.2 nm) were

achieved for the ACM3. As the charge density of CM increased, the carboxylate group of lignin reacted with amine groups of chitosan and induced crosslinked structure more intensely.

The morphologies of the ACH, AKL, ACM1, ACM2, and ACM3 aerogels are reported in **Figure 5.3**(a−e). ACH showed an irregular 3D porous structure (**Figure 5.3**(a)), which was attributed to hydrogen bonds. However, by adding KL, the specific surface area of the aerogels increased [69, 70]. In addition, by adding the CM samples, the microstructures of aerogel were changed to a lamellar bridge-like (e.g., honeycomb) structure [71, 72]. Moreover, with increasing the charge density of CM samples, the structure of the aerogels became compacted with more layers that covered the pores [73]. As a result, the aerogel of ACM1 with a low charge density CM1 was more porous than other aerogels of ACM2, ACM3, ACH, and AKL. As observed, the KL, CM1, CM2, and CM3 intertwined without any discernible organization into a network of aerogels via hydrogen bonding, electrostatic interactions between the positive NH_3^+ groups and the negative COO^- groups, and chemical reaction between amine and carboxymethyl groups [74, 75].

5.4.2.6. Water interaction of aerogels

The wettability test was measured for all aerogels, with the results in **Figure 5.3**(f). ACH and AKL had similar water absorption trends, with AKL showing the lowest absorption due to the limited charge density and hydrophobicity of KL. The results suggest that different charges influence the water absorption of aerogels, as ACM3 reached maximum absorption at 10.7 g/g after 2500 seconds, followed by saturation. In comparison, ACM1 displayed lower absorption than ACM2 and ACM3, with saturation occurring at 300 seconds for both ACM1 and ACM2, with water absorption levels of 6.2 g/g and 8.2 g/g, respectively. For a better understanding of the hydrophobicity of samples, the contact angle test was conducted for the corresponding hydrogels that were coated on glass, as reported in **Figure 5.3**(g). The samples of ACH and AKL had the highest contact angle (74°). Apparently, the limited dosage of KL in AKL marginally affected the contact angle of the hydrogel. However, by adding CM, the hydrophilicity of samples increased, and more intensely for higher charged CM, reaching 46° for ACM3.

Table 5.1. Structural characteristics of ACH, AKL, ACM1, ACM2, and ACM3.

Sample ID	Density (g/cm^3)	Surface area (m^2/g)	Pore volume (cm^3/g)	Pore size (nm)
ACH	0.030	205.0	0.183	1.8
AKL	0.038	266.0	0.270	2.0
ACM1	0.036	211.2	0.198	1.9
ACM2	0.038	197.3	0.183	1.9
ACM3	0.037	152.5	0.167	2.2

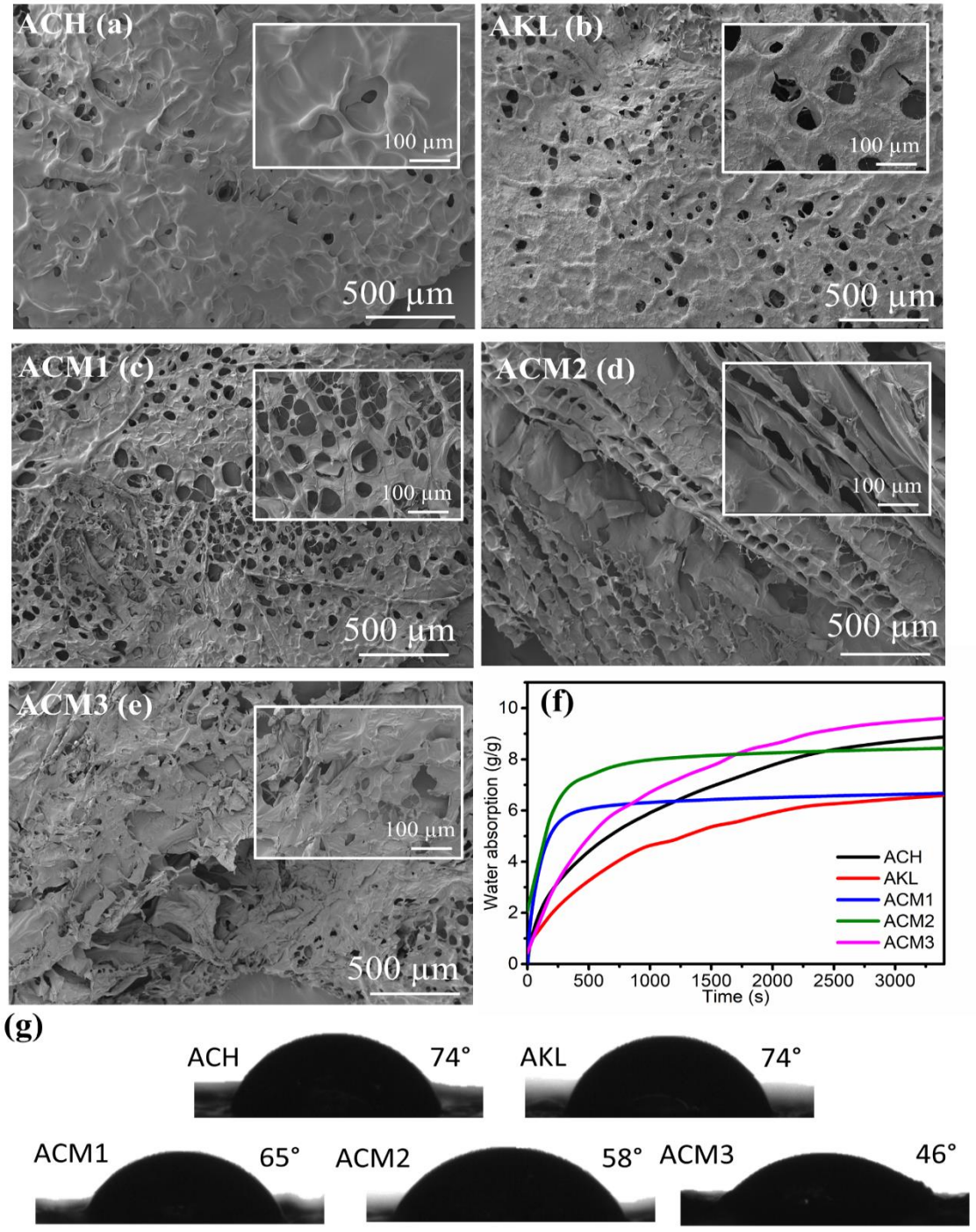

Figure 5.3. 5.3. (a–e) the SEM images, (f) aerogel powder wettability test, and (g) water contact angle of coated hydrogel on glass for samples of ACH, AKL, ACM1, ACM2, and ACM3.

5.4.2.7.Mechanical properties

The effect of the charge density of lignin derivatives on the mechanical strength of aerogels is displayed in **Figures 5.4**(a) and 5.**4**(b). The stress-strain curve consisted of three regions: linear elastic, plastic collapse (plateau), and densification region [76]. Initially, the stress increased slowly owing to dissipation, leading to a linear increase in stress with strain. Then, it sharply increased because the porosity of the aerogels significantly reduced as a result of the compression [77, 78].

The results show that the ACH had a linear elastic deformation reaching 80% strain at 220 kPa. However, after adding KL, there was no significant improvement in the compression strength of the aerogel. In addition, there was a decrement in Young's modulus from 1.61 MPa for ACH to 0.62 MPa for AKL, which can be associated with the unstable internal structure of AKL [79].

A comparison of three aerogels with different charge densities (ACM1, ACM2, and ACM3) to ACH and AKL demonstrated that the compression of the aerogel was enhanced when CM was used. At 80% strain, the maximum compressive strength was 0.28 MPa for ACM1, i.e., greater than other samples. Also, the Young's modulus of the aerogels increased from 1.61 MPa (for ACH) and 0.62 MPa (for AKL) to 3.87 MPa (for ACM1).

These results can be ascribed to the crosslinking degree with more porosity and more homogenous properties preventing pore walls from collapsing under compression [79, 80]. The porous structure of aerogels, especially for ACM1, can resist deformation and promote load transfer due to the high porosity [77]. Moreover, as the charge density of CM increased, the chitosan chains were more winding with chemical crosslinking and perhaps weaker physical interaction, such as hydrogen bonding and charge interaction, which collapsed the pores and decreased the compression modulus (**Table S5.4**). The reduced porosity made the aerogel more susceptible to compression by external forces, reducing compressive strength [81].

Indentation was performed to investigate the hardness and elasticity of aerogels at the microscale, and the results are reported in **Figure 5.4**(c) and (d), respectively. By adding KL or CM1 to CH, the hardness of aerogels decreased from 0.0095 to 0.004 MPa, showing that penetration resistance was reduced compared with ACH. However, by increasing the charge density of CM, the hardness of aerogel increased from 0.004 to 0.03 MPa that is because of the improved crosslinking of KL and CH as well as strong network and interfacial bonds (**Figure 5.4**(c)) [82, 83]. More importantly, by increasing the charge density, the elasticity increased, and ACM3 had the highest elasticity (0.595 MPa) compared with other aerogels due to the high chemical crosslinking and more electrostatic interactions. It can be concluded that both physical and chemical crosslinking played important roles in the microscale performance of the aerogels under different mechanical stresses.

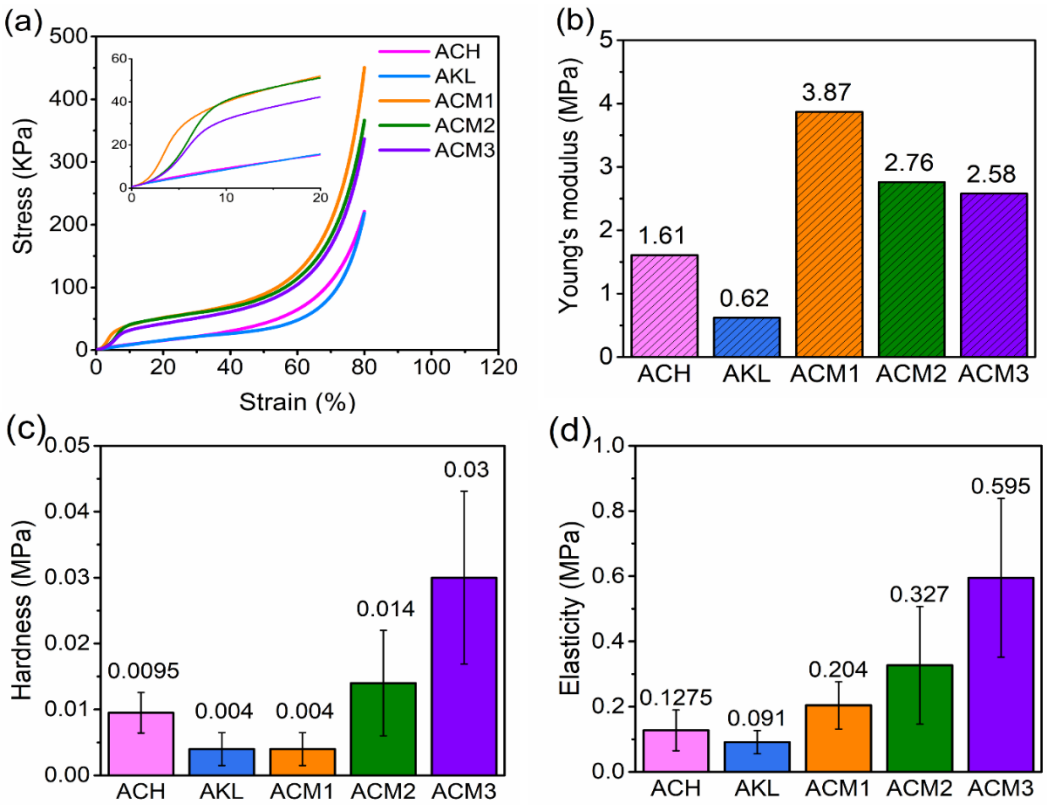

Figure 5.4. (a) compressive stress-strain, (b) Young's modulus, (c) hardness, and (d) elasticity of CH, AKL, ACM1, ACM2, and ACM3

5.4.2.8. Thermal properties

Thermogravimetric analysis (TGA) of aerogel was reported in **Figure 5.5**(a–c). According to the TGA curve of aerogels, weight loss occurred in three steps [84]. The first weight loss could be attributed to moisture removals. The second and third stages were related to the depolymerization, complete thermal degradation, and decomposition of acetyl groups [85]. The decomposition temperature (T_{onset}) of aerogels peaked at around 300 °C for both ACH and AKL. As the temperature continued to increase, the mass loss of the aerogels began to decrease sharply (**Figure 5.5**(a)). In the range of 600−800 °C, AKL and ACH aerogels exhibited substantial weight loss with the residue amount of 38 wt.% and 30 wt.%, respectively. The maximum weight loss temperature (T_{max}) rate was 330 °C for both ACH and AKL. By adding KL, the weight loss rate decreased due to the presence of KL, which would cause crosslinking and condensation of aromatic structures at high temperatures with less degradation [86].

The decomposition temperature (T_{onset}) decreased to 260 °C for both ACM1 and ACM2 and 280 °C for ACM3. The maximum rate of weight loss (T_{max}) for these aerogels decreased by increasing the charge density because of more carboxyl groups and crosslinking. Furthermore, the peaks observed at 600 °C in ACM1 and ACM2 are ascribed to the chemical crosslinking between amine and carboxymethyl groups, which require high temperatures to break. Increased crosslinking would typically enhance the thermal stability of a polymer by creating a tightly interconnected structure that would limit the mobility of polymer chains, thereby increasing resistance to thermal degradation [87]. However, the peak was less pronounced for ACM3, possibly due to excessive crosslinking, which could result in improved brittleness [88].

Interestingly, the incorporation of KL and CM3 into CH resulted in an increased ash content of 38 wt.%. This increase was primarily attributed to the presence of additional carboxyl groups, which produced more char [89, 90]. In contrast, ACM1 and ACM2 exhibited lower ash content compared to AKL and ACM3 with residues of 15 wt.% and 20 wt.%, respectively.

The thermal conductivity study evaluated the heat transfer of aerogels through the thermal gradient experiment, and the results are reported in **Figure 5.5**(d)**.** Thermal insulation properties are essential for different applications, especially in the field of building insulation [91]. High porosity and low density would lead to the low thermal conductivity of aerogels, and internal thermal convection in the aerogel is greatly impacted by the porosity [92, 93]. ACH demonstrated the highest thermal conductivity among the aerogels, recorded at 0.043 W/mK. However, the incorporation of KL resulted in a slight decrease in thermal conductivity to 0.041 W/mK. This reduction is attributed to the increased surface area (**Table 5.1**). The lowest thermal conductivity was observed for ACM1 (0.035 W/mK), while ACM2 and ACM3 exhibited thermal conductivities of approximately 0.038–0.039 W/mK. These values were influenced by crosslinking and porosity, as detailed in **Table 5.1**. Overall, the thermal conductivity of the synthesized aerogels with various CM ranged from 0.035–0.039 W/mK, which is comparable to other commercial insulators, such as cellular glass (0.034–0.045 W/mK) and glass wool (0.031–0.043 W/mK) [94].

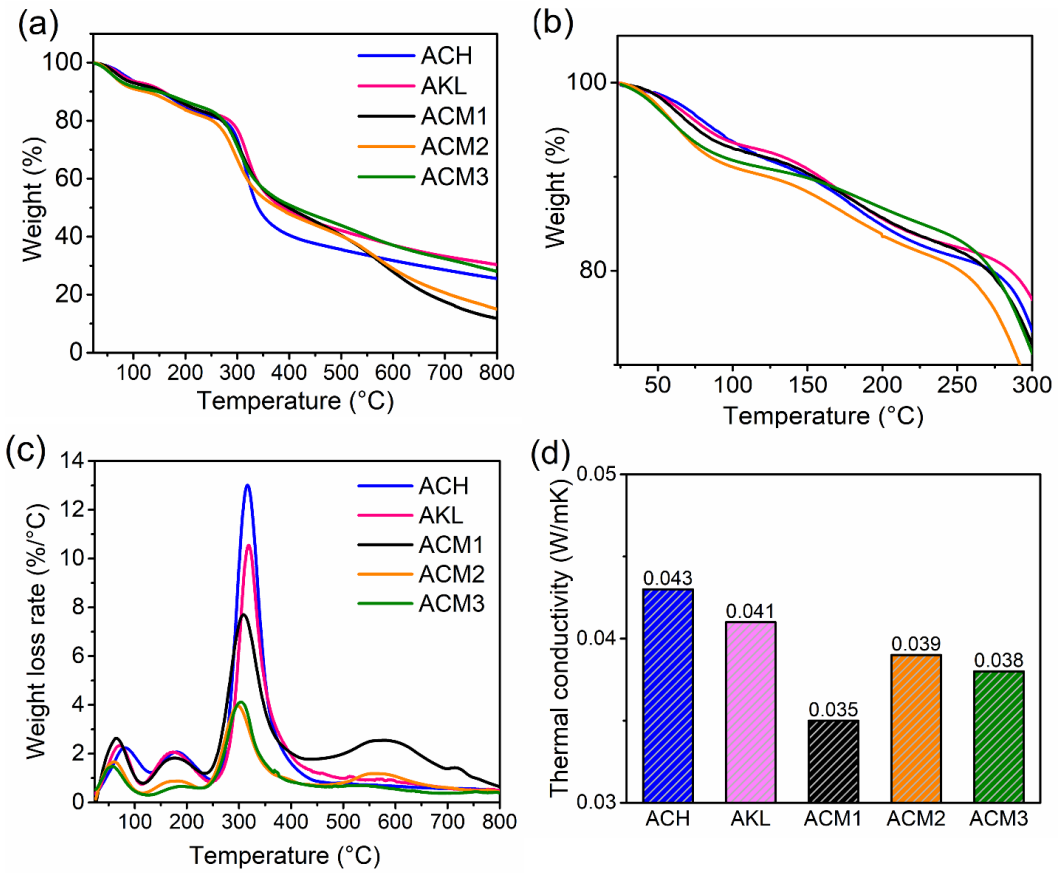

Figure 5.5. (a) Thermogravimetric analysis of weight loss, and (b) maximized weight loss in the range of 25–300 °C, (c) weight loss rate, and (d) and thermal conductivity of ACH, AKL, ACM1, ACM2, and ACM3.

5.5. Biodegradability performance

Figure 5.6 depicts the biodegradation performance of aerogels (ACM1, ACM2, ACM3, AKL, and ACH) alongside KL and CH. Wheat starch was selected as a reference sample for the biodegradability test due to its favorable biodegradability, reaching approximately 50% degradation within 12 days [95]. All samples revealed a lag phase characterized by minimal discernible microbial degradation under the specified aqueous conditions. This initial phase could be attributed to the microbial acclimatization process and the environmental conditions [24]. Notably, KL, with its greater hydrophobicity, required a longer duration of approximately 1 day for microbial action due to its increased resistance to chain cleavage, as opposed to ACM1, ACM2, ACM3, and ACH, which exhibited a lag phase of approximately 1 hour, likely owing to its comparatively higher hydrophilic properties. CH exhibited the lowest biodegradability among the tested

materials, with a degradation rate of approximately 10%. This limited biodegradability can primarily be attributed to its poor solubility in water, necessitating acidic conditions for effective dissolution. Despite this challenge, the presence of amine and hydroxyl functional groups in chitosan facilitated molecular interactions, which contributed to a slight enhancement of its biodegradability [96]. All modified lignin aerogels exhibited a plateau phase in the biodegradability assessment in a shorter time than AKL and KL, suggesting that microorganisms had more immediate access to the biodegradable component of carboxymethylated lignin-chitosan aerogel than KL [97]. Moreover, AKL showed high biodegradability in comparison with KL due to the presence of chitosan in AKL aerogel. Multiple factors may contribute to the biodegradability of aerogels of ACMs exhibiting higher biodegradability, reaching 21–26 % compared to AKL at 19%. Carboxymethylation introduces carboxyl groups ($–COO^–$) and improves the hydrophilicity of CM, making them more accessible to microorganisms, thereby facilitating enzymatic breakdown. Moreover, the biodegradability of polymers, such as lignin and chitosan, is largely influenced by the accessibility of their functional groups to microbial enzymes. This trend can be attributed to the balance between hydrophilicity, charge density, and enzyme accessibility, in which ACM3 showed the highest biodegradability among other ACM aerogels because of high charge density.

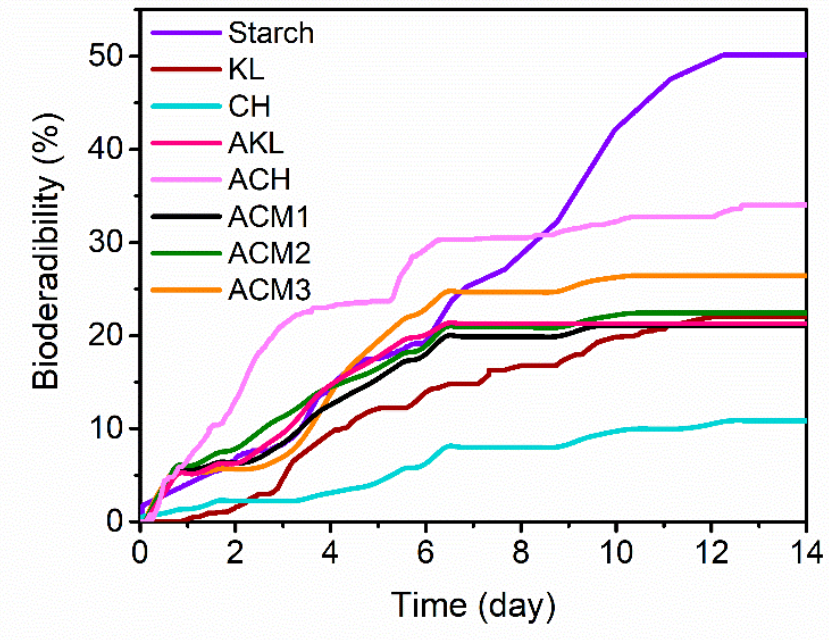

Figure 5.6. Biodegradability analysis of starch, KL, CH, AKL, ACH, ACM1, ACM2, and ACM3.

5.6. Dosage of CM1 in A CM1 aerogel

In this experiment, CM1 was selected as the best CM sample due to its best performance in improving the compression strength and thermal insulation of aerogels. In this experiment, the compression strength and thermal conductivity of aerogels were selected as key characteristics (**Figure 5.7**). The concentration of CM1 influences crosslinking density by creating a stronger network structure through its interaction with CH, which impacts pore structure and compression strength [98]. By increasing the concentration from 2 wt.% to 3.2 wt.%, Young's modulus decreased from 3.87 MPa to 2.02 MPa at 80% strain. The excessive amount of CM1 perhaps disrupted the network's uniformity, causing defects and lowering performance, which lowered Young's modulus [99]. Similarly, the thermal conductivity of aerogel was increased due to the change in crosslinking, which affected porosity and the network structure. However, excessive amounts of CM1 could lead to phase separation and defects, which compromise both thermal and mechanical properties due to the change in network structure. It can be concluded that the concentration of CM1 influenced crosslinking density and porosity, both of which affected Young's modulus and thermal conductivity. An increase in Young's modulus corresponds to a decrease in thermal conductivity in ACM1 at 2 wt.%. In the future, efforts should be made to increase the concentration of CM1 in ACM with acceptable properties.

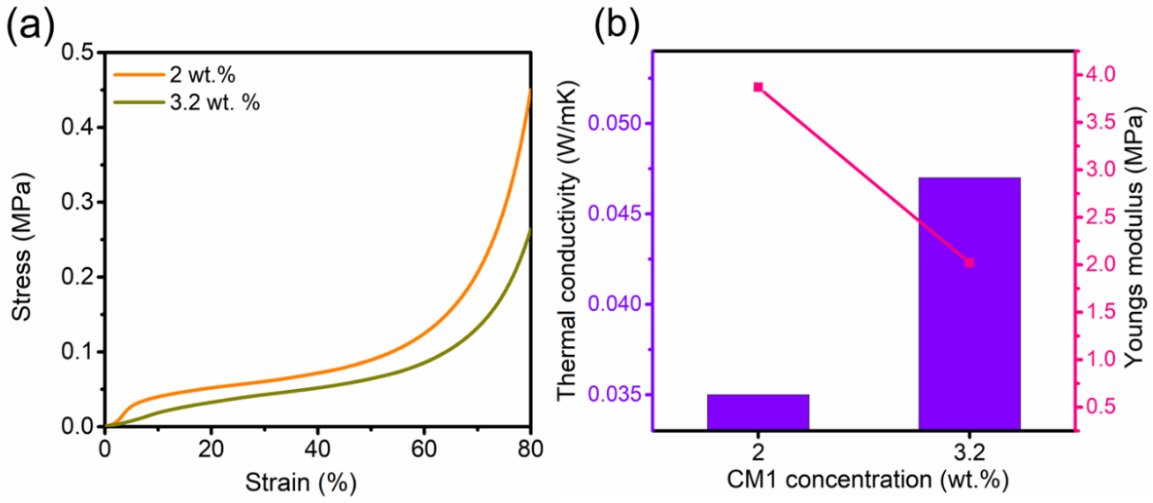

Figure 5.7. (a) Compressive stress-strain, (b) thermal conductivity and Young's modulus of CM1 concentration 2 and 3.2 wt. %.

5.7. Discussion

Figure 5.8 shows the physicochemical insights of chitosan derivatives. FTIR, XRD, solid-state NMR, and XPS analyses successfully confirmed the chemical structures of carboxymethylated lignin-chitosan aerogels. ACH developed hydrogen bonding between hydroxyl and amine groups, as confirmed by FTIR (**Figure 5.1**(b)). Moreover, KL induced aerogel with new bond C–O–C, which was confirmed by FTIR analysis in **Figure 5.1**(b) and XPS in **Figure 5.2**(b). The addition of KL disrupted the crystalline structure of CH, suggesting slight interlayer expansions of CH sheets (**Figure 5.1**(b)). KL also increased the specific surface area of aerogel and changed the irregular structure to a regular 3D structure. By adding KL to CH, the electrostatic interaction and hydrogen bonding were increased due to the presence of carboxyl groups and hydroxyl groups in KL. This high interaction made the aerogels denser, which was attributed to the improved interaction of CH and KL's functional groups. The hydrophilicity of aerogel decreased as KL was more hydrophobic than CH. The incorporation of KL reduced Young's modulus from 1.61 MPa to 0.62 MPa, likely due to structural instability caused by weak chemical interactions (**Figure 5.3**(a) and (b)). Adding KL improved thermal stability due to crosslinking and reduced the thermal conductivity of the aerogels.

Also, the addition of CM to CH mimicked aerogel with a new O=C–N bond via amino condensation reaction and C–O–C bond, which were confirmed by FTIR and XPS in **Figure 5.1**(b) and **Figure 5.2**, respectively. The hydrophobicity of the aerogel was decreased due to the presence of CM (**Figure 5.3**(f)). However, ACM1 had the highest compressive strain (0.45 MPa) and Young's modulus (3.87 MPa), attributed to increased crosslinking and better structural uniformity.

Furthermore, the increased charge density intensified the chemical bonding, such as O=C–N, C–O–C, as well as hydrogen bonding and electrostatic interaction (**Figures 5.1**(b) **and 5.2**). By increasing the charge density, the hydrophobicity decreased more intensely as ACM3 was more hydrophilic (**Figure 5.3**(a–f)). By increasing CM's charge density, the porosity decreased due to the improved interactions of CM and CH, which collapsed the pores of the aerogels, as confirmed by BET and SEM analyses. Moreover, the

compression strength and Young's modulus of aerogel were decreased by increasing the charge density. However, due to the high chemical interaction, the elasticity and hardness of aerogel improved. The lowest elasticity and hardness of ACM1 were due to its less rigid and packed structure.

The CM1, with the lowest charge density (1 mmol/g), induced ACM1 with a surface area of 211.2 m^2/g, pore volume of 0.198 cm^3/g, and pore size of 1.87 nm. It showed the lowest water absorption among ACM derivatives due to the lower hydrophilic performance and smaller pore size.

In addition, produced aerogels were biodegradable, which can provide a suitable alternative for petrochemical-based foams. As the thermal conductivity of the generated biodegradable aerogel was < 0.06 W/mK [10], its density was in the range of (~ 0.003 g/cm^3), it was highly porous (pore size<100 nm) [100], and strong (compression strength of 3.87 MPa), the material can be used for thermal insulation.

Generally, CH aerogel derivatives have thermally and mechanical deficiencies, and our results confirmed that these deficiencies could be addressed by incorporating CM or KL. The graphical interaction of each aerogel was illustrated and explained in detail in **Figure 5.8**.

Increasing the concentration to 3.2 wt.% collapsed the porosity, which affected Young's modulus and thermal conductivity. In the future, efforts should be made to improve the characteristics of lignin-incorporated chitosan-based aerogels at higher than 2 wt.% lignin content. As this hybrid aerogel was generated in an aqueous system with only sustainable ingredients, the manufacturing process of this aerogel was not only green but also made the product a sustainable material. This was confirmed by biodegradability analysis promoting sustainability in the manufacturing and use of environmentally friendly aerogels in construction applications as thermal insulators.

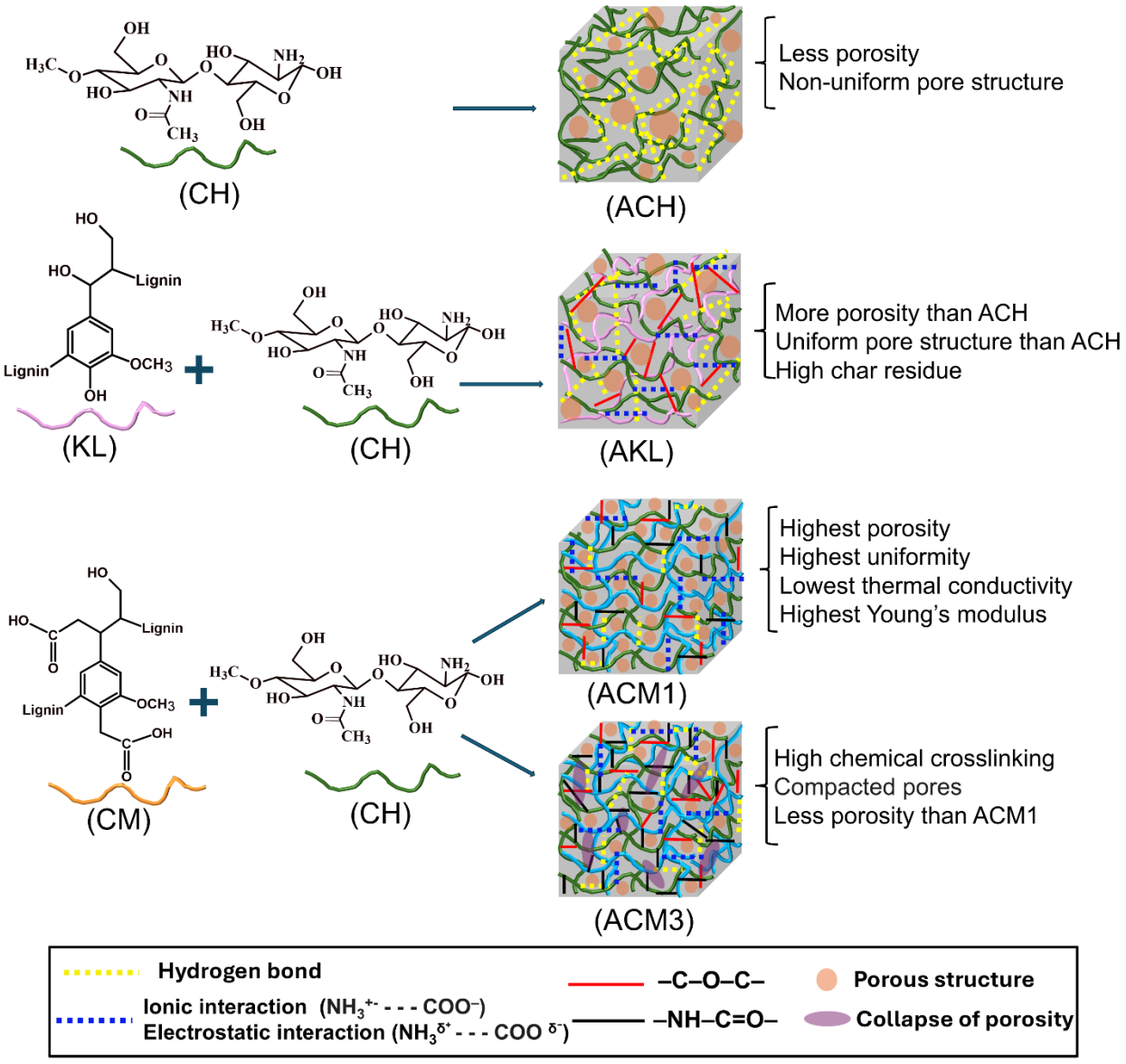

Figure 5.8. Schematic illustration of crosslinking and pore structure in ACH, AKL, ACM1, and ACM3.

5.8. Conclusion

The hybrid lignin-chitosan aerogel demonstrated significant potential as a sustainable thermal insulator. The formation of new O=C–N bonds via amino condensation was confirmed by FTIR, solid-state NMR, and XPS, highlighting the successful chemical crosslinking. Optimization studies revealed that a charge density of 1 mmol/g and a concentration of 2 wt.% were ideal for producing aerogels with enhanced properties. Carboxymethylation of KL was particularly effective in improving the compression strength while also contributing to lower thermal conductivity, a desirable characteristic for insulation applications. It seems that by using the lignin derivative with a higher charge density, the

crosslinking density was intensified such that it hampered the porous structure of the aerogel, reducing its compression strength while improving the elasticity. Regardless of the charge density, the carboxymethylated lignin derivatives increased the water absorption of aerogel, which should be addressed in the future. To mitigate this issue, coating the aerogel with silane-based materials can be explored to preserve its structural integrity and functionality over time. This study underscores the potential of carboxymethylated lignin-chitosan aerogels as a sustainable alternative for insulation materials, balancing thermal performance and mechanical durability.

5.9. References

[1] Rojas, C.; Cea, M.; Iriarte, A.; Valdés, G.; Navia, R.; Cárdenas-R, J. P. Thermal Insulation Materials Based on Agricultural Residual Wheat Straw and Corn Husk Biomass, for Application in Sustainable Buildings. *Sustain. Mater. Technol.* **2019**, *20*, e00102.

[2] Schiavoni, S.; D'Alessandro, F.; Bianchi, F.; Asdrubali, F. Insulation Materials for the Building Sector: A Review and Comparative Analysis. *Renew. Sustain. Energy Rev.* **2016**, *62*, 988–1011.

[3] Zou, F.; Budtova, T. Polysaccharide-Based Aerogels for Thermal Insulation and Superinsulation: An Overview. *Carbohydr Polym.* **2021**, *266*, 118130.

[4] Hebalkar, N.; Kollipara, K. S.; Ananthan, Y.; Krishna Sudha, M. Nanoporous Aerogels for Defense and Aerospace Applications. *Springer International Publishing* **2020**, 121–163.

[5] Nita, L. E.; Ghilan, A.; Rusu, A. G.; Neamtu, I.; Chiriac, A. P. New Trends in Bio-Based Aerogels. *Pharmaceutics* **2020***, 12,* 449.

[6] Zuo, L.; Zhang, Y.; Zhang, L.; Miao, Y. E.; Fan, W.; Liu, T. Polymer/Carbon-Based Hybrid Aerogels: Preparation, Properties and Applications. *Materials* **2015***, 8,* 6806-6848.

[7] Zhao, S.; Malfait, W. J.; Guerrero-Alburquerque, N.; Koebel, M. M.; Nyström, G. Biopolymer-Aerogele Und -Schäume: Chemie, Eigenschaften Und Anwendungen. *Angew. Chem.* **2018**, *130*, 7704–7733.

[8] Guerrero-Alburquerque, N.; Zhao, S.; Adilien, N.; Koebel, M. M.; Lattuada, M.; Malfait, W. J. Strong, Machinable, and Insulating Chitosan-Urea Aerogels: Toward Ambient Pressure Drying of Biopolymer Aerogel Monoliths. *ACS. Appl. Mater. Interf.* **2020**, *12*, 22037–22049.

[9] Zhu, F. Starch Based Aerogels: Production, Properties and Applications. *Trends. Food. Sci. Technol.* **2019**, *89*, 1–10.

[10] Koebel, M.; Rigacci, A.; Achard, P. Aerogel-Based Thermal Superinsulation: An Overview. *J. Solgel. Sci. Technol*. **2012**, *63*, 315–339.

[11] Zheng, L.; Zhang, S.; Ying, Z.; Liu, J.; Zhou, Y.; Chen, F. Engineering of Aerogel-Based Biomaterials for Biomedical Applications. *Int. J. Nanomedicine* **2020**, *15*, 2363–2378.

[12] Wahba, M. I. Enhancement of the Mechanical Properties of Chitosan. *Biomater. Sci.* **2019**, *31*, 350–375.

[13] Wang, W.; Xue, C.; Mao, X. Chitosan: Structural Modification, Biological Activity and Application. *Int. J. Biol. Macromol*. **2020**, *164*, 4532-4546.

[14] Liu, K.; Du, H.; Zheng, T.; Liu, W.; Zhang, M.; Liu, H.; Zhang, X.; Si, C. Lignin-Containing Cellulose Nanomaterials: Preparation and Applications. *Green Chem*. **2021**, *23*, 9723–9746.

[15] Gigli, M.; Crestini, C. Fractionation of Industrial Lignins: Opportunities and Challenges. *Green Chem*. **2020**, *22*, 4722–4746.

[16] Komisarz, K.; Majka, T. M.; Pielichowski, K. Chemical and Physical Modification of Lignin for Green Polymeric Composite Materials. *Materials* **2023**, *16*, 16.

[17] Aldajani, M.; Alipoormazandarani, N.; Fatehi, P. Two-Step Modification Pathway for Inducing Lignin-Derived Dispersants and Flocculants. *Waste Biomass Valor.* **2022**, *13*, 1077–1088.

[18] Konduri, M. K.; Kong, F.; Fatehi, P. Production of Carboxymethylated Lignin and Its Application as a Dispersant. *Eur. Polym. J.* **2015,** *70*, 371-383.

[19] Ahmadloo, H.; Losada, R.; Wandrey, C. Effect of Very High Charge Density and Monomer Constitution on the Synthesis and Properties of Cationic Polyelectrolytes. *Polymers* **2016**, *8*, 234.

[20] Shang, K.; Yang, J. C.; Cao, Z. J.; Liao, W.; Wang, Y. Z.; Schiraldi, D. A. Novel Polymer Aerogel toward High Dimensional Stability, Mechanical Property, and Fire Safety. *ACS Appl. Mater. Interf.* **2017**, *9*, 22985–22993.

[21] Konduri, M. K.; Kong, F.; Fatehi, P. Production of Carboxymethylated Lignin and Its Application as a Dispersant. *Eur. Polym. J.* **2015**, *70*, 371–383.

[22] Kenny, J. K.; Medlin, J. W.; Beckham, G. T. Quantification of Phenolic Hydroxyl Groups in Lignin via 19 F NMR Spectroscopy. *ACS Sustain. Chem. Eng*. **2023**, *11*, 5644–5655.

[23] Xu, L.; Sun, D.; Ma, J.; Sun, G.; Ling, S.; Hu, M. Applications of Depth-Sensing Indentation on Asphalt Materials: A Review. *Constr. Build. Mater.* **2021**, *268*, 121195.

[24] Muniyasamy, S.; Patnaik, A. Biodegradable Behavior of Waste Wool and Their Recycled Polyester Preforms in Aqueous and Soil Conditions. *J. Renew. Mater.* **2021**, *9*, 1661–1671.

[25] Šašinková, D.; Serbruyns, L.; Julinová, M.; FayyazBakhsh, A.; De Wilde, B.; Koutný, M. Evaluation of the Biodegradation of Polymeric Materials in the Freshwater Environment—An Attempt to Prolong and Accelerate the Biodegradation Experiment. *Polym. Degrad. Stab.* **2022**, *203*, 110085.

[26] Pang, Y. X.; Qiu, X. Q.; Yang, D. J.; Lou, H. M. Influence of Oxidation, Hydroxymethylation, and Sulfomethylation on the Physicochemical Properties of Calcium Lignosulfonate. *Colloids Surf. A. Physicochem. Eng. Asp.* **2008**, *312*, 154–159.

[27] Eraghi Kazzaz, A.; Hosseinpour Feizi, Z.; Fatehi, P. Grafting Strategies for Hydroxy Groups of Lignin for Producing Materials. *Green Chem.* **2019**, *21*, 5714–5752.

[28] Chen, P.; Xie, F.; Tang, F.; McNally, T. Structure and Properties of Thermomechanically Processed Chitosan/Carboxymethyl Cellulose/Graphene Oxide Polyelectrolyte Complexed Bionanocomposites. *Int. J. Biol. Macromol.* **2020**, *158*, 420–429.

[29] Khan, M. N.; Chowdhury, M.; Rahman, M. M. Biobased Amphoteric Aerogel Derived from Amine-Modified Clay-Enriched Chitosan/Alginate for Adsorption of Organic Dyes and Chromium (VI) Ions from Aqueous Solution. *Materials Today Sustain.* **2021**, *13*, 100077.

[30] Kaur, K.; Jindal, R.; Jindal, D. RSM-CCD Optimized Microwave-Assisted Synthesis of Chitosan and Gelatin-Based PH Sensitive, Inclusion Complexes Incorporated Hydrogels and Their Use as Controlled Drug Delivery Systems. *J. Drug. Deliv. Sci. Technol.* **2018**, *48*, 161–173.

[31] Kumari, S.; Chauhan, G. S.; Monga, S.; Kaushik, A.; Ahn, J. H. New Lignin-Based Polyurethane Foam for Wastewater Treatment. *RSC. Adv.* **2016**, *6*, 77768–77776.

[32] Ahmed, M. A.; Mearaj, S.; Thithai, V.; Weon, C. J. Production and Characteristic Features of Lignin-PVA Aerogels for Oil Spillage Applications. *Mater. Chem. Phys.* 2022, *289*, 126455.

[33] Tran, V. T.; Le, T. M.; Trinh, T. T. N.; Tran, C. L.; Duong, Y. H. P.; Huynh, V. Q.; Le, D. T.; Le, P. K. Development of Facile and Green Fabrication of Cellulose–Chitosan Composite Aerogel and Lignin/Silica Hybrid from Agro-Wastes. *Fibers Polym.* **2023**, *24*, 403–411.

[34] Zhu, Y.; Qi, B. K.; Lv, H. N.; Gao, Y.; Zha, S. H.; An, R. Y.; Zhao, Q. S.; Zhao, B. Preparation of DES Lignin-Chitosan Aerogel and Its Adsorption Performance for Dyes, Catechin and Epicatechin. *Int. J. Biol. Macromol.* **2023**, *247,* 125761.

[35] Ali, M. E. A.; Aboelfadl, M. M. S.; Selim, A. M.; Khalil, H. F.; Elkady, G. M. Chitosan Nanoparticles Extracted from Shrimp Shells, Application for Removal of Fe(II) and Mn(II) from Aqueous Phases. *Sep. Sci. Technol.* **2018**, *53*, 2870–2881.

[36] Vedula, S. S.; Yadav, G. D. Wastewater Treatment Containing Methylene Blue Dye as Pollutant Using Adsorption by Chitosan Lignin Membrane: Development of Membrane, Characterization and Kinetics of Adsorption. *Journal of the Indian Chemical Society* **2022**, *99*, 100263.

[37] Zhu, W.; Jiang, X.; Liu, F.; You, F.; Yao, C. Preparation of Chitosan-Graphene Oxide Composite Aerogel by Hydrothermal Method and Its Adsorption Property of Methyl Orange. *Polymers (Basel)* **2020**, *12*, 12092169.

[38] Gao, G.; Dallmeyer, J. I.; Kadla, J. F. Synthesis of Lignin Nanofibers with Ionic-Responsive Shells: Water-Expandable Lignin-Based Nanofibrous Mats. *Biomacromolecules* **2012**, *13*, 3602–3610.

[39] Fan, S.; Chen, J.; Fan, C.; Chen, G.; Liu, S.; Zhou, H.; Liu, R.; Zhang, Y.; Hu, H.; Huang, Z.; Qin, Y.; Liang, J. Fabrication of a CO2-Responsive Chitosan Aerogel as an Effective Adsorbent for the Adsorption and Desorption of Heavy Metal Ions. *J. Hazard. Mater.* **2021**, *416*, 126225.

[40] Ko, E.; Kim, H. Preparation of Chitosan Aerogel Crosslinked in Chemical and Ionical Ways by Non-Acid Condition for Wound Dressing. *Int. J. Biol. Macromol.* **2020**, *164*, 2177–2185.

[41] Takeshita, S.; Zhao, S.; Malfait, J.; Koebel, M. M. Chemistry of Chitosan Aerogels: Three-Dimensional Pore Control for Tailored Applications. *Carbohydr Polym.* **2020**, *251*, 117089.

[42] Wang, D.; Jang, J.; Kim, K.; Kim, J.; Park, C. B. "Tree to Bone": Lignin/Polycaprolactone Nanofibers for Hydroxyapatite Biomineralization. *Biomacromolecules* **2019**, *20*, 2684–2693.

[43] Sun, J.; Wang, C.; Stubbs, L. P.; He, C.; Sun, J.; He, C.; Wang, C.; Stubbs, L. P. Carboxylated Lignin as an Effective Cohardener for Enhancing Strength and Toughness of Epoxy. *Macromol. Mater. Eng.* **2017**, *302*, 1700341.

[44] Andriani, F.; Karlsson, M.; Elder, T.; Lawoko, M. Lignin Carboxymethylation: Probing Fundamental Insights into Structure−Reactivity Relationships. *ACS. Sustain. Chem. Eng.* ***2024***, *12*, 1705–1713.

[45] Labidi, A.; Salaberria, M.; Labidi, J.; Abderrabba, M. Preparation of Novel Carboxymethylchitosan-Graft-Poly (Methylmethacrylate) under Microwave Irradiation as a Chitosan-Based Material for Hg 2+ Removal. *Microchem. J*. **2019**, *148*, 531-540.

[46] Guan, X.; Zhang, B.; Li, D.; Ren, J.; Zhu, Y.; Sun, Z.; Chen, Y. Semi-Unzipping of Chitosan-Sodium Alginate Polyelectrolyte Gel for Efficient Capture of Metallic Mineral Ions from Tannery Effluent. *Chem. Eng. J.* **2023**, *452*, 139532.

[47] Wang, K.; Liu, Q. Chemical Structure Analyses of Phosphorylated Chitosan. *Carbohydr. Res.* **2014**, *386*, 48–56.

[48] Zhang, M.; Jiang, S.; Han, F.; Li, M.; Wang, N.; Liu, L. Anisotropic Cellulose Nanofiber/Chitosan Aerogel with Thermal Management and Oil Absorption Properties. *Carbohydr. Polym.* **2021**, *264*, 118033.

[49] Reif, B.; Ashbrook, S. E.; Emsley, L.; Hong, M. Solid-State NMR Spectroscopy. *Nature Revi. Meth. Prim.* **2021**, *1*, 1–23.

[50] Wang, F.; Zhang, R.; Wu, Q.; Chen, T.; Sun, P.; Shi, A. C. Probing the Nanostructure, Interfacial Interaction, and Dynamics of Chitosan-Based Nanoparticles by Multiscale Solid-State NMR. *ACS Appl. Mater. Interf.* 2014, *6*, 21397–21407.

[51] Facchinatto, W. M.; Santos, D. M. dos; Fiamingo, A.; Bernardes-Filho, R.; Campana-Filho, S. P.; Azevedo, E. R. de; Colnago, L. A. Evaluation of Chitosan Crystallinity: A High-Resolution Solid-State NMR Spectroscopy Approach. *Carbohydr. Polym.* **2020**, *250*, 116891.

[52] Saito, H.; Tabeta, R.; Ogawa, H. High-Resolution Solid-State 13C NMR Study of Chitosan and Its Salts with Acids: Conformational Characterization of Polymorphs and Helical Structures as Viewed from the Conformation-Dependent 13C Chemical Shifts. *Macromolecules* **1980**, *20*, 2424-2430.

[53] Jusner, P.; Bacher, M.; Simon, J.; Bausch, F.; Khaliliyan, H.; Schiehser, S.; Sumerskii, I.; Schwaiger, E.; Potthast, A.; Rosenau, T. Analyzing the Effects of Thermal Stress on Insulator Papers by Solid-State 13C NMR Spectroscopy. *Cellulose* **2022**, *29*, 1081–1095.

[54] Bortoluz Alexandra Cemin Luis Rafael Bonetto Fabrício Ferrarini Valdemar Inocêncio Esteves Marcelo Giovanela, J.; Bortoluz Á Cemin Á L R Bonetto Á M Giovanela, J. A.; Ferrarini, F.; Esteves, V. I. Isolation, Characterization and Valorization of Lignin from Pinus Elliottii Sawdust as a Low-Cost Biosorbent for Zinc Removal. *Cellulose* **2019**, *26*, 4895–4908.

[55] Fodil Cherif, M.; Trache, D.; Brosse, N.; Benaliouche, F.; Tarchoun, A. F. Comparison of the Physicochemical Properties and Thermal Stability of Organosolv and Kraft Lignins from Hardwood and Softwood Biomass for Their Potential Valorization. *Waste Biomass Valor.* **2020**, *11*, 6541–6553.

[56] Mun, J. S.; Pe, J. A.; Mun, S. P. Chemical Characterization of Kraft Lignin Prepared from Mixed Hardwoods. *Molecules* **2021**, *26*, 164861.

[57] Wang, F.; Deng, Z.; Yang, Z.; Sun, P. Heterogeneous Dynamics and Microdomain Structure of High-Performance Chitosan Film as Revealed by Solid-State NMR. *J. Phys. Chem. C.* **2021**, *125*, 13572–13580.

[58] Kostryukov, S. G.; Petrov, P. S.; Kalyazin, V. A.; Masterova, Y. Y.; Tezikova, V. S.; Khluchina, N. A.; Labzina, L. Y.; Alalvan, D. K. Determination of Lignin Content in Plant Materials Using Solid-State 13C NMR Spectroscopy. *Polym. Sci. B.* **2021**, *63*, 544–552.

[59] Feng, Y.; Lan, J.; Ma, P.; Dong, X.; Qu, J.; He, H. Chemical Structure and Thermal Properties of Lignin Modified with Polyethylene Glycol during Steam Explosion. *Wood. Sci. Technol.* **2017**, *51*, 135–150.

[60] Milotskyi, R.; Szabó, L.; Takahashi, K.; Bliard, C. Chemical Modification of Plasticized Lignins Using Reactive Extrusion. *Front. Chem.* **2019**, *7*, 00633.

[61] Gomide, R. A. C.; de Oliveira, A. C. S.; Rodrigues, D. A. C.; de Oliveira, C. R.; de Assis, O. B. G.; Dias, M. V.; Borges, S. V. Development and Characterization of Lignin Microparticles for Physical and Antioxidant Enhancement of Biodegradable Polymers. *J. Polym. Environ.* **2020**, *28*, 1326–1334.

[62] Xie, H.; Zhang, H.; Liu, X.; Tian, S.; Liu, Y.; Fu, S. Design and Preparation of Multiple Function-Integrated Lignin/Tannin/ZnONP Composite Coatings for Paper-Based Green Packaging. *Biomacromolecules* **2021**, *22*, 3251–3263.

[63] Daniyal, W. M. E. M. M.; Fen, Y. W.; Saleviter, S.; Chanlek, N.; Nakajima, H.; Abdullah, J.; Yusof, N. A. X-Ray Photoelectron Spectroscopy Analysis of Chitosan–Graphene Oxide-Based Composite Thin Films for Potential Optical Sensing Applications. *Polymers (Basel).* **2021**, *13*, 1–19.

[64] Zhang, D.; Xiao, J.; Guo, Q.; Yang, J. 3D-Printed Highly Porous and Reusable Chitosan Monoliths for Cu(II) Removal. *J. Mater. Sci*. **2019**, *54*, 6728-6741.

[65] Antonino, L. D.; Gouveia, J. R.; de Sousa Júnior, R. R.; Garcia, G. E. S.; Gobbo, L. C.; Tavares, L. B.; Dos Santos, D. J. Reactivity of Aliphatic and Phenolic Hydroxyl Groups in Kraft Lignin towards 4,4′ Mdi. *Molecules* **2021**, *26*, 082131.

[66] Bodnar, M.; Hartmann, J. F.; Borbely, J. Preparation and Characterization of Chitosan-Based Nanoparticles. *J. Borbely*, **2005**, *6*, 2521-7.

[67] Obaidat, R. M.; Tashtoush, B. M.; Bayan, M. F.; T. Al Bustami, R.; Alnaief, M. Drying Using Supercritical Fluid Technology as a Potential Method for Preparation of Chitosan Aerogel Microparticles. *Aaps Pharmscitech* **2015**, *16* (6), 1235–1244.

[68] Chu, R.; Guo, X.; Zhang, Y.; Zhao, X.; Xiong, X.; Zhang, X.; Zhang, F.; Zhang, K.; Wang, Y. Rapid Immobilization of Cr(VI) from Aqueous Waste through Multi-Functionalized Surface-Modified Lignin-Based Aerogels: Dynamic and Mechanism Analyses. *Mater. Today. Commun.* **2024**, *38*, 107676.

[69] Chen, H.; Liu, T.; Meng, Y.; Cheng, Y.; Lu, J.; Wang, H. Novel Graphene Oxide/Aminated Lignin Aerogels for Enhanced Adsorption of Malachite Green in Wastewater. *Colloids. Surf. A. Physicochem. Eng. Asp.* **2020**, *603*, 125281.

[70] Yi, Y.; Liu, P.; Zhang, N.; Gibril, M. E.; Kong, F.; Wang, S. A High Lignin-Content, Ultralight, and Hydrophobic Aerogel for Oil-Water Separation: Preparation and Characterization. *J. Porous Mater.* **2021**, *28*, 1881–1894.

[71] Jiang, X.; Zhang, J.; You, F.; Yao, C.; Yang, H.; Chen, R.; Yu, P. Chitosan/Clay Aerogel: Microstructural Evolution, Flame Resistance and Sound Absorption. *Appl. Clay. Sci.* **2022**, *228*, 106624.

[72] Xiao, W.; Wang, P.; Song, X.; Liao, B.; Yan, K.; Zhang, J. J. Facile Fabrication of Anisotropic Chitosan Aerogel with Hydrophobicity and Thermal Superinsulation for Advanced Thermal Management. *ACS. Sustain. Chem. Eng.* **2021**, *9*, 9348–9357.

[73] Li, S. S.; Wang, X. L.; An, Q. Da; Xiao, Z. Y.; Zhai, S. R.; Cui, L.; Li, Z. C. Upon Designing Carboxyl Methylcellulose and Chitosan-Derived Nanostructured Sorbents for Efficient Removal of Cd(II) and Cr(VI) from Water. *Int. J. Biol. Macromol.* **2020**, *143*, 640–650.

[74] Bartczak, P.; Wysokowski, M.; Szylińczuk, K.; Odalanowska, M.; Jesionowski, T.; Borysiak, S. Green Synthesis of Chitin/Lignin Based-Polyurethane Composites. *Ind. Crops. Prod.* **2023**, *204*, 117237.

[75] Do, N. H. N.; Truong, B. Y.; Nguyen, P. T. X.; Le, K. A.; Duong, H. M.; Le, P. K. Composite Aerogels of TEMPO-Oxidized Pineapple Leaf Pulp and Chitosan for Dyes Removal. *Sep. Purif. Technol.* **2022**, *283*, 120200.

[76] Hoque, M. E.; San, W. Y.; Wei, F.; Li, S.; Huang, M. H.; Vert, M.; Hutmacher, D. W. Processing of Polycaprolactone and Polycaprolactone-Based Copolymers into 3D Scaffolds, and Their Cellular Responses. *Tissue. Eng. Part. A.* **2009**, *15*, 3013–3024.

[77] Luo, J.; Fan, C.; Zhou, X. Functionalized Graphene Oxide/Carboxymethyl Chitosan Composite Aerogels with Strong Compressive Strength for Water Purification. *J. Appl. Polym. Sci.* **2021**, *138*, 50065.

[78] Katti, A.; Shimpi, N.; Roy, S.; Lu, H.; Fabrizio, E. F.; Dass, A.; Capadona, L. A.; Leventis, N. Chemical, Physical, and Mechanical Characterization of Isocyanate Cross-Linked Amine-Modified Silica Aerogels. *Chem.Mater.* **2006**, *18*, 285–296.

[79] Ye, W.; Xi, J.; Sun, Y.; Meng, L.; Bian, H.; Xiao, H.; Wu, W. Superelastic Chitin Nanofibril/Chitosan Aerogel for Effective Circulating and Continuous Oil-Water Separation. *Int. J. Biol. Macromol.* **2023**, *249*, 125958.

[80] Wang, Q.; Li, L.; Kong, L.; Cai, G.; Wang, P.; Zhang, J.; Zuo, W.; Tian, Y. Compressible Amino-Modified Carboxymethyl Chitosan Aerogel for Efficient Cu(II) Adsorption from Wastewater. *Sep. Purif. Technol.* **2022**, *293*, 121146.

[81] Xia, J.; Liu, Z.; Chen, Y.; Cao, Y.; Wang, Z. Effect of Lignin on the Performance of Biodegradable Cellulose Aerogels Made from Wheat Straw Pulp-LiCl/DMSO Solution. *Cellulose* **2020**, *27*, 879–894.

[82] Zhang, L.; An, L.; Wang, Y.; Lee, A.; Schuman, Y.; Ural, A.; Fleischer, A. S.; Feng, G. Thermal Enhancement and Shape Stabilization of a Phase-Change Energy-Storage Material via Copper Nanowire Aerogel. *Chem. Eng. J.* **2019**, *373*, 857–869.

[83] Cheng, Z.; Ye, Z.; Natan, A.; Ma, Y.; Li, H.; Chen, Y.; Wan, L.; Aparicio, C.; Zhu, H. Bone-Inspired Mineralization with Highly Aligned Cellulose Nanofibers as Template. *ACS Appl. Mater. Interf.* **2019**, *11*, 45, 42486–42495.

[84] Ozen, E.; Yildirim, N.; Dalkilic, B.; Ergun, M. E. Effects Of Microcrystalline Cellulose On Some Performance Properties Of Chitosan Aerogels. *Maderas: Cienciay Tecnologia* **2021**, *23*, 1–10.

[85] Pan, J.; Li, Y.; Chen, K.; Zhang, Y.; Zhang, H. Enhanced Physical and Antimicrobial Properties of Alginate/Chitosan Composite Aerogels Based on Electrostatic Interactions and Noncovalent Crosslinking. *Carbohydr. Polym.* **2021**, *266*, 118102.

[86] Nair, V.; Panigrahy, A.; Vinu, R. Development of Novel Chitosan–Lignin Composites for Adsorption of Dyes and Metal Ions from Wastewater. *Chem. Eng. J.* **2014**, *254*, 491–502.

[87] Mashhadikhan, S.; Ahmadi, R.; Ebadi Amooghin, A.; Sanaeepur, H.; Aminabhavi, T. M.; Rezakazemi, M. Breaking Temperature Barrier: Highly Thermally Heat Resistant Polymeric Membranes for Sustainable Water and Wastewater Treatment. *Renew. Sust. Energ.* **2024**, *189*, 113902.

[88] Tolinski, M. Crosslinking. Additives for Polyolefins. *William Andrew Pub.: Oxford, UK.* **2009**, 215–220.

[89] Rizal, S.; Yahya, E. B.; Abdul Khalil, H. P. S.; Abdullah, C. K.; Marwan, M.; Ikramullah, I.; Muksin, U. Preparation and Characterization of Nanocellulose/Chitosan Aerogel Scaffolds Using Chemical-Free Approach. *Gels* **2021**, *7*, 246.

[90] Zhu, Y.; Qi, B.-K.; Lv, H.-N.; Gao, Y.; Zha, S.-H.; An, R.-Y.; Zhao, Q.-S.; Zhao, B. Preparation of DES Lignin-Chitosan Aerogel and Its Adsorption Performance for Dyes, Catechin and Epicatechin. *Int. J. Biol. Macromol.* **2023**, *247*, 125761.

[91] Du, C.; Xu, Y.; Yan, C.; Zhang, W.; Hu, H.; Chen, Y.; Xu, M.; Wang, C.; Li, B.; Liu, L. Facile Construction Strategy for Intrinsically Fire-Safe and Thermal-Insulating Bio-Based Chitosan Aerogel. *Sustain. Mater. Technol.* **2024**, *39*, e00794.

[92] Druel, L.; Bardl, R.; Vorwerg, W.; Budtova, T. Starch Aerogels: A Member of the Family of Thermal Superinsulating Materials. *Biomacromolecules* **2017**, *18*, 4232–4239.

[93] Tran, V. T.; Le, T. M.; Trinh, T. T. N.; Tran, C. L.; Duong, Y. H. P.; Huynh, V. Q.; Le, D. T.; Le, P. K. Development of Facile and Green Fabrication of Cellulose–Chitosan Composite Aerogel and Lignin/Silica Hybrid from Agro-Wastes. *Fibers Polym.* **2023**, *24* (2), 403–411.

[94] Chen, H. B.; Chiou, B. Sen; Wang, Y. Z.; Schiraldi, D. A. Biodegradable Pectin/Clay Aerogels. *ACS. Appl. Mater. Interf.* **2013**, *5*, 1715–1721.

[95] Harutyunyan, L. R.; Lasareva, E. V. Chitosan and Its Derivatives: A Step Towards Green Chemistry. *Biointerface. Res. Appl. Chem*. **2023**, *13*, 578.

[96] Junior, I. T.; Dal Bosco, T. C.; Bertozzi, J.; Michels, R. N.; Mali, S. Biodegradability Assessment of Starch/Glycerol Foam and Poly(Butylene Adipate-Co-Terephthalate)/Starch Film by Respirometric Tests. *Braz. J. Food Technol.* **2020**, *23*, e2018248.

[97] Chavda, H.; Patel, C. Effect of Crosslinker Concentration on Characteristics of Superporous Hydrogel. *Int. J. Pharm. Investig.* **2011**, *1*, 17.

[98] Su, G.; Jiang, P.; Guo, L.; Zhang, H.; Cheng, X.; Zhang, H. Robust Cellulose Composite Aerogels with Enhanced Thermal Insulation and Mechanical Properties from Cotton Waste. *Ind. Crops. Prod.* **2024**, *211*, 118242.

[99] Wu, Y.; Wang, X.; Yao, L.; Chang, S.; Wang, X. Thermal Insulation Mechanism, Preparation, and Modification of Nanocellulose Aerogels: A Review. *Molecules* **2023**, *28*, 5836.

[100] Thapliyal, P. C.; Singh, K. Aerogels as Promising Thermal Insulating Materials: An Overview. *J. Mater.* **2014**, *1*, 127049.

6. Pickering or non-Pickering dilemma: a complicated system of anionic lignin incorporated oil-water emulsions

*Saba Khodavandegar[1,2,3], Ulrica Edlund[2], Peter Rättö[3], Illia Dobryden[3], Pedram Fatehi[*1,4]*

Under review in Colloid and Interface Science

[1] Biorefining Research Institute, Lakehead University, 955 Oliver Road, Thunder Bay, Ontario, P7B 5E1, Canada.

[2]Fibre and Polymer Technology, KTH Royal Institute of Technology, Stockholm, Sweden.

[3]RISE Research Institutes of Sweden, Drottning Kristinas vag 61, 114 28 Stockholm, Sweden.

[4]Department of Chemical Engineering, Lakehead University, 955 Oliver Road, Thunder Bay, ON P7B 5E1, Canada

First author, email: skhodava@lakeheadu.ca, address: 955 Oliver Road, Thunder Bay, ON, Canada, P7B 5E1.

Corresponding author, email: pfatehi@lakeheadu.ca, address: 955 Oliver Road, Thunder Bay, ON, Canada, P7B 5E1.

The contribution of Saba Khodavandegar to this work was the conception of the original draft, visualization, validation, formal analysis, data curation, and conceptualization.

Graphical abstract

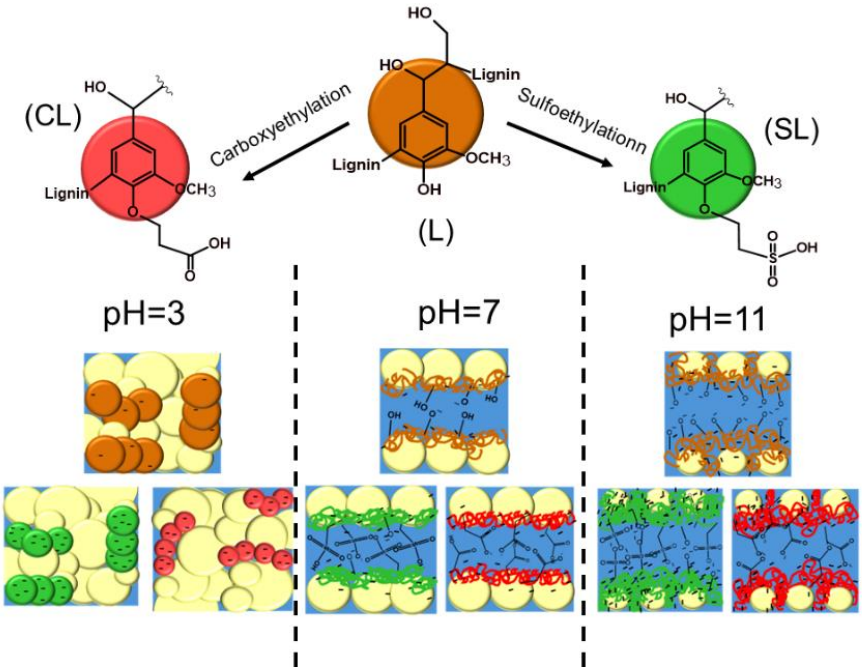

6.1. Abstract

Emulsifiers are vital for creating stable mixtures of immiscible liquids, but most currently used emulsifiers are synthetic based, which can pose environmental and health concerns. Lignin (L) stabilized emulsions have gained interest as a sustainable alternative, leveraging lignin's unique physicochemical characteristics. Despite their advantages, it is still unclear how lignin derivatives would interact with oil and water in emulsion systems. In this work, we verified a hypothesis that different modification strategies would generate lignin derivatives with different emulsifying performances even if lignin is anionically charged to a similar degree. To verify this hypothesis, we generated sulfoethylated (SL) and carboxyethylated (CL) lignin (L) as functional emulsifiers for soybean water emulsion systems. It was observed that the more negative zeta potential (ζ-potential) of lignin derivatives and smaller oil particles induced more stable emulsions via developing electrostatic repulsion at alkaline than acidic or neutral pH. Due to well-dispersed oil droplets and a strong electrostatic system, the viscosity of emulsions was lower at alkaline conditions. All emulsions had G' > G" exhibited high elasticity, confirming more electrostatic repulsion at pH 11. It

was also noted that SL and CL generated Pickering emulsions via depositing on oil droplets and developing steric hindrance with oil droplet sizes of 436 and 452 nm at acidic pH. However, such systems had shorter lifespans under acidic environments, implying indirectly that steric hindrance was insufficient to generate emulsions with long-term stability. This system had higher viscosity under acidic conditions due to the Pickering effect. Interestingly, the SL-included emulsion system was more stable because of its higher interaction with soybean oil. These findings verified the involvement of different mechanisms for stabilizing oil emulsion at different pH and the importance of lignin upgrading techniques in generating functional emulsifiers.

Keywords: lignin, sulfoalkylation, carboxyalkylation, soybean oil, emulsion, nano particles.

6.2. Introduction

Oil-water emulsions hold critical importance across multiple industries due to their distinctive properties. They contribute to the production of stable food products, such as margarine, mayonnaise, and chocolates [1], enhance the biodiversity of pharmaceutical compounds [2], and improve the sensual characteristics of cosmetic formulations [3]. Emulsions are stabilized through the incorporation of surfactants, which function by lowering the interfacial tension between the oil and aqueous phases [4]. Additionally, stabilization can be achieved using solid particles, such as silica, clay, proteins, and polysaccharides, following Pickering emulsion principles that enhance the emulsion's structural integrity [5–7].

The use of surfactants in oil-water emulsions is associated with limitations, including environmental toxicity and restricted biodegradability [8]. Surfactants, e.g., alkylbenzene sulfonates, are most derived from petroleum-based products [9]. However, there is an increasing shift toward utilizing renewable and sustainable alternatives to replace petroleum-based surfactants, including biopolymers, e.g., starch and chitosan [10]. Despite their advantages, there are grand challenges associated with the use of such biopolymers in emulsion systems, such as oxidative stability and incompatibility [11]. Thanks to its acceptable biodegradability and abundance, lignin can be a suitable alternative for emulsion systems [12–

14]. It is the second most abundant biopolymer on earth, demonstrating significant potential for emulsion stabilization owing to its inherent environmentally friendly, non-toxicity, and antioxidant characteristics [15]. Interestingly, lignin can act as a natural stabilizer due to its amphiphilic nature, reducing interfacial tension and stabilizing emulsions [16]. In addition, its complex three-dimensional structure with phenylpropane units and different functional groups enhances its steric hindrance potential once deposited on a surface [14].

The use of lignin in emulsion systems has been studied in the past. Rudwolt et al. esterified lignin in the solvent-based reaction system to fabricate soluble kraft lignin as a stabilizer for water-in-oil emulsions [18]. It was observed that esterified lignin exhibited surfactant-like behavior, significantly reducing interfacial tension and stabilizing water-in-oil emulsions [17]. Yuliestyan et al. explored the application of cationic lignin as an emulsion stabilizer, which originated from bioethanol production [18]. Gao et al. investigated the potential of lignin nanoparticles as efficient emulsifiers in enhanced oil recovery applications [19]. Although these studies reported the stabilization potential of lignin for emulsions, the precise mechanisms behind its role in emulsion stability require further investigation. Fundamentally, lignin stabilizes emulsions by adsorbing at the oil-water interface, reducing interfacial tension and forming a protective layer around oil droplets. In this case, by its deposition at the interface, lignin can create steric hindrance between oil droplets and stabilize the emulsions [20]. However, if lignin is charged, it can introduce surface charges on droplets and stabilize emulsions via electrostatic repulsions. To understand the principal mechanism of lignin in stabilizing emulsions, both systems of steric hindrance and electrostatic repulsion should be studied.

It is well known that altered parameters impact the stability of emulsions. Among them, pH plays a critical factor since it affects the surface functionality and interfacial activity of emulsion components [21, 22]. Emulsion has different applications at different pH, such as pharmaceuticals (injectable emulsions pH 7), food industry (salad dressing pH 3), cosmetics and skin absorption (pH 4 and 6) [23], drug delivery and textile industry (pH 11) [5, 24, 25]. Principally, pH influences the ionization, solubility, and charge density

of emulsifiers, and thus, the interaction of emulsifiers and oil/water affects the stability of emulsions [26, 22] . Specifically, due to its broad functional group, e.g., aromatic and aliphatic OH, lignin can behave differently at different pHs, impacting its potential use in emulsion systems. Therefore, it is crucial to understand how lignin-stabilized oil-water emulsions can behave differently at altered pH in order to understand the stabilization mechanism of lignin in emulsion systems and widen its use in different applications, such as cosmetics, biomedical, and environmental applications [27, 28].

Lignin can be modified to alter its performance in emulsion systems [29]. The broad presence of the hydroxyl group on lignin facilitates its chemical modification to improve its functionality, which facilitates its upgrading. Ethylation is a preferred upgrading strategy because it strikes a balance between hydrophilicity and lipophilicity, providing a safer environment for use in food and cosmetic applications [30]. Therefore, anionic ethylating-based fabrication techniques, e.g., sulfoethylation and carboxyethylation, would improve lignin's emulsification performance in oil-water emulsions by increasing hydrophilicity, charge density, and solubility [31]. However, these reactions may have altered functionalization yield and would impart functional groups with different pKa to lignin, potentially affecting lignin's importance in emulsion systems. In addition to grafting charged groups on lignin, these reaction strategies incorporate additional ethyl groups to lignin, enhancing lignin's amphiphilic nature. However, the impact of the charge density of lignin on its emulsifying performance has been discussed well [32]. It is well known that the charge density of -1.5 mmol/g would make lignin water soluble, similar to lignosulfonate and other charged lignin derivatives available in the market. Fundamentally, such a charge density is considered moderate, probably being able to be significantly neutralized via protonation but still hydrophobic to interact with oil [33, 34]. It is hypothesized that if lignin is sulfoethylated or carboxymethylated with a charge density of 1.5 mmol/g, it would act as an emulsifier for oil-water emulsions since it is water soluble but still contain hydrophobic features. However, the type of charged groups would impact its performance at different pH alterably as the charge groups have different pKa (i.e., 2.8 for sulfonate, 4 for carboxylate, and 10 for phenolic OH) [35–36].

Among many oils, soybean oil is a nutritious and stable source of essential fatty acids, vitamins E and K, with good oxidative stability [37, 38]. Its versatility in food, cosmetics, and pharmaceuticals makes it an ideal ingredient for emulsions, while its neutral flavor and light color make it cost-effective for large-scale productions [39, 40]. Soybean oil is utilized in various industries, including the food industry for stable emulsions, cosmetics for moisturizing properties, and pharmaceuticals for stability and bioavailability in medications and supplements [41]. Due to its tremendous applications, it was selected for lignin-reinforced oil-water emulsions in this study.

In this work, we performed two chemical modifications on lignin, sulfoethylation, and carboxyethylation, to enhance its effectiveness as an emulsifier. Each modification was optimized with Taguchi to achieve a charge density of 1.5 mmol/g, ensuring consistent comparison among the two modifications to study their stability in emulsions. It is hypothesized that sulfomethylation and carboxyethylation of lignin would improve its activity as a stabilizer in the emulsion system with soybean oil. The functional group activity and particle size of lignin could be changed by pH, which could affect the microstructure and interaction of oil and water. The objective of this work was to study how two different modifications of sulfoethylation and carboxyethylation of lignin can affect the stability of soybean oil emulsions in various pH to widen the use of lignin derivatives in emulsion systems.

6.3. Methodology

6.3.1. Materials

Softwood kraft lignin (L) produced via the LignoBoost technology was received from RISE, Sweden. 2-bromoethanesulfonate (SBS), 3-chloropropionic acid (CPA), sodium hydroxide (NaOH, 97%), dimethyl sulfoxide-d_6 (DMSO-d_6) (99.8 %), deuterium oxide (D_2O-d_6), 3-(trimethylsilyl)propionic-2,2,3,3-d4 acid sodium salt tetramethyl silane (TMSP) (≥98.5 %), cyclohexanol (99 %), 3- 2-chloro-4,4,5,5-tetramethyl-1,3,2- dioxaphospholane (CDP) (95 %), chromium (III) acetylacetonate (97 %), sodium azide (NaN3) (≥99.5 %), poly (diallyl dimethylammonium chloride) (PDADMAC) (100–200 kg/mol), pyridine,

cyclohexanol, deuterium oxide (D_2O), sodium nitrate ($NaNO_3$), and hydrochloric acid (HCl) (37 %) were all purchased from Millipore Sigma, Oakville, Canada. Hydrochloric acid (HCl, 37%), pyridine, cyclohexanol, poly (ethylene oxide), cellulose membranes with a molecular weight cut-off of 1000 g/mol, and soybean oil (triglycerides and other lipids) were obtained from Sigma–Aldrich.

6.3.2. Sulfoethylation (SL) and carboxyethylation (CL) modification

The sulfoethylation and carboxyethylation reactions of lignin were optimized using the Taguchi design methodology. The modification reaction utilized 2-bromoethanesulfonate (SBS) and 3-chloropropionic acid (CPA) as the sulfoethylation and carboxyethylation reagents, respectively. In each experimental setup, 1.5 g of kraft lignin (L) was dispersed in deionized (DI) water (50 g/L), and its pH was adjusted as reported in **Tables S6.1** and **S6.2**. The mixture was stirred at room temperature for 24 hours to complete deprotonation. Various concentrations of SBS and CPA were added to the L solution. The mixtures were then transferred to three-neck round-bottom flasks equipped with a reflux condenser and placed in a water bath. After the reaction, the mixtures were cooled to room temperature, neutralized with 1 M HCl, and purified via dialysis in DI water for 48 hours to remove unreacted reagents and salts. The final product was dried at 60 °C in an oven. This procedure was repeated under varying conditions of L: SBS and L: CPA molar ratios, pH values, reaction times, and temperatures to optimize such reactions based on charge density and solubility outcomes (**Tables S6.1** and **S6.2**). Overall, 9 reactions were carried out for sulfoethylation and carboxyethylation, and the samples were labeled SL1–SL9 and CL1–CL9.

The reactions were monitored to achieve soluble products with a charge density of 1.5 mmol/g. These optimized conditions were determined through systematic variation and analysis, ensuring efficient and effective modification of lignin for subsequent emulsion preparation. The optimized conditions for sulfoethylation were a lignin concentration of 0.5 g/mL and a reaction temperature of 80 °C for 4 hours at pH 13. The optimized conditions for carboxyethylation were the lignin concentration of 4 g/mL, reaction temperature of 40 °C for 12 hours, and pH 13. The elemental analysis (**Table S6.3**) confirms the changes

in elemental content by the modification. However, L contained sulfur even after dialysis that remained from the kraft pulping and lignin production processes [42].

6.3.3. Lignin included emulsion preparation

Lignin nanoparticles were prepared following an acid precipitation method as described in previous studies [35]. Specifically, 2.5 g/L concentration of L, SL, and CL samples were prepared in Milli-Q water, and the pH of the solution was adjusted to 12 by adding approximately 20 mL of 0.1 M NaOH under continuous stirring at 300 rpm. The formation of nanoparticles was initiated by gradually lowering the pH of the solution using 0.1 M HCl until reaching the target pH values. In this study, a pH of 3.2 was selected to achieve particles for further application.

Stock aqueous solutions of SL and CL (2.5 g/L) at pH 3, 7, and 11 were prepared for fabricating soybean oil-water emulsions at the volume ratio of (1:1 v:v). Emulsions with balanced oil-to-water ratios (1:1 v:v) have been shown to provide stable formulations with ideal viscosity, which is essential for use in medicine delivery systems, adhesives, and coatings [43]. This ratio helps the hydrophobic component, e.g., oil, disperse well in aqueous environment, e.g., water, guaranteeing consistency in commercial formulations [44]. The mixtures were prepared in clean glass vials and emulsified using an ultrasonic device (Omni-Ruptor 4000, Omni International Int.) at room temperature, 240W power, and a 30 s emulsification process with 3 s intervals.

6.3.4. Characterization of lignin derivatives

The charge density of L, SL, and CL samples was determined using a Particle Charge Detector (PCD 04, Mutek, Wessling, Germany). In this experimental procedure, 0.2 g of the dried sample was added to 20 mL of deionized water and stirred at 300 rpm for 24 hours and at room temperature. Following this step, the samples were centrifuged for 5 minutes at 1000 rpm, and the resulting supernatants were collected for the charge density analysis. Subsequently, 1 mL of the supernatant was titrated against PDADMAC (0.0069 M), a standard cationic solution, to determine the charge density of the samples. To evaluate solubility, 0.2

g of L, SL, or CL were added to 20 mL of deionized water (DI) and stirred at 300 rpm for 24 hours under ambient conditions. Following this step, each sample was centrifuged for 5 minutes at 1000 rpm. The resulting supernatants were then dried overnight in an oven set to 100 °C. The solubility of the samples was determined as previously described [45].

Gel permeation chromatography (GPC, Malvern GPCmax VE2001 Module + Viscotek TDA305) with multi-detectors and poly Analytic 206 and PAA203 columns was used to determine the molecular weight (MW) of samples. Samples were prepared by dissolving 50 mg of sample in 10 mL of 0.1 M NaN_3 and produced solutions were filtered through a 0.2 µm filter and evaluated according to a previously established procedure [2]. The column and detector temperatures were set at 35 °C, and a flow rate of 0.7 mL/min was maintained. In this test, 0.7 mL of each sample was analyzed by an RI detector of the GPC instrument.

The organic element compositions of the samples were determined using a Vario EL organic elemental analyzer, following the combustion method [47]. The chemical structures of L, SL, and CL samples were analyzed using FTIR spectroscopy with a Bruker Tensor 37 instrument (Germany) equipped with an ATR accessory. Also, the chemical bonds of L, SL, and CL samples were analyzed using various nuclear magnetic resonance (NMR) techniques, including ^{1}H and ^{31}P. These analyses were performed with a Bruker Advance spectrometer (AVANCE Neo NMR-500 MHz instrument, Fällanden, Switzerland) under ambient conditions. For ^{1}H NMR analysis, approximately 70 mg of L was dissolved in 1 mL of DMSO-d_6, and 70 mg of SL and CL was dissolved in D_2O. The ^{31}P NMR analysis aimed to quantify the aliphatic hydroxyl, phenolic hydroxyl, and carboxyl groups of lignin. This analysis was conducted in a $CDCl_3$/pyridine mixture using 2-chloro-4,4,5,5-tetramethyl-1,3,2-dioxaphospholane as the phosphorylation reagent and cyclohexanol as the internal standard. To prepare the sample, 70 mg of dried powder was placed in a clean 20 mL sample vial. Under a fume hood, 1 mL of pyridine/$CDCl_3$, 140 µL of relaxing agent, and 70 µL of internal standard were added to the vials and mixed overnight. Before analysis, 200 µL of phosphorylating reagent was added to the vials and mixed for a few minutes. The solution was then transferred to an NMR tube using a long-neck Pasteur pipette for analysis.

Sulfonate, phenolic hydroxy, and carboxylate groups in lignin before and after sulfoethylation and carboxyethylation were determined via conductometric titration. The mixture was prepared and calculated following the procedure previously reported [48]. The mixture was titrated with 0.1 M HCl for sulfonate and 0.1 M NaOH for phenolic and carboxylate hydroxyl groups using an automatic potentiometer, Metrohm, 905 Titrado, Switzerland.

The static contact angle (θ) of the lignin samples was measured using an optical tensiometer (Theta Lite, Biolin Scientific, Finland) equipped with a digital camera and a manually adjustable tilting stage. In this analysis, the prepared suspensions at different pH were applied onto glass slides via spin coating and subsequently dried at room temperature overnight. A sessile drop of water was placed on the glass with the syringe, which was controlled through the One Attention software. Each sample was tested in triplicate, and the results were reported as mean values along with their standard deviations. A drop of deionized (DI) water (5 μL) was placed on the coated glass slides, and the contact angle of L, SL, and CL at the water-air interface (WCA) was measured using the static contact angle method with the sessile drop technique at 25°C over 10 seconds. The three-phase contact angle of particles at the oil/water interface was determined when a dried lignin film was horizontally submerged in a transparent quartz container filled with soybean oil. A water droplet was then deposited onto the film's surface using a syringe. The moment the droplet contacted the film, its shape was promptly captured by a camera, enabling the measurement of the contact angle analysis [34].

The surface morphology of the lignin nanoparticle samples was assessed using transmission electron microscopy (TEM). To conduct this measurement, particle suspensions at different pH were dried, and a diluted suspension (1 wt.%) of L, SL, and CL was prepared and placed on a carbon-coated TEM grid and left to dry at room temperature overnight. The imaging of particles was performed using a Hitachi 7700 TEM (Japan) at an accelerating voltage of 100, 20, and 8 kV, and particle sizes were determined from the obtained images.

6.3.5. Characterization of emulsions

The emulsions were visually analyzed using an optical microscope (Olympus IX 51, 60x 0.1-0.2, UPlanApo Olympic) equipped with a camera. A 10 µL volume of the emulsion was deposited onto a clean glass slide, followed by the addition of a single drop of water to dilute the sample. The emulsion was then covered with a cover slip. Droplet size and distribution were analyzed using an image pro software and coloring the images with blue to red. The Raman spectra of emulsions were acquired using a RENISHAW Raman spectrometer (Gloucestershire GL 12 8JR, UK). The spectra of the samples were collected at a laser excitation wavelength of 785 nm, and the data acquisition time was set at 10 seconds. The Raman spectra of each sample were scanned in the regions of 600–3000 cm^{-1}.

The rheological characteristics of the formulated emulsions were assessed at room temperature and pH levels of 3, 7, and 11. The experiments were conducted using a hybrid rheometer (TA Instruments, Discovery HR-2) with an 8 mm parallel plate geometry and a 500 mm gap. The emulsions were tested immediately after preparation, with 1 mL of each emulsion pipetted onto the lower plate of the instrument. Each sample underwent a 3-minute pre-shear at 100 s^{-1} before data recording. Viscosity variations were measured from 0.1 to 1000 s^{-1} at 23 °C. To identify the linear viscoelastic region of L, SL, and CL emulsions, an amplitude sweep test was conducted within the range of 0.01–100 s^{-1} at a frequency of 10 rad s^{-1}. A strain of 0.1% was selected from the linear viscoelastic region for frequency sweep measurements, which were performed in the range of 0.1–1000 rad s^{-1}. The solutions were prepared at an initial pH of 7 and then readjusted to the desired range of 3–11 ± 0.5 using 1 mM NaOH or HCl.

Additionally, the zeta potential (ζ-potential) of the prepared solutions was determined using a ZetaPALS analyzer (Brookhaven Instruments Corp., USA). A dynamic light scattering (DLS) analyzer (BI-200SM, Brookhaven Instruments Corp., USA), equipped with a -35mW laser power source, was utilized to measure the hydrodynamic diameters (D_h) of L, SL, and CL at different pH levels. The test conditions included a wavelength of 637 nm, a scattering angle of 90°, and a temperature of 25°C. For the D_h and ζ-potential

analyses, the emulsions were diluted to 1 wt.% concentration with DI water prior to measurement. After a stabilization period of 2 hours, the hydrodynamic radius (D_h) of the samples was measured.

The long-term stability of emulsions was assessed immediately after adjusting the pH for solutions and emulsion preparation using a digital camera and monitored for 24 hours at room temperature with a vertical scan analyzer (Turbiscan Lab Expert, Formulation, France). The stability index (TSI) was determined for both the top and bottom sections of the emulsion systems, considering coalescence and settling phenomena.

The confocal Raman microscopy measurements were carried out using a WITec Alpha 300 RAS (Oxford Instruments, Germany) system equipped with 532 nm and 785 nm excitation lasers. The Raman spectra were collected using a Raman spectrometer, 50X ZEISS LD EC Epiplan-Neofluar Dic 50x / NA 0.55 with a Nikon CFI Plan NCG 100x/NA 0.9 objectives. The laser power was set to 1–2 mW to provide the best signal-to-noise ratio and to avoid lignin incineration. The spectrometer diffraction grating at 600 mm^{-1} was implemented in the study. A WITec Project Plus 5.1 software was used to analyze the measured spectra and to identify compounds and their distribution in the maps. The reconstructed Raman maps for all individual compounds and combined maps were then created. All spectra were analyzed with applied standard cosmic ray removal and baseline correction filters.

6.4. Results and discussion

6.4.1. Derivatization of lignin

6.4.1.1. Reaction optimization

The Taguchi design methodology was applied to optimize the sulfoethylation (SL) and carboxyethylation (CL) reactions through the systematic variation of key factors, including concentration, reaction time, temperature, and pH of the reaction solution. This robust design strategy enabled the identification of the most critical factors influencing the charge density and solubility of the modified compounds. The results of this study are reported in **Tables S6.1** and **S6.2**. As the mechanism of these reactions was studied earlier, we did not focus on such mechanisms [34, 33], and discussion on the optimization of such reactions is

available in the Appendix 6A. For sulfoethylation, the optimal conditions were a lignin concentration of 0.5 g/mL, a reaction time of 4 hours, a temperature of 80 °C, and a pH of 13. For carboxyethylation, the optimal conditions were a lignin concentration of 4 g/mL, a reaction time of 12 hours, a temperature of 40 °C, and a pH of 13. Under these conditions, the samples were water soluble at 10 g/L concentration and had 1.5 mmol/g charge density, which was selected for the emulsion preparation with soybean oil.

6.4.1.2. . Lignin characterization

The chemical structures of the L, SL, and CL were analyzed by FTIR, ^{31}P NMR, and ^{1}H NMR, and the results are illustrated in **Figure 6.1**(a–c), and the summary of these results is tabulated in **Table 6.1**. Previous studies have identified the FTIR characteristic bands of L comprehensively [49]. The broad O–H stretching band at 3400 cm^{-1} was weakened after sulfoethylation and carboxyethylation, indicating its involvement in the reactions. The spectral analysis reveals C–H stretching vibrations in methylene and methyl groups, C–C and C=C stretching associated with the phenylpropane monomer and aromatic structures, and ether-related C–O–C and C–O stretching vibrations (**Table 6.1**). Additionally, the aromatic C–H out-of-plane deformation signal for S units shifted slightly in L after modification [50]. In SL, the spectral peaks resemble those of L, with additional bands indicating S=O and S–O vibrations (**Table 6.1**) [51]. The stronger C=O stretching band in CL suggests its higher carboxylate group concentration than L's [33].

The ^{31}P NMR assessment of L, SL, and CL (**Figure 6.1**(b) and **Table 6.1**) reveals distinct hydroxyl groups of the samples. L had the highest aliphatic and phenolic OH, which decreased after modification due to the participation of these OHs in the reaction. SL showed a smaller concentration of OH groups than L, while CL had the lowest concentrations of these OH groups but the highest carboxylic acid OH. These differences highlight the successful sulfoethylation and carboxyethylation modifications of L on both aliphatic and phenolic hydroxyl groups.

Table S6.4 illustrates the substitution degrees of various hydroxyl groups in SL and CL, which were calculated following Eq. S1. When L underwent sulfoethylation, aliphatic (17.7 mol%) and phenolic

hydroxyl (28.8 mol%) groups participated in the reaction. Interestingly, CL had an even higher substitution degree, with 24.5% aliphatic–OH and 41% phenolic–OH. These changes indicate that carboxyethylation was more effective than sulfoethylation in substituting the aliphatic and phenolic hydroxyl groups of L. That carboxyethylation was perhaps more robust than sulfomethylation in altering the physicochemical characteristics of lignin. In addition, this analysis suggests that SL had more pristine aliphatic and phenolic OH than CL, which did not attend to the reaction.

Tables 6.1 and **S6.5** present the functional group composition of different samples (L, SL, and CL) based on their phenolic, aliphatic, methoxy, carboxylate, and sulfonate contents determined by ^{1}H NMR, ^{31}P NMR, and titration analyses. The results highlight notable differences in the functional group concentrations of the samples, specifically carboxylate and sulfonate groups, which are responsible for the overall charges of SL and CL samples. Phenolic content varied among the samples, with L exhibiting the highest concentration (H: 2.21 mmol/g, P: 4.04 mmol/g, T: 3.27 mmol/g), while SL and CL had lower concentrations. A similar trend is observed for aliphatic OH groups, where L had slightly higher concentrations than SL and CL. Carboxylate and sulfonate groups, which contribute significantly to the charges of SL and CL, display noticeable differences. Carboxylate content increased from L (0.3 mmol/g) to CL (1.02 mmol/g in P). Similarly, the sulfonate group content increased from L (0.6 mmol/g) to SL (1.17 mmol/g in the T), while CL's sulfonate group concentration was similar to that of L's. The presence of both sulfonate and carboxylate groups in SL and CL suggests that these functional groups were the primary contributors to their charge characteristics. The increase in these groups likely enhanced the solubility and reactivity of SL and CL, making them distinct from L

^{1}H NMR spectra of L, SL, and CL are reported in **Figure 6.1**(c). The DMSO for L and D_2O for SL and CL are assigned to the peaks at 2.5 and 4.5 ppm, respectively. The methoxy ($–OCH_3$), aromatic, and aliphatic groups are characterized by broad signal peaks within the ranges of 3.5 to 4.5 ppm, 6.0 to 7.8 ppm, and 1.0 to 3 ppm, respectively [52, 53]. In SL, the incorporation of sulfonic acid groups ($–SO_3H$) results in a shift and broadening of peaks, especially within the aliphatic region, due to the attachment of ethyl sulfonic

groups to the lignin backbone. In comparison to the L, the distinct aliphatic proton signals of SL at 2.9 and 3.3 ppm (**Figure 6.1**(c)) arose from the coupling of $CH_2CH_2SO_3H$ groups. This data provides strong evidence for the reaction between L and SBS, aligning with previous studies [54]. Similarly, in CL, the presence of carboxylic acid groups (–COOH) results in additional peaks or shifts in the 2–3 ppm range, particularly from the $–CH_2CH_2COOH$ side chains [52]. Both modifications reduced the intensity of the aromatic region and intensified signals in the aliphatic region, indicating the successful attachment of sulfoethyl and carboxyethyl groups to the lignin structure.

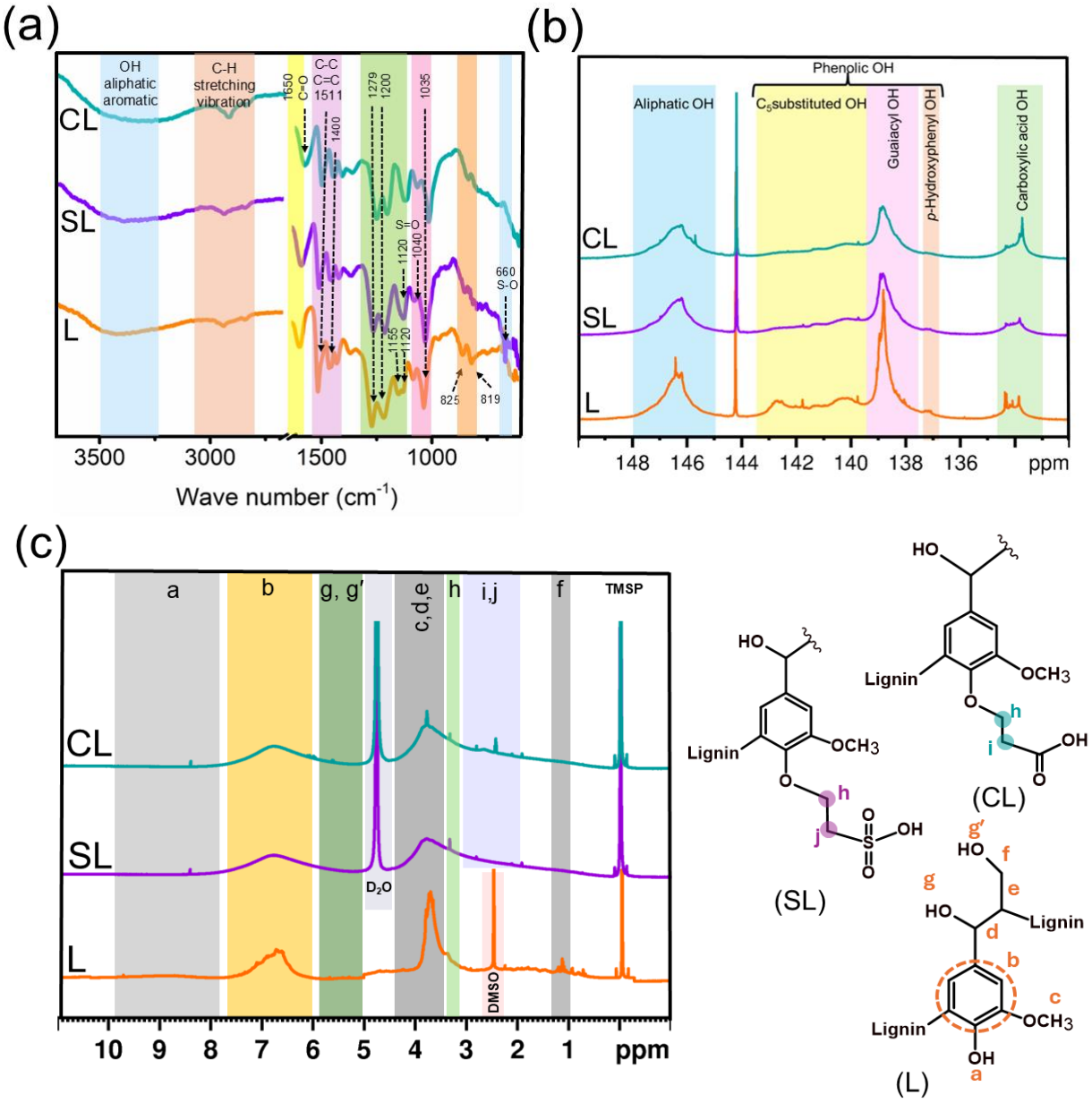

Figure 6.1. (a) FTIR spectra, (b) quantitative ^{31}P NMR, and (c) ^{1}H NMR spectra of L, SL, and CL.

Table 6.1. Structural components of L, SL, and CL with FTIR, ^{31}P NMR, and ^{1}H NMR.

Polymer	FTIR, (cm^{-1})	^{31}P NMR (ppm), OH functional group content (mmol/g)	^{1}H NMR (ppm), Functional groups/protons	Conductometric titration, OH functional group content (mmol/g)
L	Aromatic and aliphatic-OH (3400), C-H stretching and vibration (2830 and 2930), C–C (1511), C=C (1400), C–O–C stretching and vibration (1279 and 1200), C–O stretching and vibration (1155 and 1120), Aromatic C–H out-of-plane (819 and 825) [49]	Aliphatic-OH (148-145), (1.75), Phenolic-OH (144-136.5), (4.05), Carboxylic-OH (134.5-133), (0.3)	2.5 (DMSO-d6), 6.2-7.8 (aromatic), 3.5-4.5 (methoxy), 1-3 (aliphatic) [52, 53]	Phenolic (3.27), Carboxylic (0.4), Sulfonate (0.6)
SL	Aromatic and aliphatic-OH (3400), S=O symmetric and asymmetric (1120 and 1040), S–O (660) [51]	Aliphatic-OH (148-145), (1.44), Phenolic-OH (144-136.5), (2.88), Carboxylic-OH (134.5-133), (0.3)	4.7 (D_2O), 6.2-7.8 (aromatic), 3.5-4.5 (methoxy), 1-3 (aliphatic), 2.9-3.3 (coupling of $CH_2CH_2SO_3H$) [54]	Phenolic (2.28), Carboxylic (0.48), Sulfonate (1.17)
CL	Aromatic and aliphatic-OH (3400), C=O stretching (1650) [33]	Aliphatic-OH (148-145), (1.32), Phenolic-OH (144-136.5), (2.39), Carboxylic-OH (134.5-133), (0.6)	4.7 (D_2O), 6.2-7.8 (aromatic), 3.5-4.5 (methoxy), 1-3 (aliphatic), 2-3 (–CH_2CH_2COOH) [52]	Phenolic (2.31), Carboxylic (1.02), Sulfonate (0.6)

6.4.1.3. 6.4.1.3. Lignin nanoparticle formation and characterization

In this study, L, SL, and CL were completely dissolved in an aqueous solution at pH 11. Subsequently, nanoparticles were formed through acid precipitation by adding HCl to the lignin solution. To understand the stability of lignin solutions, we measured the D_h and ζ-potential of solutions at different pH levels. The results are illustrated in **Figures 6.2**(a) and (b). Moreover, the particle size distributions of SL and CL are reported in **Figures 6.2**(c) and (d), while that of L is available in **Figure S6.1**. The addition of sulfonate and carboxyl groups to L significantly increased the negative ζ-potential, enhancing the electrical double layer [55, 56, 34].

At pH 11, SL and CL reached their most negative zeta potentials due to the complete ionization of sulfonate and carboxyl groups [57]. CL's and SL's additional functional groups, compared with L, increased their negative zeta potential. This trend confirms that the introduction of functional groups, i.e., sulfonate and carboxylate, to L for producing SL and CL enhanced their charge stability, making them more resistant than L to aggregation [58]. By reducing the pH of the solutions to 3, the D_h increased significantly. In a previous study, it was reported that the pKa of the sulfonic group is 2.8±0.1 and the carboxylic group is 4.7±0.1 [34], implying that these groups would promote the agglomeration of particles at different pH values [59, 60]. However, the pKa of phenolic hydroxyl groups is around 10, and that of aliphatic OH is around 15.6 [61, 62]. Since L had a lower concentration of acidic functional groups and more concentration of phenolic OH (**Table 6.1**), its electrostatic charges were protonated more readily (i.e., ζ-potential of -5.1 mV). Thus, L had more pronounced agglomeration (**Figure 6.2**(b)) [34]. Due to the lower pKa of sulfonate groups, one may expect a more controlled lignin nanoparticle formation for SL than CL, which can happen if SL and CL have full phenolic and aliphatic OH substitution (or at least the same level of substitution). As SL had a smaller substitution degree (**Table 6.1**), it contained more proportion of pristine phenolic OH group and thus behaved more like L. As a result of the balance between the protonation of different functional groups, the D_h of SL and CL was measured to be 420 and 343 nm at pH 3 (**Figure 6.2**(c) and (d)), respectively. These results are well aligned with the TEM observations (**Figure 6.2**(e)) but also confirm that the drying process reduced the size of nanoparticles by approximately 50 nm [63]. It is also noteworthy that nanoparticles were absent in the dried samples at pH 11 and 7 (**Figure S6.2**).

The water contact angles (θ) were measured on glass surfaces coated with L, SL, and CL at different pH, and the results are presented in **Figures S6.3**, **6.3**(a), and **6.3**(b), respectively. The surfaces become more hydrophobic at lower pH values as the contact angle rises. The reason for this is because a lower pH deprotonated surface functional groups (**Figure 6.2**(b)), which lowered surface charge and increased hydrophobic interactions [64]. Water droplets are, therefore, less prone to disperse over the surface, increasing the contact angle [34, 65]. The above facts are valid if the physicochemical characteristics of lignin derivatives are not changed significantly. However, by decreasing the pH to 3, the protonation of

functional groups would disrupt the hydrogen bonding, leading to hydrophobic groups of lignin into the core of formed lignin nanoparticles, while hydrophilic regions exposing on the surface of the nanoparticles, making nanoparticles' surface more hydrophilic [29]. Therefore, nanoparticles with probably more hydrophilic surfaces would be formed. The deposition of such nanoparticles (rather than dissolved lignin) on the surface would affect the hydrophobicity and roughness of the coated surface [66–68], both of which would impact WCA.

The stability of lignin solutions, as reported by TSI values, was evaluated at three different pH levels of 3,7, and 11, and the results were reported in **Figures 6.3**(c) and (d) for SL and CL, respectively, and **Figure S6.4** for L. The results indicated that biopolymers exhibited altered degrees of stability across these pH values. The deprotonation of such groups in L at a higher pH of 11 enhanced solubility (**Table S6.4**) and electrostatic repulsion (ζ-potential of -18 mV, **Figure 6.2**(b)) between L molecules, preventing aggregation and destabilization [69]. At pH 7, the TSI was lower, indicating better stability due to the deportation of some functional groups [70]. At pH 3, the TSI of L was relatively high, reflecting instability due to the protonation of functional groups, as observed by ζ-potential and D_h changes (**Figures 6.2**(a) and (b)) [71]. Also, this study found that SL and CL exhibited enhanced stability under acidic, neutral, and alkaline conditions (with TSI <10) due to improved electrostatic repulsion (**Figure 6.2**(b)). However, CL exhibits greater stability than SL at pH 3 as it contains more substituted groups (**Table S6.4**).

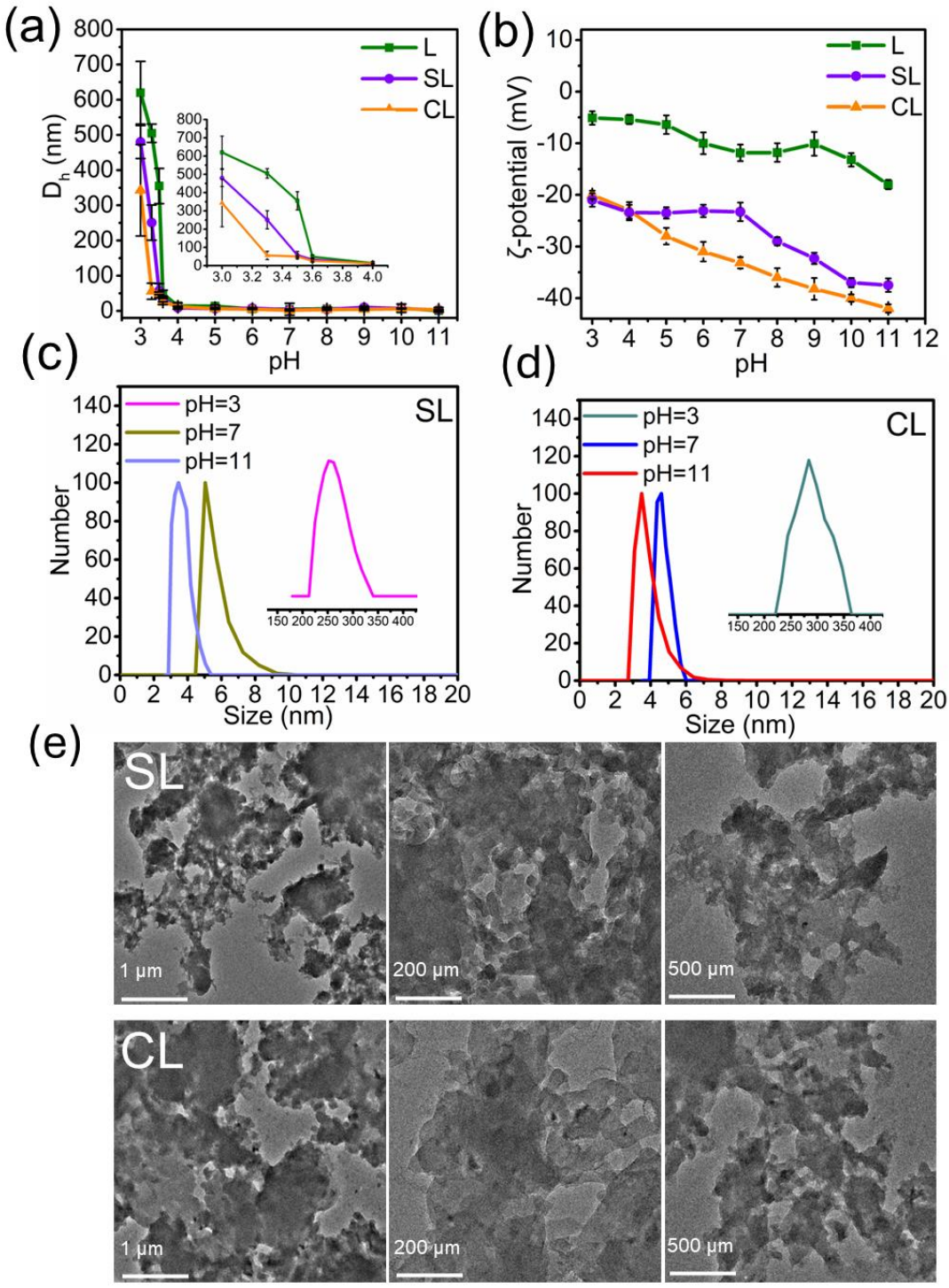

Figure 6.2. (a) D_h, (b) ζ-potential of L, SL, and CL solutions, particle distribution of (c) SL, (d) CL at pH 3, 7, and 11. (e) TEM images of SL and CL at pH 3 in a dried state (V 1μm, 200 μm, and 500 μm).

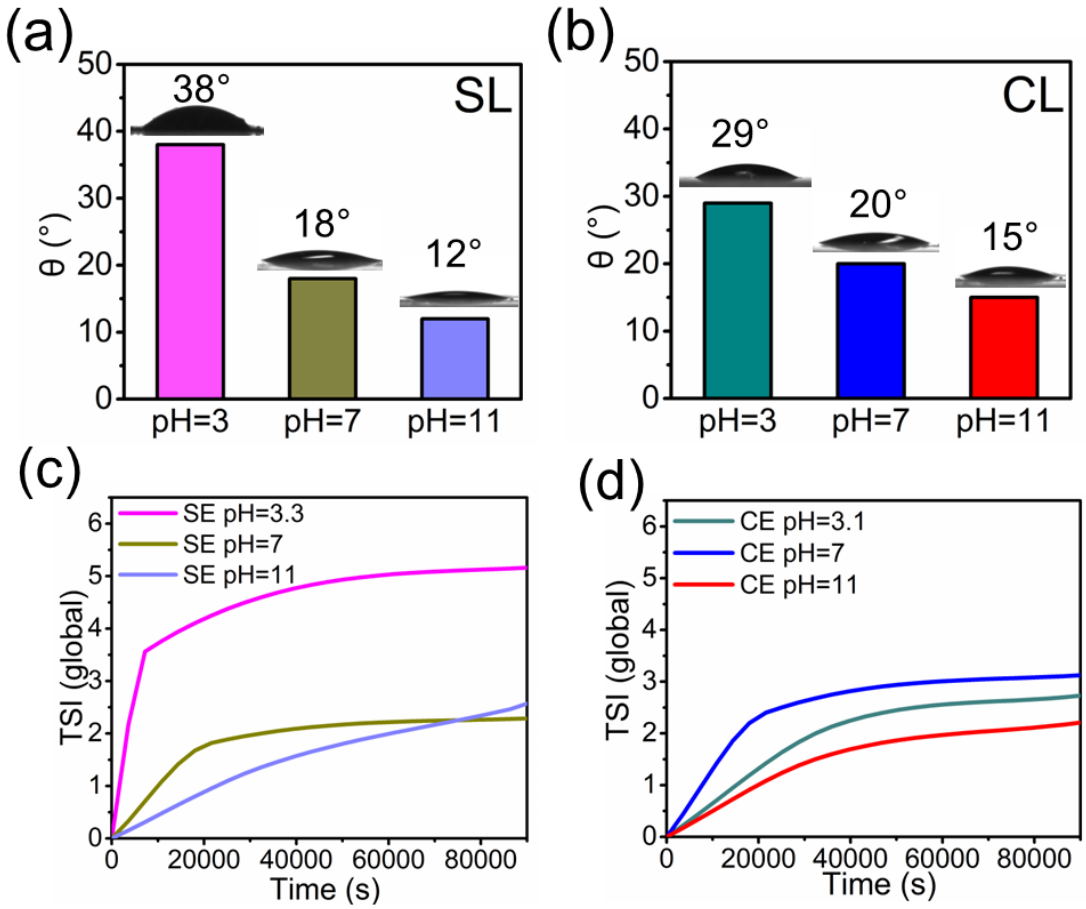

Figure 6.3. Water contact angle of (a) SL and (b) CL of coated solutions on glass. Stability analysis of (b) SL and (c) CL solutions in different pH levels.

6.4.2. Emulsion insights

When justifying emulsion stability, it's essential to verify the results of wettability along side TSI, D_h, and zeta potential. Together, these factors provide a comprehensive view of emulsion stability. The three-phase contact angle (OCA) of coated glass with L, SL, and CL at different pH is represented in **Figures S6.5, 6.4**(a) and (b), and respectively [67]. As the pH increased from 3 to 11, all water droplets had lower contact angles exhibiting greater hydrophilicity, likely due to increased ionization of lignin at the interface, which was confirmed by ζ-potential results (**Figures S6.7, 6.5**(a) and (b)). Generally, the induced conformational changes in the functional groups of polyelectrolytes would enhance solvation and ionic dissociation,

amplifying water affinity and reducing the contact angle [72–74]. The TSI results of the generated emulsion mixtures are reported in **Figures S6.6, 6.4**(c) and (d), and. At the acidic pH, the L-containing system demonstrated the lowest stability due to lower solubility (**Table S6.6**) and weaker electrostatic repulsion generated by lignin in the system (ζ-potential of -5 mV, **Figure 6.2**(b)). At a neutral pH of 7, L demonstrated more stable emulsion stability than acidic (**Figure S6.6**). As discussed earlier, L was partially soluble (Table S6) with a small hydrodynamic size (**Figure 6.2**(a)), which implies that the electrostatic repulsion, observed as the ζ of -10 mV (**Figure 6.2**(d)), was insufficient to generate a stable emulsion (TSI of 13, **Figure S6.6**) [75]. These results confirmed that, even though L was turned into nanoparticles at acidic pH and probably adsorbed on the surface oil (**Figure 6.6**), the nanoparticles did not have sufficient tendency to maintain oil particles stable in the emulsion system. As L generated nanoparticles, which were probably adsorbed on the oil surface in the oil-water mixture, the nanoparticle created steric hindrance, stabilizing the oil droplets in the system to some degree. However, the lack of sufficient surface charges promoted the disability of the system, inducing a short lifespan. At pH of 11, the deprotonation of L's functional groups made L water soluble, enhanced the ζ-potential, and eventually stabilized the emulsion system (**Figure S6.7**). In other words, even though nanoparticles were not formed at alkaline pH, L was able to generate a stable emulsion with the oil droplet D_h of about 400 nm and emulsion ζ-potential of -25.7 mV (**Figure S6.6**).

A similar pH pattern was observed for SL and CL-incorporated oil and water mixtures. However, these polymers generated a more stable emulsion than L (**Figure 6.4**(c) and (d)). The primary reason for this phenomenon was the extra repulsion force created by the additional sulfonate or carboxylate groups of these lignin derivatives (**Figure 6.2**(b)).

The emulsion was stable at pH 11, which exhibited a higher ζ-potential because of deprotonation of the charged groups and thus sufficient electrostatic repulsion (**Figure S6.7, 6.5**(a) and (b)) [55]. In addition, microscopic analysis (**Figures S6.8, 6.5**(c) and (d)) revealed smaller oil particles at pH 11 for all polymers. As stated earlier, L and SL generated larger nanoparticles than CL did (**Figure 6.2**(a)). The interaction of such nanoparticles with oil droplets generated sufficient steric hindrance to stabilize the system. Still, the

CL, with its smaller size, did not have sufficient affinity to stabilize the system in a short period, even though it had some surface charges. These results confirmed that the steric hindrance created by the deposition of nanoparticles was not as strong as electrostatic repulsion to stabilize the systems in the long run (**Figure 6.5**(e)). It should also be stated that SL behaved better than L as it generated smaller particles with more negative zeta potential, stabilizing the system better irrespective of pH. Interestingly, this analysis, alongside ζ-potential and $D_{h,}$ confirmed that SL emulsions create a more stable emulsion system.

It should also be stressed that because nanoparticle-adsorbed droplets were not stable in the emulsions at pH 3, the larger droplets with more limited surface charges were probably coalesced. As a result, only smaller droplets with more charged lignin nanoparticles (and thus with higher electrostatic repulsions) remained in the emulsions influencing the ζ-potential values of emulsions (**Figure 6.5**(a) and (b)) [76]. Thus, the slightly more negative ζ-potential at pH 3 might be attributed to those droplets with more charged lignin nanoparticles on their surfaces that remained suspended in the emulsions.

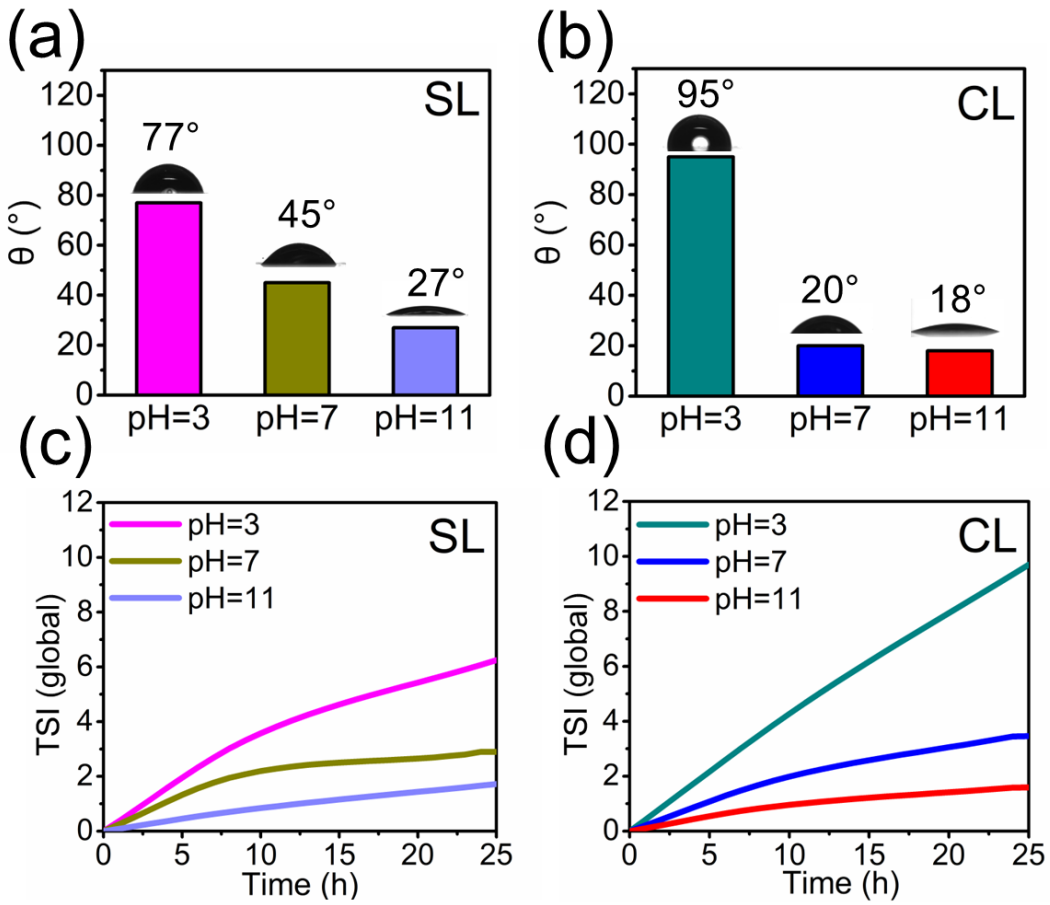

Figure 6.4. Three phase contact angles of (a) SL, (b) CL emulsions, and stability analysis of (c) SL and (d) CL emulsions in three different pH.

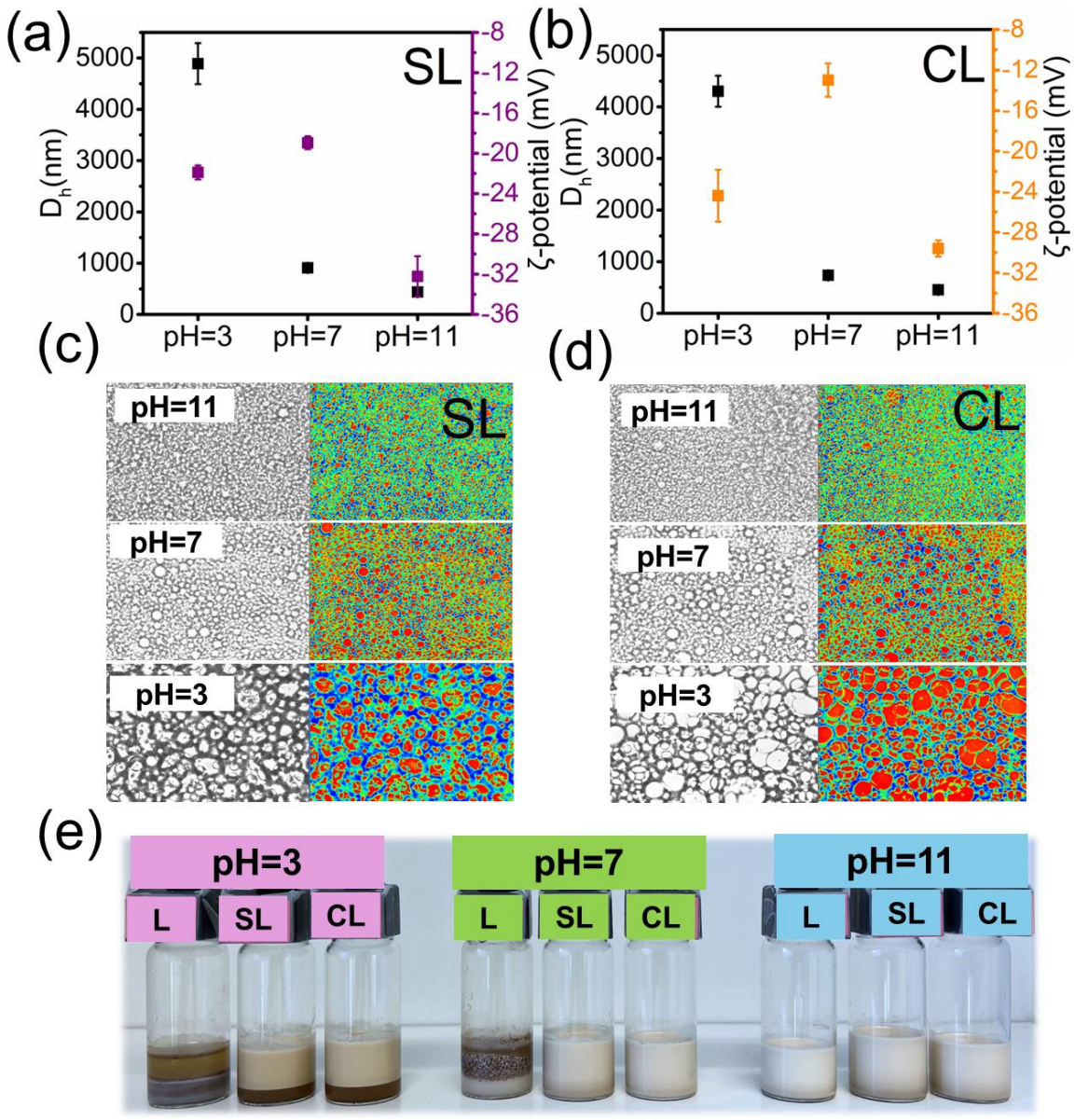

Figure 6.5. ζ-potential and D_h of (a) SL and (b) CL. Microscopic analysis of (c) SL and (d) CL emulsions. Colors represent oil (red), aqueous phase (blue), and green (polymers). (e) digital picture of emulsions after 14 days for L, SL, and CL.

As the emulsion system was more stable at alkaline pH, the emulsions were analyzed at this pH via Raman confocal spectroscopy in **Figure 6.6**. Raman spectra of L showed two spectra, one for soybean oil (yellow color) and the other for the aqueous phase (blue color) (**Figure 6.6**). In a previous study, several peaks confirmed the existence of CH_2, formation C=O band, R–C=O and C–C, and CO–O–C at 2930 cm^{-1}, 1700 cm^{-1}, 800 to 900 cm^{-1}, and 372 cm^{-1}, respectively [77]. Characteristically, Raman bands between 1050 cm^{-1} and 1150 cm^{-1} are related to C–C stretching vibrations [78]. The detection of chemical bonds of SL and CL confirmed the existence of such biopolymers on the surface of oil droplets [79]. SL formed an interfacial layer with 3D coverage of particles on the oil surface (green color shown in **Figure 6.6**). SL emulsions exhibited distinct OSO_3 and C–H bands at 1070 cm^{-1} and 2900 cm^{-1}, confirming SL's presence at the water-oil interface [80]. SL emulsions exhibited broad C=O bands, suggesting weaker interactions compared to CL oil (**Figure 6.6**). In the CL emulsion, the interaction appeared in red, representing a thin particle layer with a smaller thickness than that of SL emulsions. The Raman analysis confirmed the presence of SL and CL biopolymers at the oil-water interface, with SL forming a more structured interfacial layer. At the same time, CL exhibited weaker interactions and a thinner particle layer.

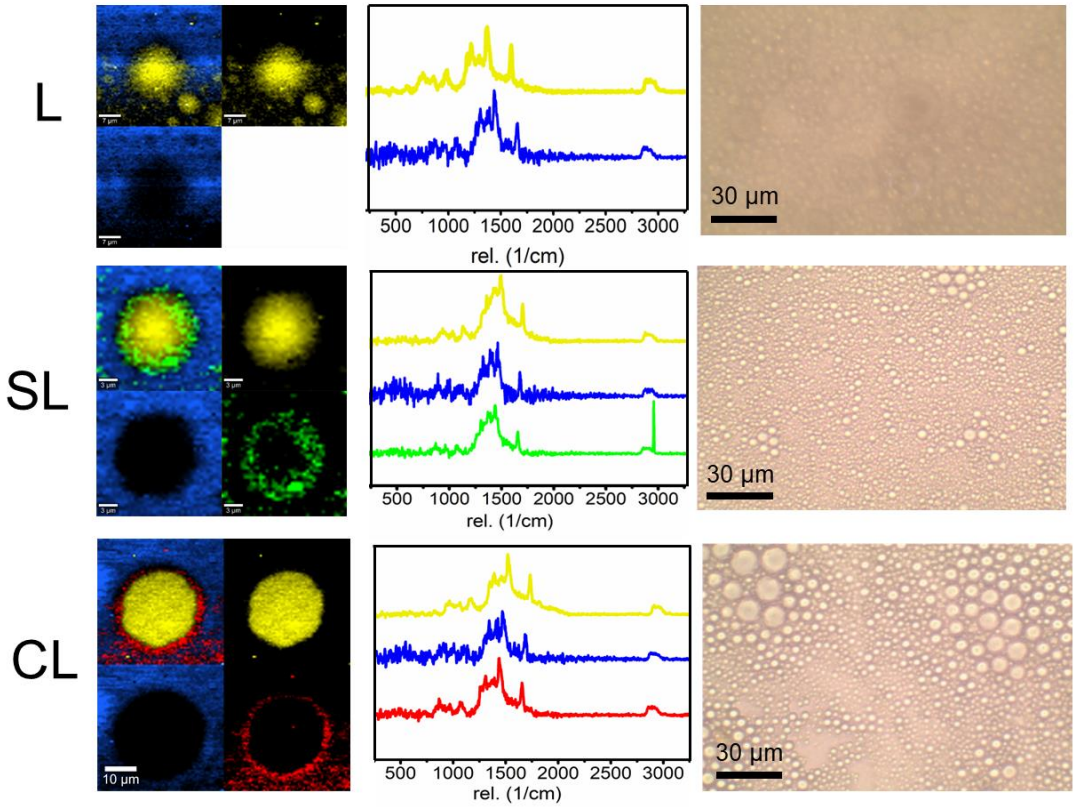

Figure 6.6. Laser scanning confocal microscopy image of the L, SL, and CL emulsions. Colors represent oil (yellow), aqueous phase (blue), green (SL), and red (CL).

6.4.3. Rheological study

The viscoelastic properties of emulsions stabilized by L, SL, and CL were assessed using steady shear viscosity measurements and frequency sweep tests. The results of these analyses are shown in **Figures S6.9**(a) and (b) for L and in **Figures 6.7**(a–c) for SL and CL. In general, all emulsions exhibited elastic characteristics, likely due to the interfacial attraction energy between droplets [81]. As depicted in the Figures, the viscosity of all emulsions decreased significantly with increasing shear rate, indicating shear-thinning behavior probably due to the alignment of emulsion droplets under shear [82]. However, L had the lowest viscosity in comparison with SL and CL, which is due to less hydrophilicity and, thus, lower interaction with water. In other words, the improved hydrophilicity of lignin elevated its interaction with

water and, thus, its viscosity for SL and CL samples. Also, structural changes from chemical modifications resulted in more extended molecular conformations (**Figure 6.1**(c)), further contributing to viscosity enhancement [83, 84 , 52].

The frequency sweep results, shown in **Figure S6.9**(b), identified two distinct regimes: a viscous or liquid-like regime, where the storage (G') < the loss (G") modulus, and an elastic or gel-like regime, where G' > G" [85]. Prior studies suggested that G' was influenced by droplet-droplet attraction strength [86]. Strong interaction between droplets could increase the G', which would lead to elastic behavior. This behavior is characteristic of systems with a more solid-like or structured nature, where strong internal networks or particle interactions are present [87]. The dispersion of SL and CL around the oil droplets supports the observed strong interactions, where G' > G" (**Figures 6.7**(c) and (d)), indicating elastic behavior and the formation of a three-dimensional network within the emulsions, which was proved by Raman confocal microscopy and microscopic microstructural analysis (**Figures 6.6**, **6.5**(c) and (d)) [88]. The comparison among samples proves that, after modification, the viscoelastic properties of modified samples were improved, especially at pH 11.

Generally, the viscosity of emulsions is the balance among solubility, electrostatic repulsion, and droplet dispersion [89]. All biopolymers, i.e., L, SL, and CL, showed higher viscosity in acidic pH, which is likely due to the agglomeration of oil droplets (**Figures S6.8**, **6.5**(c) and **6.6**(d)) and the presence of lignin nanoparticles in the system. As pH influenced the stability of the dispersed phase and the ionization state of lignin derivatives (**Figure S6.6, 6.4**(c) and (d)), it impacted the rheology and viscosity of emulsions. It created a structured network of oil droplets in Pickering systems [90].

At pH 7, the systems were least stable (**Figures 6.4**(c) and (d)) reducing electrostatic interactions and resulting in lower viscosity. Based on the above discussion, L, SL, and CL at pH 11 had a low viscosity in comparison with other pH. Higher pH would result in deprotonated lignin derivatives with high repulsion energy, which would break down oil droplet aggregates, and thus, the viscosity decreases (**Figure 6.7**(a)

and (b)). At pH 11, deprotonation increased negative charges and electrostatic repulsion, and lignin derivatives were soluble. They did not produce steric hindrance, which helped them to disperse more effectively and thus reduced viscosity [22].

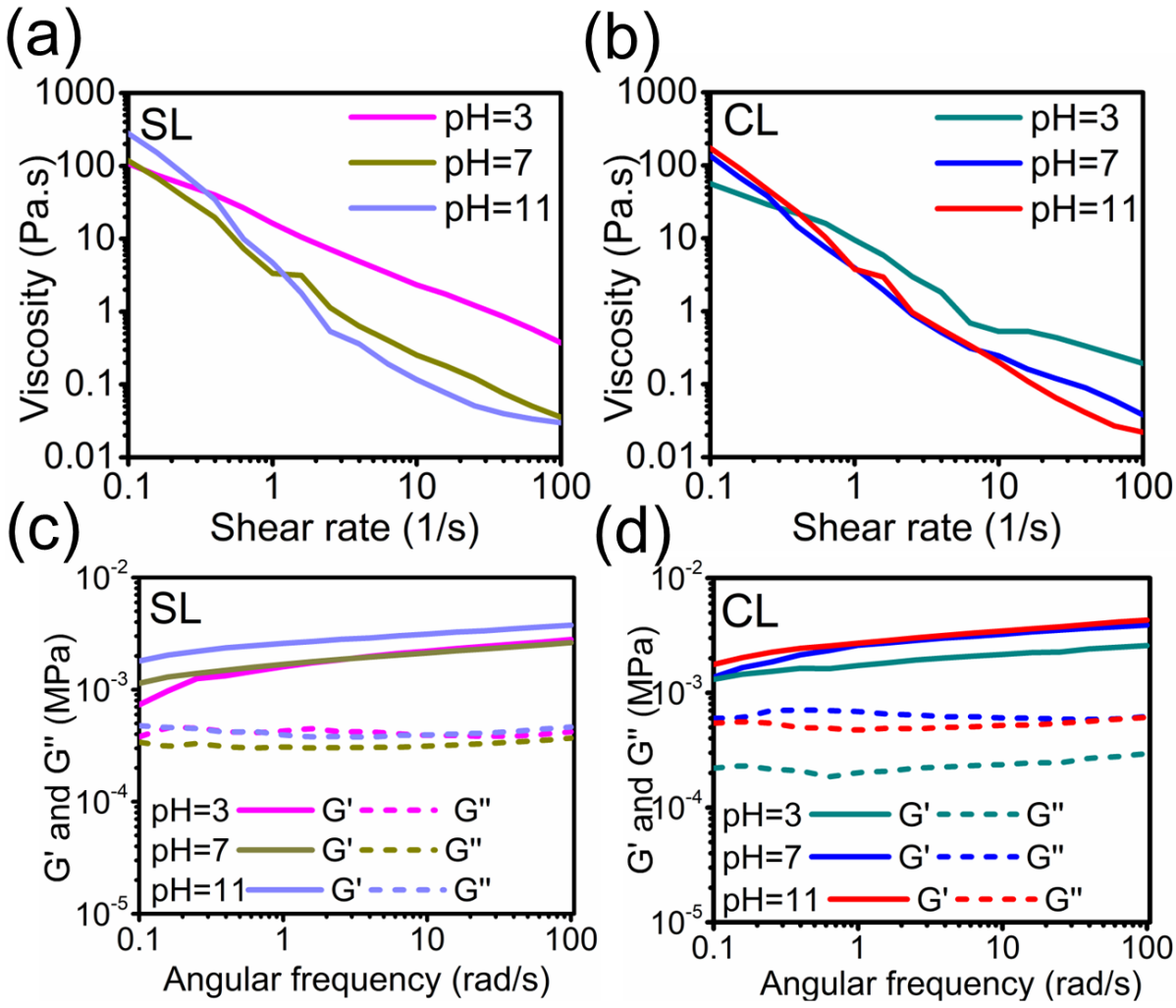

Figure 6.7. (a) SL and (b) CL viscosity as a function of shear rate, (c) SL, and (d) CL storage and loss modulus as a function of angular frequency emulsions.

6.5. Discussion

6.5.1. Physicochemical characteristics of lignin derivatives in different systems

Carboxyethylation and sulfoethylaion of L reduced the aliphatic and aromatic OH groups of L and introduced the new chemical groups of $–SO_3H$ and $–CO_2H$ to L (**Figure 6.1**(a–c)). The incorporation of such groups improved the solubility and anionic charge density of L to -1.5 mmol/g for SL and CL (**Tables S6.1** and **S6.2**). Apart from the charged group, L was less impacted via sulfomethylation than carboxyethylation (**Table S6.4**), implying that SL contained fewer numbers of charged (SO_3H) groups than CL (containing COOH groups). However, due to the high polarity of the phenolic group, it can be easily deprotonated at pH 11, resulting in an increased surface charge.

These polymers (L, SL, and CL) changed to nanoparticles with lower surface charges at acidic pH. At the same time, they stated soluble with smaller D_h and higher ζ-potential at alkaline pH (**Figure 6.2**(a) and (b)). Interestingly, by decreasing the pH to 3, the L's D_h reached 620 nm, while that of SL and CL reached 420 nm and 343 nm, respectively. The balance between the strength and number of functional groups contributed to the particle size of lignin derivatives, as lignin with more OH groups generated larger nanoparticles. Generally, the water contact angle measurements of L, SL, and CL revealed their surface becoming more hydrophobic at lower pH due to deprotonation of functional groups (Figure **S6.3**, **6.3**(a) and (b)). However, the deposition of nanoparticles (rather than dissolved lignin) with more surface hydrophilicity on the surface would impact the surface hydrophilicity and roughness, impacting WCA at pH rather surprisingly. Also, the lignin-containing solutions were more stable at pH 11 (**Figures S6.4**, **6.3**(c) and (d)) than at other pH.

Three-phase contact angle (OCA) measurements revealed increasing hydrophilicity of the systems at higher pH, while ζ-potential analysis (**Figure 6.5**(a) and (b)) exhibited increased electrostatic interactions. Emulsions were least stabile at pH 3. L and CL-containing emulsions were less stable than SL ones as L

and CL generated Pickering emulsions, and their primary driving force for emulsion stabilization was steric hindrance. At acidic pH, due to limited charge density, the L-derived nanoparticles contributed to the steric hindrance but did not have sufficient charges to create stable Pickering emulsions. As CL generated smaller nanoparticles (and probably less steric hindrance and less electrostatic repulsion as it dominantly contained COOH groups with the pKa of 4.7), it created a less stable system than SL. Apparently, SL generated nanoparticles with sufficiently small size and electrostatic repulsion that generated the most stable emulsion systems. In this case, the unmodified portion of SL contributed to the creation of steric hindrance, while the dominated sulfonate group with pKa of 2.8 created sufficient electrostatic repulsion for the deposited SL on the oil droplet to stabilize the system. Such results confirm that a combination of steric hindrance and the surface charge is important for the long-run stability of emulsion. All emulsions had a particle size ranging from 400 nm to 453 nm at pH 11 (**Figure S6.7**, **6.5**(a) and (b)). The stability, ζ-potential, particle size and Raman spectroscopy revealed that emulsions were stable at alkaline pH due to strong electrostatic repulsion in the system. Apparently, the repulsion force is an important aspect of long-term stability, even though steric hindrance can contribute to emulsion stability at lower pH. L, SL, and CL stabilized emulsions exhibiting gel-like behavior (G' > G"). As pH increased (3 to 11), it reduced D_h and enhanced interactions, forming smaller droplets and a stable network for improved stability (**Figure S6.9**(b), **6.7**(c) and (d)).

The G' was the lowest in all emulsions at pH 3, which confirms less interaction of these polymers with oil. The SL and CL emulsions showed higher viscosity at acidic pH due to the Pickering effect, which would reduce electrostatic repulsion among lignin particles, facilitating their aggregation. This aggregation can lead to the formation of a network structure within the emulsion, consequently enhancing its viscosity [91, 58]. SL at pH 11 showed greater viscoelasticity than CL, indicating stronger interactions (**Figures 6.7** (a–d) and **S6.9**).

6.5.2. 6.5.2. Emulsion stability mechanism

The mechanism stability of L, SL, and CL at different pH in the presence of soybean oil is shown in **Figure 6.8**. At pH 11, the functional groups of L, such as hydroxyl and carboxyl groups, ionized and increased their negative charge, stabilizing the emulsion. This stabilization can be via hydrogen bonding with water molecules [92]. Moreover, van der Waals interaction via intermolecular forces between aromatic rings of L and oil can contribute to the stabilization [93]. Both SL and CL have the same interactions but with higher intensity due to the protonation of sulfoethyl and carboxyethyl functional groups, respectively. However, sulfonate groups are more polar and hydrophilic in comparison with carboxyl groups, oriented towards the aqueous phase in oil-water mixtures. Their interaction with oil is primarily through hydrophobic tails, which can engage in van der Waals interactions [94]. Sulfonate groups can form conjugated systems with two double bonds, allowing π-electrons to delocalize and interact with oil droplets to stabilize emulsions [95].

At pH 7, Due to the protonation of some functional groups, which would lower their charge densities, their interaction with oil would diminish. Because the functional groups were partly protonated, their interactions were weaker. SL and CL had more functional groups than L, which would retain some charges but with more limited interaction intensity. At pH 3, the protonation of functional groups would decrease electrostatic repulsion between L, SL, and CL particles, promoting agglomeration and nanoparticle formation. Their deposition generated steric hindrance, but the lack of sufficient surface charges hampered the oil droplet stability in the emulsions. However, the SL-containing system seemed to work better than other lignin derivatives due to its larger nanoparticle size and surface charges, inducing a thicker layer with more repulsion forces in the oil droplet in the emulsion systems. Overall, modifying lignin altered its behavior in emulsion systems. Although both modifications contributed to emulsion stability, SL was more effective than CL across the pH range. This could be due to the more limited modification of OH groups but with stronger functional groups (i.e., sulfonate vs carboxylate).

Table 6.2 summarizes key findings from various studies on the stabilization of emulsions using different types of lignin and lignin-based emulsifiers. The pH levels in these studies play a crucial role in emulsion stability. For instance, softwood kraft lignin (pH 2, 7, 11) exhibited stability of oil in water emulsions with soybean oil at pH 2 and under ultrasonication, while alkali lignin showed effectiveness at pH 4 in the presence of weak polar oils. In comparison, the present work demonstrates high stability at pH 11, highlighting its strong potential in alkaline environments. In a related study, sulfoethylated lignin with a higher charge density (-2.8 mmol/g) was found to effectively stabilize xylene oil emulsions at various pH levels (3, 7, and 11) in comparison, which aligns with the findings of the present work emphasizing the impact of surface repulsion. In this work, we examined two waterborne systems to generate anionic lignin with a moderate charge density, only to make the lignin derivatives water soluble. The results suggested that the characteristics of modified lignin significantly impacted their performance at different pH levels and, ultimately, in emulsion systems. The mechanisms of emulsion stabilization would be fundamentally different at different pH. Despite the promising results, a research gap still exists in understanding how the charge density of such lignin nanoparticles may impact their performance in emulsion systems and how lignin nanoparticles would behave in different oil-water emulsion systems. As these facts are important for product fabrication, future research should focus on such systems.

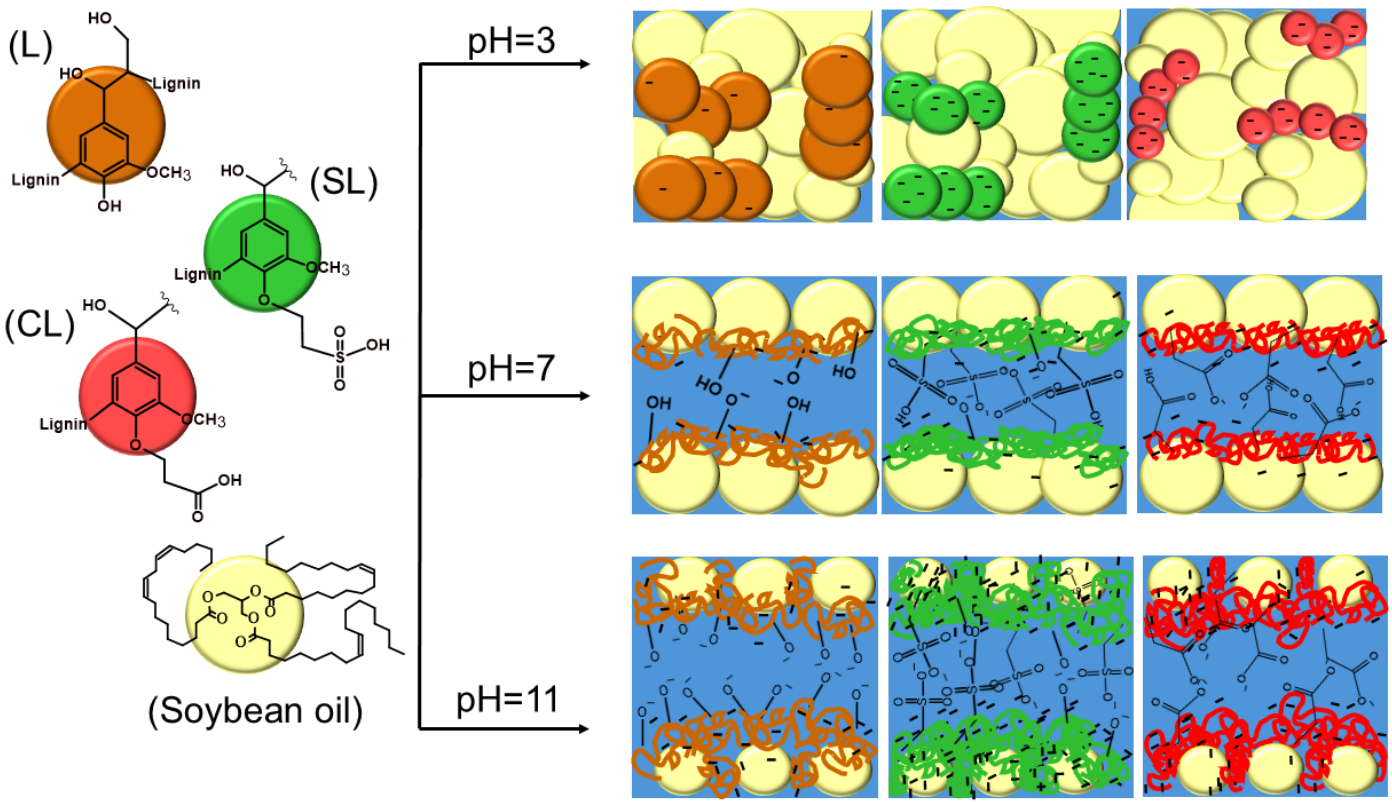

Figure 6.8. The stability mechanism of Pickering and non-Pickering systems of L, SL, and CL in soybean oil-water interface at different pH of 11, 7, and 3.

Table 6.2. Comparative available study in a literature study of different lignin and modification with different oils in emulsion preparation.

Lignin type	pH	Oil type	D_h (nm)	Dosage of lignin derivatives, (g/L)	Oil/Water ratio and type	Zeta potential (mV)	Rheology	Stability test (TSI)	Key findings	Ref
Alkali lignin	4	Cyclohexane, n-decanol	354, 125, 3547	50, 75, 100	5:5, O/W	–	–	–	effective on weak polar cyclohexane, high concentration of lignin	[96]
Softwood kraft lignin	2, 7, 11	Soybean	488, 580	5	1:1 O/W	~-45– -40	Storage > loss modulus	–	Stable in acidic pH and	[97]

									ultrasonication process	
Alkali lignin and SiO_2 nanoparticles	3, 4, 7	Soybean, n-decane, and paraffin	-	5	5:5, O/W	~ -40− 15	Storage > loss modulus	0.25− 3	Stable in the pH 3-4	[98]
lignosulfonic acid, calcium salt, and alkali lignin, whey protein	Natural pH and 7	Sunflower oil	-	0.0005; 0.005 and 0.05	1:9-, O/W	~ -14− -25	1.13– 1.49 mPa.s	12−20	At the Effective highest kraft lignin concentration	[70]
Carboxymethylated lignin	pH>4	kerosene	2500	40	5:5, O/W	~ -20 − -13	Shear-thinning flow	30 days	Stable at low pH or high salt concentration	[43]
cationic lignin (aminated)	2− 6	Toluene, olive, and silicone	259	2.5-7.5	1:1, O/W	~ -28− -20	−	−	Stable in the pH 2-6	[99]
Sulfoethylated lignin	3, 7, 11	Xlene	9 − 750±50	2.5(charge density -2.8 mmol/g)	5:5, O/W	-50 − −10	Storage > loss modulus	10−50	High stability at pH 3	[34]
alkaline and organosolv lignin	Less than 4	Olive, toluene, and silicone oil	115 to 300, and 270 to 680	0.0005	4:1, -	-25 to − -35	−	−	Lignin type affects the stability.	[100]
Solfoethylated and carboxyethylated lignin	3, 7, 11	Soybean oil	620, 420, 343	2.5	5:5, O/W and W/O	-40− -5	Storage > loss modulus	2−6	Solfoethylated lignin was effective in comparison with carboxyethylated at pH 11	This work

6.6. Conclusion

This study comprehensively analyzed the fabrication of anionic lignin derivatives with a moderate charge density and their impact on oil-water emulsion stability. At alkaline pH, L was soluble with deprotonated OH groups of aromatic and aliphatic groups, which maximized the ζ-potential of the emulsion and mimicked the emulsion's viscoelasticity and stability over 14 days. At pH 3, the protonation of L made it insoluble and nanosized, which decreased the stability and ζ-potential of the emulsion. The WCA and OCA results of L confirmed the more hydrophobic nature of L at acidic pH, facilitating its nanoparticle formation and its Pickering performance via steric hindrance development. However, The L-based system was not stable in the long run at acidic pH. Thanks to the anionic functionality of SL and CL (with a charge of -1.5 mmol/g), SL and CL exhibited stronger electrostatic interactions and superior viscoelasticity in comparison with L. Due to a strong repulsion force, these lignin polymers generated stable emulsions at pH 11. At alkaline pH, emulsions with the oil particle sizes of 436.8 and 452 with the ζ-potentials of -32 and -29 were fabricated for SL and CL-based systems via strong electrostatic repulsion, respectively. By introducing a sulfonate group for SL and a carboxylate group for CL fabrication, lignin became more water soluble and hydrophilic. However, the protonation of SL and CL at pH 3 did not neutralize all of their charges, mimicking zeta potential to -20 mV and nanoparticles with the sizes of 420 and 343 nm, respectively. Such anionically charged and nanosized particles generated partially stable oil-water emulsions (TSI< 10) via steric hindrance and some electrostatic repulsion.

This study successfully verified a hypothesis that the type of chemical modifications of L would significantly impact its properties and, thus, its interaction behavior with oil and water and, ultimately, in emulsion systems. The emulsions stabilized by SL and CL in this work behaved better than lignin-incorporated oil/water emulsion systems stated previously (**Table 6.2**) based on TSI, D_h, ζ-potentials, Microscopic, and Raman confocal microscopy data. It should be stressed that the SL had fewer but stronger functional groups of the sulfonate group than CL, which had more but weaker functional groups of

carboxylates. As a result, SL generated larger nanoparticles with stronger surface charges than CL with smaller but weaker surface charges. The deposition of these nanoparticles made SL-containing Pickering emulsions more stable than CL-incorporated Pickering emulsions at pH 3. Both systems, however, promoted emulsions at alkaline pH via electrostatic repulsions. Such systems can be used in agriculture, cosmetics, pharmaceuticals, and environmental management [101, 102, 96]. To further develop the stabilized emulsions, the effect of surface charge density of nanoparticles, the dosage of lignin nanoparticles, and altered oil-water emulsion systems should be studied in the future.

6.7. References

[1] G. Muschiolik, Multiple emulsions for food use, Curr. Opin. Colloid. Interface. Sci. 12 (2007) 213–220.

[2] T. F. Tadros, Emulsion Formation and Stability, Emulsion Formation and Stability. (2013) 1-75.

[3] R. Korać, D. Krajišnik, and J. Milić, Sensory and instrumental characterization of fast inverting oil-in-water emulsions for cosmetic application, Int. J. Cosmet. Sci.38, no. 3 (2016) 246–256.

[4] Q. Zhang, D. Hu, Y. Li, and C. Yang, Positively charged fibrous membrane for efficient surfactant stabilized emulsion separation via coalescence, J. Environ. Chem. Eng. 9 (2021) 106524.

[5] L. Cassani and A. Gomez-Zavaglia, Pickering emulsions in food and nutraceutical technology: from delivering hydrophobic compounds to cutting-edge food applications, Open Exploration. 2 (2019) 408–442.

[6] Y. Yang, Z. Fang, X. Chen, W. Zhang,Y. Xie, Y. Chen, Z. Liu, and W. Yuan, An overview of pickering emulsions: solid-particle materials, classification, morphology, and applications, Front Pharmacol. 8 (2017) 287.

[7] Z. Sun, X. Yan, Y. Xiao, L. Hu, M. Eggersdorfer, D. Chen, Z. Yang, and D.A. Weitz, Pickering emulsions stabilized by colloidal surfactants: Role of solid particles, Particuology. 64, (2022) 153–163.

[8] M. J. Scott and M. N. Jones, The biodegradation of surfactants in the environment, Biochimica et Biophysica Acta (BBA) – Biomembranes. 1508 (2000) 235–251.

[9] X. Zhao, L. Gong, G. Liao, H. Luan, Q. Chen, D. Liu, and Y. Feng, Micellar solubilization of petroleum fractions by heavy alkylbenzene sulfonate surfactant, J. Mol. Liq. 329 (2021) 115519.

[10] S. Rebello, A. K. Asok, S. Mundayoor, and M. S. Jisha, Surfactants: Toxicity, remediation and green surfactants, Environ. Chem. Lett. 12 (2014) 275–287.

[11] J. Musakhanian, J. D. Rodier, and M. Dave, Oxidative stability in lipid formulations: a review of the mechanisms, drivers, and inhibitors of oxidation, AAPS Pharm. Sci. Tech. 23 (2022) 1–30.

[12] C. Burgos-Díaz, K. A. Garrido-Miranda, D. A. Palacio, M. Chacón-Fuentes, M. Opazo-Navarrete, and M. Bustamante, Food-grade oil-in-water (o/w) pickering emulsions stabilized by agri-food byproduct particles, Colloids and Interfaces. 7 (2023) 27.

[13] F. Kelmer Müller and F. F. Costa, Innovations and stability challenges in food emulsions, Sustainable Food Technology. 3 (2025) 96–122.

[14] D. M. D. Carvalho, M. H. Lahtinen, M. Bhattarai, M. Lawoko, and K. S. Mikkonen, Active role of lignin in anchoring wood-based stabilizers to the emulsion interface, Green Chemistry. 23 (2021) 9084–9098.

[15] Q. Chen, Y. Zhao, Z. Yang, R. Guo, S. Huan, B. Wang, and G. Yang, Pickering emulsion via interfacial assembly of lignin particles and cationic surfactant: Formation of robust anchoring layer, Colloids. Surf. A. Physicochem. Eng. Asp. 701 (2024) 134893.

[16] K. S. Mikkonen, Strategies for structuring diverse emulsion systems by using wood lignocellulose-derived stabilizers, Green Chemistry. 22 (2020) 1019–1037.

[17] J. Ruwoldt, B. Handiso, M. Øksnes Dalheim, A. Solberg, S. Simon, and K. Syverud, Interfacial adsorption of oil-soluble kraft lignin and stabilization of water-in-oil emulsions," Langmuir. 40 (2024) 5409–5419.

[18] A. Yuliestyan, P. Partal, F. J. Navarro, R. Martín-Sampedro, D. Ibarra, and M. E. Eugenio, "Emulsion stabilization by cationic lignin surfactants derived from bioethanol production and kraft pulping processes, Polymers. 14 (2022) 2879.

[19] K. Gao, J. Liu, X. Li, H. Gojzewski, X. Sui, and G. J. Vancso, Lignin nanoparticles as highly efficient, recyclable emulsifiers for enhanced oil recovery, ACS Sustain. Chem. Eng. 10 (2022) 9334–9344.

[20] E. Kimiaei,M. Farooq, R. Grande, K. Meinander. and M. Österberg, Lignin nanoparticles as an interfacial modulator in tough and multi-resistant cellulose–polycaprolactone nanocomposites based on a pickering emulsions strategy, Adv. Mater. Interfaces.9 (2022) 2200988.

[21] K. Östbring, M. Matos, A. Marefati, C. Ahlström, and G. Gutiérrez, The effect of pH and storage temperature on the stability of emulsions stabilized by rapeseed proteins, Foods. 107 (2021)1657.

[22] J. E. Strassner, Effect of pH on interfacial films and stability of crude oil-water emulsions, Journal of Petroleum Technology. 20 (1968) 303–312.

[23] M. Lukić, I. Pantelić, and S. D. Savić, "Towards optimal pH of the skin and topical formulations: from the current state of the art to tailored products, Cosmetics. 8 (2021), 69.

[24] E. Guzmán, F. Ortega, and R. G. Rubio, Pickering emulsions: a novel tool for cosmetic formulators, Cosmetics. 9 (2022) 68.

[25] M.S. Hasan, M.R. Sardar, A.A. Shafin, M.S. Rahman, M. Mahmud, and M.M. Hossen, Brief review on applications of lignin, J. Chem. Rev. 5 (2023) 56–82.

[26] J. S. U. Tabaniag, M. Q. D. Abad, C. J. R. Morcelos, G. V. B. Geraldino, J. L. M. Alvarado, and E. C. R. Lopez, Stabilization of oil/water emulsions using soybean lecithin as a biobased surfactant for enhanced oil recovery, J. Eng. Appl. Sci. 70 (2023) 1–26.

[27] T. Xia, C. Xue, and Z. Wei, Physicochemical characteristics, applications and research trends of edible pickering emulsions, Trends Food. Sci. Technol. 107 (2021) 1–15.

[28] A. Plucinski and B. V. K. J. Schmidt, pH sensitive water-in-water emulsions based on the pullulan and poly(N , N -dimethylacrylamide) aqueous two-phase system, Polym. Chem. 13 (2022) 4170–4177.

[29] J. Gan, J. Fan, Y. Zhan, J. Wang, Q. Gao, C. Huang, W. Yu, and K. Zhang, Pickering multiphase materials using plant-based colloidal lignin nanoparticles, Green Chemistry. 27 (2025) 1300–1330.

[30] P. Ahmadi, A. Jahanban-Esfahlan, A. Ahmadi, M. Tabibiazar, and M. Mohammadifar, Development of ethyl cellulose-based formulations: a perspective on the novel technical methods, Food Reviews International. 38 (2022) 685–732.

[31] A. Eraghi Kazzaz, Z. Hosseinpour Feizi, and P. Fatehi, Grafting strategies for hydroxy groups of lignin for producing materials, Green Chemistry. 21 (2019) 5714–5752.

[32] N. Ghavidel and P. Fatehi, Interfacial and emulsion characteristics of oil-water systems in the presence of polymeric lignin surfactant, Langmuir. 37 (2021) 3346–3358.

[33] K. Bahrpaima and P. Fatehi, Synthesis and characterization of carboxyethylated lignosulfonate,Chem. Sus. Chem. 11 (2018) 2967–2980, Sep.

[34] N. Ghavidel and P. Fatehi, Pickering/non-pickering emulsions of nanostructured sulfonated lignin derivatives, Chem. Sus. Chem. 13 (2020) 4567–4578.

[35] Z. Shomali and P. Fatehi, Carboxyalkylated lignin nanoparticles with enhanced functionality for oil−water pickering emulsion systems, ACS. Sustain. Chem. Eng, 50 (2022)16563–16577.

[36] M. Nagy, M. Kosa, H. Theliander, and A. J. Ragauskas, Characterization of CO_2 precipitated kraft lignin to promote its utilization, Green Chemistry. 12 (2010) 31–34.

[37] A. S. Martin-Rubio, P. Sopelana, and M. D. Guillén, Assessment of soybean oil oxidative stability from rapid analysis of its minor component profile, Molecules. 25 (2020) 4860.

[38] M. F. Mendes, F. L. P. Pessoa, and A. M. C. Uller, An economic evaluation based on an experimental study of the vitamin E concentration present in deodorizer distillate of soybean oil using supercritical CO_2, J. Supercrit. Fluids.23 (2002) 257–265.

[39] S. P. Hariyatno, V. Paramita, and R. Amalia, The effect of surfactant, time and speed of stirring in the emulsification process of soybean oil in water, Journal of Vocational Studies on Applied Research. 3 (2021) 21–25.

[40] C. Su, Y. Feng, J. Ye, Y. Zhang, Z. Gao, M. Zhao, N. Yang, K. Nishinari, and Y. Fang, Effect of sodium alginate on the stability of natural soybean oil body emulsions,RSC Adv. 8 (2018) 4731–4741.

[41] J. Kim and E. Choe, Effect of the pH on the lipid oxidation and polyphenols of soybean oil-in-water emulsion with added peppermint (Mentha piperita) extract in the presence and absence of iron, Food. Sci. Biotechnol. 27 (2018) 1285–1292.

[42] S. Constant,H.L. Wienk, A.E. Frissen, P. De Peinder, R. Boelens, D.S. Van Es, R.J. Grisel, B.M. Weckhuysen, W.J. Huijgen, R.J. Gosselink, and P.C. Bruijnincx, New insights into the structure and composition of technical lignins: a comparative characterisation study, Green Chemistry. 18 (2016) 2651–2665.

[43] S. Li, J. A. Willoughby, and O. J. Rojas, Oil-in-water emulsions stabilized by carboxymethylated lignins: properties and energy prospects, Chem. Sus. Chem. 9 (2016) 2460–2469.

[44] G. Shulgaq, S. Livcha, B. Neiberte, A. Verovkins, S. Vitolina, and E. Zhilinska, “The ability of different lignins to stabilize the oil-in-water emulsion, Advanced Aspects of Engineering Research. 7 (2021) 76–85.

[45] M. K. Konduri, F. Kong, and P. Fatehi, Production of carboxymethylated lignin and its application as a dispersant, Eur. Polym. J. 70 (2015) 371–383.

[46] F. Kong, S. Wang, J. T. Price, M. K. R. Konduri, and P. Fatehi, Water soluble kraft lignin-acrylic acid copolymer: synthesis and characterization, Green Chemistry. 17 (2015) 4355–4366.

[47] G. S. Dhaliwal, N. Gupta, S. S. Kukal, and M. Kaur, Standardization of automated vario EL III CHNS analyzer for total carbon and nitrogen determination in soils, Commun. Soil. Sci. Plant. Anal. 42 (2011) 971–979.

[48] W. Gao, Z. Alkhalifa, and P. Fatehi, Generation of sulfonated kraft lignin acrylic acid polymer and its use as a flocculant, Separation Science and Technology (Philadelphia). 56 (2021) 1601–1611.

[49] S. Khodavandegar, and P. Fatehi, Phytic acid derivatized lignin as a thermally stable and flame retardant material, Green Chemistry. 26 (2024) 10070–10086.

[50] M. Fodil Cherif, D. Trache, N. Brosse, F. Benaliouche, and A. F. Tarchoun, Comparison of the physicochemical properties and thermal stability of organosolv and kraft lignins from hardwood and softwood biomass for their potential valorization, Waste Biomass Valorization. 11 (2020) 6541–6553.

[51] K. Charradi, Z. Landolsi, L. Gabriel, W. Mabrouk, A. Koschella, Z. Ahmed, A. Elnaggar, T. Heinze and S.M. Keshk, Incorporating of sulfo ethyl cellulose to augment the performance of sulfonated poly (ether ether ketone) composite for proton exchange membrane fuel cells, Journal of Solid State Electrochemistry. 27 (2-23) 3415–3423.

[52] H. A. Qulatein, W. Gao, and P. Fatehi, Carboxyalkylated lignin as a sustainable dispersant for coal water slurry, Polymers (Basel).16 (2024) 2586.

[53] S.G. Ion, T. Brudiu, A. Hanganu, F. Munteanu, M. Enache, G.M. Maria, M. Tudorache and V. Parvulescu, Biocatalytic strategy for grafting natural lignin with aniline, Molecules. 25 (2020) 4921.

[54] H. Zhang, Y. Bai, W. Zhou, and F. Chen, Color reduction of sulfonated eucalyptus kraft lignin, Int. J. Bio.l Macromol. 97 (2017) 201–208.

[55] R.A.C. Gomide, A.C.S. Oliveira, D.A.C. Rodrigues, C.R. Oliveira, O.B.G. Assis, M.V. Dias and S.V. Borges, Development and characterization of lignin microparticles for physical and antioxidant enhancement of biodegradable polymers, J. Polym. Environ. 28 (2020) 1326.

[56] M. Aldajani, N. Alipoormazandarani, and P. Fatehi, Two-step modification pathway for inducing lignin-derived dispersants and flocculants, Waste Biomass Valorization.13 (2022) 1077–1088.

[57] L.T.M. Pham, K. Deng, T.R. Northen, S.W. Singer, P.D. Adams, B.A. Simmons and K.L. Sale, Experimental and theoretical insights into the effects of pH on catalysis of bond-cleavage by the lignin peroxidase isozyme H8 from Phanerochaete chrysosporium, Biotechnol Biofuels. 14 (2021) 1–11.

[58] S. Pradyawong, R. Shrestha, P. Li, X. S. Sun, and D. Wang, Effect of pH and pH-shifting on lignin–protein interaction and properties of lignin-protein polymers, J. Polym. Environ. 30 (2022) 1908–1919.

[59] Q. Tang, Y. Qian, D. Yang, X. Qiu, Y. Qin, and M. Zhou, Lignin-based nanoparticles: a review on their preparations and applications, Polymers. 12 (2020) 2471.

[60] J.D. Zwilling, X. Jiang, F. Zambrano, R.A. Venditti, H. Jameel, O.D. Velev, O.J. Rojas and R. Gonzalez, Understanding lignin micro- and nanoparticle nucleation and growth in aqueous suspensions by solvent fractionation, Green Chemistry. 23 (2021) 1001–1012.

[61] M. Helander, H. Theliander, M. Lawoko, G. Henriksson, L. Zhang and M.E. Lindström, Fractionation of technical lignin: Molecular mass and pH effects, BioResources. 8(2) (2025) 2270-2282.

[62] D. J. dos Santos, L. B. Tavares, L. D. Antonino, R. R. de Sousa Junior, P. Homem-de-Mello, and C. R. Leão, Kraft lignin-based polyurethanes: Bulk properties, stability and adhesion to native aluminum surfaces, Polymer (Guildf). 309 (2024)127457.

[63] S. Kalliola, E. Repo, V. Srivastava, F. Zhao, J.P. Heiskanen, J.A. Sirviö, H. Liimatainen, and M. Sillanpää, Carboxymethyl chitosan and its hydrophobically modified derivative as ph-switchable emulsifiers, Langmuir. 34 (2018) 2800–2806.

[64] J. Wang, Y. Qian, L. Li, and X. Qiu, Atomic force microscopy and molecular dynamics simulations for study of lignin solution self-assembly mechanisms in organic-aqueous solvent mixtures, Chem.Sus.Chem. 13 (2020) 4420–4427.

[65] J. Mao, H. Tan, B. Yang, W. Zhang, X. Yang, Y. Zhang, and H. Zhang, , Novel hydrophobic associating polymer with good salt tolerance, Polymers. 10 (2018) 849.

[66] J. Ruwoldt, F. H. Blindheim, and G. Chinga-Carrasco, Functional surfaces, films, and coatings with lignin – a critical review, RSC Adv.13 (2023) 12529–12553.

[67] N. R. Morrow, Effects of surface roughness on contact angle with special reference to petroleum recovery, Journal of Canadian Petroleum Technology. 14 (1975) 42–53.

[68] N. Alipoormazandarani, T. Benselfelt, L. Wang, X. Wang, C. Xu, L. Wågberg, S. Willfor, andP. Fatehi, Functional lignin nanoparticles with tunable size and surface properties: fabrication, characterization, and use in layer-by-layer assembly, ACS. Appl. Mater. Interfaces. 13 (2021) 26308–26317.

[69] S.A. Mayr, R. Subagia, R. Weiss, N. Schwaiger, H.K. Weber, J. Leitner, D. Ribitsch, G.S. Nyanhongo, and G.M. Guebitz, Oxidation of various kraft lignins with a bacterial laccase enzyme, Int. J. Mol. Sci. 22 (2021) 13161.

[70] A. Czaikoski, A. Gomes, K. C. Kaufmann, R. B. Liszbinski, M. B. de Jesus, and R. L. da Cunha, Lignin derivatives stabilizing oil-in-water emulsions: Technological aspects, interfacial rheology and cytotoxicity, Ind. Crops. Prod.154 (2020) 112762.

[71] S.E. Klein, J. Rumpf, P. Kusch, R. Albach, M. Rehahn, S. Witzleben, and M. Schulze, Unmodified kraft lignin isolated at room temperature from aqueous solution for preparation of highly flexible transparent polyurethane coatings, RSC. Adv. 8 (2018) 40765–40777.

[72] H. Zhao, J. Liu, Q. Ran, Y. Yang, and X. Shu, Effect of methyl groups on conformational properties of small ionized comb-like polyelectrolytes at the atomic level, J. Mol. Model. 23 (2017) 1–9.

[73] T. Araki, Conformational changes of polyelectrolyte chains in solvent mixtures, Soft. Matter. 12 (2016) 6111.

[74] M.M. Pereira, K.A. Kurnia, F.L. Sousa, N.J. Silva, J.A. Lopes-da-Silva, J.A. Coutinho, and M.G. Freire, Contact angles and wettability of ionic liquids on polar and non-polar surfaces, Physical Chemistry Chemical Physics. 17 (2015) 31653–31661.

[75] A.P. Gasparelo, C.D. Pizzol, P.F.C. De Menezes, R.V. Knapik, M.T. Costa, M.M. Prado, and C.E.D.O. Praes, Zeta potential and particle size to predict emulsion stability, Cosmet. Toilet, 129 (2014) 34-41.

[76] V. Uskoković, Z. Castiglione, P. Cubas, L. Zhu, W. Li, and S. Habelitz, Zeta-potential and particle size analysis of human amelogenins, J. Dent. Res. 89 (2010) 149.

[77] G.F. Ghesti, J.L. Macedo, V.S. Braga, A.T. Souza, V.C. Parente, E.S. Figuerêdo, I.S. Resck, J.A. Dias, and S.C. Dias, Application of raman spectroscopy to monitor and quantify ethyl esters in soybean oil transesterification, J. Am. Oil. Chem. Soc. 83 (2006) 597–601.

[78] M.Y. Lv, X. Zhang, H.R. Ren, L. Liu, Y.M. Zhao, Z. Wang, Z.L. Wu, L.M. Liu, and H.J. Xu, A rapid method to authenticate vegetable oils through surface-enhanced Raman scattering, Scientific Reports. 6(2016) 1–7.

[79] Z. Wei, J. Cheng, and Q. Huang, Food-grade Pickering emulsions stabilized by ovotransferrin fibrils, Food Hydrocoll. 94 (2019) 592–602.

[80] A.R. Paschoal, A.P. Ayala, R.C.F. Pinto, C.W.A. Paschoal, A.A. Tanaka, J.S. Boaventura Filho, and N.M Jose, About the SDS inclusion in PDMS/TEOS ORMOSIL: a vibrational spectroscopy and confocal Raman scattering study, Journal of Raman Spectroscopy. 42 (2011) 1601–1605.

[81] X. Zhao, G. Yu, J. Li, Y. Feng, L. Zhang, Y. Peng, Y. Tang, and L. Wang, Eco-Friendly Pickering emulsion stabilized by silica nanoparticles dispersed with high-molecular-weight amphiphilic alginate derivatives, ACS. Sustain. Chem. Eng. 6 (2018) 4105–4114.

[82] M. E. Rosti and S. Takagi, Shear-thinning and shear-thickening emulsions in shear flows, Physics of Fluids. 33 (2021) 83319.

[83] J. Ruwoldt, A critical review of the physicochemical properties of lignosulfonates: chemical structure and behavior in aqueous solution, at surfaces and interfaces, Surfaces. 3 (2020) 622-648.

[84] N. Delgado, F. Ysambertt, G. Chávez, B. Bravo, D. E. García, and J. Santos, Valorization of kraft lignin of different molecular weights as surfactant agent for the oil industry, Waste Biomass Valorization. 10 (2019) 3383–3395.

[85] C. Celia, E. Trapasso, D. Cosco, D. Paolino, and M. Fresta, Turbiscan lab expert analysis of the stability of ethosomes and ultradeformable liposomes containing a bilayer fluidizing agent, Colloids. Surf. B. Biointerfaces. 72 (2009) 155–160.

[86] S. Gharehkhani, N. Ghavidel, and P. Fatehi, Kraft lignin-tannic acid as a green stabilizer for oil/water emulsion, ACS. Sustain. Chem. Eng. 7 (2019) 2370–2379.

[87] W. Liu, J. Cao, Q. Zhang, W. Wang, Y. Ye, S. Zhang, and L. Wu, Interfacial properties and structure of emulsions and foams co-stabilized by span emulsifiers of varying carbon chain lengths and egg yolk granules, Foods. 14 (2024) 35.

[88] H. W. Tan and M. Misran, Stability of concentrated olive oil-in-water emulsion, Chin. J. Chem. 26 (2008) 1963–1968.

[89] P. Kundu, V. Kumar, and I. M. Mishra, Modeling the steady-shear rheological behavior of dilute to highly concentrated oil-in-water (o/w) emulsions: Effect of temperature, oil volume fraction and anionic surfactant concentration, J. Pet. Sci. Eng. 129 (2015) 189–204.

[90] R. Pal, A simple model for the viscosity of pickering emulsions, Fluids. 3 (2018) 2.

[91] G. Hu, J. Hu, H. Chen, S. Song, and F. Chu, Influence of pH and ionic strength on the aggregation behaviors of xylan rich hemicelluloses with alkaline lignins, Bioresources. 16 (2021) 7608–7622.

[92] L. Bai, L.G. Greca, W. Xiang, J. Lehtonen, S. Huan, R.W.N. Nugroho, B.L. Tardy, and O.J. Rojas, Adsorption and assembly of cellulosic and lignin colloids at oil/water interfaces, Langmuir. 35 (2019) 571–588.

[93] Y. Bai, X. Wang, X. Wang, X. Yang, X. Li, H. Xin, D. Sun, and J. Zhou, Self-assembled/composited lignin colloids utilizing for therapy, cosmetics and emulsification, Front Chem. 10 (2022) 1107643.

[94] R. Jiang, X. Jing, L. Zhou, Z. Jiang, and X. Zhang, Molecular dynamics simulation of potassium perfluorooctanesulfonate at the oil/water interface, Struct Chem, 35 (2024) 897–906.

[95] P. Thuéry, Y. Atoini, and J. Harrowfield, The sulfonate group as a ligand: a fine balance between hydrogen bonding and metal ion coordination in uranyl ion complexes, Dalton Transactions. 48 (2019) 8756–8772.

[96] Y. Pang, Y. Luo, Z. Li, Y. Luo, H. Lou, and M. Zhou, Pickering emulsion stabilized by lignin particles: Influence of oil phase, lignin concentration, and particle size, Colloid. Polym. Sci. 302 (2024) 901–909.

[97] J. Tian, J. Chen, J. Guo, W. Zhu, M.R. Khan, Q. Fu, Y. Jin, H. Xiao, J. Song, and O.J. Rojas, Pickering emulsions produced with kraft lignin colloids destabilized by in situ pH shift: Effect of emulsification energy input and stabilization mechanism, Colloids. Surf. A. Physicochem. Eng. Asp. 670 (2023) 131503.

[98] S. Lu, D. Yang, M. Wang, M. Yan, Y. Qian, D. Zheng, and X. Qiu, Pickering emulsions synergistic-stabilized by amphoteric lignin and SiO_2 nanoparticles: Stability and pH-responsive mechanism, Colloids. Surf. A. Physicochem. Eng. Asp. 585 (2020) 124158.

[99] M. H. Sipponen, M. Smyth, T. Leskinen, L. S. Johansson, and M. Österberg, All-lignin approach to prepare cationic colloidal lignin particles: stabilization of durable Pickering emulsions, Green Chemistry. 19 (2017) 5831–5840.

[100] M. R. V. Bertolo et al., Lignins from sugarcane bagasse: Renewable source of nanoparticles as Pickering emulsions stabilizers for bioactive compounds encapsulation, Ind. Crops. Prod.140 (2019) 111591.

[101] J. Tomasich, S. Beisl, and M. Harasek, Production and characterisation of pickering emulsions stabilised by colloidal lignin particles produced from various bulk lignins, Sustainability. 15 (2023) 3693.

[102] M.B. Agustin, N. Nematollahi, M. Bhattarai, E. Oliaei, M. Lehtonen, O.J. Rojas, and K.S. Mikkonen, Lignin nanoparticles as co-stabilizers and modifiers of nanocellulose-based Pickering emulsions and foams, Cellulose. 30 (2023) 8955–8971.

7. Conclusion and Future Perspectives

7.1. Highlights of this Thesis

A sustainable, bio-based flame retardant was developed by phosphorylating kraft lignin with phytic acid through polycondensation in an aqueous system. The reaction conditions were optimized to achieve high phosphorus content, enhanced solubility, and improved thermal stability. The strong flame retardant properties of lignin result from the replacing of its phenolic and aliphatic hydroxyl groups with flame retardant P–O–C linkages. Thermal analysis (TGA and DSC) confirmed increased char formation and greater thermal resistance. The addition of phosphorylated lignin solution to wood coating increased the LOI of wood from 21.8% to 26.0% and decreased smoke density rate from 34.0% to 17.7%. The combustion completion showed a change in sample morphology and an increase in phosphorus intensity at 800 °C. This phosphorylated lignin can be used as a flame retardant with outstanding performance for coating

applications. Moreover, the development of fully bio-based flame retardant phosphorylated lignin chitosan-based aerogels was conducted. Phosphorylated kraft lignin boosted porosity and mechanical properties through chemical and physical bonds while phosphorylation improved thermal stability and fire resistance. The aerogels with optimized properties demonstrated both a well-organized 3D network structure and outstanding compressive strength along with exceptional flame resistance which earned a V-0 rating and a limiting oxygen index of 33%. This study presents an environmentally friendly manufacturing method for producing high-performance bio-based aerogels suitable for thermal insulation and fire protection, which can be used in industrial applications. Functionalized lignin's charge density affects porosity structure because crosslinking degrees vary as shown through studies on carboxymethylated lignin chitosan aerogels. Analysis showed that O=C–N bond formation demonstrated chemical crosslinking success and optimization determined that a charge density of 1 mmol/g together with a 2 wt.% concentration produced optimal properties. Higher charge densities resulted in lower porosity and increased elasticity, whereas carboxymethylation improved lignin's compression strength and decreased its heat conductivity. Using silane-based coatings to boost material durability can help overcome the problem of increasing water absorption. Aerogels made of carboxymethylated lignin and chitosan offer an environmentally friendly insulating option that strikes a compromise between thermal efficiency and mechanical robustness.

The effects of sulfoethylation, carboxyethylation, and anionic lignin alterations on the stability of oil-water emulsions were examined, and the contribution of pH and charge density to stabilizing performance was examined. Strong electrostatic repulsion was demonstrated by sulfonated (SL) and carboxylated (CL) lignin derivatives at alkaline pH, improving emulsion stability with smaller oil particle sizes and greater ζ-potentials. On the other hand, protonation decreased solubility and encouraged the production of nanoparticles at acidic pH, stabilizing emulsions through steric hindrance. SL produced larger, more stable nanoparticles than CL, which had smaller particles and weaker carboxylate functions, because SL had fewer but stronger sulfonate groups. Both methods demonstrated efficacy in stabilizing emulsions for possible

uses in environmental management, medicines, cosmetics, and agriculture. In conclusion, we have developed effective and high-performing synthesis techniques to incorporate lignin, a biopolymer, into coating, aerogels, flame retardant and thermal insulation composites.

7.2. Future perspectives

The solvent-free phosphorylation process offers a viable way to incorporate lignin into fire-resistant coatings and composite materials for phosphorylated lignin-based flame retardants. Future studies could concentrate on expanding this procedure for industrial use, especially in thermally stable biopolymer composites and environmentally acceptable wood treatments. Additionally, exploring the long-term durability, UV resistance, and weathering effects on phosphorylated lignin coatings would be essential for practical implementation. Phosphorylated lignin has demonstrated significant promise for thermal insulation and fire prevention when included into chitosan-based bio-based aerogels. To further improve their mechanical and thermal properties, future research might investigate different crosslinking techniques and hybrid aerogels that incorporate additional biopolymers or nanomaterials. To increase the long-term durability of these aerogels in humid conditions, the use of hydrophobic coatings to lessen water absorption issues should also be looked at.

In terms of lignin-based emulsifiers, the functionalization of lignin through sulfoethylation and carboxyethylation has demonstrated strong potential for stabilizing oil-water emulsions. Future research could focus on optimizing lignin different range of charge density, functional groups, and molecular weight to tailor emulsion properties for specific industrial applications, such as cosmetics, pharmaceuticals, and sustainable agrochemical formulations. Additionally, the potential of lignin nanoparticles in Pickering emulsions for long-term stability and controlled release systems should be explored for broader commercial applications.

Appendix 3A: Supporting information: Phytic acid derivatized lignin as thermally stable and flame retardant material

Saba Khodavandegar, [a] *Pedram Fatehi* *[a,b]

Published in Green Chem., 2024, 26, 10070, 17 July 2024, https://doi.org/ 10.1039/d4gc03169e

[a] Biorefining Research Institute, Lakehead University, 955 Oliver Road, Thunder Bay, Ontario, P7B 5E1, Canada.

[b] Laboratory of Natural Materials Technology, Åbo Akademi University, Henrikinkatu 2, Turku FI-20500, Finland

First author, email: skhodava@lakeheadu.ca, address: 955 Oliver Road, Thunder Bay, ON, Canada, P7B 5E1

Corresponding author, email: pfatehi@lakeheadu.ca, address: 955 Oliver Road, Thunder Bay, ON, Canada, P7B 5E1

Material

Softwood kraft lignin (KL) was obtained from FPInnovations and produced via Lignoforce technology. Phytic acid sodium salt hydrate, $C_6H_{18}O_{24}P_6$, (PHA), sodium hydroxide (NaOH) (≥97 %), sulfuric acid (H_2SO_4) (≥98 %), deuterium oxide (D_2O-d_6) (99.9 %), dimethyl sulfoxide-d_6 (DMSO-d_6) (99.8 %), 3-(trimethylsilyl)propionic-2,2,3,3-d4 acid sodium salt tetramethylsilane (TMSP) (≥98.5 %), cyclohexanol (99 %), 3- 2-chloro-4,4,5,5-tetramethyl-1,3,2-dioxaphospholane (CDP) (95 %), chromium(III) acetylacetonate (97 %), sodium azide (NaN_3) (≥99.5 %), poly (diallyl dimethylammonium chloride) (PDADMAC) (100–200 kg/mol), nitric acid (HNO_3), and hydrochloric acid (HCl) (37 %) were all purchased from Millipore Sigma, Oakville, Canada. Filter paper with porosity of Coarse, fast flow rate, with 15 cm diameter was purchased from Fisher. PLA Nature Works® 3100HP, was obtained from Nature Works Corporation (USA). The 1000 g/mol cut-off dialysis membrane made of cellulose acetate was purchased from Spectrum Labs. Pinewood (untreated, ALEXANDRIA, made in Canada) was purchased from Canadian Tire Inc, Canada, Thunder Bay store, with two different sizes and barcodes and used for different analyses, i.e., 00010-3196C for limiting oxygen index analysis and 00015-30096C for smoke density analysis.

Charge density, solubility, elemental analysis, and molecular weight measurements

To assess the charge density, PK samples with 1 wt.% concentration was stirred at 200 rpm for 24 h at 25°C. Then, the prepared suspensions were centrifuged at 1000 rpm for 5 min to separate soluble and insoluble parts. Afterward, 1 mL of the soluble portion of the samples was titrated against 0.005 mol/L PDADMAC solution to determine the charge density of the samples. Solubility analysis was conducted by adding 0.2 g of lignin derivatives to 19.8 mL of deionized water. The suspensions were shaken in a water bath (Innova 3100, Brunswick Scientific, Edison, NJ, USA) for 12 h at 200 rpm and 25°C. Organic elemental analysis was conducted for samples that were oven-dried at 60°C for 24 h, and then 0.02 g of them were transferred into the carousel chamber of the elemental analyzer. The sample's carbon, hydrogen, sulfur, and nitrogen contents were assessed by combusting the samples at 1200°C and analyzing the generated gases. Molecular weight measurement was investigated for samples that was prepared by dissolving 50 mg of sample in 10 mL of 0.1 M NaN_3 for anionic samples. The prepared solutions were filtered using a 0.2 μm filter and analyzed following a standard method.[53] The temperature of the column and detector were set at 35°C, and a flow rate of 0.7 mL/min was maintained. An RI detector used 70 μL of each sample for analysis in this test.

^{1}H, HSQC, HMBC, and ^{31}P NMR analyses

^{1}H, HSQC, and ^{1}H-^{31}P HMBC NMR samples were prepared by dissolving approximately 75-85 mg of KL in 1 mL of DMSO-d_6 and PK17 (i.e., the PK produced under the optimized conditions) in D_2O-d_6 and stirred at 200 rpm for 24 hours, and then 5-6 mg of TMSP was added to the sample as the internal standard. Adjustments for ^{1}H NMR were set to a total of 16 scans per sample, a 3.28 s acquisition time, with a 30° pulse, and 1.00 s of relaxation delay time. The ^{1}H-^{13}C HSQC assessment was performed under the conditions of a 90° pulse width of 48.17 μs, a relaxation delay of 1.5 s, an acquisition time of 0.15 s, and 16 scans.

^{1}H-^{31}P HMBC were performed under the conditions of a relaxation delay of 7 s, a 90° pulse width of 13.5 μs, 16 scans, an acquisition time of 0.36 s, and 25°C. In this analysis, 75-85 mg of PK17, as the optimized sample, was dissolved in D_2O-d_6 and stirred at 200 rpm for 24 hours. The Top Spin 4.0.9 software was used to process NMR data points and spectra (2020 Bruker BioSpin GmbH).

^{31}P NMR spectroscopic samples were prepared with dissolving 70 mg of the samples in 1 mL of pyridine/$CDCL_3$ (1.6:1) mixture, then 200 μL of 2-chloro-4,4,5,5-tetramethyl-1,3,2-dioxaphospholane was added to the mixture as the phosphorylation reagent in the presence of 70 μL of cyclohexanol as the internal standard. The quantitative data of ^{31}P NMR was collected at a pulse angle of 90°, room temperature, 0.65 acquisition time, and 25 s pulse delay with spectral parameters of a decoupling pulse sequence. The spectra were obtained using a nuclear magnetic resonance spectroscopy (AVANCE NEO-1.2 GHz, Bruker Corporation, USA) with 1024 scans per sample at 25°C, a 0.6 s acquisition time, a 90° pulse, and 5 s relaxation delay time. Qualitative ^{31}P NMR was conducted by dissolving 80 mg of KL in DMSO-d_6 and PK in D_2O-d_6. The spectra were collected at room temperature, with 256 scans, 0.72 s acquisition time, a 2 s pulse delay, a 30° pulse width, and a relaxation time of 2 s with spectral parameters of a decoupling pulse sequence.

FTIR analysis

FTIR analysis was conducted with the 50 mg powder sample which previously was dried at 60°C. Samples were analyzed at the resolution of 4 cm^{-1} with spectral width ranging between 4000 to 500 cm^{-1} and 32 scans in an adsorbent mode.

ICP-AES and XPS analyses

Phosphorous content of samples was measured with ICP-AES by digesting 500 mg of sample from a homogenous and grind solid in nitric and hydrochloric acids at 180±5°C with a CEM Mars Xpress microwave oven using I-CHEM glass vessels. Once the digestion was complete, the samples were diluted to 40 mL according to EPA Method 3051A. The ICP-AES Varian (Agilent) Vista Pro Radial CETAC ASX-

510 analysed the digested samples. The surface chemical composition was analysed by Xray Photoelectron Spectroscopy (XPS) with a monochromatic Al Kα X-ray source (1486.7 eV) operating at 15 kV (90 W) in a FAT mode (fixed analyser transmission) when 10 mg of a dried sample was tested at 60°C. The energy pass amount was 40 eV for the ROI region and 80 eV for the Survey region. A voltage of 284.6 eV was used to calibrate the C 1s binding energy (Note: carbon tape graph was deleted from raw data). Full-spectrum, narrow high-energy resolution spectra, elemental composition, and functional groups were assessed using ESCape software for fitting graphs, elemental composition, functional groups binding energy, and mass concentration of bonds.

Thermal analysis

Thermogravimetric analysis (TGA) was investigated with samples that were dried in a 60°C oven for 24 hours. Then, 78 mg of the samples were analyzed under a nitrogen gas atmosphere in a thermal analyzer (TGA i1000, Instrument Specialists Inc.) with a gas flow rate of 20–30 psi and 15 mL/min in the temperature range of 25-800°C at the rate of 10°C/min. In another set of experiments, the samples were collected from the TGA instrument when heated in different temperatures of 220°C, 320°C, 600°C, and 800°C for their elemental analysis by XPS. Differential scanning calorimetry (DSC) analysis was carried out with placing 10 to 12 mg of dried samples in hermetic Tzero® aluminum pans. It loaded to a differential scanning calorimeter (DSC Q2000, TA Instruments, DE, USA) with a nitrogen gas flow rate of 50°C/min. This experiment was performed in two heating and one cooling cycles. In the first cycle, to erase the thermal history, the temperature was raised from 20°C to 230°C, then cooled from 230°C to 20°C at 5.0°C/min. In the second cycle, a heating cycle was performed from 20°C to 230°C at 10.0°C/min for the T_g determination. This analysis was conducted twice; the standard deviations and average values were reported.

Flame retardant analysis

The fire resistance behavior of coated wood samples was measured by the limiting oxygen index (LOI) with the sample size of (140mm×20mm×10mm) at room temperature and samples were marked 50 mm

from the wood top to the bottom. Coated samples were placed in a vertical glass column of the instrument with a flow rate of 40 mm/s of oxygen and nitrogen gas. The length of the flame was adjusted to 20 mm. The minimum amount of oxygen needed to ignite the sample was recorded as an LOI. Smoke density analysis in this analysis, the propane gas pressure was adjusted to 42 psi. The coated sample with the dimension of (4.5 mm × 4.5 mm × 1 mm) was placed on the square metal screen for burning, and the propane burner exposed the sample. The smoke density apparatus software was used for analysis, and data was collected based on the smoke density rate and light adsorption percentage.

Table S3.1. The effect of different parameters on reaction

Sample ID	Ratio KL/PHA (mol: mol)	Time (min)	Temperature (°C)	Solvent	pH adjustment strategy [a]	Solubility (%)	Charge density (mmol/g)
PK1	1:0.02	240	80	DI Water	1	97	-1.8
PK2	1:0.06	240	80	DI Water	1	93	-2.3
PK3	1:0.16	240	80	DI Water	1	94	-2.9
PK4	1:0.2	240	80	DI Water	1	98	-2.8
PK5	1:0.3	240	80	DI Water	1	97	-3.1
PK6	1:0.4	240	80	DI Water	1	72	-4.3
PK7	1:0.4	240	80	DI Water	2	97	-4
PK8	1:0.4	240	80	Urea	2	97	-3.8
PK9	1:0.4	240	100	Urea	2	98	-4
PK10	1:0.4	240	120	Urea	2	98	-3.9
PK11	1:0.4	20	80	DI Water	2	97	-4.2
PK12	1:0.4	40	80	DI Water	2	97	-3.8
PK13	1:0.4	60	80	DI Water	2	95	-3.5
PK14	1:0.4	120	80	DI Water	2	98	-3.4

PK15	1:0.4	180	80	DI Water	2	98	-3.7
PK16	1:0.4	240	80	DI Water	2	97	-4
PK17	1:0.4	20	20	DI Water	2	97	-4.2
PK18	1:0.4	20	40	DI Water	2	93	-4
PK19	1:0.4	20	60	DI Water	2	96	-4
CK		240	80	DI Water	2	93	-0.8

[a] the strategies explained in section: (1) after adding the reagent, the reaction was exploited without pH adjustment, and the samples were neutralized and dialyzed after the reaction; (2) after adding the reagent, the pH of the reaction was adjusted to 11 and the reaction ran at pH 11. Afterward, the reaction medium was neutralized and dialyzed.

Table 3.2. Elemental analysis of CHNS, ICP-AES, and XPS.

Sample ID	CHNS				ICP-AES	XPS	M_w	M_n
	C (%)	H (%)	N (%)	S (%)	P (%)	P (%)	(g/mol)	(g/mol)
PK1	54.64	6.49	0	1.17	0.8	0.8	3900	2543
PK2	52.11	5.59	0	1.15	1.3	1.7	4380	3779
PK3	48.25	5.92	0	1.07	3.3	4	4561	4194
PK4	47	5.92	0	1.02	3.7	3	4577	4161
PK5	45.46	5.44	0	0.93	4.2	4.4	4528	4139
PK6	43.21	4.99	0	0.84	4.3	4.2	4560	4233
PK7	44.42	5.6	0	0.01	7	–	4668	4412
PK8	44.27	5.6	0	0.01	7	–	4747	4482
PK9	51.07	6.81	0	0.01	7	–	4778	4641

PK10	49.44	6.35	0	0.01	6	–	4781	4642
PK11	39.23	5.22	0	0.72	7.2	–	4671	4383
PK12	41.47	5.37	0	0.82	7.1	–	4659	4378
PK13	41.47	5.65	0	0.83	6.7	–	4664	4382
PK14	43.15	5.74	0	0.84	6.2	–	4670	4429
PK15	40.31	5.56	0	0.76	6.7	–	4652	4240
PK16	42.63	5.69	0	0.82	7.4	–	4668	4412
PK17	40.29	5.66	0	0.84	7.2	7	4800	4624
PK18	41.16	5.66	0	0.86	7.1	–	4784	4589
PK19	41.27	5.63	0	0.84	7.6	–	4811	4640
CK	60.53	6.64	0	1.3	<2	0	3268	1690
KL	62.71	6.82	0	1.6	0	0	-	-

Table S3.2.

Table S3.3. The assignments of the $^{13}C–^{1}H$ cross signals obtained from HSQC NMR spectra.

Label	δC /δH (ppm)	Assignment
OCH_3	57.3/3.7	C-H in -OCH_3 (methoxy)
B_β	55/3.2	C $_\beta$-H_β phenyl coumarane units
C_β	55.2/3	C_β-H_β in resinol units
A_γ	62/3.4	C_γ-H_γ in β-O-4′ linkage
C_γ	64/3.7	C_γ-H_γ in phenyl coumarane
P_γ	63.3/4.1	C_γ-H_γ in p-hydroxycinnamyl alcohol end groups
B_γ	72.7/3.7-4.1	C_γ-H_γ in resinol units
A_α	72.8/4.7	C_α-H_α in β-O-4′ linkage
A_β	85.6/4.3	C_β–H_β in β-O-4 linked to G units
B_α	86.9/4.6	C_α-H_α in resinol units
C_α	88.6/5.5	C_α-H_α in phenylcoumaran substructures
G_2	111/6.9	C_2-H_2 in guaiacyl units
G'_2	112.5/7. 5	C_2-H_2 in oxidized (C_α=O) guaiacyl units
G_5	116/6.6	C_5-H_5 in guaiacyl units
G_6	121.5/6.7	C_6-H_6 in guaiacyl units
G'_6	124.6/7.4	C_6-H_6 in oxidized (C_α=O) guaiacyl units
D_β	128.6/6.8	C_β-H_β in cinnamaldehyde end groups
$H_{2,6}$	127.7/7.2	$C_{2,6}$-$H_{2,6}$ in p-hydroxybenzoate units

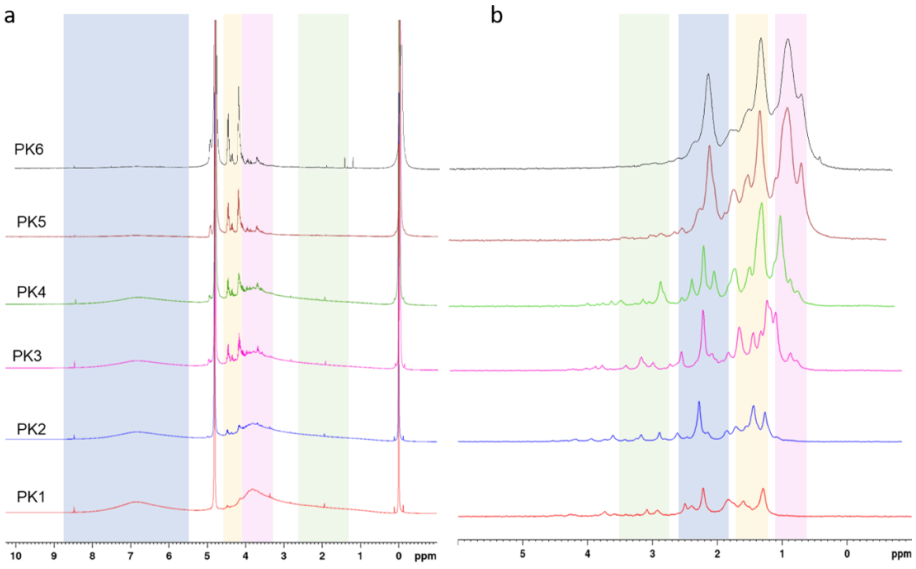

Figure S3.1. ^{1}H NMR spectra for PK samples (a) and ^{31}P NMR spectra for PK samples to study the effect of molar ratio (b).

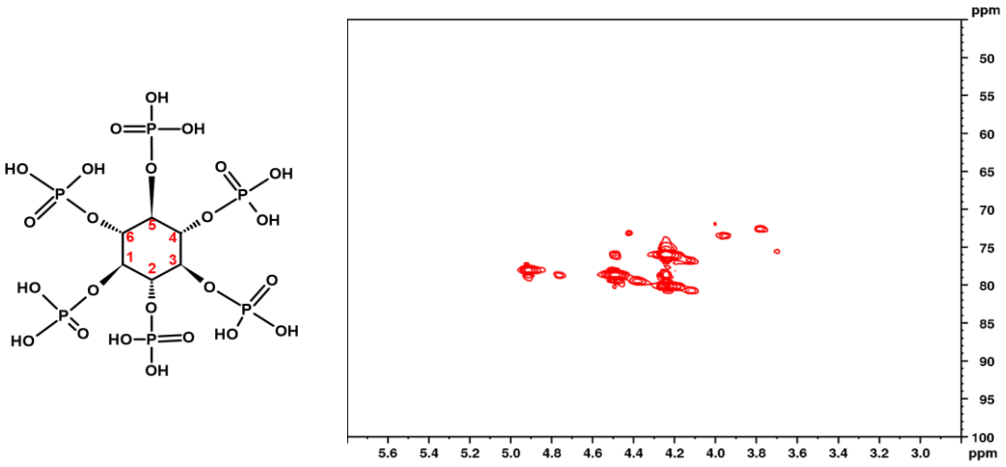

Figure S3.2. HSQC of Phytic acid.

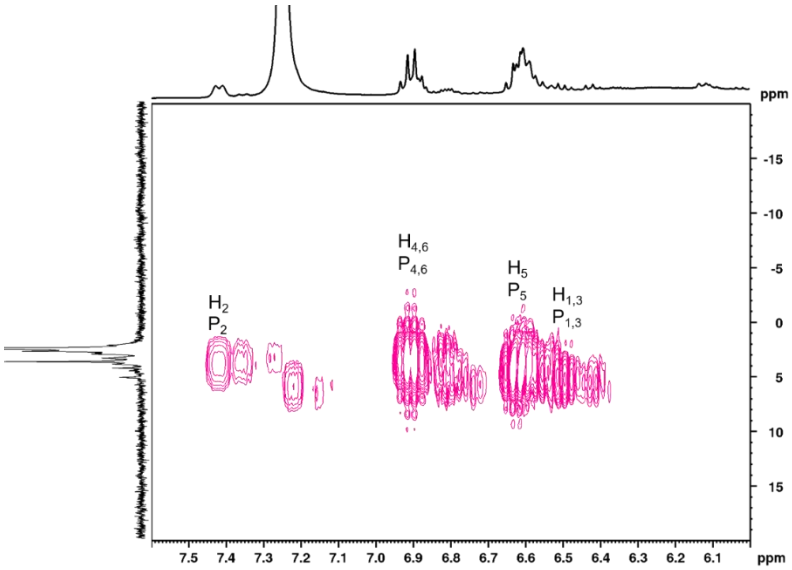

Figure S3.3. ^{1}H-^{31}P HMBC spectra of the PK18 in D_2O.

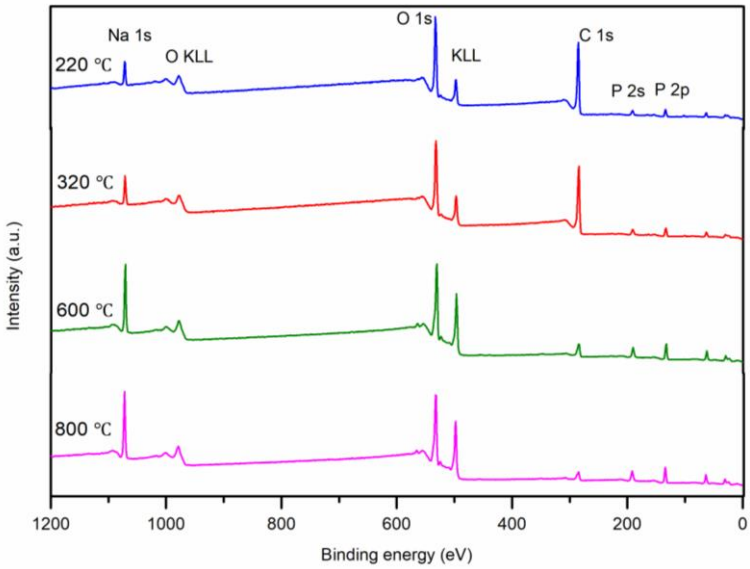

Figure S3.4. XPS wide spectra of PK17 after burning in different temperatures.

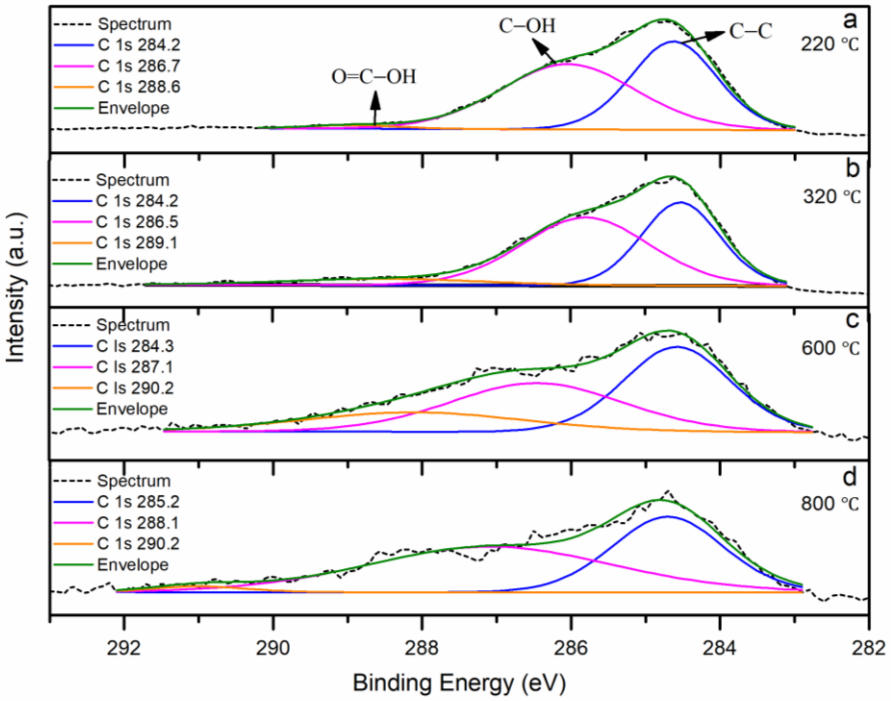

Figure S3.5. XPS spectra of C 1s for PK17 after burning in different temperatures: (a) 220℃, (b) 320℃, (c) 600 ℃, and (d) 800℃.

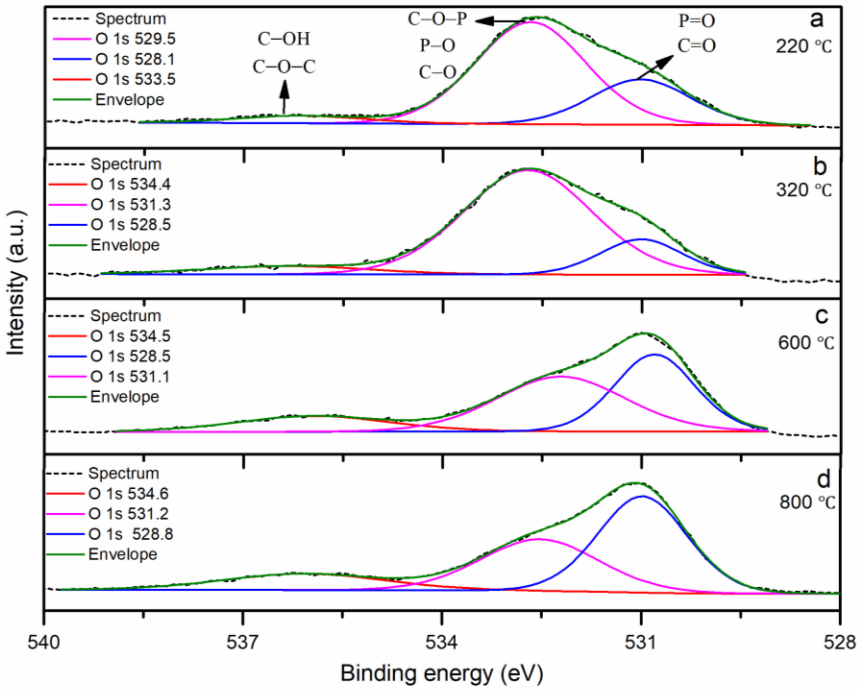

Figure S3.6. XPS spectra of O 1s for PK17 after burning in different temperatures: (a) 220℃, (b) 320℃, (c) 600℃, and (d) 800℃.

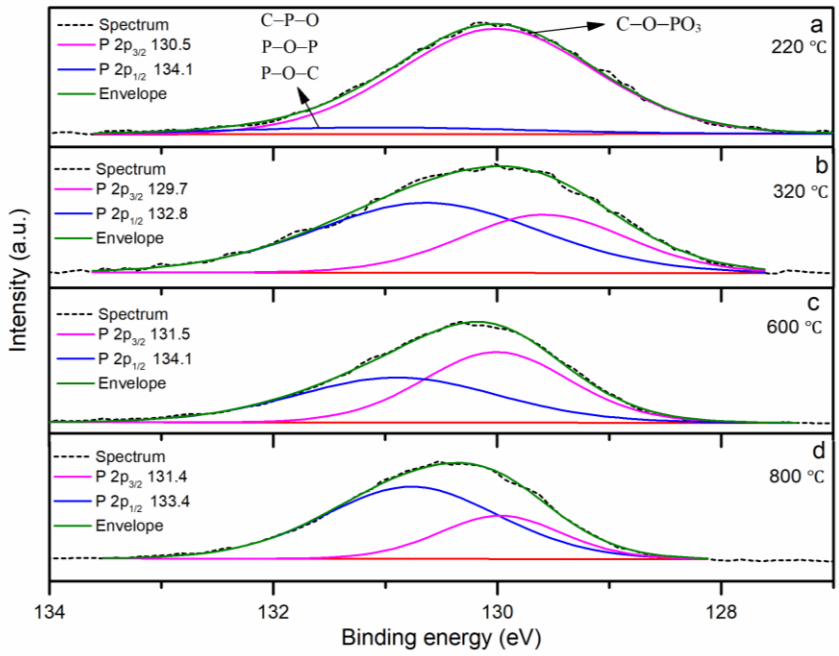

Figure S3.7. XPS spectra of P 2p for PK17 after burning in different temperatures: (a) 220℃, (b) 320℃, (c) 600℃, and (d) 800℃.

Table S3.4. Mass percentage concentration of major elements for KL, PK18, and burned PK17 from TGA in different temperature

Samples	Mass concentration (%)		
	C 1s	O 1s	P 2p
KL 25 ℃	74	24.25	0
PK17 25 ℃	60	32.26	7
PK17 220 ℃	59.78	32.95	7.27
PK17 320 ℃	57.93	33.57	8.50
PK17 600 ℃	21.39	54.85	23.75
PK17 800 ℃	15.12	58.02	26.86

Table S3.5. Mass percentage concentration of C 1s for KL, PK18, and burned PK17 from TGA in different temperature

Samples	Mass concentration (%)		
	C 1s		
	C–C	C–OH	O=C–OH
KL25 ℃	42.44	55.21	2.35
PK17 25 ℃	48.41	51.04	0.55
PK17 220 ℃	45.28	52.82	1.9
PK17 320 ℃	39.56	52.70	7.74
PK17 600 ℃	41.23	41.94	16.83
PK17 800 ℃	41.93	55.40	2.67

Table S3.6. Mass percentage concentration of O 1s for KL, PK18, and burned PK17 from TGA in different temperature

Samples	Mass concentration (%)		
	O 1s		
	C–OH C–O–C	C–O–P P–O C–O	P=O C=O
KL	96.49	–	3.51
PK17 25 ℃	81.31	10.76	7.93
PK17 220 ℃	5.77	67.40	26.83
PK17 320 ℃	7.78	75.81	16.41
PK17 600 ℃	15.42	45.16	39.42
PK17 800 ℃	15.22	35.30	49.49

Table S3.7. Mass percentage concentration of P 2p for KL, PK17, and burned PK18 from TGA in different temperature

Samples	Mass concentration (%)	
	P 2p	
	C–O–PO_3	C–P–O P–O–P
KL	–	–
PK17 25 ℃	95.64	4.36
PK17 220 ℃	91.34	8.66
PK17 320 ℃	38.01	61.99
PK17 600 ℃	53.09	46.91
PK17 800 ℃	29.67	70.33

Table S3.8. The FWHM of different bonds in KL and PK17.

KL	BE (eV)	FWHM (eV)
C 1s 281.7	**280.99**	**1.31**
C 1s 284.2	**282.40**	**1.98**
C 1s 285.7	**285.66**	**1.18**
O 1s 529.3	**529.58**	**1.91**
O 1s 527.4	**527.86**	**1.36**

PK17	BE (Ev)	FWHM (eV)
C 1s 280.7	**280.83**	**1.05**
C 1s 282.8	**282.35**	**1.64**
C 1s 284.8	**284.84**	**1.74**
O 1s 529.5	**529.10**	**1.86**
O 1s 527.0	**527.53**	**0.80**
O 1s 526.8	**526.86**	**0.68**
P $2p_{3/2}$ 129.6	**129.74**	**1.68**
P $2p_{1/2}$ 131.5	**131.53**	**0.78**

Figure S3.8. PLA film mixed with PK17, before and after LOI test.

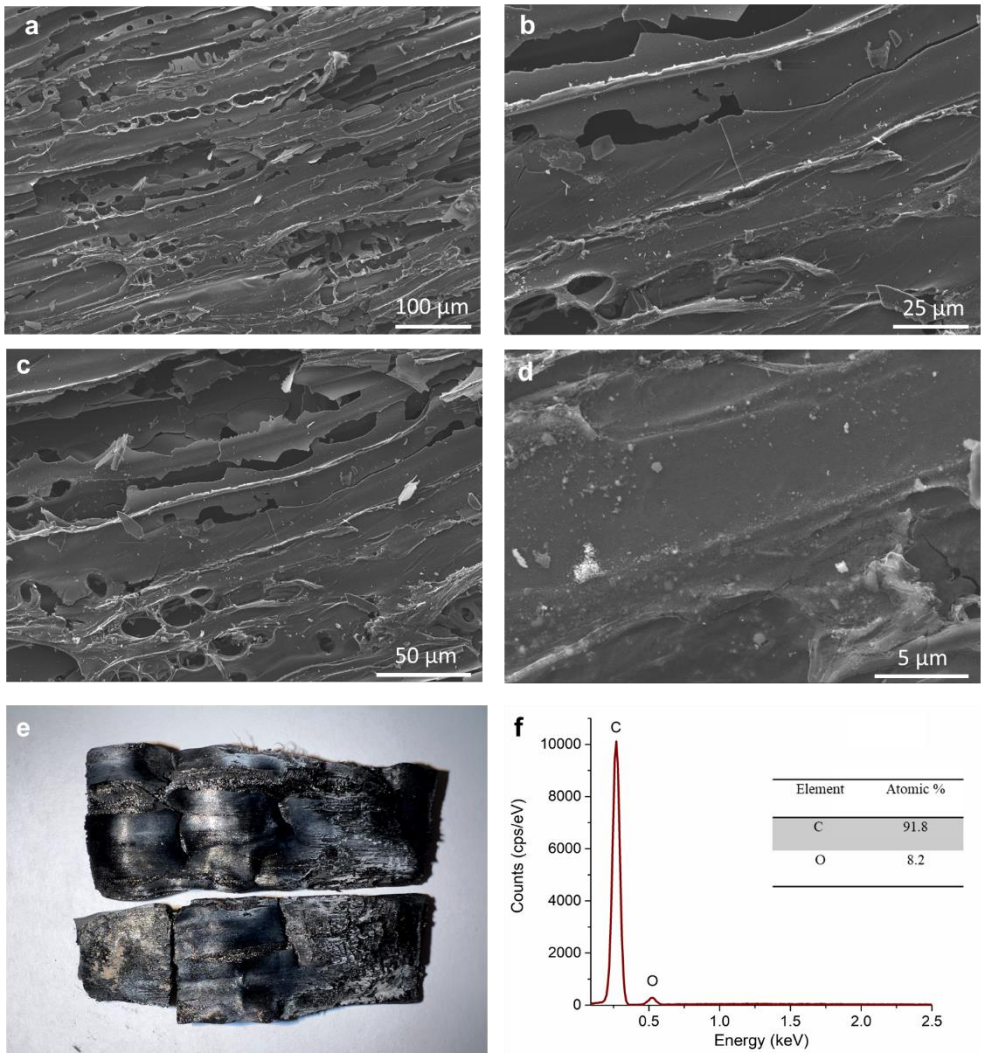

Figure S3.9. SEM images (a-d), digital picture (e), and EDX graph (f) of char residue after burning UW in smoke density analysis.

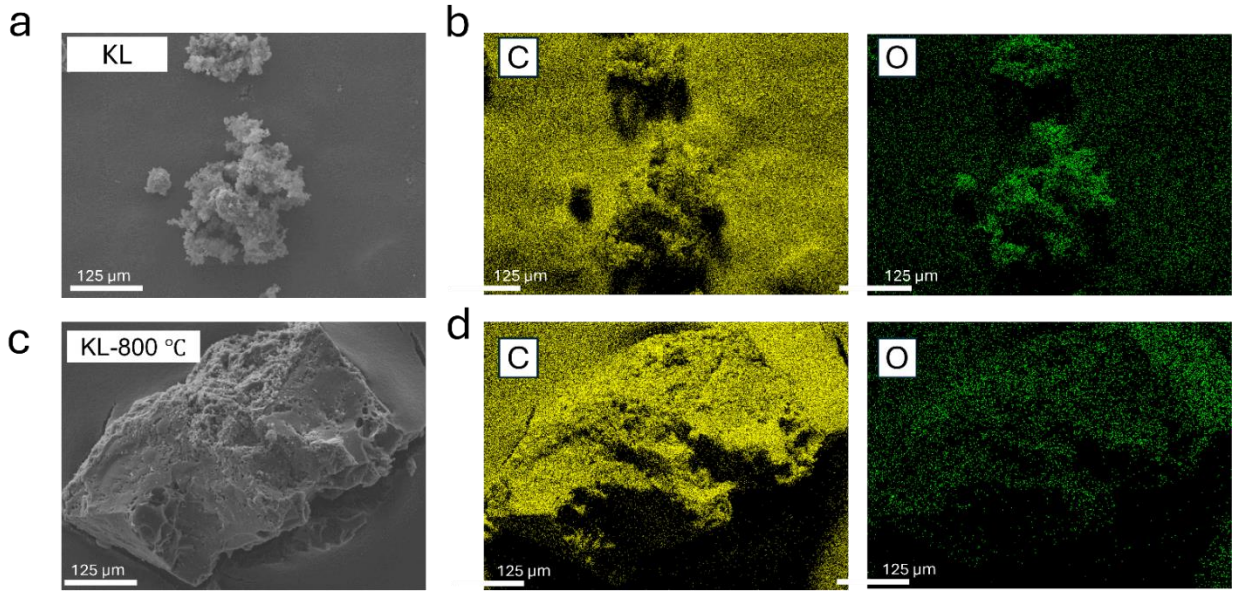

Figure S3.10. The SEM images (a and c), and the EDS elemental mapping (b and d) of KL before and after combustion.

Appendix 4A. Supporting information: Fully biobased flame retardant lignin incorporated chitosan derived aerogel

Saba Khodavandegar, Pedram Fatehi *

Green Processes Research Center and Chemical Engineering Department, Lakehead University, 955 Oliver Road, Thunder Bay, ON P7B5E1, Canada

Corresponding author: E-mail: pfatehi@lakehadu.ca

Charge density and solubility measurement

The Particle Charge Detector (PCD 04, BTG Mütek GmbH, Germany) was utilized to assess the charge density samples containing 1 wt. % were prepared overnight, followed by centrifugation of the suspensions at 1000 rpm for 5 minutes to separate the soluble and insoluble components. The charge density was determined by titrating 1 mL of the soluble portion of the samples with a 0.005 mol/L PDADMAC solution.

Solubility was tested by dissolving 0.2 g of lignin derivatives in 19.8 mL of deionized water. The suspensions were then agitated for 12 hours at 200 rpm and 25 °C in a water bath (Innova 3100, Brunswick Scientific, Edison, NJ, USA). The solubility test followed a previously published procedure [1].

Table S4.1. The reaction condition of phosphorylated KL.

Sample ID	**Concentration ratio of KL:PHA (mol: mol)**	**Time (h)**	**Temperature (℃)**	**Charge density (mmol/g)**	**Solubility (%)**
PK1	1:0.01	1	25	1±0.01	99±0.2
PK2	1: 0.2	1	25	3±0.07	99±0.9
PK3	1: 0.4	1	25	5±0.16	98±0.5

Table S4.2. Taguchi design for aerogel preparation.

Sample ID	PK charge density (mmol/g)	PK solution concentration (wt.%)	Chitosan Mw (Low, medium, high)	Reaction temperature (℃)
AAL	1	3.2	Low	60
ABL	3	2	Low	90
ACL	5	0.8	Low	30
ADM	1	0.8	Medium	90
AEM	3	3.2	Medium	30
AFM	5	2	Medium	60
AGH	1	2	High	30
AHH	3	0.8	High	60
AIH	5	3.2	High	90

Characterization of Taguchi design samples

Viscometer analysis of hydrogels

Rheological tests are essential for measuring the viscoelastic properties of hydrogel structures. These tests were conducted to evaluate the crosslinking characteristics of the gels. The viscosity of the hydrogels is

shown in **Figure 4.1**(a–c). The analysis revealed that the viscosity behavior of hydrogels is influenced by Mw, charge density, concentration of PK, and temperature. **Figure S4.1**(a) shows how Mw of CH can affect the viscosity behavior, and it can be concluded that the increase in Mw increased the viscosity of samples. **Figure S4.1**(b) demonstrates that increasing the charge density results in a slight increase in the viscosity of hydrogels.

Additionally, concentration and temperature impact the viscoelasticity (**Figure S4.1**(c) and **S4.1**(d)), indicating that by increasing the PK concentration, there is an increase and then a decrease in viscosity. In contrast, the increment in temperature decreased the viscosity. Overall, in low Mw CH aerogels, as was reported in **Figure 4.1**(a), ACL showed the highest viscosity with 5 mmol/g charge density, 0.2 g/25mL PK concentration, and a reaction temperature of 30 ℃ with the amount of 540 Pa.s at the shear rate of 10 1/s. There is not any specific trend for the factors in low Mw aerogels. However, ACL and AAL showed the same trend, but ABL has the shear thinning behavior by increasing the shear rate.

In medium Mw CH hydrogels **Figure 4.1**(b), the AFM hydrogel with a 5 mmol/g charge density, 0.5 g/25 mL PK concentration, and a reaction temperature of 60 ℃ exhibited the highest viscosity. The increment in the charge density led to an increase in viscosity from 2700 to 20396 Pa.s. Both AFM and AEM showed the shear thinning behavior after 30 and 25 shear stress, respectively. However, with the Newtonian regime, the ADM has the lowest viscosity among these aerogels.

The highest amount for the hydrogels with high Mw is related to sample AGH with the 1 mmol/g charge density, 0.5 g/25 mL PK concentration at 30 ℃, which is also the highest amount among all hydrogels.

Intermolecular interactions are also critical in determining how tightly two molecules adhere to each other and their resistance to flow. This is evident when comparing the hydrogels with similar Mw but different reaction conditions.

All factors influence the viscoelasticity behavior of hydrogels, and it can not be correct the highest amount in all parameters will have the highest viscosity. Moreover, the effect of two parameters on viscosity was reported in **Figure S4.1**(e–g).

Mechanical properties of aerogels

The effect of each factor on young's modulus is presented in **Figure S4.2**(a–d). It can be observed that low and medium Mw CH do not influence the young's modulus significantly. However, the addition of high Mw CH increases young's modulus. An increase in charge density from 1 to 3 mmol/g also increases young's modulus, but a further increase from 3 to 5 mmol/g shows no additional effect. Additionally, increasing the PK concentration enhances young's modulus.

Regarding temperature, both 30 °C and 60 °C exhibit similar effects, whereas increasing the temperature to 90 °C results in a higher young's modulus. The combined effect of these factors on young's modulus is also illustrated in **Figure S4.2**(e–g). Notably, low Mw CH aerogels with a charge density of 3 mmol/g, PK concentration of 0.5 g/25 mL, and temperature of 90 °C exhibit the highest young's modulus, with about 700 MPa stress at 100% strain. This aerogel also shows a significant difference in porosity compared to other low Mw aerogels. In medium Mw aerogels, the high young's modulus is for the AEM sample with the 3 mmol/g charge density, 0.8 PK concentration, at 30 ℃.

In the high Mw CH sample, the highest young's modulus is 9.37 MPa, corresponding to the AIH sample, which has the following parameters 5 mmol/g charge density, 0.8 g/25 mL PK concentration, and a temperature of 90 ℃. This can be interpreted as an increase in crosslinking points due to the high values of charge density, PK concentration, Mw of CH, and temperature. The high charge density and Mw allow the negatively charged PK polymer chains to attach more effectively to the positively charged CH. Additionally, the interactions between phosphates and amine groups enhance physical and chemical bonding strength [2].

Thermal conductivity and density measurements of aerogels

The effect of various factors on the thermal conductivity of the aerogels is presented in **Figure S4.3**(a–d). An increase in both the Mw and charge density leads to a decrease and subsequent increase in the thermal conductivity of the aerogels, respectively. The PK concentration exhibits a noticeable impact on thermal conductivity; as it increases from 0.2 g/25 mL, the thermal conductivity decreases initially, then increases when the concentration reaches 0.8 g/25 mL. Conversely, the reaction temperature follows a different trend, showing an increase in thermal conductivity from 30 °C to 60 °C, followed by a decrease upon reaching 90 °C.

In the low Mw aerogels, AAL and ACL exhibited similar thermal conductivity values of 0.0447 W/mK and 0.0445 W/mK, respectively. In contrast, ABL demonstrated the lowest thermal conductivity among the low Mw aerogels, with a value of 0.0411 W/mK. For aerogels with medium and high Mw, AFM and AIH showed higher thermal conductivity values of 0.0436 W/mK and 0.0459 W/mK, respectively. and S4(a–d). The Mw does not have a significant impact on the density of aerogels. However, the other three factors—charge density, PK concentration, and temperature increase the density as each factor rises.

In low Mw aerogels, the sample denoted as ACL exhibited the lowest density with a charge density of 5 mmol/g, a PK concentration of 0.2 g/25 mL, and a reaction temperature of 30 ℃. This low density is likely due to the high crosslinking of the aerogel under these conditions. For medium Mw aerogels, the sample ADM had a lower density compared to other medium Mw aerogels, with a charge density of 1 mmol/mol, a PK concentration of 0.2 g/25 mL, and a reaction temperature of 90 ℃. In aerogels with high Mw, there is a significant change in density due to variations in reaction conditions. The highest density was observed in the sample AIH, which had a high Mw, a charge density of 5 mmol/g, a PK concentration of 0.8 g/25 mL, and a reaction temperature of 90 ℃, resulting in a density of 0.07 g/cm³.

The internal crosslinking of aerogels, which varies significantly with changes in reaction conditions, affects pore size and consequently density. It can be concluded that while high Mw alone does not affect density, other factors such as charge density, PK concentration, and temperature also play a significant role in influencing this change.

Swelling ratio measurement

In low Mw aerogels, no specific trend in swelling ratio is observed. This is because various factors, in addition to charge, influence the sample structure, thereby affecting water absorption. It is evident that the swelling of the samples initially decreases and then increases with rising charge density, with the highest swelling observed in the ADL aerogel at 41.5%. Among the medium Mw aerogels, ADM with a charge density of 1 mmol/g, 0.2 g/25 mL PK concentration, and tested at 90 ℃ exhibited the highest swelling rate at 50.75%. The other two samples, AEM and AFM, demonstrated nearly identical swelling ratios. High Mw aerogels showed a significant change in swelling ratio with increasing charge density under various conditions. The sample AGH exhibited the highest swelling at 74.9%, with a charge density of 1 mmol/g, 0.5 g/25 mL PK concentration, and a reaction temperature of 30 ℃. However, for two other samples, the swelling ratio decreased as the charge density increased from 3 to 5 mmol/g, PK concentration rose from 0.2 to 0.8 g/25 mL, and reaction temperature increased from 60 ℃ to 90 ℃, resulting in swelling ratios of 57.5% and 9.25%, respectively. The AIH sample had the lowest swelling ratio among all aerogels, attributed to high crosslinking, which compacted the pores.

Table S4.3. Taguchi design response for optimization.

Sample	Viscosity at shear rate 10 (Pa.s)	Young modulus (MPa)	Thermal conductivity (W/mk)	Density (g/cm^3)
AAL	120	2.91	0.0447	0.05465
ABL	240	7.19	0.0411	0.05023
ACL	540	1.8	0.0445	0.03817
ADM	2700	2.83	0.0414	0.0364
AEM	18236	4.1	0.0420	0.0514
AFM	20396	3.35	0.0436	0.04798
AGH	23215	3.7	0.0386	0.03474
AHH	11757.5	3.52	0.0433	0.0341
AIH	960	9.37	0.0459	0.07

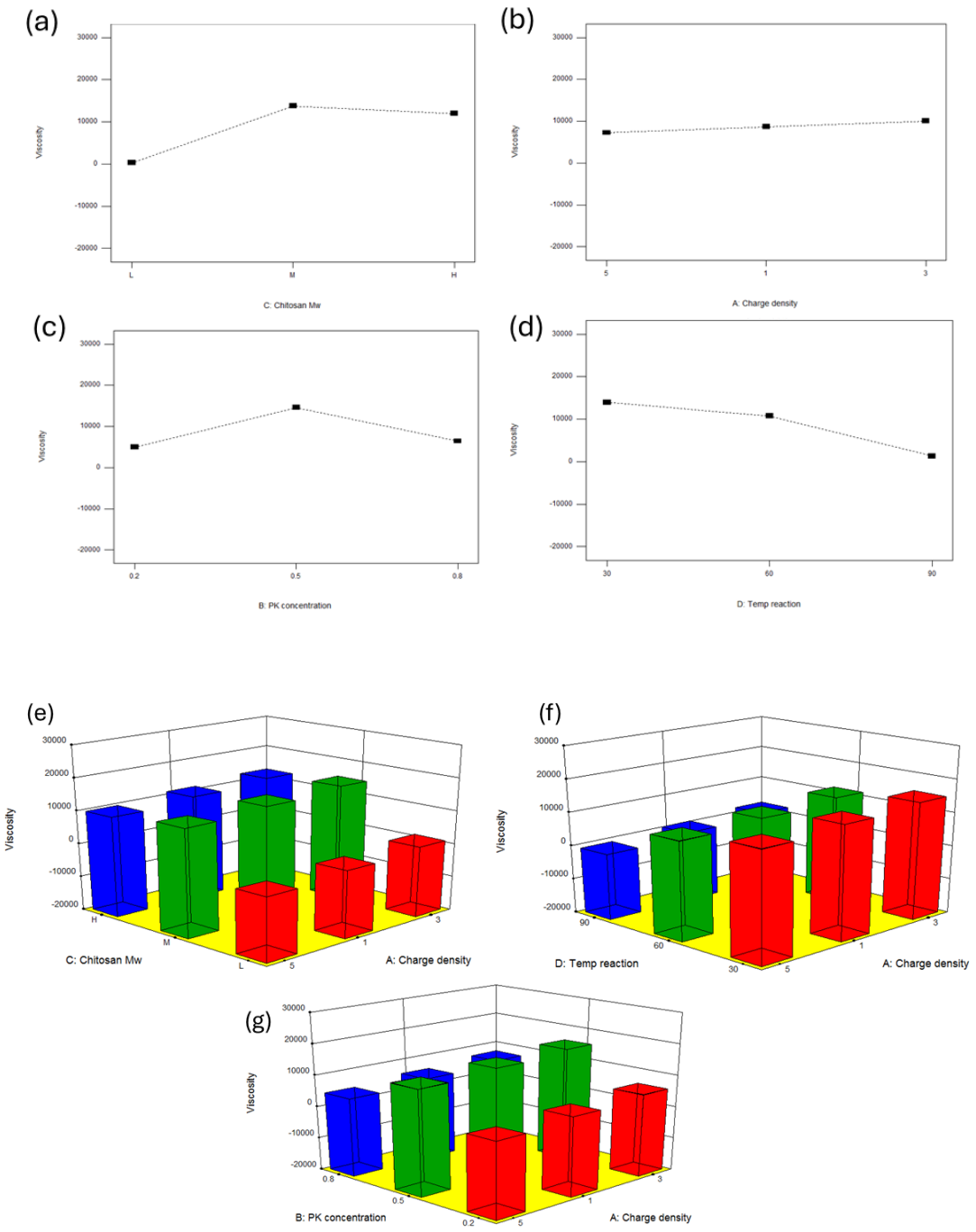

Figure S4.1. The effect of CH Mw, charge density and concentration of PK, and reaction temperature on viscosity of hydrogels (a-d), the effect of two parameters on viscosity (e-g).

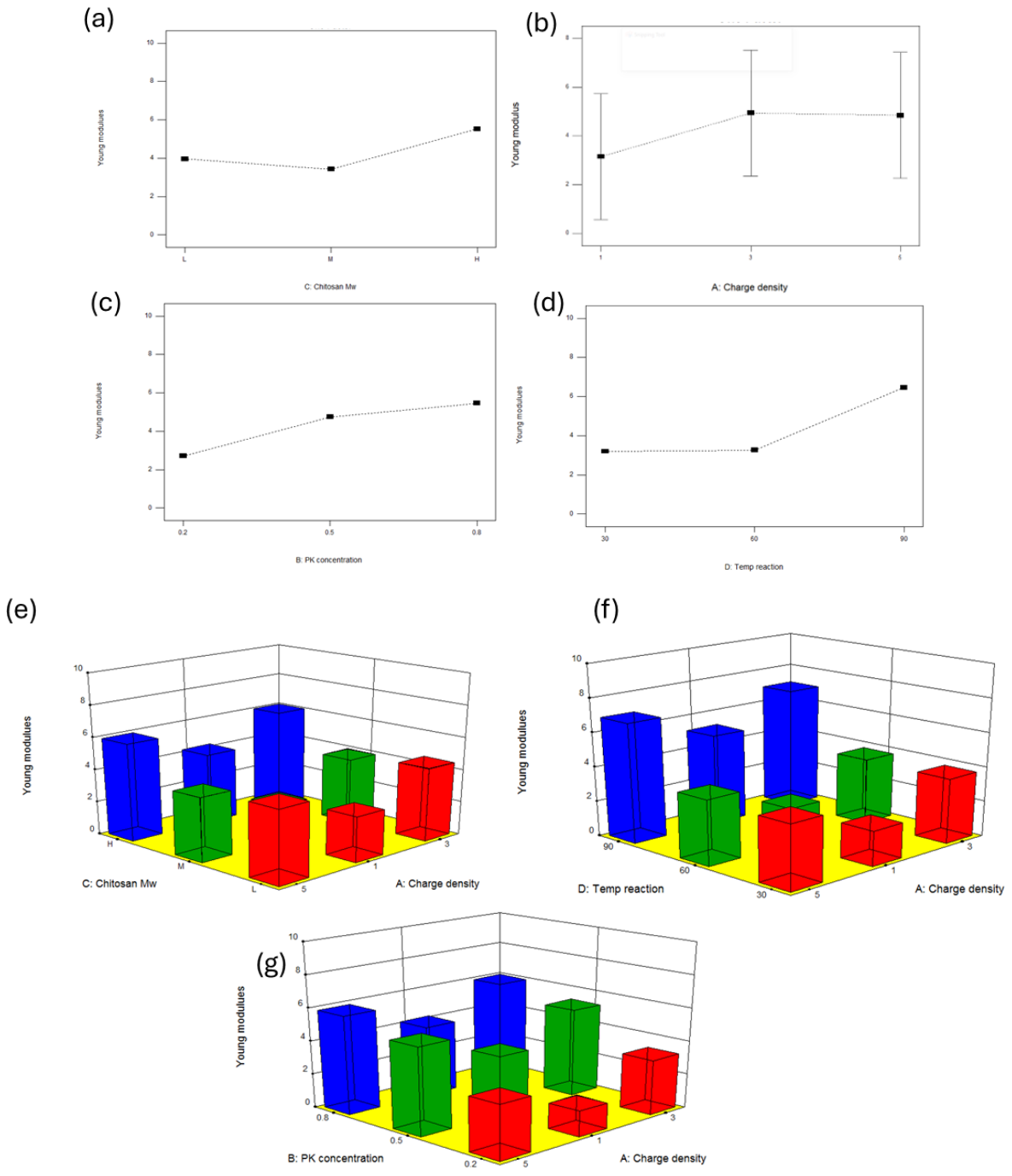

Figure S4.2. The effect of CH Mw, charge density and concentration of PK, and reaction temperature on the youngs modulus of aerogels (a-d), the effect of two parameters on youngs modulus (e-g).

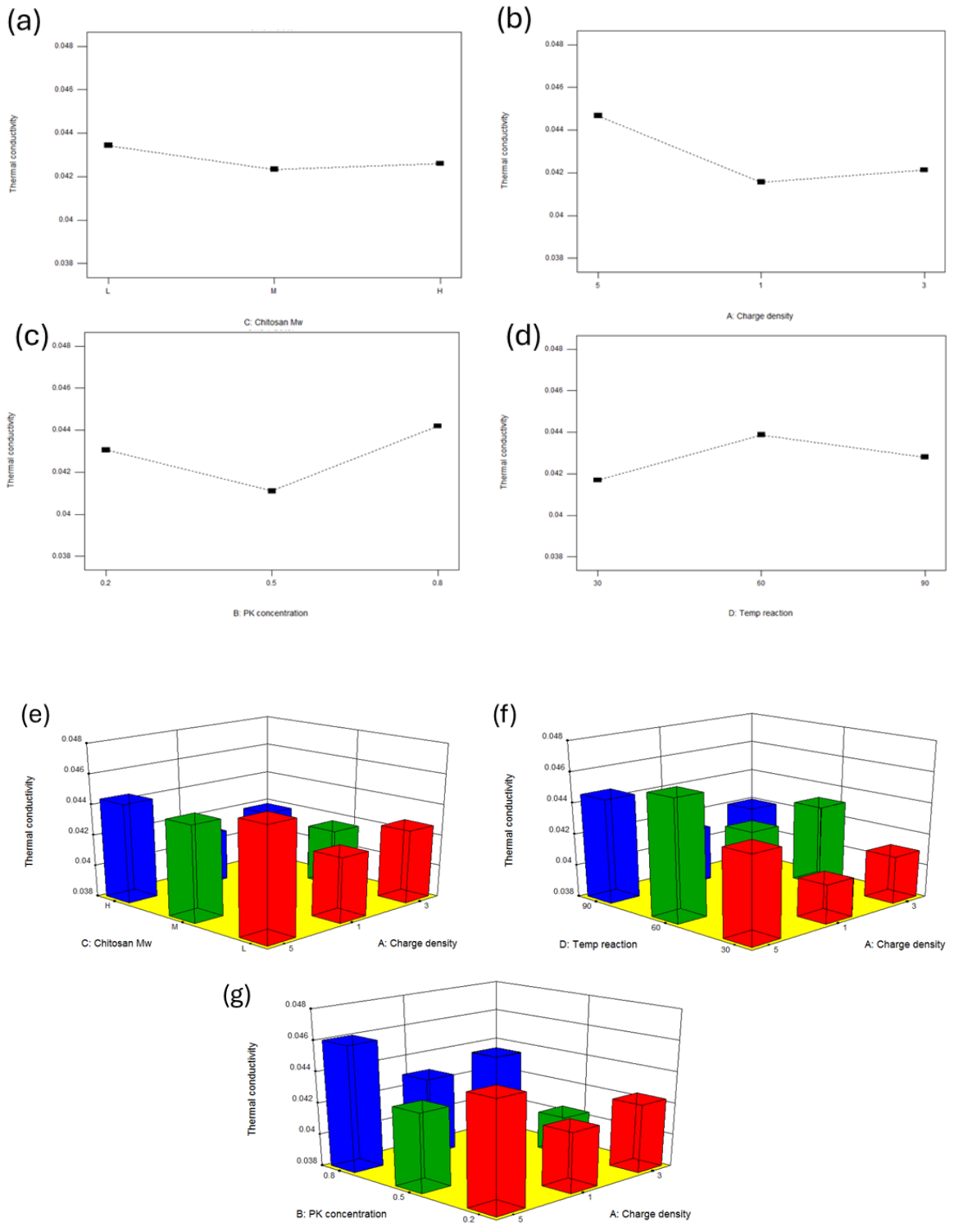

Figure S4.3. The effect of CH Mw, charge density and concentration of PK, and reaction temperature on the thermal conductivity of aerogels (a-d), the effect of two parameters on themal conductivity (e-g).

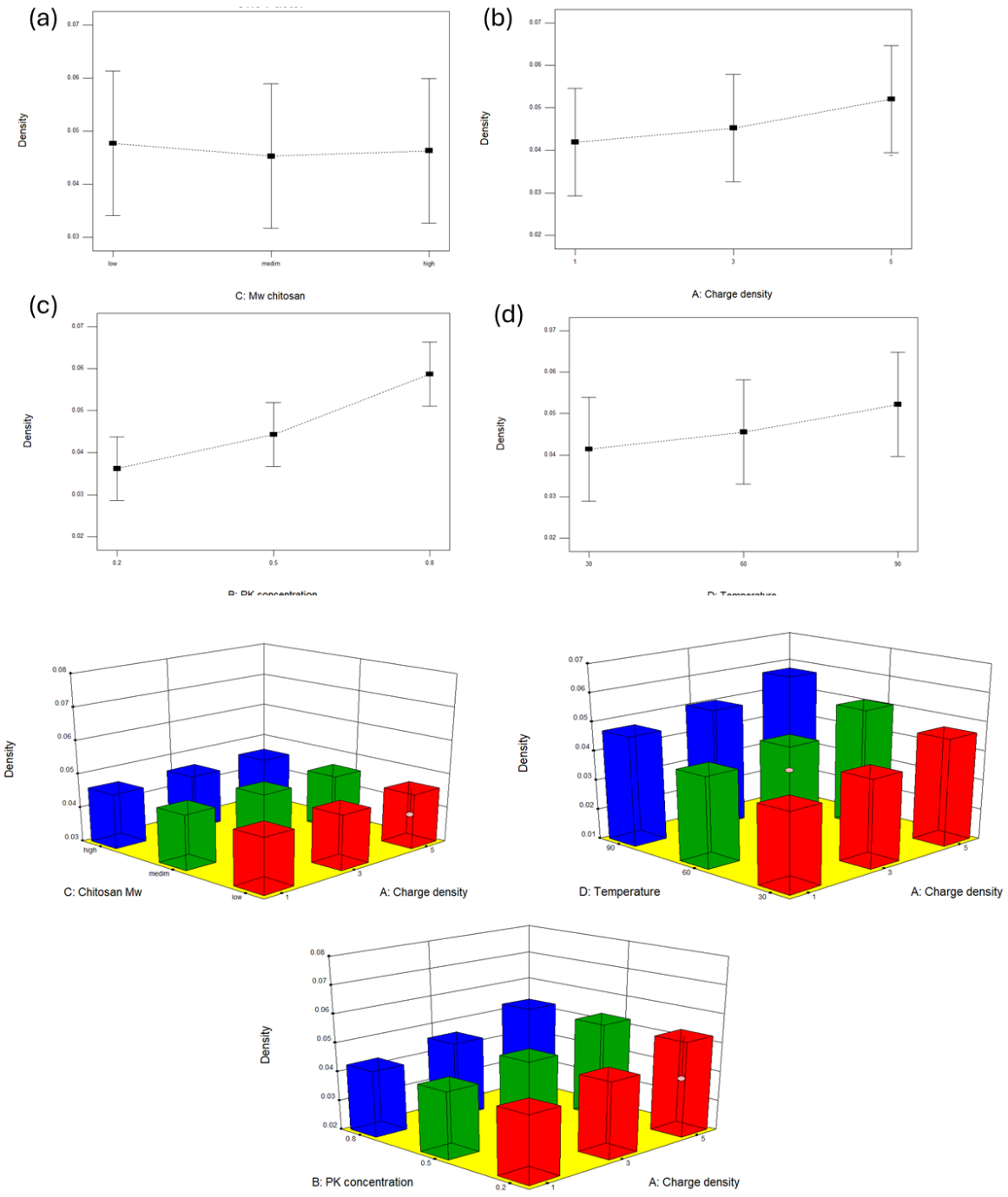

Figure S4.4. The effect of CH Mw, charge density and concentration of PK, and reaction temperature on the density of aerogels (a-d), the effect of two parameters on density (e-g).

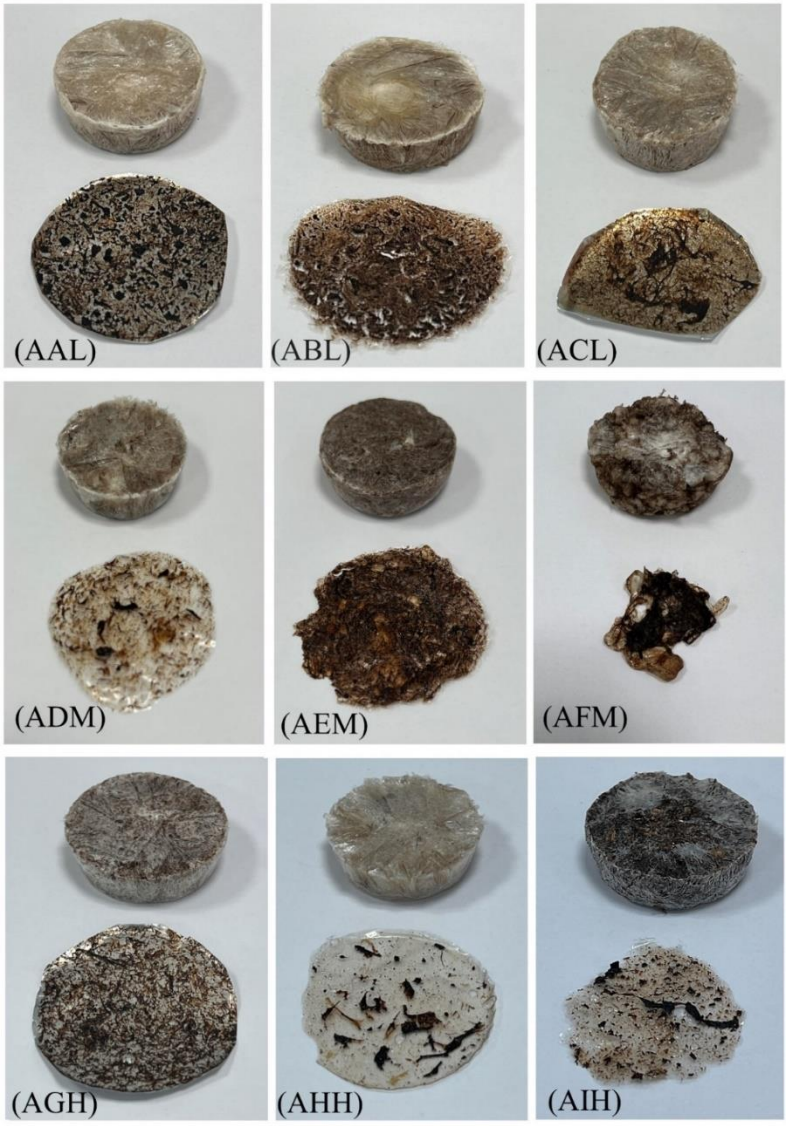

Figure S4.5. Digital photos of aerogel and dried hydrogels in room temperature for crosslinking study.

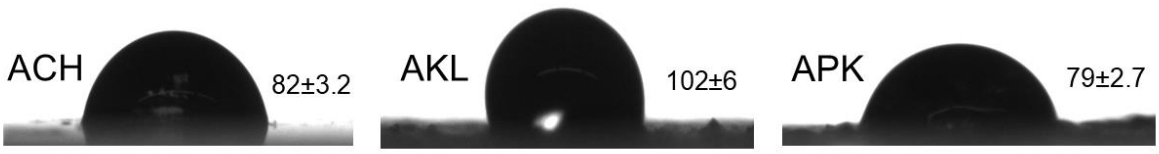

Figure S4.6. Contact angle of dried hydrogels on glass.

Table S4.4. Chitosan lignin aerogels in different applications.

Aerogel materials	**Method and drying**	**Crosslinking type**	**Application**	**Ref**
Chitosan, methyl phosphonic acid	Ion exchange reaction, directional freeze-drying	Physical interactions	Thermal insulation	[3]
Chitosan, DES lignin (choline chloride/lactic acid)	solution blending method, lyophilized drying	Hydrogen bonding and electrostatic interactions, Π-orbit interactions.	Dye adsorption	[4]
Chitosan, lignin-silica, cellulose	freeze–thaw process, Freeze drying	Physical interactions	--------	[5]
Chitosan carbon, Lignin carbon quantum dots	Freeze drying	Hydrogen bonds, polymerization	efficient solar evaporation	[6]
Chitosan, aminated lignin, lanthanum	Freeze drying		Phosphorus removal adsorbents	[7]
Chitosan, graphene oxide, lignosulfonate	Freeze drying	Physical interactions	adsorption of methylene blue	[8]
Chitosan/lignin and chitosan/lignin-carbon nanoparticles, epichlorohydrin, alkaline/urea solvent	Freeze drying	Sol-gel method, freeze-thaw cycle process,	Wastewater treatment	

			Ether bonds with the hydroxyl groups	
Chitosan, phytic acid, halloysite nanotubes	oven-dried at 60 °C	Layer by layer assembly on bamboo foams, charge attraction and hydrogen bonding	thermal insulation, and sound absorption	[9]

References

[1] S. Gharehkhani, N. Ghavidel, P. Fatehi, Kraft Lignin-Tannic acid as a green stabilizer for oil/water emulsion, ACS. Sustain. Chem. Eng. 7 (2019) 2370–2379. https://doi.org/10.1021/acssuschemeng.8b05193.

[2] X. Wang, X. Yang, Z. Wu, X. Liu, Q. Li, W. Zhu, Y. Jiang, L. Hu, Enhanced mechanical stability and hydrophobicity of cellulose aerogels via quantitative doping of nano-lignin, Polymers (Basel). 15 (2023). https://doi.org/10.3390/polym15051316.

[3] C. Du, Y. Xu, C. Yan, W. Zhang, H. Hu, Y. Chen, M. Xu, C. Wang, B. Li, L. Liu, Facile construction strategy for intrinsically fire-safe and thermal-insulating bio-based chitosan aerogel, Sustain. Mater. Technol. 39 (2024) e00794. https://doi.org/10.1016/j.susmat.2023.e00794.

[4] Y. Zhu, B.K. Qi, H.N. Lv, Y. Gao, S.H. Zha, R.Y. An, Q.S. Zhao, B. Zhao, Preparation of DES lignin-chitosan aerogel and its adsorption performance for dyes, catechin and epicatechin, Int. J. Biol. Macromol. 247 (2023) 125761. https://doi.org/10.1016/j.ijbiomac.2023.125761.

[5] V.T. Tran, T.M. Le, T.T.N. Trinh, C.L. Tran, Y.H.P. Duong, V.Q. Huynh, D.T. Le, P.K. Le, Development of facile and green fabrication of cellulose–chitosan composite aerogel and lignin/silica Hybrid from Agro-wastes, Fibers and Polymers 24 (2023) 403–411. https://doi.org/10.1007/S12221-023-00097-9.

[6] Z. Li, D. Li, S. Wei, X. Jin, Z. Zhang, L. Liu, Y. Ge, Z. Li, Chitosan-derived carbon aerogel modified with lignin carbon quantum dots for efficient solar evaporation, J. Chem. Eng. 486 (2024) 150157. https://doi.org/10.1016/j.cej.2024.150157.

[7] R. Cui, J. Ma, X. Li, J. Zhang, Z. Liu, J. Zhang, R. Sun, Chitosan-amidated lignin aerogel beads efficiently loaded with lanthanum hydroxide for phosphate removal from aqueous solutions, Int. J. Biol. Macromol. 279 (2024) 135319. https://doi.org/10.1016/j.ijbiomac.2024.135319.

[8] M. Yan, W. Huang, Z. Li, Chitosan cross-linked graphene oxide/lignosulfonate composite aerogel for enhanced adsorption of methylene blue in water, Int. J. Biol. Macromol. 136 (2019) 927–935. https://doi.org/10.1016/j.ijbiomac.2019.06.144.

[9] X. Yu, X. Jin, Y. He, Z. Yu, R. Zhang, D. Qin, Eco-friendly bamboo pulp foam enabled by chitosan and phytic acid interfacial assembly of halloysite nanotubes: Toward flame retardancy, thermal insulation, and sound absorption, Int. J. Biol. Macromol. 260 (2024) 129393. https://doi.org/10.1016/j.ijbiomac.2024.129393.

Appendix 5A. Supporting information: Carboxymethylated lignin incorporated chitosan aerogel as thermal insulator

Saba Khodavandegar, Rozita Zare, Pedram Fatehi *

Under review in Biomacromolecule journal

Green Processes Research Center and Chemical Engineering Department, Lakehead University, 955 Oliver Road, Thunder Bay, ON P7B5E1, Canada

First Author, email: skhodava@lakeheadu.ca, address: 955 Oliver Road, Thunder Bay, ON, Canada, P7B 5E1

Corresponding author: email: pfatehi@lakehadu.ca, address: 955 Oliver Road, Thunder Bay, ON, Canada, P7B 5E1

The contribution of Saba Khodavandegar to this work was writing original draft, methodology, investigation, visualization, validation, experiment, and data analysis.

Table S5.1. Reaction condition for carboxymethylation.

ID	L:SC mol:mol	Time (hour)	Temp (°C)
CM1	1:0.5	2	40
CM2	1:3	4	60
CM3	1:6	24	60

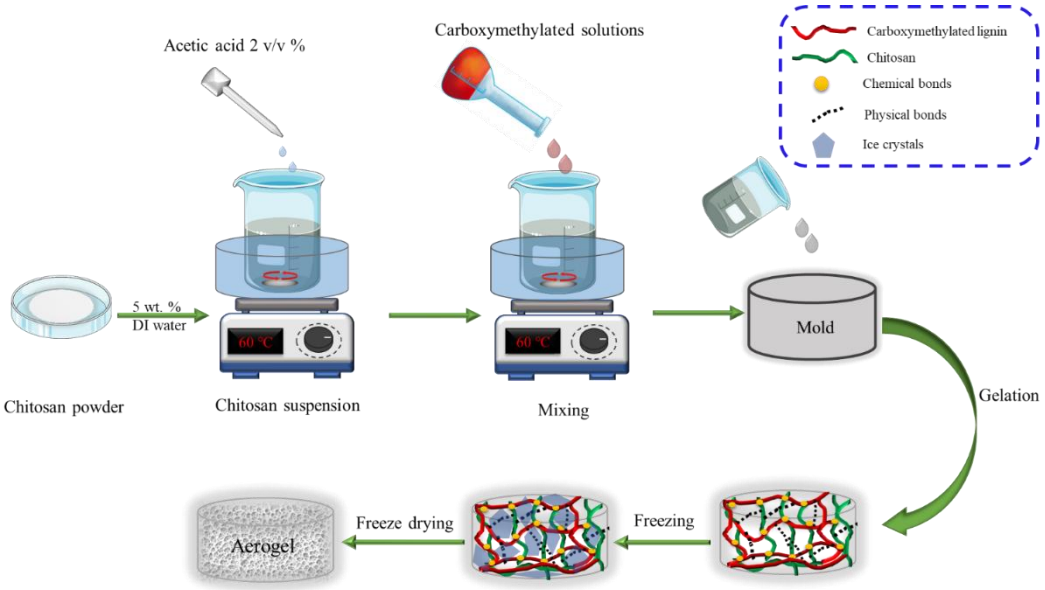

Figure S5.1. Schematic illustration of aerogel preparation.

Methodology

Charge density, solubility, molecular weight, and elemental analysis

The charge density of lignin derivatives was evaluated using a Particle Charge Detector (PCD 04, BTG Mütek GmbH, Germany). Samples at 1 wt.% concentration in water were prepared overnight, and the suspensions were then centrifuged at 1000 rpm for 5 minutes to separate the soluble and insoluble components. The charge density of the samples was determined by titrating 1 mL of the soluble part of the samples against 0.005 mol/L of PDADMAC solution. The solubility of the samples was tested by dissolving 0.2 g of lignin derivatives in 19.8 mL of deionized water. The suspensions were shaken for 12 h at 200 rpm and 25 °C in a water bath (Innova 3100, Brunswick Scientific, Edison, NJ, USA). The solubility of the samples was determined following a previously published procedure [1].

Gel permeation chromatography (GPC, Malvern GPCmax VE2001 Module + Viscotek TDA305 with multi-detectors) using poly Analytic 206 and PAA203 columns was used to determine the molecular weight (MW) of samples. Samples were prepared by dissolving 50 mg of sample in 10 mL of 0.1 M NaN_3, and produced solutions were filtered through a 0.2 µm filter and evaluated according to a previously established

procedure [2]. The column and detector temperatures were set to 35 °C, and a flow rate of 0.7 mL/min was maintained. In this test, 0.7 mL of each sample was analyzed by an RI detector.

The samples' organic elements were determined using an organic Elemental analyzer, Vario EL, utilizing the combustion method as described in detail [3]. The samples (0.02 g) were oven-dried for 24 hours at 60 °C before being transported to the elemental analyzer's carousel chamber. The samples' carbon, hydrogen, nitrogen, and sulfur contents were determined by burning them at 1200 °C and examining the resulting gases.

Apparent density and water uptake measurement

The apparent density (ρ) of aerogel was calculated using the following Equation (S5.1):

$$\rho = \frac{4m}{\pi D2H} \qquad \text{(S5.1)}$$

Where ρ denotes the apparent density of the aerogel (gcm^{-3}), m is the weight of the aerogel (g), D is the diameter of the aerogel cross-section (cm), and H is the height of the aerogel (cm) [4].

Results and discussions

Charge density, solubility, molecular weight, and elemental results

The effect of molar ratio (KL:SE), time, and temperature on the charge density and solubility of the lignin derivatives was discussed in the literature [5]. Based on this literature and our experiment, by increasing the molar ratio from 1:0.5 to 1: 6 (L:SE, mol: mol), charge density increased from 1 to 2 mmol/g. In addition, the solubility increased to 100 % after carboxymethylation for all three samples, as reported in **Table S5.2**. By adding more carboxymethyl functional groups on the KL structure, the Mw increased from 1707 to 2308 mmol/g, which is proof of more grafting of carboxymethyl groups.

For more information about elemental analysis, the CHNS was conducted, and it is evident that the amount of oxygen increased, and the amount of hydrogen decreased in the modified lignin compared to the

unmodified sample, confirming the carboxymethylation of KL. These findings support the presence of a carboxylate group in the lignin due to carboxymethylation using sodium chloroacetate reagent.

Table S5.2. The result of charge density, solubility, Mw, and elemental analysis of carboxymethylated samples.

ID	Solubility (%)	Charge density (mmol/g)	Molecular weight (g/mol)	Mn	PDI	CHNS			
						C	H	N	S
CM1	99±0.15	1±0.013	1707	719	2.38	61.01	6.535	0.01	1.824
CM2	100±0.47	1.5±0.114	1844	1007	1.83	60.21	7.127	0.01	1.555
CM3	99±0.43	2±0.03	2308	1356	1.71	58.28	6.424	0	1.355

Quantitative ^{31}P NMR

The chemical structure of the KL and modified samples (CM1, CM2, and CM3) was confirmed using ^{31}P NMR spectroscopy, and the result of this analysis is available in the decrement in the aliphatic and phenolic hydroxyl groups demonstrates that these groups were involved in the modification reaction. The considerable decrease in the phenolic hydroxyl group from 3.25 mmol/g to 2.60 mmol/g verified the high activity of phenolic hydroxyl groups in KL. The aliphatic hydroxyl group in KL dropped from 1.64 mmol/g to 1.26 mmol/g after carboxymethylation. Furthermore, the carboxylic hydroxyl concentration increased significantly from 0.32 mmol/g to 0.68 mmol/g, indicating that the reaction occurred and carboxymethyl groups graft on KL structure.

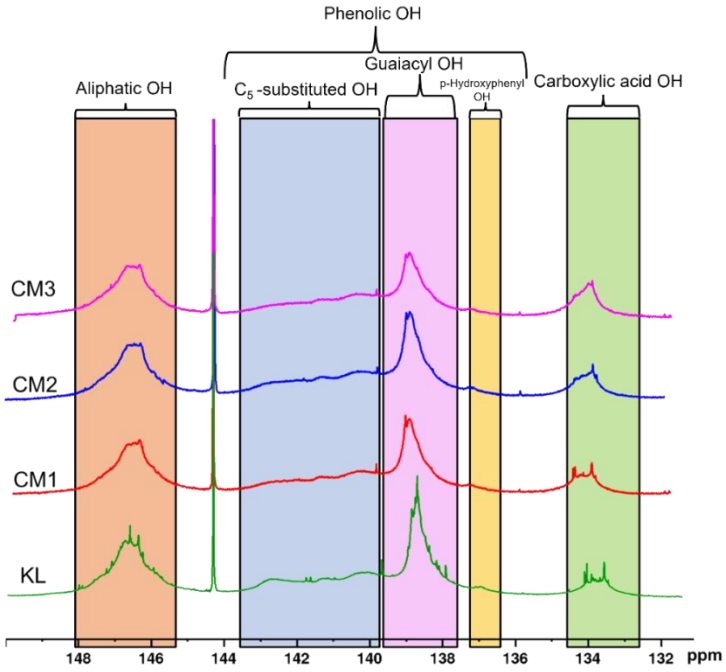

Figure S5.2. quantitative ^{31}P NMR of KL and carboxymethylated samples (CM1, CM2, and CM3). Shaded peaks indicate the type of OH functional group.

Table S5.3. The OH functional group content mmol/g determined via quantitative ^{31}P NMR analysis.

	Aliphatic OH (mmol/g)	**Aromatic OH (mmol/g)**	**C_5 OH (mmol/g)**	**Guaciayl OH (mmol/g)**	**p-Hydroxyl OH (mmol/g)**	**Carboxylic OH (mmol/g)**
KL	1.64	3.25	1.34	1.53	0.14	0.32
CM1	1.58	2.96	1.29	1.34	0.14	0.44
CM2	1.32	3.14	1.49	1.35	0.11	0.56
CM3	1.26	2.60	1.25	1.06	0.11	0.68

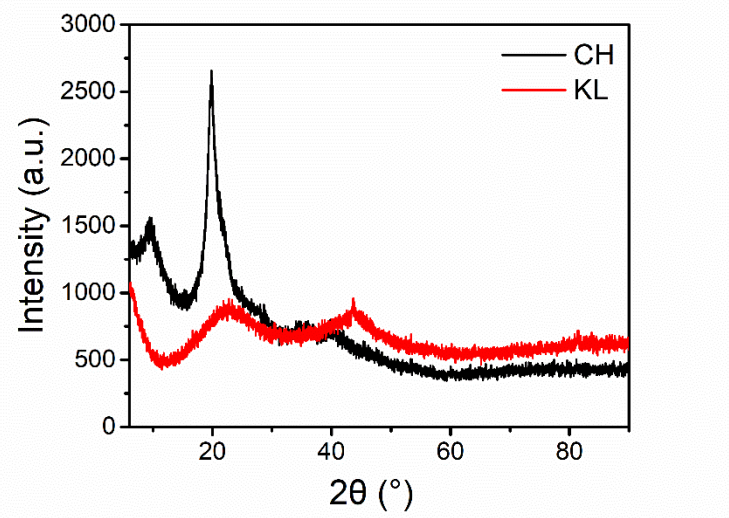

Figure S5.3. XRD spectra of CH and KL.

FTIR

Weak signals for KL and CM1 samples between 1700 cm^{-1} to 1750 cm^{-1} are for conjugated carbonyl groups [6]. Additionally, the increment in the intensity of two characteristic peaks at 1614 cm^{-1} and 1100 cm^{-1}, which are related to O=C–OH and C–O, demonstrated the success of carboxymethylation modification [7].

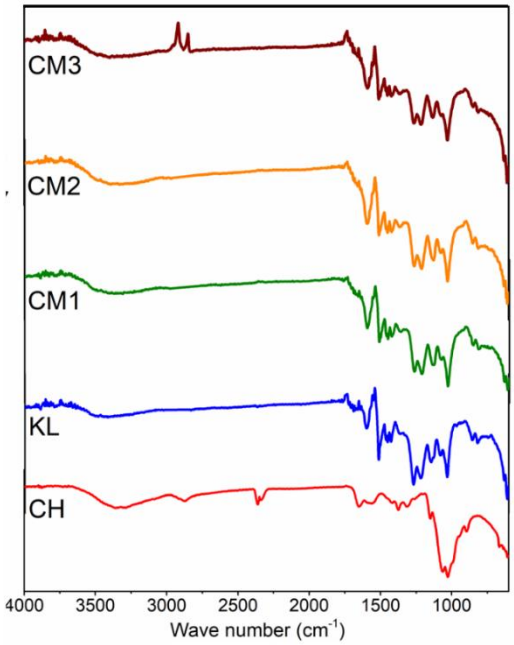

Figure S5.4. FTIR spectra of KL and CM1, CM2, and CM3.

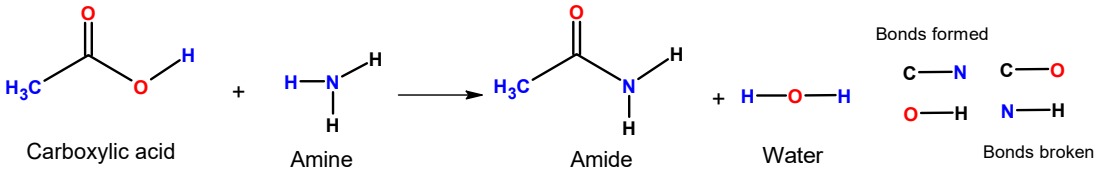

Figure S5.5. Amide condensation reaction [8].

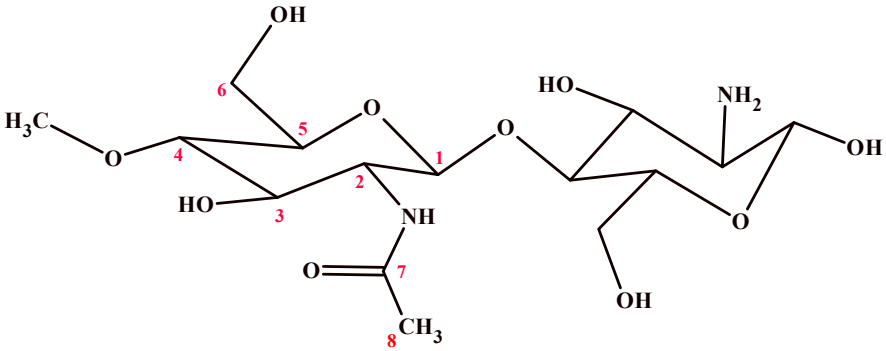

Figure S5.6. CH structure with labeling the atoms with numbers for solid-state NMR study.

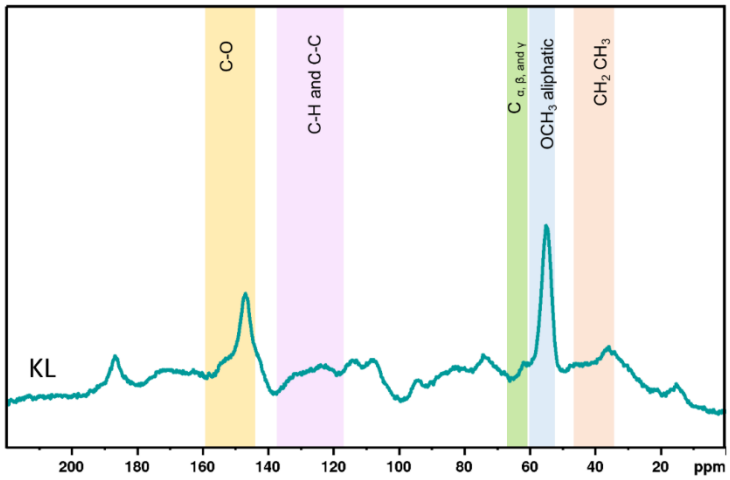

Figure S5.7. Solid state NMR spectra of KL with labeling the bonds.

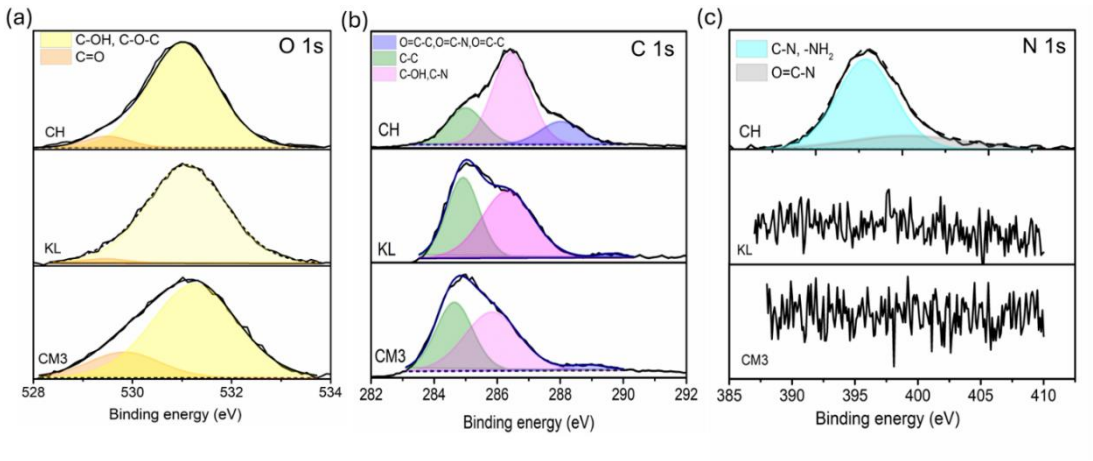

Figure S5.8. The XPS spectra, O 1s (a), C 1s (b), and N 1s (c) of CH, KL, and CM3.

Table S5.4. Compressive strain for ACH, AKL, ACM1, ACM2, and ACM3 aerogels.

Sample ID	Compressive strain (MPa)
ACH	0.24
AKL	0.22
ACM1	0.45
ACM2	0.37
ACM3	0.34

References

[1] Gharehkhani, S.; Ghavidel, N.; Fatehi, P. Kraft Lignin-Tannic Acid as a Green Stabilizer for Oil/Water Emulsion. *ACS. Sustain. Chem. Eng.* **2019**, *7*, 2370–2379.

[2] Kong, F.; Wang, S.; Price, J. T.; Konduri, M. K. R.; Fatehi, P. Water Soluble Kraft Lignin-Acrylic Acid Copolymer: Synthesis and Characterization. *Green Chemistry* **2015**, *17*, 4355–4366.

[3] Dhaliwal, G. S.; Gupta, N.; Kukal, S. S.; Kaur, M. Standardization of Automated Vario EL III CHNS Analyzer for Total Carbon and Nitrogen Determination in Soils. *Commun. Soil. Sci. Plant. Anal.* **2011**, *42*, 971–979.

[4] Yi, Y.; Liu, P.; Zhang, N.; Gibril, M. E.; Kong, F.; Wang, S. A High Lignin-Content, Ultralight, and Hydrophobic Aerogel for Oil-Water Separation: Preparation and Characterization. *Journal of Porous Materials* **2021**, *28*, 1881–1894.

[5] Konduri, M. K.; Kong, F.; Fatehi, P. Production of Carboxymethylated Lignin and Its Application as a Dispersant. *Eur. Polym. J.* **2015**, *70*, 371–383.

[6] Fodil Cherif, M.; Trache, D.; Brosse, N.; Benaliouche, F.; Tarchoun, A. F. Comparison of the Physicochemical Properties and Thermal Stability of Organosolv and Kraft Lignins from Hardwood and Softwood Biomass for Their Potential Valorization. *Waste Biomass Valorization* **2020**, *11*, 6541–6553.

[7] Schieppati, D.; Dreux, A.; Gao, W.; Fatehi, P.; Boffito, D. C. Ultrasound-Assisted Carboxymethylation of LignoForce Kraft Lignin to Produce Biodispersants. *J. Clean. Prod.* **2022**, *366*, 132776.

[8] A-aminodiethylacetic acid. *Organic Syntheses* **1942**, *22*, 13.

Appendix 6A: Supplementary information: Pickering or non-Pickering dilemma: a complicated system of anionic lignin incorporated oil-water emulsions

*Saba Khodavandegar[1,2,3], Ulrica Edlund[2], Peter Rättö[3], Illia Dobryden[3], Pedram Fatehi[*1,4]*

Under review in Colloid and Interface Science

[1] Biorefining Research Institute, Lakehead University, 955 Oliver Road, Thunder Bay, Ontario, P7B 5E1, Canada.

[2]Fibre and Polymer Technology, KTH Royal Institute of Technology, Stockholm, Sweden.

[3]RISE Research Institutes of Sweden, Drottning Kristinas vag 61, 114 28 Stockholm, Sweden.

[4]Department of Chemical Engineering, Lakehead University, 955 Oliver Road, Thunder Bay, ON P7B 5E1, Canada

First author, email: skhodava@lakeheadu.ca, address: 955 Oliver Road, Thunder Bay, ON, Canada, P7B 5E1.

Corresponding author, email: pfatehi@lakeheadu.ca, address: 955 Oliver Road, Thunder Bay, ON, Canada, P7B 5E1.

Table S6.1. Taguchi design for sulfoethylation (SL).

	Factors				Response	
Sample ID	**Concentration L: SBS (mol: mol)**	**Time (h)**	**Temperature (℃)**	**pH L solution**	**Charge density (meq/g)**	**Solubility (%)**
SL1	1:1	4	40	12	1.1±0.04	97±1.7
SL2	1:1	8	80	11	1±0.01	98±0.31
SL3	1:2	8	40	13	1.2±0.01	99±0.6
SL4 **(SL)**	1:0.5	4	80	13	1.5±0.02	98±1.5
SL5	1:2	1	80	12	1±0.08	98±1.2
SL6	1:2	4	60	11	1±0.008	98±0.65
SL7	1:0.5	8	60	12	1.2±0.04	98±0.5
SL8	1:1	1	60	13	0.9±0.02	99±1
SL9	1:0.5	1	40	11	0.9±0.02	87±0.9

Table S6.2. Taguchi design for carboxyethylation (CL).

Sample ID	Factors				Response	
	Concentration L: CPA (mol: mol)	**Time (h)**	**Temperature (°C)**	**pH L solution**	**Charge density (meq/g)**	**Solubility (%)**
CL1	1:2	6	60	13	1.4±0.02	99±0.8
CL2	1:0.5	6	40	11	1±0.02	97±0.3
CL3 **(CL)**	1:4	12	40	13	1.5	98±1
CL4	1:2	24	40	12	1.3±0.06	100
CL5	1:4	24	60	11	1.2±0.01	97±1.2
CL6	1:0.5	24	80	13	1.8±0.05	94±1.1
CL7	1:0.5	12	60	12	1.6	96±0.08
CL8	1:4	6	80	12	1.1±0.01	95±0.12
CL9	1:2	12	80	11	1.1±0.04	95±0.79

Table S6.3. Elemental analysis of L, SL, and CL.

Sample ID	Mw (g/mol)	CHNS (%)			
		C	H	N	S
L	-	64.59	5.15	0.06	0.4
SL	2884	58.19	4.17	0	0.80
CL	3892	58.06	4.8	0	0.36

$$\alpha = \frac{L_{OH\ -SL\ or\ CL_{OH}}}{L_{OH}} \times 100 \qquad \text{Eq. S6.1}$$

Table S6.4. Substitution degree of aliphatic, aromatic, and carboxylic OH in SL and CL reactions based on Eq. S6.1.

	Substitution, %		
Sample ID	Aliphatic-OH	Phenolic-OH	Carboxylic-OH
L	-	-	-
SL	17.7	28.8	-
CL	24.5	41	100

Table S6.5. Calculation of changes in different groups based on integration of ^{1}H NMR, ^{31}P NMR, and conductometric titration.

	Phenolic (mmol/g)		**Aliphatic (mmol/g)**		**Methoxy (mmol/g)**		**Carboxylate (mmol/g)**		**Sulfonate (mmol/g)**	
ID	**H***	**P**	**H**	**P**	**H**	**P**	**H**	**P**	**H**	**P**
L	2.21	4.04	1.63	1.75	-	3.3	-	0.3	-	-
SL	1.5	2.88	1.7	1.44	-	1.6	-	0.3	-	-
CL	1.03	2.39	1.7	1.32	-	1.2	-	0.6	-	-

The calculation of aliphatic and aromatic H and OH, methoxy, sulfonate, and carboxylate from: H is the ^{1}H NMR integration, H* is the total of aromatic and phenolic H integration from ^{1}H NMR, and P is the ^{31}P NMR integration.

Table S6.6. Solubility measurements for L, SL, and CL in three different pH.

	Solubility (%)		
pH	**L**	**SL**	**CL**
3	4±1.8	8±2.1	5±3
7	20±1	98±1.5	98±1
11	100	100	100

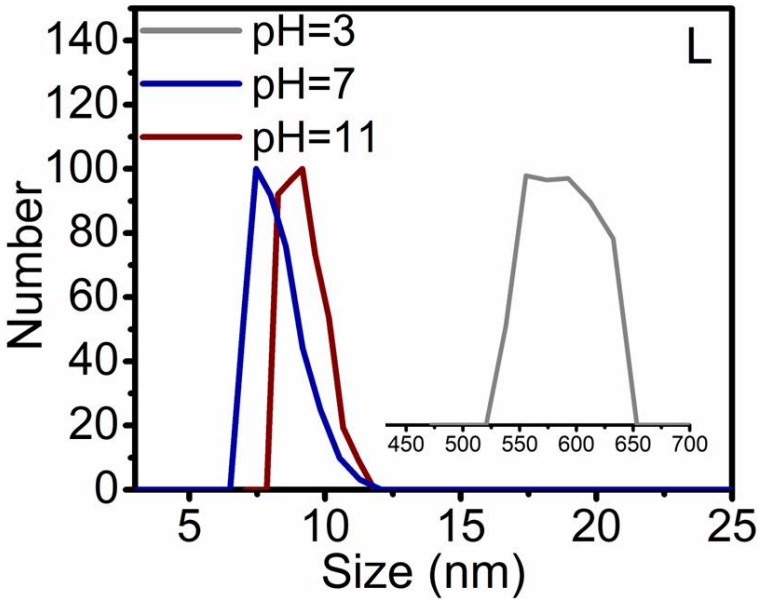

Figure S6.1. Particle size distribution of L in pH

.

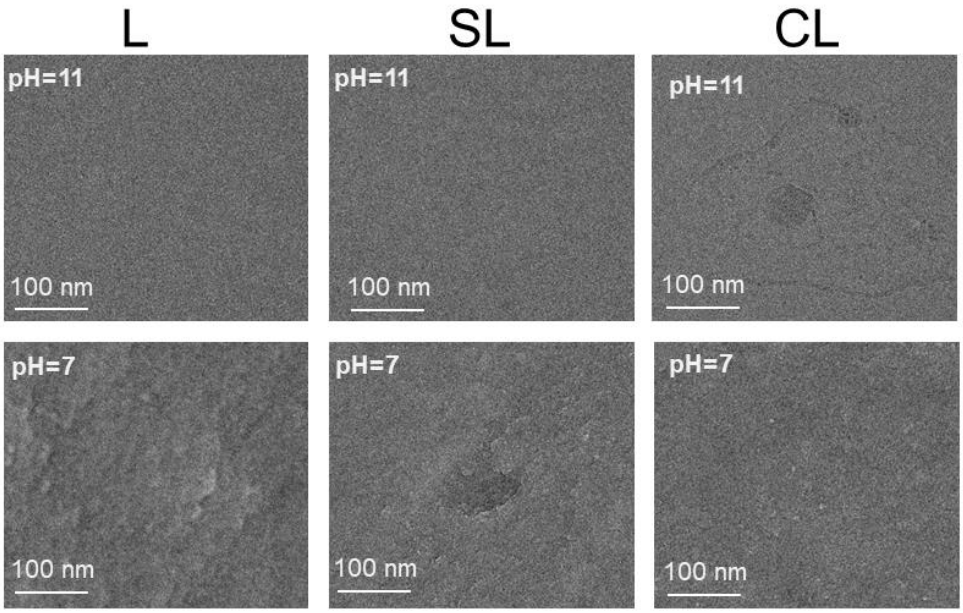

Figure S6.2. TEM images of L, SL, and CL at pH 11 and 7 in a dried state.

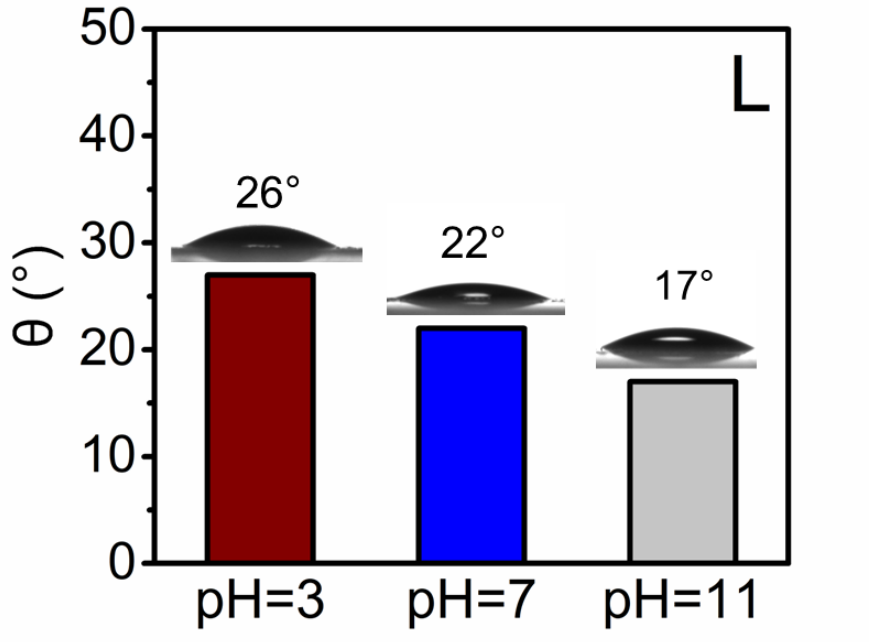

Figure S6.3. Contact angle measurement for coated L solution on glass at three different pH

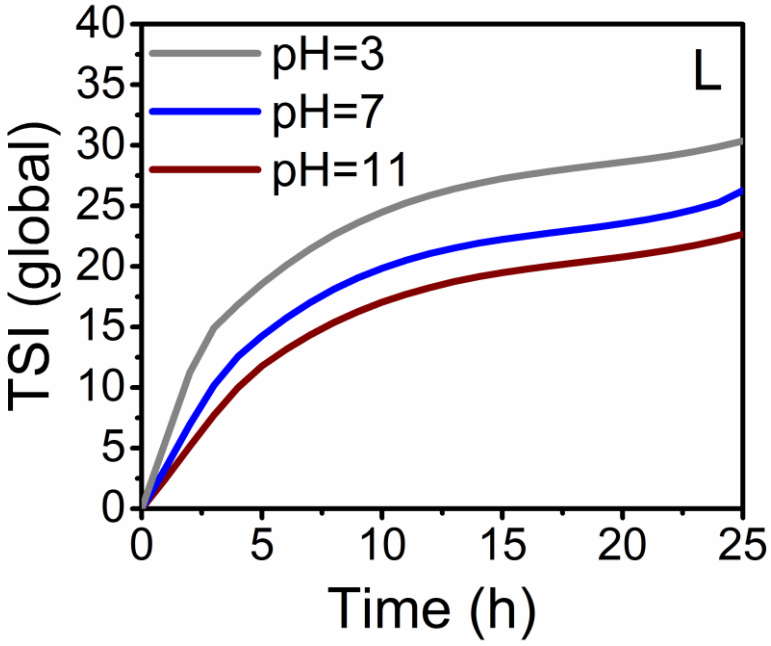

Figure S6.4. Stability analysis of L in pH 3, 7, and 11.

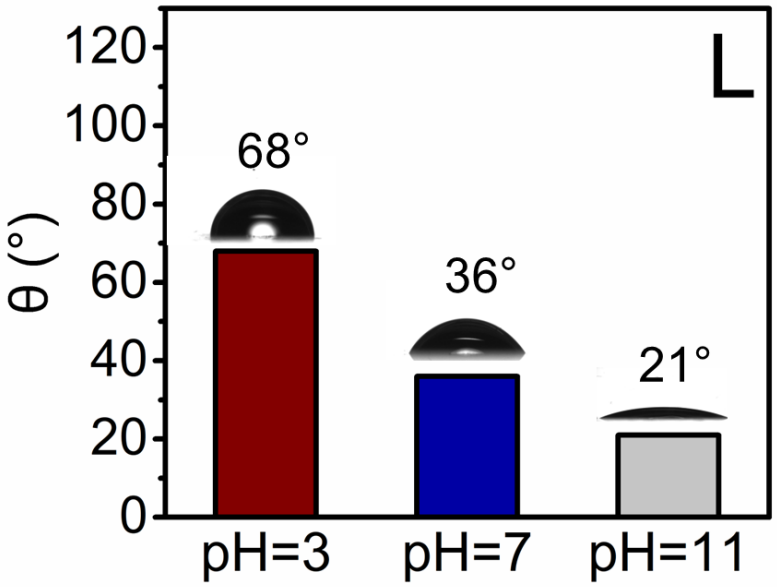

Figure S6.5. Three phase contact angles in different pH for L.

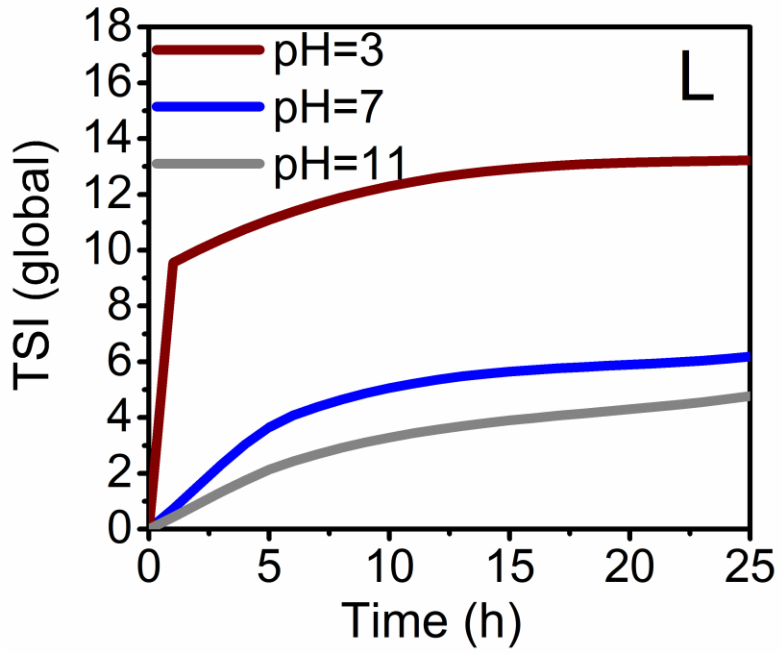

Figure S6.6. Stability analysis of L emulsions at pH 3, 7, and 11.

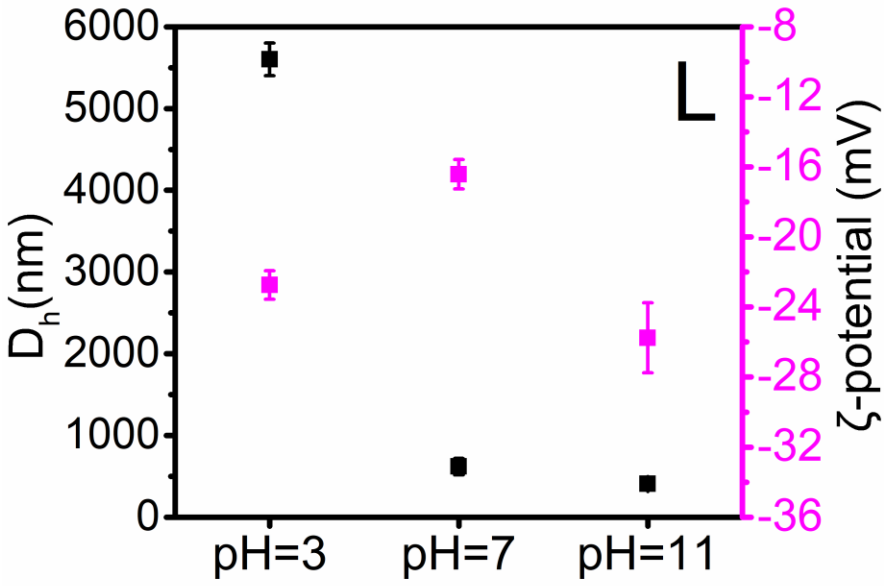

Figure S7. D_h and ζ-potential analysis of L emulsions in pH 3, 7, and 11.

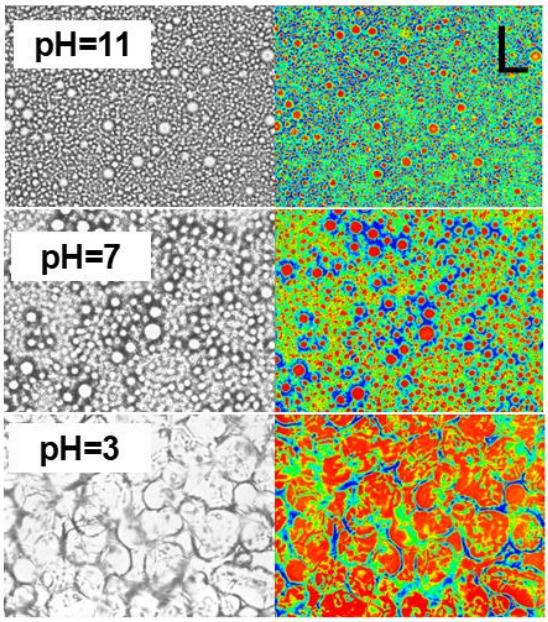

Figure S6.8. Optical micrographs of the emulsion for L in three different pH. The red color shows the oil, blue water, and green the pickering particles.

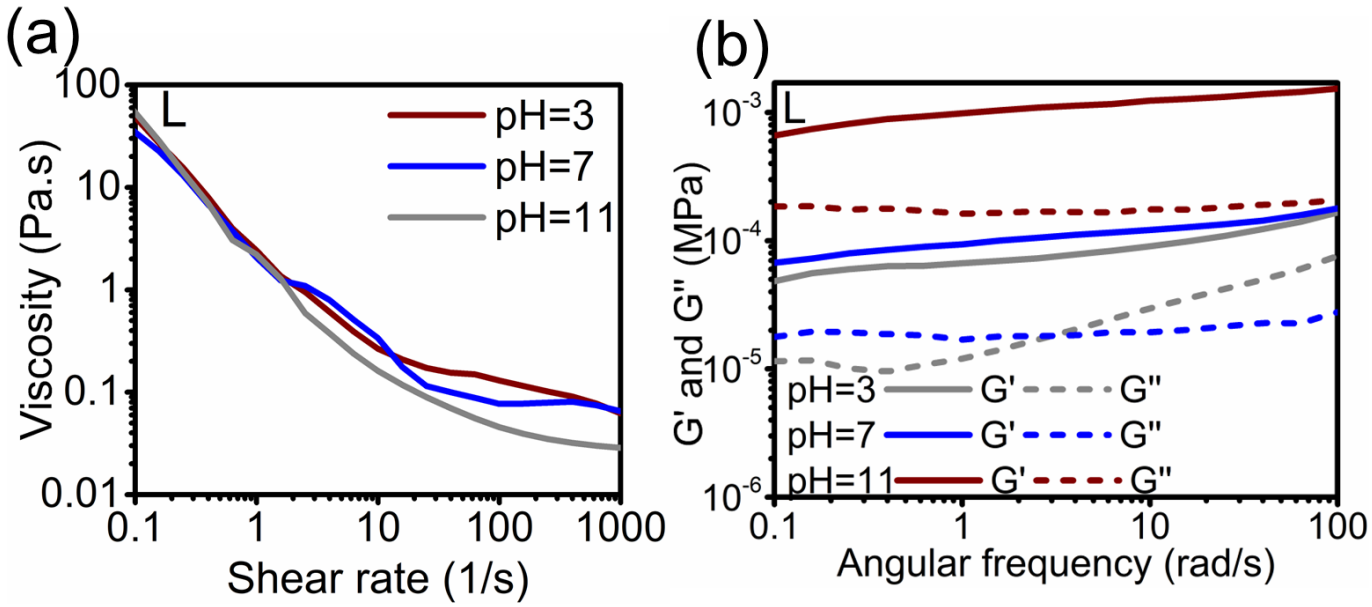

Figure S6.9. Rheological study, (a) L, viscosity as a function of shear rate, (b) L, storage and loss modulus as a function of angular frequency emulsions.